
***In situ* FTIR studies
on nanoscaled electrocatalysts
for the ethanol oxidation
in direct liquid fuel cells**

vorgelegt von
Dipl.-Ing.
Nina Felicitas Erini
aus Aachen

Von der Fakultät II – Mathematik und Naturwissenschaften
der Technischen Universität Berlin
zum Erlangen des akademischen Grades

Doktorin der Ingenieurwissenschaften
- Dr.Ing. –

genehmigte Dissertation

Promotionsausschuss:

Vorsitzender: Prof. Dr. T. Friedrich (TU Berlin)
Gutachter: Prof. Dr. P. Strasser (TU Berlin)
Gutachter: Prof. Dr. R.-A. Eichel (RWTH Aachen)

Tag der wissenschaftlichen Aussprache: 22. Oktober 2015

Berlin 2016

Die vorliegende Arbeit wurde unter der Leitung von Herrn Prof. Peter Strasser in der Zeit vom 15.11.2011 bis zum 30.04.2015 im Fachbereich Chemie am Institut für Technische Chemie der Technischen Universität Berlin angefertigt.

Table of Content

Zusammenfassung	iii
Abstract	iv
1. Introduction	1
1.1. Electrocatalysis	2
1.2. Direct ethanol fuel cell	3
1.3. Motivation, goals and objectives	6
2. Theoretical Aspects and experimental techniques	7
2.1. Synthesis of electrocatalysts for the electrooxidation of ethanol	8
2.2. Electrochemical <i>in situ</i> FTIR spectroscopy	12
2.3. Electrochemical methods	12
2.4. Physico-chemical characterization	16
2.5. Experimental procedures	18
2.5.1. Electrochemical characterization	18
2.5.2. Physico-chemical characterization	18
2.5.3. <i>In situ</i> Fourier transform infrared spectroscopy (FTIR)	20
3. Validation of the <i>in situ</i> FTIR electrochemical setup	21
3.1. <i>In situ</i> FTIR spectroscopy	22
3.2. Concept and design of an electrochemical <i>in situ</i> FTIR cell	29
3.3. FTIR <i>in situ</i> EOR measurements in acidic and alkaline media	35
3.4. Focus on the cell prism, penetration depth into the sample medium and resolution	37
3.5. Electrochemistry in the <i>in situ</i> cell: Ethanol and carbon monoxide oxidation	43
4. Strain effects on the catalytic properties of alloyed and dealloyed PtNi₃ surfaces studied by <i>in situ</i> ATR spectroscopy of the electrooxidation of adsorbed CO.	51
4.1. CO adsorption on catalytic surfaces: the role of CO _L intermediates for the EOR activity	52
4.2. Dealloying of bimetallic nanoparticles and strain effect on the surface	53
4.3. Experimental access to the strain effect due to dealloying: <i>in situ</i> FTIR spectroscopy	57
5. Ethanol electro-oxidation on ternary Platinum-Rhodium-Tin nanocatalysts: Insights in the atomic 3D structure of the active catalytic phase	63
5.1. Introduction	64
5.2. Experimental	66
5.3. Results and discussion	68

6.	Comparative assessment of synthetic strategies toward active Platinum-Rhodium-Tin electrocatalysts for efficient ethanol electro-oxidation	83
6.1.	Abstract	84
6.2.	Introduction	84
6.3.	Experimental section	85
6.3.1.	Catalyst preparation	85
6.3.2.	Catalyst characterization	86
6.3.3.	Electrochemical measurements	86
6.4.	Results and discussion	87
6.4.1.	Structural characterization of the Pt-Rh-Sn catalysts	87
6.4.2.	Electrochemical characterization of the Pt-Rh-Sn catalysts	89
6.5.	Conclusions	94
7.	Exceptional Activity of a Pt-Rh-Ni Ternary Nanostructured Catalyst for the Electrochemical Oxidation of Ethanol: Study of optimal oxygen-donating species for the ternary electrocatalytical system.	95
7.1.	Introduction	96
7.2.	Experimental	97
7.3.	Results and discussion	99
7.4.	Conclusions	107
8.	Exceptional early onset potential for C-C bond breaking on highly active shaped Pt₃Ni₁-Rh_x/C alloy nanoparticles as novel electrocatalysts for the Ethanol Oxidation Reaction in alkaline media	108
8.1.	Abstract	109
8.2.	Introduction	109
8.3.	Results and discussion	110
8.4.	Conclusions	121
8.5.	Experimental	121
9.	Summary and conclusions	124
9.1.	Summary	125
9.2.	Conclusions	128
9.3.	Perspectives	129
	References	131
	List of abbreviations	I
	Table of figures	II
	List of tables	VIII

Zusammenfassung

Ethanol als Brennstoff in Direkt-Alkohol-Brennstoffzellen erfüllt nahezu alle Ansprüche einer umweltschonenden, nachhaltigen Energiequelle. Der komplizierte Reaktionsmechanismus der Ethanoloxidation stellt eine große Herausforderung für Elektrokatalysatormaterialien dar, welche die C-C Bindung effizient spalten sollen. Hohe Aktivitäten müssen mit den entsprechenden Selektivitäten einhergehen um die Vergiftung der Katalysatoroberfläche durch organische Nebenprodukte zu minimieren. Ein vielversprechender Lösungsansatz für diese Problematik der Entwicklung höchst aktiver und selektiver Materialien ist der Zusatz von Co-Katalysatoren zu Platin.

Das Ziel dieser Arbeit war die Entwicklung neuer, hoch aktiver Elektrokatalysatorkonzepte zur Ethanoloxidation in sauren und alkalischen Elektrolyten, wobei Synthese-Aktivitäts-Beziehungen und Selektivitätsuntersuchungen im Mittelpunkt standen. Um basierend auf etablierten Konzepten neue ternäre Nanokatalysatoren mit verbesserten elektrokatalytischen Oberflächeneigenschaften zu entwickeln wurden Platin und Rhodium mit Zinn oder Nickel kombiniert, was dank gleichzeitiger erleichterter Adsorption von Ethanol, verbesserter Spaltung der intramolekularen Bindung und erhöhter Bereitstellung von Sauerstoffspezies auf der Oberfläche zur vollständigen Oxidation von Ethanol führt. Ihre Aktivität wurde in Abhängigkeit der Zusammensetzung, Morphologie, Bulk- und Oberflächenstruktur und Syntheseinflüssen untersucht. Anschließend wurde die Selektivität der Elektrokatalysatorkonzepte mit einem optimierten, selbstentwickelten *in situ* FTIR Messaufbau untersucht. Im Gegensatz zu gängigen *in situ* FTIR Messmethoden entsprachen die hier gemessenen elektrochemischen Daten denen von standardisierten Messmethoden der Elektrokatalyse und zeigen wenig bis keine Begrenzungen durch Massentransport. Die aufgenommenen Spektren von gelösten und adsorbierten Spezies auf und über dem Katalysator konnten verschiedenen Reaktanden der Ethanoloxidation zugeordnet werden.

Die in dieser Arbeit präsentierten Ergebnisse zeigen, dass höher geordnete, formkontrollierte ternäre Bulkstrukturen zu höheren Konzentrationen aktiver Oberflächenensembles bestehend aus allen drei Metallen führen. Die hier vorgestellten Katalysatoren übertrafen die Aktivität bisheriger, vergleichbarer Katalysatorkonzepte sowohl in sauren als auch in alkalischen Elektrolyten und besitzen die Fähigkeit schon bei niedrigen Überpotentialen nahe dem Gleichgewichtspotential die C-C Bindung zu spalten und Ethanol erfolgreich zu oxidieren.

Abstract

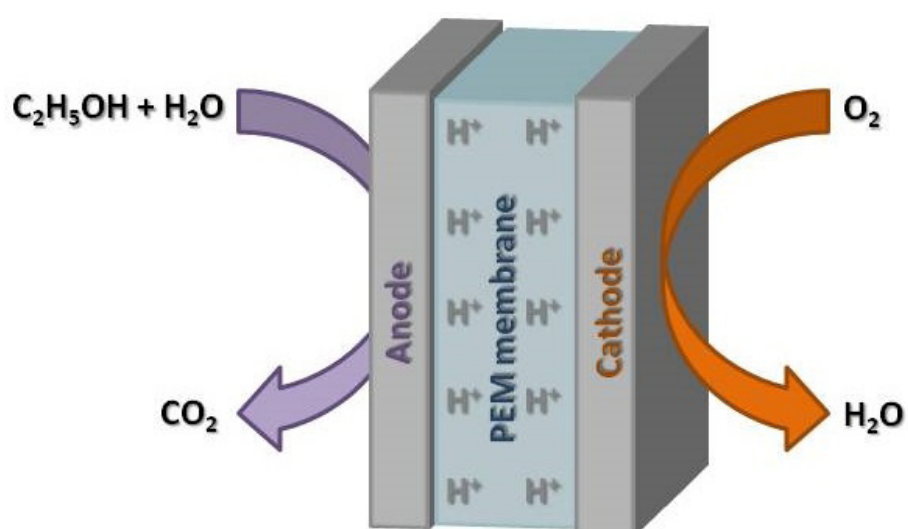
Ethanol in direct liquid fuel cells is an almost ideal source for sustainable energy. Efficient electrocatalytic material research for its oxidation has to deal with a complicated reaction mechanism, i.e. the need for C-C bond breaking. High activity and selectivity are both desired in unison while avoiding poisoning effects due to possible organic byproducts. In order to address these problems of incomplete oxidation of ethanol efforts to develop highly active and selective electrocatalysts have been focused on the addition of co-catalysts to platinum.

The overall objective of this thesis was to develop new highly active electrocatalytic concepts for the ethanol oxidation reaction in acidic and alkaline media, while emphasizing on synthesis-activity relations and selectivity investigations. To achieve this, platinum and rhodium have been combined with either tin or nickel, aiming for novel ternary single phased nanocatalysts with enhanced electrocatalytic surface properties in order to successfully adsorb ethanol, facilitate the intermolecular bond break and supply active oxygen-containing species for the complete oxidation at the same time. Their activity was matched to changes in composition, morphology, bulk and surface structure and synthetic route influences. Subsequently, the corresponding selectivity of the electrocatalytic concepts was investigated with an optimized custom build *in situ* FTIR cell setup. In contrast to other *in situ* FTIR setups, the electrochemical current responses inside the FTIR setup reported here were similar to standard electrochemical measurements and showed little to no mass transport limitation within the measuring requirements. *In situ* FTIR spectra of adsorbed species on the catalyst film as well as features from the electrolyte over the catalyst film could be detected and correlated to species involved in the electrocatalytic oxidation of ethanol.

In summary, this work determined that a higher order of a shape-controlled ternary bulk structure results in higher concentrations of active surface site ensembles consisting of all three metals. Their activity outperformed previously reported comparable catalytic systems in both acidic and alkaline media and hold the possibility to oxidize ethanol and break the C-C bond easily at early onset potentials nearly as low as the reversible potential.

1. Introduction

This chapter describes the aims of the research in this thesis and gives a short summary of the concepts of electrocatalysis, fuel cell research, and provides a short overview of full cell research related in particular to ethanol electro-oxidation. A more detailed introduction to the concept of an in situ electrochemical vibrational spectroscopic approach to fuel cell catalyst research is presented in chapter 3.



1.1. Electrocatalysis

Catalysis, as first mentioned by Berzelius in 1836, can be defined as „the effect produced in facilitating a chemical reaction, by the presence of a substance, which itself undergoes no permanent change”.¹ In more scientific terms it is the process of increasing the rate of a chemical reaction by a substance, the catalyst, which is not consumed by the chemical reaction. The four defining properties of a catalyst are its activity, selectivity, stability and for application purpose also its cost. The activity of a catalyst relates to the overall rate of the catalytic conversion of the educts whereas the selectivity is a measure for the successful acceleration of the reaction to desired products. Although theoretically a catalyst should not change during the catalytic reaction and, therefore, be re-usable indefinitely, in practice it can deactivate over time. A life span as high as possible with stable activity is an important criterion for any catalyst. The reduction of the overall costs of any chemical process determines also the industrial applicability of novel catalyst systems and leads to new approaches such as the reduction of expensive novel metal contents.

Electrocatalysis as a subgroup of catalysis in general is concerned with chemical reactions that transfer charge (electrons) across an interface between chemical phases, such as the interface between a solid (electrode surface) and a liquid (electrolyte) phase. Electrochemical reactions can occur at the surfaces of the electrode: an electrocatalyst is therefore defined as a catalyst that functions at said interface and accelerates either the provision (oxidation reaction) or withdrawal (reduction reaction) of electrons from the electrode. By connecting two different electrodes in an external circuit, the electric current between those two (i.e. the flow of electrons) gives information about the amount of exchanged electrons and therefore about the reaction itself.

In case of electrocatalysts the properties of the electrode surface are influenced by raising or dropping the electrode potential, thereby increasing or decreasing its affinity for electrons and promoting or inhibiting reactions at the electrode surface. The overpotential is defined as the difference between the electrode potential at which a reaction should theoretically occur and the potential at which it actually takes place. For example, the electrooxidation of ethanol on platinum has an onset around 0.4 V vs. RHE (reversible hydrogen electrode) while the theoretical onset lies just above 0.1 V vs. RHE, meaning the oxidation of ethanol on platinum has an overpotential of $\eta \approx 0.3$ V.

Identification of intermediates and reactants on the heterogeneous interface of any given electrocatalytic reaction has as much interesting as well as promising challenges for modern research. Molecular vibrations caused by changes of species dissolved in the electrolyte as well as adsorbed species on the interface between the electrolyte and the electrode can be detected by *in situ* Fourier transform infrared (FTIR) spectroscopy and while electrocatalytic activity is measured potentiostatic at

the electrode itself. These linked selectivity-activity information can be applied to the research fields of direct ethanol oxidation fuel cells (DEFC), where ethanol is oxidized on the anodic side of a fuel cell stack in a complicated multifunctional pathway. The ethanol oxidation reaction (EOR) proceeds often incomplete, resulting in a number of byproducts, rather than complete oxidation to CO_2 .²⁻⁶

1.2. Direct ethanol fuel cell

Development of DEFC as alternative power sources has been a subject of intensive studies for fundamental and practical applications, e.g. the development of compact portable power as well as electric vehicle range extenders operating at high temperatures.⁷⁻¹⁰ Equipping a liquid as the fuel on the anode side instead of hydrogen, as in the standard hydrogen/oxygen fuel cells, has a number of distinct advantages: Liquid fuels, like small molecule alcohols (methanol, ethanol), have higher volumetric and gravimetric energy densities, better energy efficiencies, and offer easy handling, storage and transportation, contrary to gaseous fuels.¹¹ Whereas methanol is of particular interest for mobile applications, such as electric vehicles, ethanol has some important advantages, such as a higher energy density (8 kWh kg^{-1} vs. 6 kWh kg^{-1} , respectively), low toxicity, biocompatibility and abundant availability. Ideally, ethanol could be produced by the fermentation of biomass, such as agricultural waste, capturing carbon dioxide (CO_2), a greenhouse gas, in the process. Since the oxidation of ethanol would release the captured carbon dioxide, the entire cycle would then be carbon neutral, i.e. no overall CO_2 emission or capture.

There are a number of issues in the development of DEFCs that have to be considered:

- The oxidation of ethanol does not only produce carbon dioxide, but also yields undesired products, such as acetaldehyde and acetic acid, which have a significant lower energy output and are unwanted due to their harmful nature.^{12,13}
- The oxidation of ethanol to carbon dioxide can proceed through intermediates adsorbing strongly to the electrode surface, inhibiting the catalytic activity of the electrode.¹³
- The high costs of DEFC are due to the requirement of large amounts of noble metal catalysts to compensate their lower catalytic activities in order to generate a sufficiently high power output.
- Since the oxidation of ethanol is quite slow near the equilibrium potential a high overpotential is required, which decreases the efficiency of the fuel cell.⁷
- Considerable decrease in efficiency can also result from dissolved ethanol that crosses over to the cathode side of the fuel cell.¹⁴

DEFCs can be operated in alkaline and acidic media, reaching higher oxidation and reduction rates in alkaline electrolytes resulting in a higher energy output. Since carbon dioxide is quickly converted to carbonate in alkaline media, again decreasing the efficiency, the energy output is significantly lower in comparison with acidic media.¹⁵

As already mentioned, ethanol is not easily completely oxidized to CO₂ and water. This is either attributed to difficulties in the adsorption and cleavage of C-C bonds in ethanol or to the formation of CO-intermediates leading to poisoning of the active sites on Pt catalysts.³⁻⁶ It is generally accepted that the oxidation of ethanol proceeds *via* a dual pathway.^{5,16-28} As shown in Figure 1.1 ethanol can be oxidized to C2 structured acetaldehyde and subsequently to acetic acid, transferring only 4 electrons in the process. Acetic acid marks a ‘dead end’ in the reaction pathway, since its further oxidation is very difficult under ambient conditions.¹⁸ Alternatively, the C-C bond of ethanol and also acetaldehyde can be broke, yielding adsorbed single carbon species like CO_{ads} and CH_{x,ads}.^{17,29} There is still some controversy whether the presence of CO intermediates is a key to effective ethanol oxidation,³⁰⁻³² or on the contrary, that the absence of CO intermediates correlates with promoted early onset complete oxidation.⁵ The intermediate species can subsequently be oxidized to CO₂ yielding 12 electrons in total. Unfortunately, this process requires a high overpotential,^{18,33} reducing the overall efficiency.

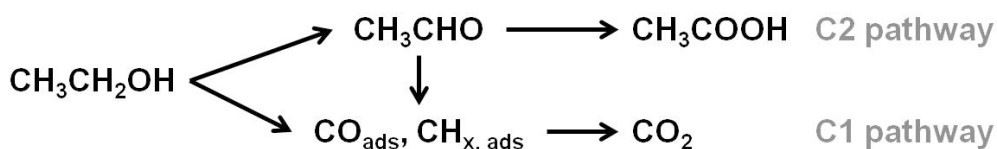
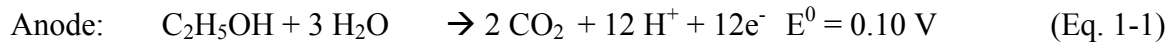


Figure 1.1: Schematic representation of the dual pathway mechanism for the electrooxidation of ethanol.

Basic working principle of a fuel cell

A fuel cell is in principle a galvanic cell, which converts the energy released in a chemical reaction into electrical energy through an electrical current. The schematic drawing of a basic DEFC (Figure 1.2) demonstrates its basic working principle: the cell consists of two electrodes, which are separated by a semi permeable proton exchange membrane (PEM). An electrolyte provides electric conductance in the fuel cell between the two electrodes, which are also connected in an external circuit. The fuel (ethanol EtOH) and the oxidant (oxygen O₂) are supplied to the two electrodes, the fuel to the anode and the oxidant to the cathode. These half cell reactions taking place in the DEFC are given in Eq. 1-1 and Eq. 1-2, respectively.



Combined these half cell reactions give the overall reaction in Eq. 1-3.

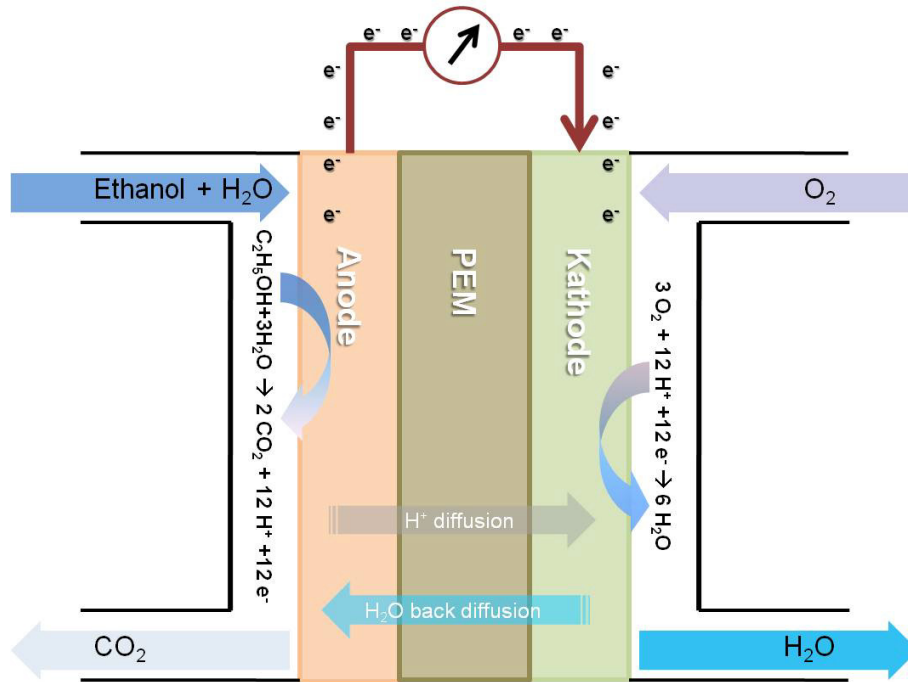


Figure 1.2: Working principle of a direct ethanol fuel cell.

At the anode, the electrode at which the electrons are provided by the chemical reaction, ethanol is, in theory, converted to carbon dioxide, Protons and electrons in an oxidation reaction (Eq. 1-1). The protons enter the electrolyte and are transported to the cathode, the electrode at which the electrons are consumed by the chemical reaction. The electrons flow through the external circuit toward the cathode, providing an electrical current. Oxygen gas is supplied to the cathode and the oxygen molecules are recombined to form water molecules in a reduction reaction with the protons from the electrolyte and electrons coming from the external circuit. The overall reaction is, therefore, a formation of CO₂ and water from ethanol and oxygen (Eq. 1-3). The theoretical potential provided by an ethanol/oxygen fuel cell under standard conditions is 1.13 V, the difference in the equilibrium potentials of the half cell reactions.³⁴

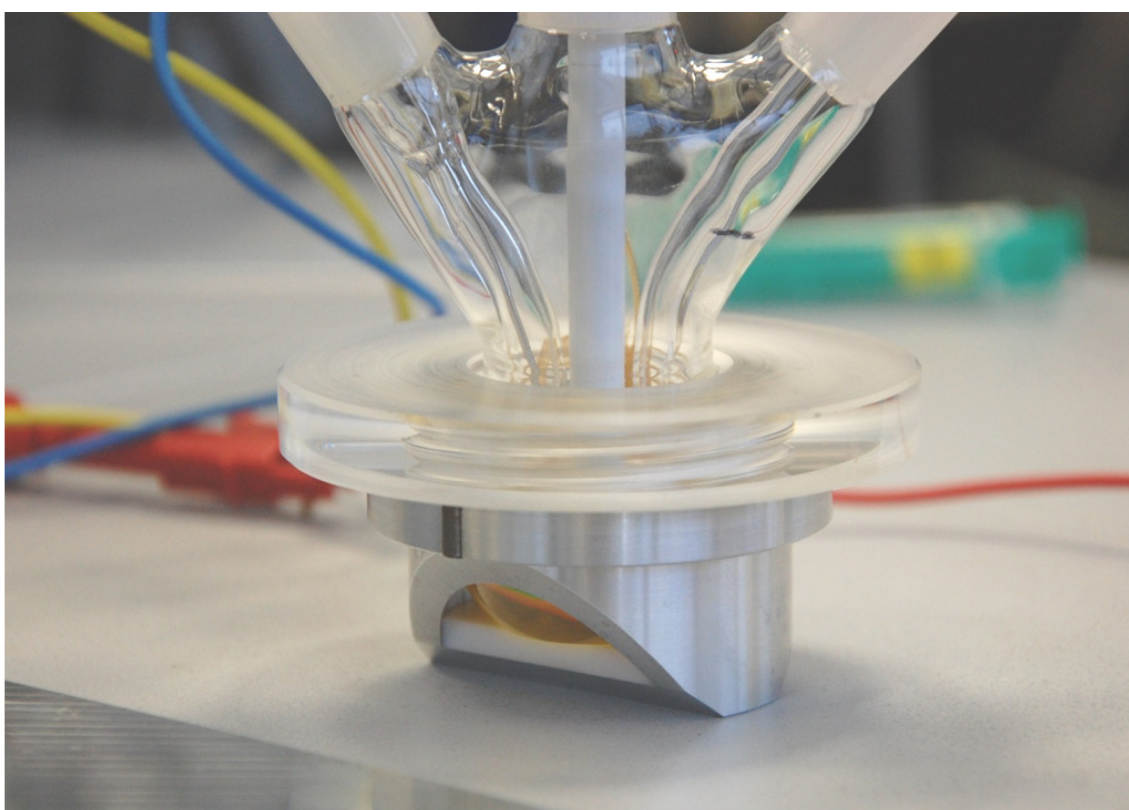
1.3. Motivation, goals and objectives

Aim of this thesis is the establishment of a new highly electrocatalytical active system for the ethanol oxidation and its probing with an optimized *in situ* FTIR cell setup. Efforts to develop highly active and selective electrocatalysts for the EOR to CO₂ have been focused on the addition of co-catalysts to platinum.³⁵⁻³⁹ Alloying Pt with highly oxophilic transition metals such as Rh, Ni or Sn has been a promising strategy to modify the electrocatalytic surface properties of Pt in order to supply active oxygen-containing species for the ethanol electrooxidation. In this work, platinum and rhodium have been combined with tin or nickel aiming for novel ternary single phased nanocatalysts with increased EOR activity. Structure-activity relations are drawn from *in situ* FTIR electrochemical experiments on these catalysts.

This chapter gives a brief introduction of the basic principles this work is based on. In chapter 2 detailed descriptions of the applied experimental techniques are introduced. The design process and validation of the *in situ* FTIR cell is presented in chapter 3. Chapter 4 presents first *in situ* vibrational band shifts of adsorbed species with CO as a probing molecule and its oxidation of differently dealloyed platinum-nickel surfaces. A novel ternary single phased hexagonal catalytic system of platinum, rhodium and tin as nanoparticle electrocatalyst for the electrooxidation of ethanol is introduced in chapter 5 followed by a comparative study of different synthesis methods for these catalysts in chapter 6. Building on the insights of the previous two chapters, the subsequent chapter 7 is about the determination of the optimal oxygen-donating species for the ternary electrocatalytical system and compares nickel or tin in combination with platinum and rhodium. Chapter 8 finally addresses the shape control of the optimal ternary system of platinum, rhodium and nickel and reports exceptionally early onset potentials for octahedral nanoparticles.

2. Theoretical Aspects and experimental techniques

This chapter gives a short overview of the experimental setup, the synthesis and techniques employed in the research described in this study. Both electrochemical techniques and in situ characterization techniques are discussed briefly. All equipped analyzing techniques as well as synthesis protocols for the studied catalysts are given in more detail in the respective chapters.



2.1. Synthesis of electrocatalysts for the electrooxidation of ethanol

Noble metal anode catalysts for DEFC are being designed to oxidize ethanol highly effective and selective to CO₂ in order to avoid the poisoning effect of adsorbed intermediate species during oxidation reaction. Therefore, Pt is combined with highly oxophilic transition metals such as Ru or Sn in order to efficiently oxidize adsorbed molecular fragments while reducing the cost of the catalyst considerably.^{2,40} To achieve this goal, the oxophilic component is assumed to be present as an oxide species, such as OH, at the surface of the operating catalyst. Significant enhancement of the electrocatalytic activity of platinum has been reported for a variety of binary combinations like: PtRu,⁴¹⁻⁴⁷ PtSn,⁴⁸⁻⁵² and PtRh.⁴⁶ It is also known that nanocrystalline Pt and its Ni based binary alloy belong to the most active binary catalysts for the catalytic oxidation of organic molecules.⁵³⁻⁵⁵ The presence of Sn in a PtSn catalyst favors dissociative adsorption of ethanol. Regarding the optimum Sn bulk composition on the catalyst, Lamy *et al.*⁵⁶ have reported that the most favorable Pt/Sn content ratios in a wide range (9:1–4:1), whereas Zhou *et al.*⁵⁷ found the optimum Sn content in the range 33–25 wt.%. Further studies on the effect of the surface composition on a well-defined alloy single-crystal are required. In terms of the mode of action of Sn in PtSn ethanol oxidation catalysts, strong disagreement exists. Colmati *et al.*⁵⁸ suggest that the high selectivity of this type of catalyst toward the oxidation of ethanol to CO₂ is attributed to the facility to break the C–C bond at lower potentials. However, results from Wang *et al.*⁵⁹ conclude that the addition of Sn does not enhance the activity for C–C bond breaking.

For this reason, the task remains unsolved to find a catalyst with the ability to improve complete oxidation of ethanol to CO₂ at lower potentials. Ternary alloys present higher activities than the original mono- and bimetallic ones, as the addition of a third component usually modifies the electronic and structural characteristics of the alloys. In recent years, many groups have paid special attention to the performance of ternary alloys with oxophilic atoms, such as PtRuSn,⁶⁰ PtRhSn⁶¹ or PtIrSn⁶². It is generally accepted that the presence of oxophilic atoms in the surface alloy enhance the oxidation of water, leading to the early formation of adsorbed hydroxides, which can act as an oxidant of the strongly adsorbed intermediate species. Kowal *et al.*⁵ have shown that their PtRhSnO₂/C electrocatalyst is capable of effectively splitting the C–C bond in ethanol at room temperature in acid solutions, facilitating its oxidation to CO₂ at low potentials with high efficiency. The reported catalytic activity of this electrocatalyst is about 100 times higher than the corresponding activity of Pt/C. The authors suggest that the activity is due to the synergy between the three constituents of the electrocatalyst. Furthermore, they propose that the dissociation of water occurs on the SnO₂, providing

OH species that oxidize the intermediate CO at Rh sites whereas the Pt atom facilitates the ethanol dehydrogenation.

Beyhan *et al.*² studied the catalytic effect of Ni and Rh added to PtSn catalyst and its influence on the cleavage of ethanol using *in situ* FTIR. According to them, Ni and Rh are more beneficial for the complete oxidation than the addition of Pd or Co. Soundararajan *et al.* synthesized a set of Pt and Pt-Ni alloy nanoparticle catalysts by electrochemical deposition, showing that the Pt-Ni alloy formation leads to higher activities in alkaline media for EOR.⁶³ Bonesi *et al.* investigated high surface area carbon-supported binary PtSn and ternary PtSnNi and PtSnRh catalysts for EOR at elevated temperatures, concluding that the ternary catalysts show elevated activities.⁶⁴

Figure 2.1 shows a schematic visualization of the different catalytic systems for the electrooxidation of ethanol investigated in this thesis. A binary PtNi system was used to validate the surface sensitivity of the new *in situ* FTIR setup used in this thesis. A variety of ternary PtRhSn nanoparticles supported on carbon were investigated in order to determine the best synthesis route towards a high concentration of active surface site ensembles. Ternary PtRhNi nanoparticles supported on carbon were used to investigate the influence of the oxygen donating species, Sn or Ni, and shape control of the synthesis was conducted to investigate selectivities on the catalyst surface.

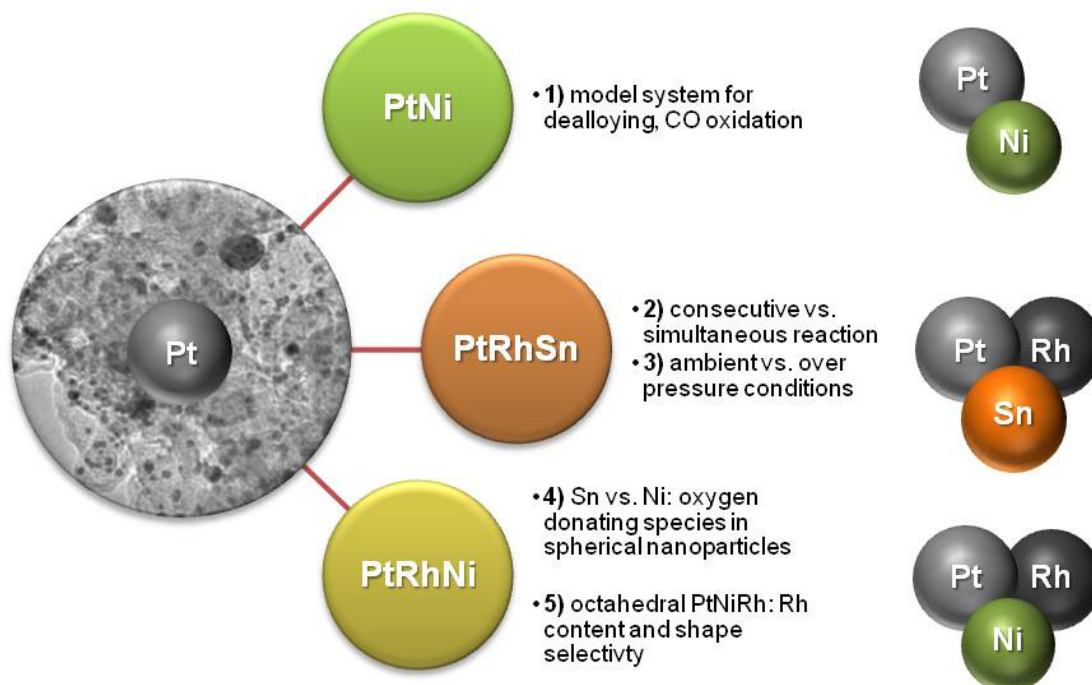


Figure 2.1: Schematic visualization of the different catalytic systems investigated for their ethanol oxidation reactivity (PtRhSn and PtRhNi systems) and for their CO oxidation behavior (PtNi).

PtNi electrocatalytic materials for CO oxidation

The binary combination of platinum and nickel is well known as an outstanding electrocatalytic material for the electroreduction of molecular oxygen. The activity of PtNi electrocatalysts is enhanced for dealloyed materials with core-shell like structures.^{54,65,66} Platinum enriches at the surface of the structure, which causes modified electronic properties due to strain effects resulting from nickel layers below the platinum surface layers. Binary PtNi is used in this thesis as a model system to study the *in situ* FTIR system and to gain better insights in the CO oxidation activity influence of the dealloying process.

PtRhSn electrocatalytic materials for EOR

As already mentioned above, the catalytic activity of ternary Pt–Rh–Sn materials is generally superior to that of their binary relatives, but important structural insights about the catalytically active bulk and surface phase are still missing. In this thesis a variety of different ternary electrocatalysts for the electrochemical ethanol oxidation has been studied. Therefore, a standard polyol synthesis method in dioctylether solvent by Loukrakpam *et al.*⁶⁷ was modified as depicted in Figure 2.2. The influence of different synthesis routes for the combination of platinum with rhodium and tin led to a multitude of electrocatalysts with different activities and selectivities towards the complete oxidation of ethanol. The detailed three-dimensional atomic arrangement of Pt, Rh, and Sn atoms of the active catalytic phase was investigated, as well as the question whether crystalline homogeneous single phase materials, crystalline multiphase materials, or even phases with limited structural coherence (partially amorphous phases) are preferred. Therefore, the sequence in which each metal component entered the synthetic process of the final catalyst material was varied, as well as the synthesis pressure and supporting conditions of the best PtRhSn/C synthesis route. The reaction temperature was controlled by a heating mantel in ambient pressure conditions or a synthesis microwave, allowing higher pressures during the synthesis of the nanoparticles.^{68,69}

PtRhNi electrocatalytic materials for EOR

Ternary PtRhNi electrocatalyst were synthesized by a polyol synthesis route as depicted in Figure 2.3. The influence of the different oxygen donating species (tin or nickel) was investigated by comparing the spherical PtRhSn with spherical PtRhNi electrocatalytic materials. Furthermore, shape selective octahedral PtRhNi electrocatalysts with varying Rh content were synthesized by a wet-chemical approach with metal carbonyls present during the reduction process, and their activity was contrasted to their spherical equivalent.

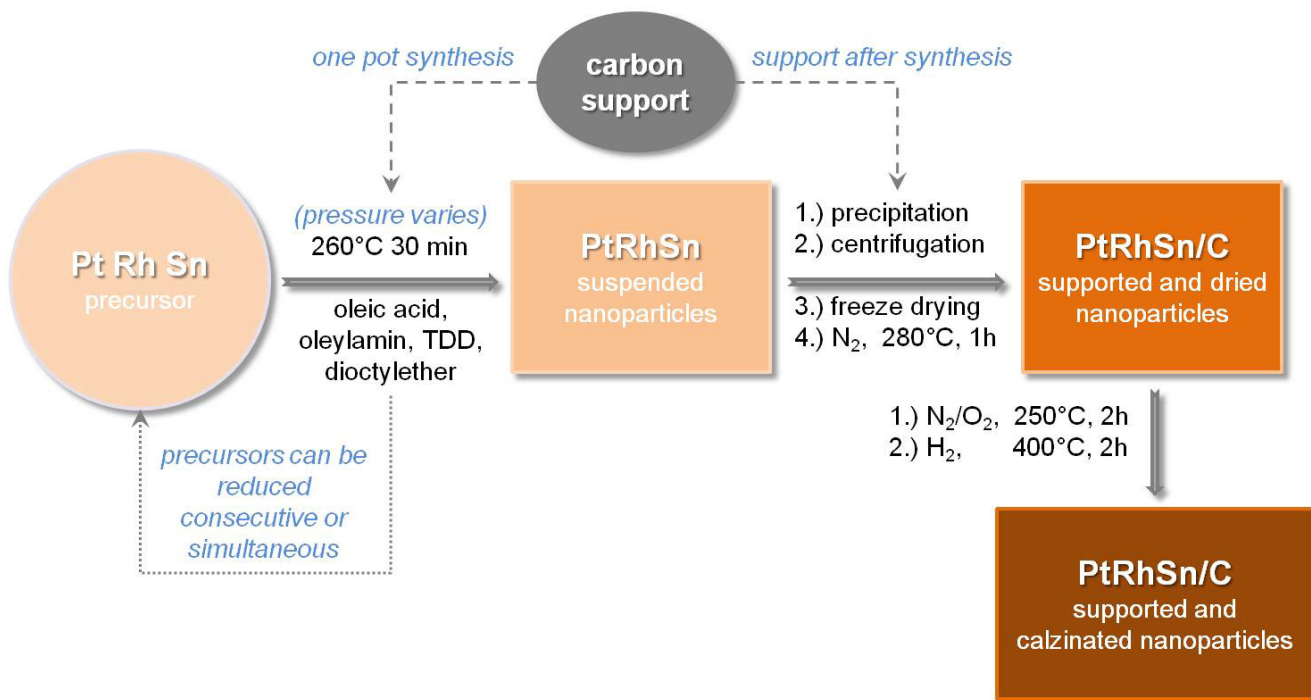


Figure 2.2: Synthesis scheme for the platinum-rhodium-tin containing electrocatalysts and the implemented variations that were used in this thesis. All precursors could be reduced consecutive or simultaneous, under different pressure conditions, and carbon support could be added during or after the reduction.

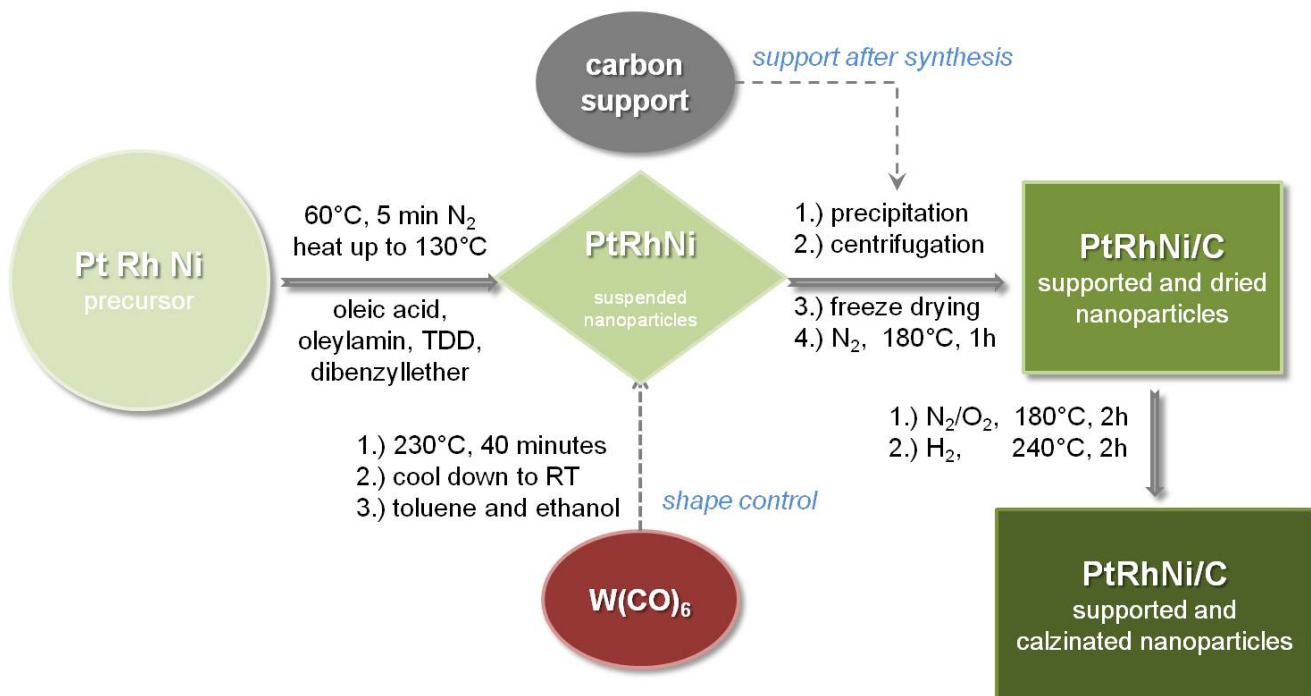


Figure 2.3: Synthesis scheme for the platinum-rhodium-nickel containing electrocatalysts and the implemented variations that were used in this thesis. All precursors could be reduced consecutive or simultaneous, under different pressure conditions, and carbon support could be added during or after the reduction.

2.2. Electrochemical *in situ* FTIR spectroscopy

Composition, structure and reaction dynamics at the electrode-electrolyte interface are most frequently probed with vibrational spectroscopy. Whereas an assortment of elaborate optical techniques has been introduced to address the experimental need of high sensitivity combined with high selectivity and depending on the experiment design, very short response times, *in situ* FTIR spectroscopy offers some distinctive advantages.⁷⁰ External reflectance (ER) spectra obtained at bulk metal electrodes or attenuated total reflection (ATR) spectra obtained with highly reflecting thin metal films, respectively, are similar to transmission spectra. The molecules at the interface produce a decrease of the high IR reflectivity and retain their spectral fingerprints, associated with the vibrational modes of their functional groups. As long as the reflectivity of the surface is high, the optical properties of the substrate are small enough and can easily be calculated out of the resulting differential spectra. IR spectra are not limited to a certain group of metal substrates and are applicable for a wide range of sample types, as long as the probed molecule shows distinctive features in the vibrational region. Chapter 3 describes in detail the theory and validation of the FTIR setup used in this thesis.

2.3. Electrochemical methods

Electrochemical setup

A conventional three-electrode electrochemical cell is shown in Figure 2.4. It consists of a single-compartment glass cell, equipped with a working electrode (WE), a counter electrode (CE) and a reference electrode (RE). The current of the investigated reaction passes between the WE and the CE, while a RE of known potential is connected to the WE through a circuit with high impedance, so that only a negligible current passes through the RE itself, i.e. its potential remains constant during the measurements. An equipped potentiostat controls the potential difference between the WE and RE while retrieving the resulting currents passing through the WE and CE. The CE and RE are each placed in separated compartments; the CE is connected through a frit and the RE through a Luggin-Haber capillary, both immersed in the same electrolyte as the WE. Both are chosen in a way they would not interact with the chosen electrolyte, leading to substances that may interfere with the reaction at the WE. The CE consists mostly of a noble metal wire, gauze or sheet with a larger surface area than the WE to avoid current limitations at the CE.

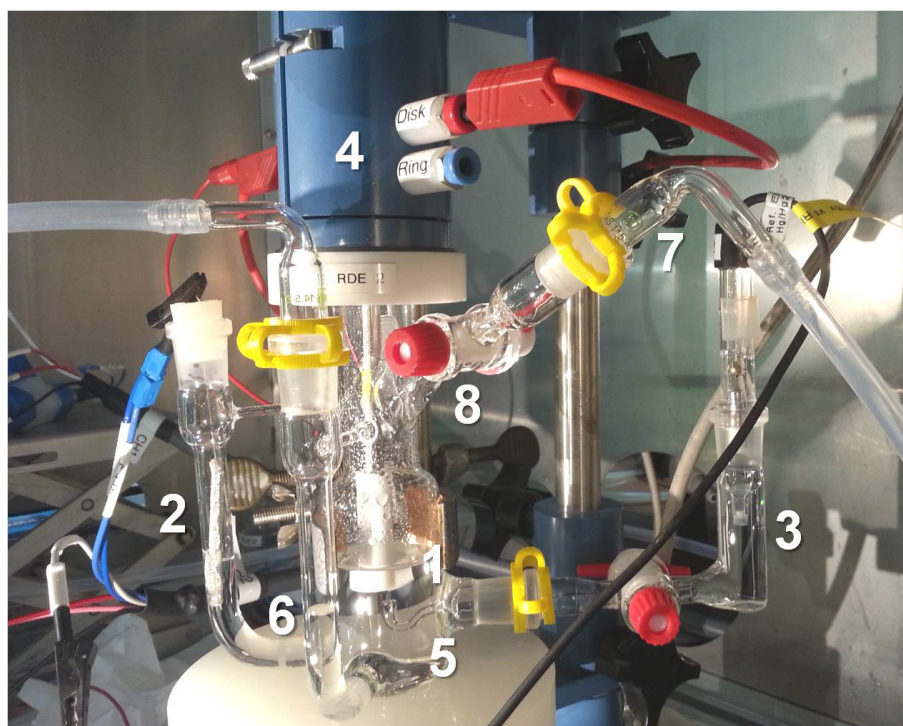


Figure 2.4: Picture of the three-electrode electrochemical cell setup. 1) working electrode WE, 2) counter electrode CE, 3) reference electrode RE, 4) rotator, 5) Luggin-Haber capillary, 6) frit, 7) gas connection and 8) faucet.

Cyclic voltammetry

The potential E (in V) of the working electrode is varied linearly in time with a certain scan rate (in $V \cdot s^{-1}$) between two vertex potentials with respect to the resulting current I (in A). During the voltammetric sweep, the measured current consists of a Faradaic and a non-Faradaic contribution. A Faradaic process is a reaction which occurs at the electrode surface and results in a charge transfer (i.e. electrons) across the electrode-electrolyte interface. According to Faraday's law the Faradaic current I_F can be defined as the change of a charge Q with time (Eq. 2-1). The charge Q relates to a Faradaic process which passes through the working electrode and equals the change of reactant N multiplied by the number of electrons exchanged in the process n_e and the Faradaic constant F . Therefore, the current can be directly related to the reaction rate v (in $\text{mol s}^{-1} \text{m}^{-2}$) for a given surface area A .

$$I_F = \frac{dQ}{dt} = n_e F \frac{dN}{dt} = n_e F A v \quad (\text{Eq. 2-1})$$

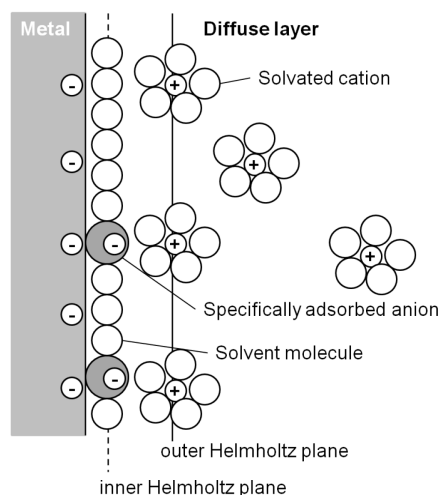


Figure 2.5: Proposed model of the double-layer region under conditions where anions are specifically adsorbed. Adapted from Bard *et al.*⁷¹

While the Faradaic processes are of main interest for an electrochemical investigation, the effect of non-Faradaic processes, e.g. processes that give rise to a current without charge being transferred across the interface, must be taken into account as well. An important non-Faradaic process is the charging and discharging of the electrochemical double layer (Figure 2.5). The charged metal plane of the electrode and a layer of electrolyte ions of opposing charge can be described as a capacitor. Therefore, a change in potential of the electrode will lead to a charging of this double layer. The double layer current is proportional to the surface area of the electrode A , the capacitance of the double layer C_{DL} and the scan rate dE/dt (Eq. 2-2). The double layer current should be so low that it becomes negligible in relation to the Faradaic current, e.g. $I_{DL} \ll I_F$.

$$I_{DL} = A \cdot C_{DL} \frac{dE}{dt} \quad (\text{Eq. 2-2})$$

Electrochemically active surface area (ECSA)

In order to assess and compare catalytic performance among Pt-containing materials, catalysis-related metrics such as surface-specific activity, Pt mass activity, and the ECSA have become routine descriptors of activity and durability within the electrochemical community. Specific activity represents the catalytic Faradaic current per active - electrochemically accessible - surface area; thus the ECSA of a Pt containing catalyst is an important empirical parameter. Under potential deposition of Hydrogen (H_{UPD}) and CO stripping are the most popular approaches to assess the ECSA for pure extended Pt catalysts as well as pure Pt nanoparticle catalysts. The evaluation of an ECSA-based specific catalytic activity of Pt and Pt-based electrocatalysts involves first the measurement of the charge Q_{ox} associated with the electrochemical oxidation of monolayers of adsorbed species such as

hydrogen or carbon monoxide. Subsequently, this charge is normalized using a surface area-specific charge Q_{ideal} of an ideal one-electron transfer (H_{UPD} , $210 \mu\text{C cm}^{-2}$) or two-electron transfer (CO , $420 \mu\text{C cm}^{-2}$), respectively, the scan rate of the measurement ν and the amount of Platinum on the electrode surface m_{Pt} (Eq. 2-3).

$$\text{ECSA} = \frac{Q_{\text{ox}}}{\nu \cdot Q_{\text{ideal}} \cdot m_{\text{Pt}}} \quad (\text{Eq. 2-3})$$

Chronoamperometry

In order to study the kinetics of an electrocatalytic system, the change of current at a constant potential over time can be examined. In chronoamperometric measurements, the potential is stepped instantaneously from one potential, where the studied reaction does not take place, to the potential of interest. The change of current of the electrochemical system on the perturbing potential step is measured over time. A detailed analysis of the current evolution with time can yield kinetic insights into electrocatalytic processes. Similar to voltammetric experiments, double layer charging/discharging should be taken into account when analyzing chronoamperometric transients. Assuming a typical electrolyte resistance of 10-100 Ω and a typical double layer capacitance of 10-100 μF , the double layer charging current should be negligible after the first 50 ms after the potential step, therefore the double layer current mainly impacts very fast processes. After the initial 50 ms, the currents can be attributed to Faradaic processes.

2.4. Physico-chemical characterization

Inductively coupled plasma optical emission spectroscopy (ICP-OES)

Inductively coupled plasma optical emission spectroscopy (ICP-OES) is a method used for detection of trace metals based on production of excited atoms and ions in a plasma that emits element specific electromagnetic radiation. The intensity of such emission gives quantitative information on concentration of a particular element.

Transmission electron microscopy (TEM)

TEM is a microscopic method that provides local information on sample structure, morphology and particle size at high magnifications with resolutions up to few nanometers or angstrom. The method is based on detection of transmitted electrons through a very thin specimen. TEM-images are visualizations of interactions of the electron beam with the atoms in the sample. At high magnifications used in high resolution TEM (HRTEM) complex wave interactions modulate the intensities on an image. This type of microscopy is based on a complex setup of various components, such as a stable high vacuum system, a well designed electron source, an optical electron beam focusing system based electrostatic or magnetic lenses. Furthermore, an elaborate aperture system provides the desired information of materials characteristics on nanometer scale.

X-ray diffraction (XRD)

X-ray diffraction is a powerful tool for crystalline particle characterization which is complementary to TEM, providing information of the bulk sample. The method supplies data with elevated statistical relevance. Crystal characteristics are governed by periodic atom arrangements defined by a unit cell of the crystal structure, which build crystal planes, as shown schematically in Figure 2.6. The technique is based on studying the diffraction patterns, which result from interference of elastically scattered x-rays. Bragg's law gives a relationship between the incident irradiation wavelength, its scattering angle and the distance between the crystal lattice planes d , where n is an integer (Eq. 2-4).

$$2d \sin\theta = n\lambda \quad (\text{Eq. 2-4})$$

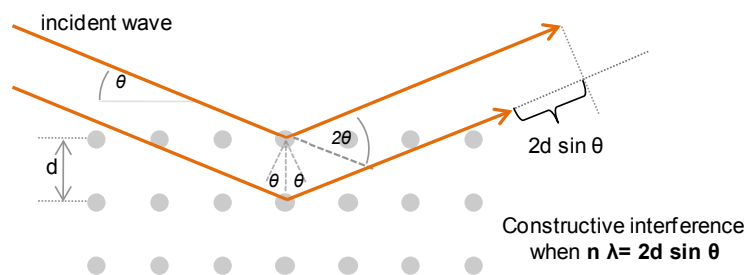


Figure 2.6: Schematic visualization of the Bragg equation. Maximum scattered intensity is only observed when the phase shift adds to a multiple of the incident wavelength.

High energy x-ray diffraction (HEXRD)

HEXRD in combination with the atomic pair distribution function (PDF) analysis explores the structural coherence of a sample. The PDF represents the degree and length of structural coherence and provides insight in the interatomic distances and atomic coordination shells incorporating contributions of both ordered and amorphous domains. The modeling of experimental PDFs provides structural motifs of the catalytically active phase. The diffraction data are reduced to the so-called structure factors, $S(q)$, and then Fourier transformed to the corresponding atomic PDFs $G(r)$ (Eq. 2-5). The wave vector q is defined as $q=4\pi\sin(\theta)/\lambda$, where θ is half of the scattering angle and λ is the wavelength of the x-rays used.

$$G(r) = \frac{2}{\pi} \int_{q=0}^{q_{\max}} q[S(q) - 1] \sin(qr) dq \quad (\text{Eq. 2-5})$$

Atomic PDFs $G(r)$ are experimental quantities that oscillate around zero and show positive peaks at real space distances, r , where the local atomic density $\rho(r)$ exceeds the average one ρ_0 . This behavior can be expressed by Eq. 2-6, which is the formal definition of the PDF $G(r)$.⁷²

$$G(r) = 4\pi\rho_0 \left[\frac{\rho(r)}{\rho_0} - 1 \right] \quad (\text{Eq. 2-6})$$

X-ray photoelectron spectroscopy (XPS)

X-ray photoelectron spectroscopy is a surface sensitive analysis that provides elemental composition, chemical state and electronic structure of a material. It is based on the element characteristic set of x-ray photoelectrons, which are detected by counting the number of photoelectrons as a function of their binding energy. Peaks from XP spectra reveal a direct identification of each element that exists on or in the top layers of a material. Those peaks correspond to specific electron configurations within the atoms (e.g. 1s, 2s, 2p etc.) and the number of electrons in each peak is directly related to the amount of an element within the irradiated area. To achieve this, the sample is excited with x-rays

while the kinetic energy and the number of electrons that escape from the top 1-10 nm of the material are analyzed.

2.5. Experimental procedures

The experimental synthesis procedures and all equipped synthesis routes are presented and discussed in the respective chapters. All electrochemical, *in situ* FTIR and physicochemical procedures equipped in this work are described in this section. The individual parameters are given in detail in the respective chapters.

2.5.1. Electrochemical characterization

Working Electrode Preparation: Catalyst inks were prepared by dispersing 6 mg of electrocatalyst powder in a mixture of 2.5 ml of ultrapure water, 0.5 ml of isopropanol, and 20 μL of 5 wt % Nafion solution (Aldrich). The mixture was ultrasonicated for 15 min. A glassy carbon disc electrode (GC-DE) (0.196 cm^2 geometrical surface area, Pine Research Instrumentation Company) was used as a support for the catalyst ink. Prior to use, the GC electrodes were prepared by polishing using a Nylon PSA sheet and 5 μm of α -alumina micropolish (0.10 mm) followed by a Microloth sheet and α -alumina micropolish (0.05 mm). The polished electrodes were rinsed thoroughly in ultrapure water and ethanol and then coated with 10 μl of a catalyst ink solution and dried in air, first at RT for 30 min and afterward at 50 $^\circ\text{C}$ for 15 min. *Electrochemical Testing.* All potentials are given versus the RHE (reversible hydrogen electrode) reference electrode. Starting from open circuit potential, cyclic voltammograms (CVs) were carried out in 0.5 M H_2SO_4 , 0.1 M HClO_4 or 0.1 M KOH to evaluate the hydrogen underpotential (H_{UPD}) charges between 0.05 and 0.40 V vs. RHE. EOR polarization curves (linear sweep voltammograms, LSVs) were collected in an electrolyte of 0.5 M $\text{C}_2\text{H}_5\text{OH}$ + 0.5 M H_2SO_4 , 0.1 M HClO_4 or 0.1 M KOH. Potential limits were adjusted between 0.05 and 0.80 V vs. RHE for EOR and between 0.05 and 1.00 V vs. RHE for CO oxidation. In chronoamperometric (CA) measurements, first the potential was dropped in steps from open circuit potential to 0.45 V for 1 h. Nitrogen gas was bubbled prior to experiments for 15 min and purged over the solution during the experiment.

2.5.2. Physico-chemical characterization

Inductively coupled plasma- optical emission spectroscopy (ICP-OES)

measurements were performed using a 715-ES-inductively coupled plasma analysis system (Varian). The standard concentrations were 5, 10, and 25 ppm for Pt; 3, 10 and 20 ppm for Sn; and 1, 3 and 10 ppm for Rh. The chosen wavelengths for concentration determination were 265.9 nm for Pt,

343.5 nm for Rh and 189.9 nm for Sn. *Sample digestion*: 5 mg of supported electrocatalyst was suspended in 2 ml of aqua regia, stirred for 30 minutes at RT, diluted with ultrapure water to 10 ml and stirred at 180 °C for 20 minutes. The suspension was filtered and the filtrate soluted to 50 ml.

Transmission electron microscopy (TEM) and energy dispersive x-ray spectroscopy (EDX)

was used to study morphology and composition. A small amount of the electrocatalysts was dispersed *via* ultrasonification in 0.5 ml of hexane. A Cu-grid with holey carbon film was impregnated with 2 μ l of the solution and air-dried. A FEI TECNAI G² 20 S-TWIN microscope, equipped with a GATAN MS794 P CCD-detector operated at 200 kV was used. The mean particle size was determined from the TEM images by counting of 50-200 particles. EDX data were collected for 120 s at an angle of 15° of the sample holder.

X-ray diffraction (XRD)

patterns were collected using a D8 Advance diffractometer (Bruker) equipped with a Lynx Eye Detector and KFL Cu 2K α x-ray tube. The diffraction patterns were collected in a 20–80° 2 θ range with a step size of 0.00142° dwelling for 30 s at every step. The XRD patterns were analyzed using the MDI Jade 8 software package. Bragg peak positions⁷³ were compared with such from reference XRD patterns (PDF data files, National Institute of Science and Technology).

High energy x-ray diffraction (HEXRD)

measurements were performed at the beam line 11IDC, at the Advanced Photon Source, Argonne National Laboratory, USA, using synchrotron x-rays of energy with wavelength of 0.1080 Å⁻¹.⁷² *Sample preparation*: the electrocatalysts were sealed inside glass capillaries.

X-ray photoelectron spectroscopy (XPS)

measurements were performed at photon energies yielding electron kinetic energies of 550 eV at the ISSS beam line of the synchrotron facility BESSYII of the Helmholtz-Zentrum Berlin^{74,75}. Samples were mounted onto a sapphire sample holder and introduced into the spectrometer, where all experiments were carried out at RT in ultrahigh vacuum (UHV). To calculate elemental ratios, the peak areas of Pt 4f, Rh 3d, and Sn 3d were corrected considering the energy dependent photon flux and tabulated cross sections⁷⁶. *Sample preparation*: the electrocatalysts were dispersed in 4 ml of H₂O and 1 ml of isopropanol with 40 μ L of Nafion solution using ultrasonication. This suspension was dropped on the silica surface and dried in air.

2.5.3. *In situ* Fourier transform infrared spectroscopy (FTIR)

In situ subtractively normalized interfacial FTIR spectroscopy (SNIFTIRS)

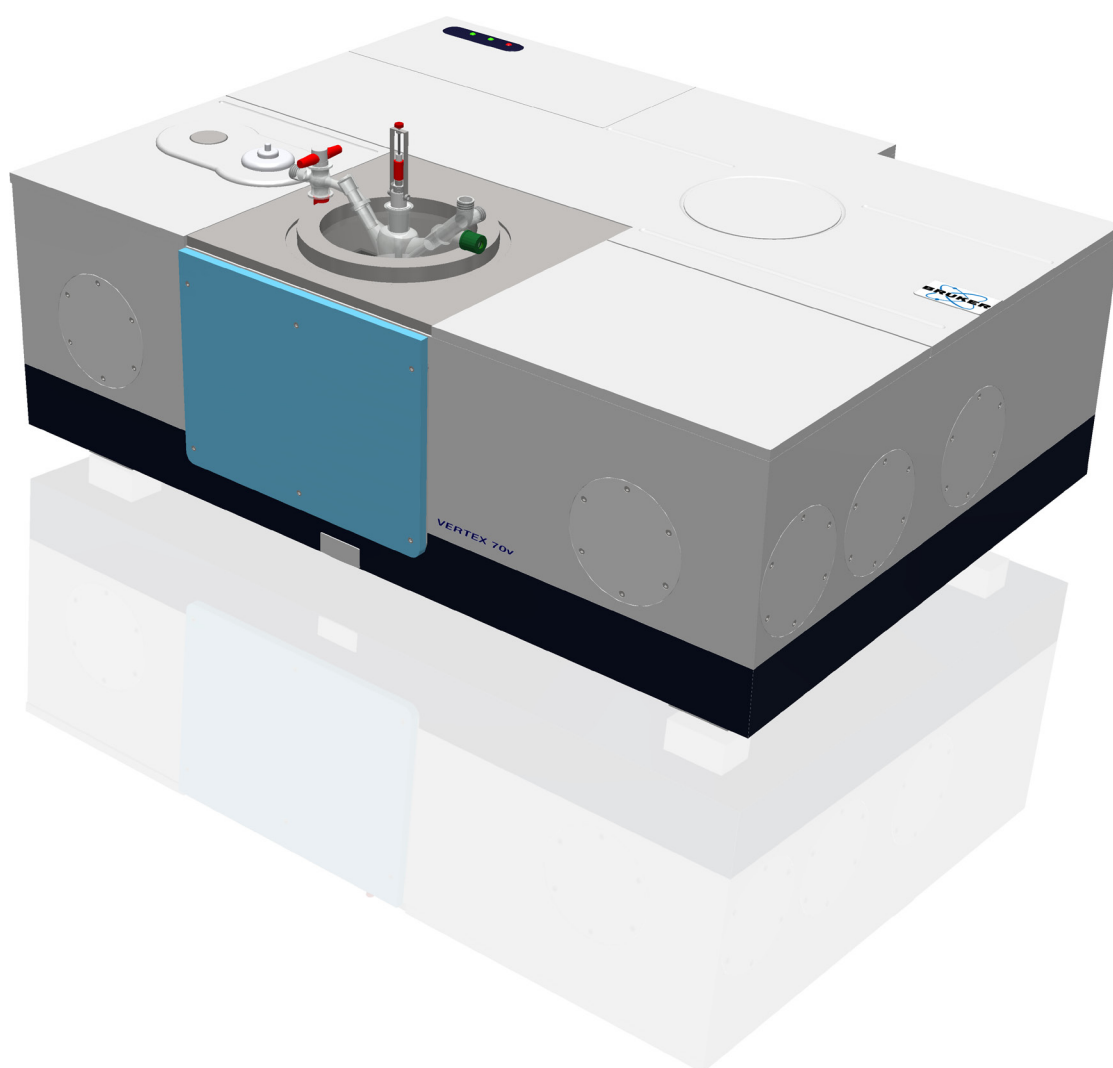
was measured using a NICOLET 6700 FTIR apparatus equipped with a MCT-A detector cooled with liquid nitrogen. The compartments were purged using compressed air free of CO₂ and H₂O at an inlet pressure of 60 psi from a Parker Balston Purge Gas Generator operating at a flow rate of 9 l/min. The electrode potential was controlled by BAS CV-27 potentiostat. A custom-made spectro-electrochemical Teflon[®] cell with a hemispherical ZnSe window was connected to the optical window (ZnSe) *via* a Teflon[®] tape. An ink made of the electrocatalyst suspended in ultrapure water, isopropanol, and nafion was put as a film on a polished Au(100) single-crystal operating as the working electrode (WE), which was placed together with the reference electrode (SCE) and counter electrode (Pt wire) in the cell filled with the electrolyte (0.1 M HClO₄ + 0.5 M C₂H₅OH). The WE was pressed against the optical window under 0.05 V vs. RHE to achieve appreciable increase of interferogram peak-to-peak signal. Afterward, the sample compartment was closed, and dry compressed N₂ was purged for 2 h to eliminate water and CO₂ from the spectrometer compartment. The background spectrum was collected at 0.15 V vs. RHE, and the potential was stepped by 0.10 V vs. RHE in positive direction to 1.15 V vs. RHE. At each potential, interferograms were collected at 8 cm⁻¹ resolution with 128 scans, with 20 s of delay between setting (potential switch) and measurements to allow the interface to reach equilibrium.

In situ attenuated total reflection FTIR spectroscopy (ATR)

was measured in a custom made glass cell with a Bruker Vertex 70v FTIR spectrometer equipped with a MCT detector cooled with liquid nitrogen. An unpolarized beam was focused with a Pine Veemax II onto the sample spot of the cell. The spectral resolution was set to 4 cm⁻¹ and 128 interferograms were added together for each spectrum. Spectra are given in reflectivity units defined as $\Delta R/R = (R_{E2} - R_{E1})/R_{E1}$ two single beam reflectivities R at applied potentials E₁ and E₂. The reference spectrum R_{E1} was collected in the same solution right before the investigated potential scan at the respective start potential. A Si or ZnSe truncated hemisphere was used as the IR window and an ink of the electrocatalyst sample (1 mg in 0.8 ml isopropanol and 0.2 ml milli-Q water) was deposited on the prism on the IR beam ATR focus spot and the contacted with Toray Paper 060 carbon cloth and a Pine glassy carbon rod fixating the carbon cloth. The complete beam pathway was under vacuum more than 24 h prior to each measurement. A build in gold mesh was used as counter electrode, a real RHE for reference. All *in situ* electrochemical measurements were controlled with a Metrohm Autolab PGSTAT204 potentiostat.

3. Validation of the *in situ* FTIR electrochemical setup

In this chapter, a more detailed introduction to the concept of an in situ electrochemical vibrational spectroscopic approach to fuel cell catalyst research is presented. Additionally, the process and validation methods equipped to construct the custom build in situ FTIR Electrochemical setup are reported in this chapter.



3.1. *In situ* FTIR spectroscopy

Vibrational spectroscopy is ideal for identifying the surface species generated upon molecular adsorption and the species generated by surface reactions, because typical energies of molecular vibrational modes are within the IR wavelength region. Any technique suitable to obtain vibrational data from solid state or gas phase samples (Infrared, Raman etc.) can be applied to the study of surfaces, and a number of techniques have been specifically developed to investigate the vibrations of molecules at interfaces, e.g. electron loss spectroscopy (EELS), sum frequency generation spectroscopy (SFG) etc. But only two techniques are routinely used for vibrational studies of molecules on surfaces: infrared spectroscopy of various forms and EELS.

Infrared spectroscopy provides a direct investigation of reactants involved in the cascade of reaction steps taking place on a catalytic surface. The development of Fourier Transform (FT) techniques significantly decreased the acquisition time down to milliseconds and even faster. FTIR Spectroscopy is a universal, fundamental tool to determine the nature of molecular bonds in a variety of probe substances. It has been commonly used for the identification of functional groups among organic molecules, involving carbon, hydrogen, oxygen, nitrogen, phosphorus, sulfur and halogens. Furthermore, the use of FTIR as a tool for *in situ* measurements in the field of catalysis has been widely established. Where traditional FTIR transmission techniques offer easy access to the desired information, modern *in situ* electrocatalytic investigation has higher and more profound challenges for setup and data analysis. Electrochemical *in situ* FTIR spectroscopy investigates IR band changes with applied potential and can, therefore, give information on adsorbed educts, generated intermediates and desorbing products on the electrode surface and the surrounding electrolyte system during the catalytic process.

Its application is limited by the sufficient number of involved IR active species in the catalytic reaction. In general, any electrocatalytic process involving an IR active surface mode or really strong bulk IR active mode of educts, intermediates or products can be investigated. Since only molecule transitions with a dynamic dipole moment μ are IR active, common applications include the oxidation of organic molecules, CO stripping, CO₂ reduction, oxygen reduction and charge-transfer complex reactions.

Attenuated total reflection (ATR)

ATR is a surface sensitive FTIR technique with a particular type of reflection geometry that allows the measurement of species adsorbed on a surface, which can be done without too strong overlapping contributions from the surrounding electrolyte. In transmission FTIR the infrared beam travels in a

straight path through a sample, whereas for ATR spectroscopy the beam is oriented to be reflected at the interface of a prism and the sample medium. The reflected infrared beam creates an evanescent wave, which projects orthogonally into the sample in intimate contact with the prism just above the point of reflection. Some of the energy of this evanescent wave is absorbed by the sample, i.e. the surface species, and the reflected radiation is returned to the detector (Figure 3.1).

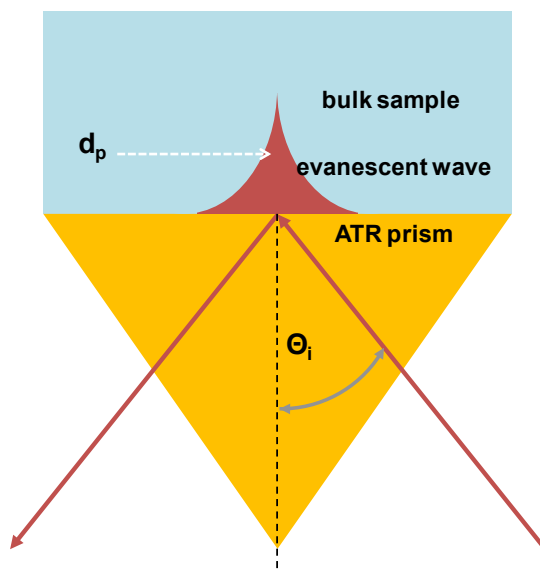


Figure 3.1: Experimental geometry for attenuated total reflection (ATR) IR spectroscopy and penetration depth of the evanescent wave from the ATR crystal into the bulk electrolyte.

When electromagnetic radiation propagating through an internal reflection element, which is a transparent optical element with a high refractive index n_1 in contact with an optically thinner medium (refractive index n_2), strikes the interface between the two media at an angle of incidence θ larger than the critical angle θ_c , total reflection occurs at that interface.⁷⁷ Calculation of the propagation of a plane wave between two media with different refractive indices under conditions of total reflection yields the electric field amplitude E near the interface where E_0 is the electric field amplitude at the interface, depending on the angle of incidence, the refractive indices and the polarization of the field (Eq. 3-1).⁷⁸

$$E = E_0 e^{-z/d_p} \quad (\text{Eq. 3-1})$$

The electric field components of the evanescent wave fall off exponentially with the distance z from the interface. A guideline value for the required proximity of the sample molecule to the interface is the penetration depth d_p (Figure 3.1). It is defined as the distance from the interface to the point where the amplitude of the electromagnetic field is equivalent to $1/e$ ($\sim 37\%$) of the amplitude at the interface. A realistic estimate of the actual dimension gives the effective penetration depth d_e (Figure 3.2). The penetration depth d_p (Eq. 3-2) and the effective penetration depth d_e (Eq. 3-3) both depend on three

variables, the wavelength λ , the angle of incidence θ and the difference of refractive indices of the optically denser medium (e.g. the FTIR prism) to the optically thinner medium (e.g. the electrolyte) $n_{21} = n_2/n_1$.

$$d_p = \frac{\lambda}{2\pi \cdot \sqrt{n_1^2 \sin^2 \theta - n_2^2}} \quad (\text{Eq. 3-2})$$

$$d_e = \frac{d_1 + d_2}{2} \text{ mit } d_1 = \frac{(\lambda/n_1) \cdot n_1^2 n_2 \cos \theta}{(n_1^2 - n_2^2) \pi \cdot \sqrt{n_1^2 \sin^2 \theta - n_2^2}} \text{ und } d_2 = \frac{d_1 \cdot (2n_1^2 \sin^2 \theta - n_2^2)}{(n_1^2 + n_2^2) \pi \sin^2 \theta - n_2^2} \quad (\text{Eq. 3-3})$$

n_1 = refraction index of optically denser medium

n_2 = refraction index of optically thinner medium

θ = angle of incidence

λ = wavelength

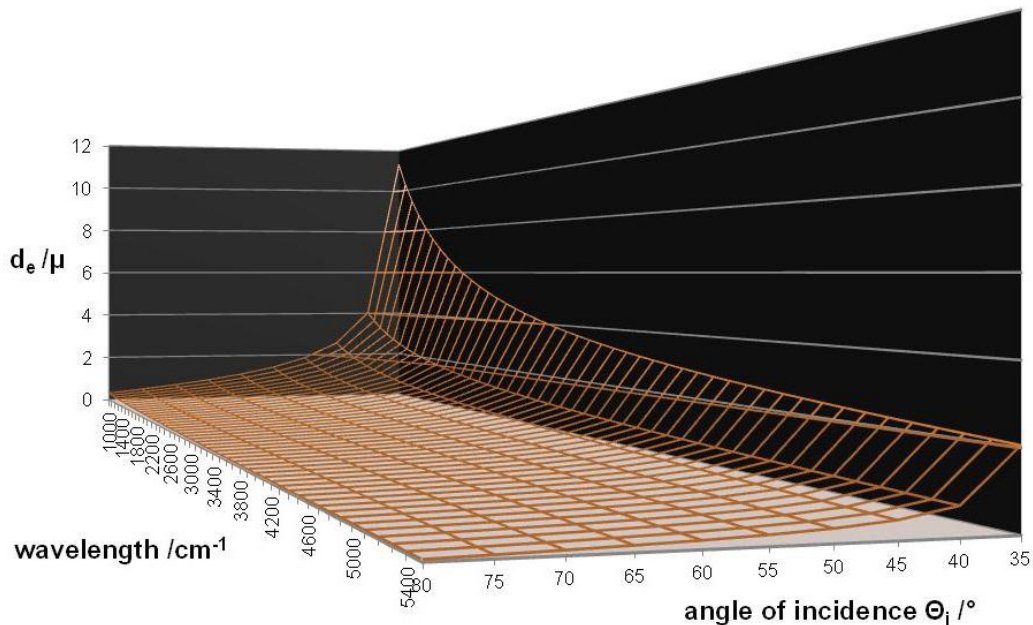


Figure 3.2: Theoretical calculation of the effective penetration depth d_e in dependence of the wavelength λ and the angle of incidence θ_i . Refraction indices are set $n_1/n_2 = 1.8$.

The ATR crystal is made of a high index of refraction crystal that absorbs minimally in the region of interest. Typical materials include, but are not limited, to zinc selenide, diamond, silicon, and germanium. ATR only measures substances within about a micrometer from the crystal surface. Another advantage is the versatility that ATR allows. Normally, *in situ* measurements (or measurements while the reaction is proceeding) can only be accomplished with a typical transmission cell in gaseous atmosphere. ATR is especially applicable for *in situ* monitoring of different species in electrocatalytic systems. Properties of interest are the refractive indices of the ATR crystal, the angle

of incidence of the IR beam and its critical angle, the depth of penetration and effective path length, the wavelength of the IR beam, the number of reflections (single or multiple reflections) and the quality of the sample contact with ATR crystal. Also the spectral window of the crystal and its alkaline and acid media resistance are of importance.

Reflectance spectroscopy

The acquisition of interfacial spectra is determined by an experimental reflectance configuration and the optical laws of reflection of light at interfaces. An optimal absorption of light at the interface and a high signal-to-noise ratio can be reached with an experimental configuration that maximizes the reflection of the IR radiation while the absorption of light by matter is due to transitions between different energy levels. It requires the interaction between the oscillating electric field of the radiation and the transition dipole moment μ , that in the case of infrared spectroscopy corresponds to variations of molecular electric dipole moments during molecular vibrations.⁷⁰ External reflection spectroscopy (ER) is also known as external reflection absorption spectroscopy (ERAS) or infrared reflection absorption spectroscopy (IRRAS). The distinguishing attribute all those techniques have in common is the reflection of an IR beam on the exterior plane of a metal, i.e. high reflective surface, with the aim to investigate thin layers of the molecules of interests, adsorbed on that surface. The sensitivity of this method of measurement is enough to measure monomolecular thin films with a layer thickness of several angstroms. In the IR region, metals have a very high optical conductivity (i.e., a high electrical conductivity at optical frequencies), which simplifies the description of reflection at the electrode-electrolyte interface and the interpretation of the corresponding IR spectra. When the high reflectivity is lost, due to other experimental setups, such as nanoparticles deposited on more opaque or even on highly reflective metallic substrates, the resulting low or moderate reflectance in the IR must be taken into account when analyzing the corresponding spectra.

The schematic drawing of the IR beam path in an IRRAS cell for solid-liquid interfaces in Figure 3.3 shows that the incident light is reflected or transmitted in fractions, while this fraction is indicated by the product of the relevant reflectance R or transmittance T , the prism angle α at the gas-liquid interface defers from the incident angle β at the metal surface.

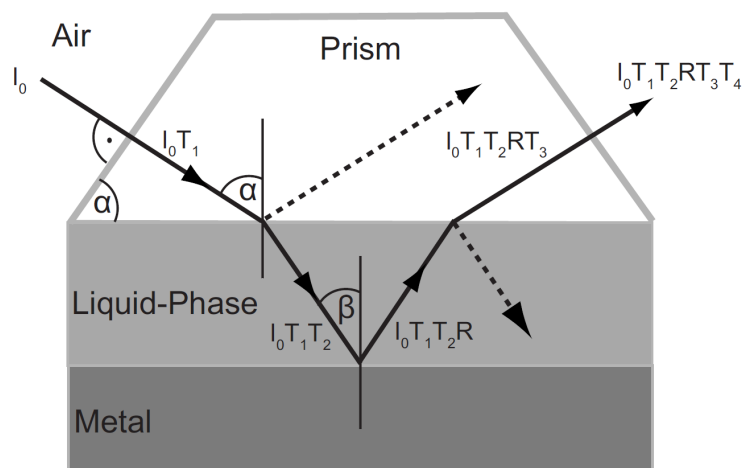


Figure 3.3: Schematic drawing of the IR beam path in an IRRAS cell for solid-liquid interface investigation. Reprinted with permission from Reference ⁷⁹. Copyright 2009, AIP Publishing LLC.

The reflectivity of an interface: the surface selection rule and its applicability

The electrical part of the incident infrared light on the surface interacts with charged species on the surface, causing dipole moment changes in certain molecular vibrations (Figure 3.4).⁸⁰ The special feature of metals is their structural composition, consisting of freely moving, negatively charged electrons and positively charged atomic cores, fixed in the metal lattice. While the interaction is due to both polarized species, of course the atomic cores don't contribute a significant polarization due to their nearly totally fixed position in comparison with the free electrons. Those are influenced strongly by the applied electromagnetic field, resulting in a polarized metal surface.

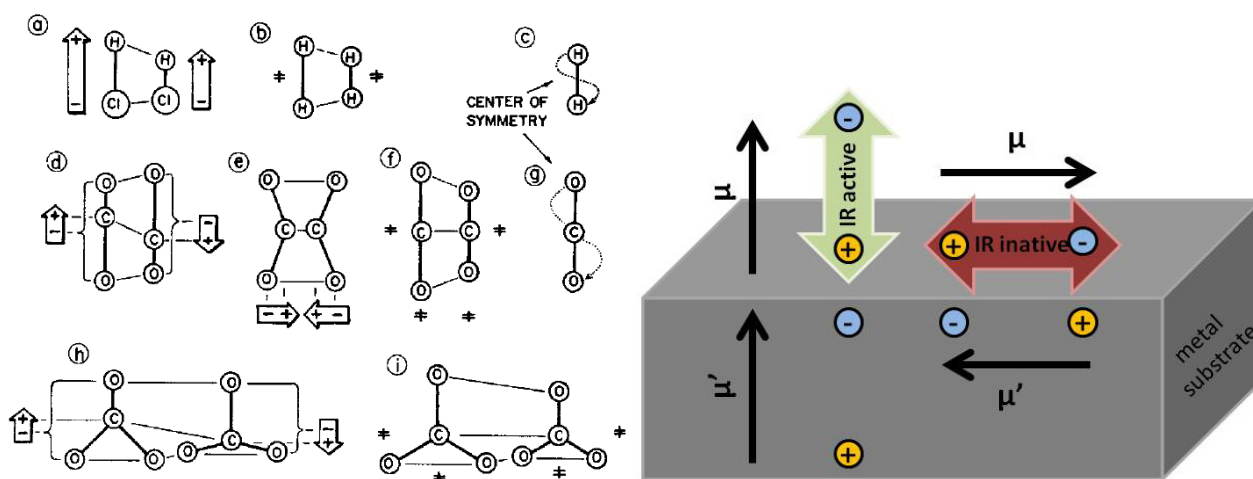


Figure 3.4: Dipole moment changes in certain molecular vibrations⁸¹ and active and inactive IR components of the dipole moment.

The incident electromagnetic wave consists of two components on the surface: parallel and perpendicular to the surface. The surface selection rule states that only vibrations with a dynamic

dipole moment component aligned perpendicular to the surface plane can interact with p-polarized incident light. As shown in Figure 3.4 the perpendicular component causes a displacement of electrons parallel to the surface. Negatively charged electrons and positively charged atomic cores accumulate and induce an electromagnetic field on the metal surface, which is in opposite direction to the incident field. This charge displacement takes place to the point where the incident and the induced field are equally strong and sum up to a total field of zero. This results in a compensation of the incident force, so that no more polarization charges are established. The component parallel to the surface however generates an external field in the same direction as the incident one, the field strength is added up and therefore the normal component of the incident field enhanced. The component of the electric field parallel to this plane is termed p-like (parallel) and the component perpendicular to this plane is termed s-like (from *senkrecht*, German for perpendicular), so light with a p-like electric field is said to p-polarized and with an s-like electric field s-polarized.

External reflection (ER)

Since the external and the incident field for s-polarized light are cancelled out on the surface, only components from the electrolyte contribute to the resulting signal, whereas p-polarized light shows enhanced contribution from the surface and the same contribution from the electrolyte as s-polarized light. This is due to the statistically distribution of components in the electrolyte. Usually, ER measurements are carried out by subtracting the signal from s-polarization and p-polarization to yield only the information from the surface components in the spectra. With the two polarizations having different signal to noise ratios, this has to be taken out carefully. Also, the field compensation for the s-like component is total only when the inertia of the electrons can be neglected, which is possible only when the electric field is not changing too fast, respectively. This will be the case for shorter wavelengths, i.e. ultraviolet region. For soft x-ray scattering, the inertia of the electrons has such a strong influence that the surface selection rules can't be applied anymore. The incident angle for ER measurements is typically chosen so that as many adsorbed molecules lie in the grazing incidence of the IR beam but the intensity of the resulting beam is not diminished too much due to poorer reflection on the surface with increasing angles of incidence. Usually, with respect to the used IR window, an optimal angle of incidence lies between 60 and 80°.

Subtractively normalized interfacial Fourier transform infrared spectroscopy (SNIFTIRS)

The SNIFTIRS approach is a method of increasing the signal-to-noise ratio and only suitable for absorptions that (i) shift in frequency with potential and (ii) do so in a completely reversible manner as the potential is switched repeatedly, since any absorption bands arising from species produced and

consumed in an irreversible manner will be averaged out. Figure 3.5 shows a scheme of a typical SNIFTIRS experiment and the multilayer configuration used in SNIFTIRS simulations. Three optically different phases are used: phase (0 and 1) represents the prism window, phase 2 is the thin electrolyte layer, phase 3 is the adsorbate layer and phase 4 is the metal. Incident and reflected intensities are denoted as I_0 and I_R , respectively.

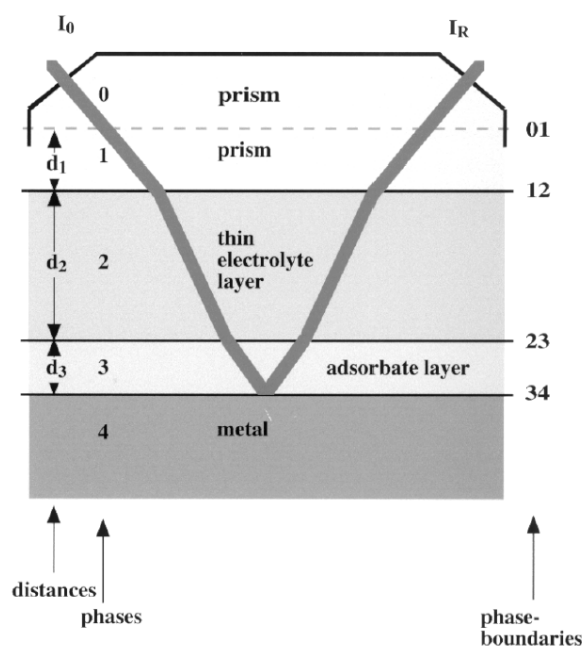


Figure 3.5: Scheme of the SNIFTIRS experiment and multilayer configuration used in SNIFTIRS simulation. Reprinted from Reference⁸² with permission from Elsevier.

The scheme also shows the method of diffraction of the incident and reflected light through the layers. Depending on the actual refractive indices it is also possible that there is a total reflection at the phase boundary between phase 1 and 2. In this case one operates under ATR conditions and only evanescent waves reach the metal interface.⁸² Another drawback of this method is the concern, that such potential modulation can influence the surface chemistry taking place.⁸³ During a typical SNIFTIRS, the electrode potential was modulated between values E_1 , sample potential (usually potential for strong adsorption of probe molecules or production of intermediates) and E_2 , background potential (where there is no adsorption of probe molecule). The spectrum is obtained by the following equation:

$$\frac{\Delta R}{R} = \frac{R(E_2) - R(E_1)}{R(E_1)} \quad (\text{Eq. 3-4})$$

where the difference between two single beam reflectivities R at applied potentials E_1 and E_2 is related to the reflectivity at potential E_1 . The goal of computing this difference (normalized) spectra is to obtain spectra of surface-bound intermediates, essentially free from bulk contribution. The SNIFTIRS

method is part of the external reflection configuration used to study structural aspects of the adsorption processes.⁸²

3.2. Concept and design of an electrochemical *in situ* FTIR cell

The conception and design of an electrochemical *in situ* FTIR cell needs to figure out all the contributing parts and their properties of the desired electrochemical reactions. The medium or rather the electrolyte pH and the solubility of the prism and cell in contact with it is as important to be considered from the beginning of the design process as the prism material itself in terms of IR light permeability and penetration depth of the IR field into the desired medium. The implemented electrodes have to be adjusted to the medium conditions and especially the working electrode has to be connected in a matter that does not interfere with the *in situ* FTIR measurement. Furthermore, working conditions like the accessibility of reaction and protection gases have to be considered as well as the optical alignment of the optical components and the readjusting possibilities under working conditions.

In situ FTIR studies are mainly conducted in two major modes: External reflection outside the IR prism on a highly reflective substrate that holds the sample (working electrode) or ATR modus with the sample (catalyst) in close contact to the prism and electrical connection to the working electrode. Usually the ATR working electrode is connected *via* a thin gold film sputtered onto the prism. A scheme of an early external reflection *in situ* FTIR cell reported by Iwasita *et al.*⁸⁴ is shown in Figure 3.6. Therein, an IR window is fitted to the bottom of the cell body *via* a screw mechanism. Indicated in the figure are working, counter and reference electrodes as well as inlet-outlet for gases and liquids. Besides the standard requirements for electrochemical experiments, this cell permits the exchange of electrolyte under conditions of potential control. This is of great advantage when studying irreversibly adsorbed species, since, after adsorption, the solution can be replaced by pure supporting electrolyte and, thereby, spectra for surface species can be obtained with a minimum of disturbance from solution species. The reference electrode is placed in a separate compartment ending in a Luggin capillary. The working electrode consists of a polished disc that can be gently pressed against the window with a glass tube, just forming a thin film of electrolyte (1-10 pm) between the polished surface and the window. Other cell designs similar to the Iwasita design have been presented in a number of publications. For example, Munk *et al.*⁸⁵ presented one of the first *in situ* external reflection cells that have been used for studies on Platinum nanoparticles supported on carbon. They pressed a basal plane graphite disc with catalyst particles supported on top against a MgF₂ IR prism in a thin film configuration.

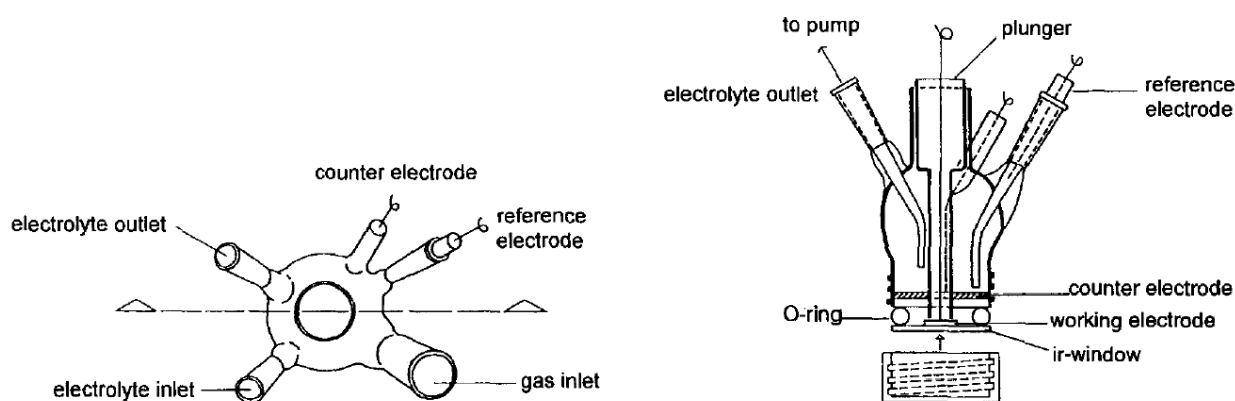


Figure 3.6: Scheme of the *in situ* IRRAS cell for pure Pt single crystal working electrodes cell by Iwasita *et al.*⁸⁴ Reprinted from Reference⁸⁴ with permission from Elsevier.

An effective method for anchoring metallic nanoparticles onto such smooth substrates has been developed by Stamenkovic *et al.* (Figure 3.7).⁸⁶ They demonstrated that an ultrathin layer of carbon-supported Pt-based catalyst can be deposited onto mirror-polished Au and/or glassy carbon surfaces by implementing a temperature-enforced procedure. Furthermore, they also extended the cell design reported by Iwasita *et al.*⁸⁴ as presented in Figure 3.6. This method provides excellent reflective properties of the sample probe and the possibility to examine CO-nanoparticle interaction by infrared reflection absorption spectroscopy (IRRAS) on the molecular level.

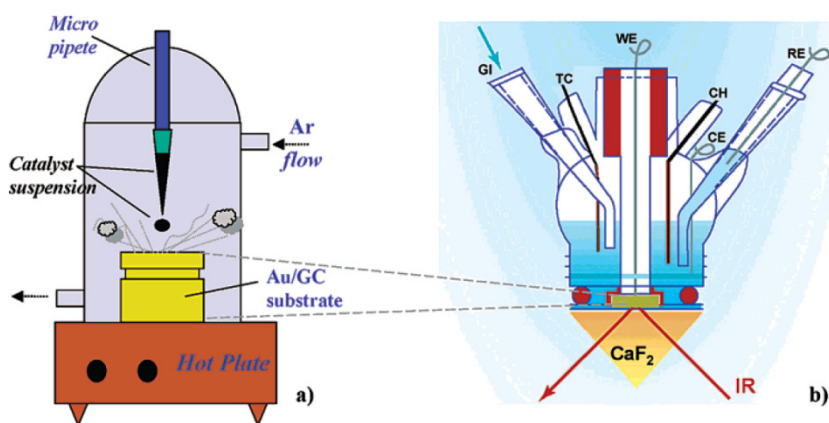


Figure 3.7: Scheme of a) the preparation chamber for thin catalyst layers for b) the upgraded spectroelectrochemical cell for *in situ* IRRAS measurements at elevated temperatures by Stamenkovic *et al.*⁸⁶ based on the initial design by Iwasita *et al.*⁸⁴. GI is the gas inlet (bubbler), TC the thermocouple, WE the working electrode, CH the cartridge heater, CE the counter electrode, and RE the reference electrode. Reprinted with permissions from Reference⁸⁶. Copyright 2004 American Chemical Society.

However, one of the biggest disadvantages of IRRAS is the required thin film configuration. The electrolyte medium between the prism and the sample molecules absorbs large portions of the IR beam

intensity and causes mass transport limitations into the layer at the same time. With the aim of minimizing this problems Zhan *et al.*⁸⁷ suggested to use a working electrode with small perforations for reactions involving high electric current and gas evolution. In order to keep a constant concentration of solution species in the thin layer, other cells were designed where the electrolyte is forced through a hole drilled in the center of the electrode (Nichols *et al.*⁸⁸) or in the center of the IR window (Roth *et al.*⁸⁹). Besides, several studies have been conducted using ATR setups, some of them abstained from a conducting gold film on the prism and contacted the catalyst film from above, similar to the conventional IRRAS setup. De Souza *et al.*⁹⁰ recently suggested the use of carbon cloth material to contact ATR films on IR prisms in order to diminish mass transport limitations of thin film configuration while keeping the advantages of an ATR setup.

A scheme of the different electrochemical *in situ* FTIR cells that were designed within this work is presented in Figure 3.8. Herein, the FTIR prisms function as the cell bottom with the IR beam passing through them from below. The cell is equipped with a reference electrode (RE) and counter electrode (CE) as well as a gas inlet. Depending on the measurement setup (external reflection or ATR) the working electrode is either a nanoparticle film on a reflective surface (ER) or a nanoparticle film deposited directly on the prism and contacted *via* a carbon cloth with a GC electrode. The working principle of a SNIFTIRS shown in Figure 3.8 was not realized in the same cell setup as the ER and ATR measurements but at the group of Brankovic *et al.*⁹¹ They pressed a gold single crystal, coated with a catalyst ink, against the ATR focus spot of the prism from above creating a thin film configuration.

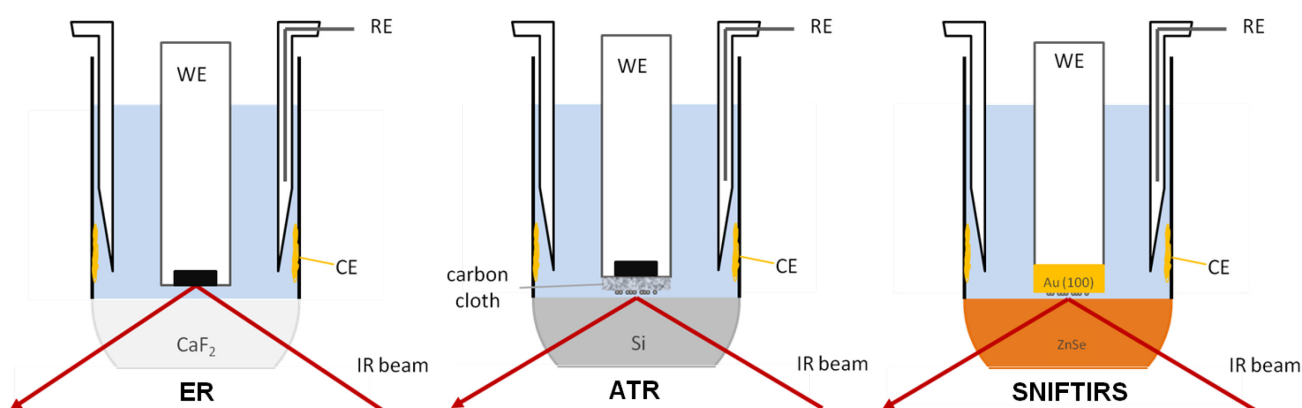


Figure 3.8: Scheme of the different electrochemical *in situ* FTIR cell working principles.

The custom-made *in situ* electrochemical setup cell for ER and ATR measurements is shown in Figure 3.9. The glass cell body is screwed vacuum tight onto an aluminum holder for the FTIR prism. The IR beam can pass through the open sides of the holder. A gold mesh is implemented in the glass cell

body, acting as the counter electrode. A conventional RHE is used as reference electrode. A non rotating glassy carbon electrode with a Teflon[®] rod (Pike Technologies) is centered in the middle of the prism through the top hole of the cell and tightened with a screw to press it gently against the window and hold the carbon cloth in place.

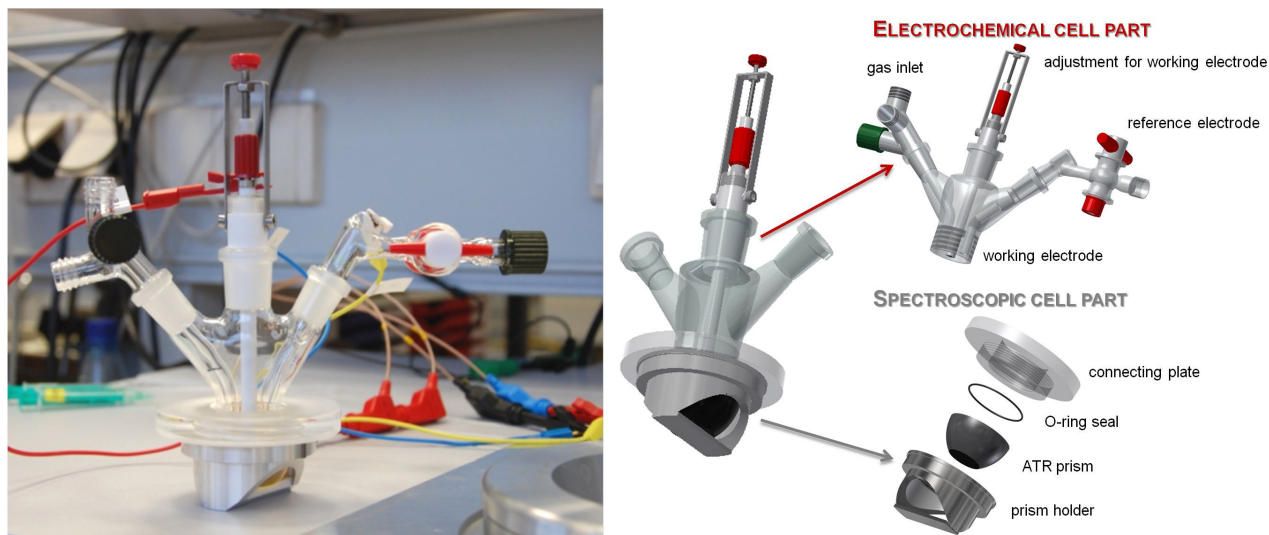


Figure 3.9: Picture (left) and sketch (right) of the custom-made *in situ* electrochemical setup cell (ER and ATR) for the investigation of the ethanol oxidation reaction. The cell consists of a spectroscopic bottom part with the ATR prism fixed by a prism holder and a connecting plate to the electrochemical glass cell that contains the gas inlet, the working electrode with an adjustment screw, the reference electrode, and the counter electrode (not included in the sketch).

Figure 3.10 depicts a sketch of the *in situ* electrochemical setup. The Veemax II angle control is located inside the sample chamber of the Bruker 70v FTIR spectrometer. The spectroelectrochemical cell is implemented on top of the Veemax with a removable aluminum top part that adjusts the ATR prism exactly on the right height above the angle incidence control, so that the focus spot of the IR beam and the evanescent field do exactly meet the working electrode pressed on top of the ATR prism (Figure 3.11). While in the sketches some planes of the setup design are transparent for better visibility, the sketch of the setup in Figure 3.12 shows the aluminum top part in wholeness as does the picture of the setup in Figure 3.13. It is sealed vacuum tight with o-ring seals, so that the complete FTIR beam pathway can be operated under vacuum conditions.

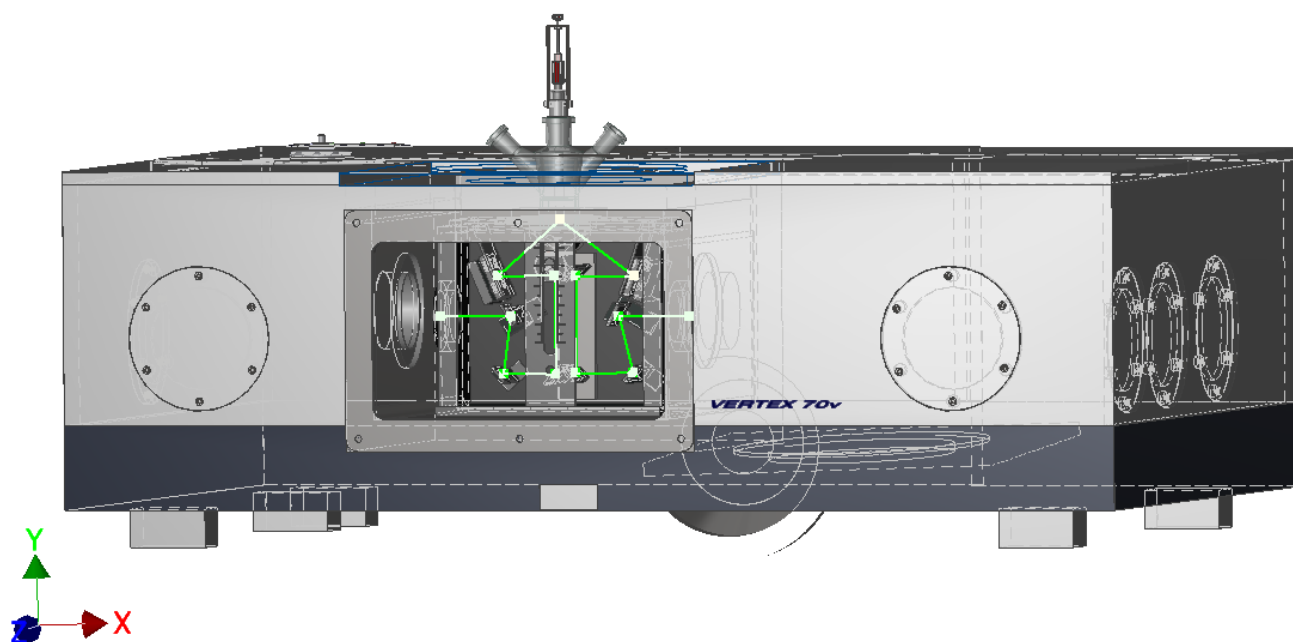


Figure 3.10: Sketch of the *in situ* FTIR ATR/ER setup implemented in the Bruker70v sample compartment. The IR beam pathway throughout the mirror system of the angle incidence control ATR Veemax II is indicated green.

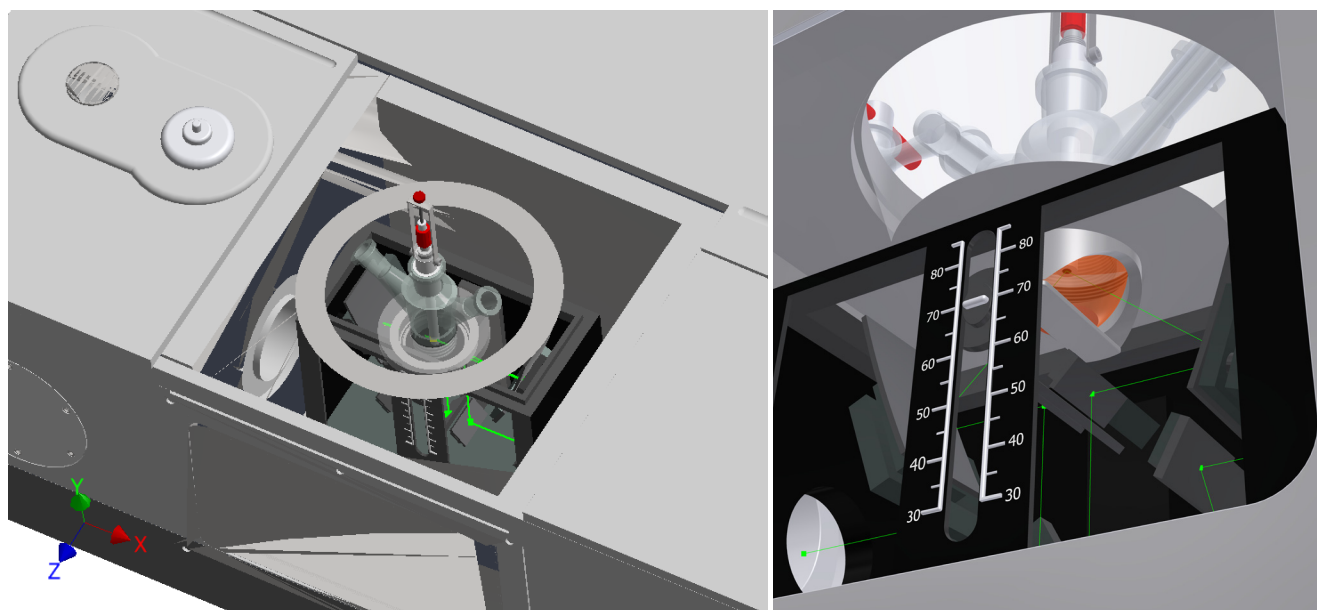


Figure 3.11: Sketch of the *in situ* FTIR ATR/ER cell from above (left) and from below (right). The cell has to be adjusted in a way that the ATR beam spot is exactly focused where the working electrode is implemented from above.

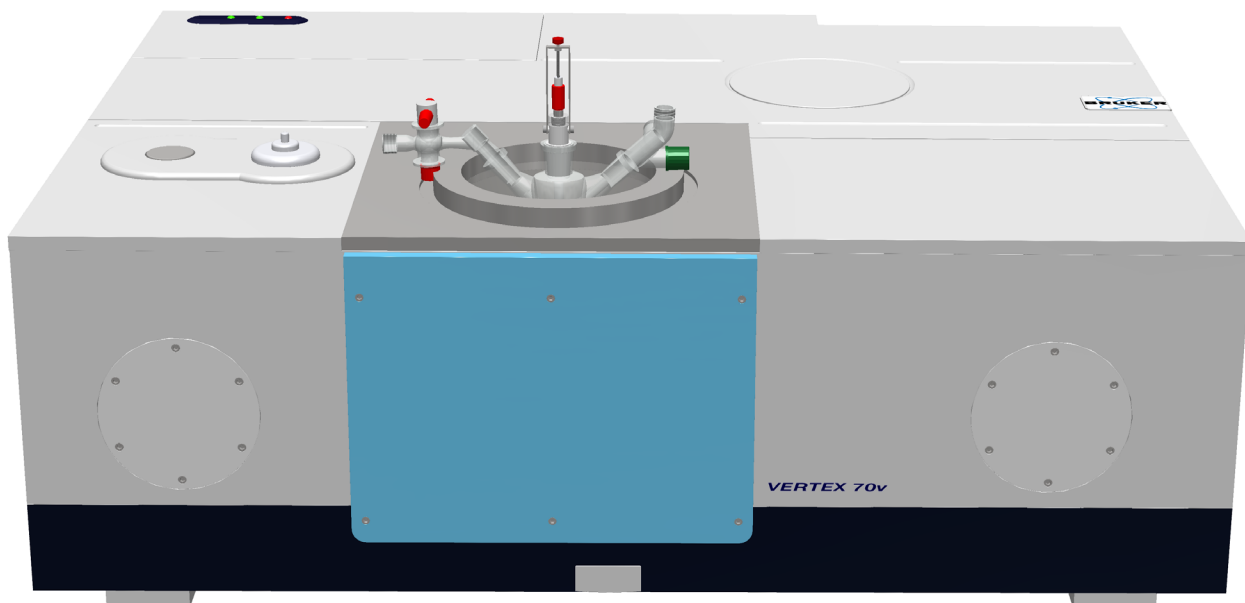


Figure 3.12: Sketch of the vacuum sealed *in situ* FTIR ATR/ER setup implemented in the Bruker70v sample compartment.

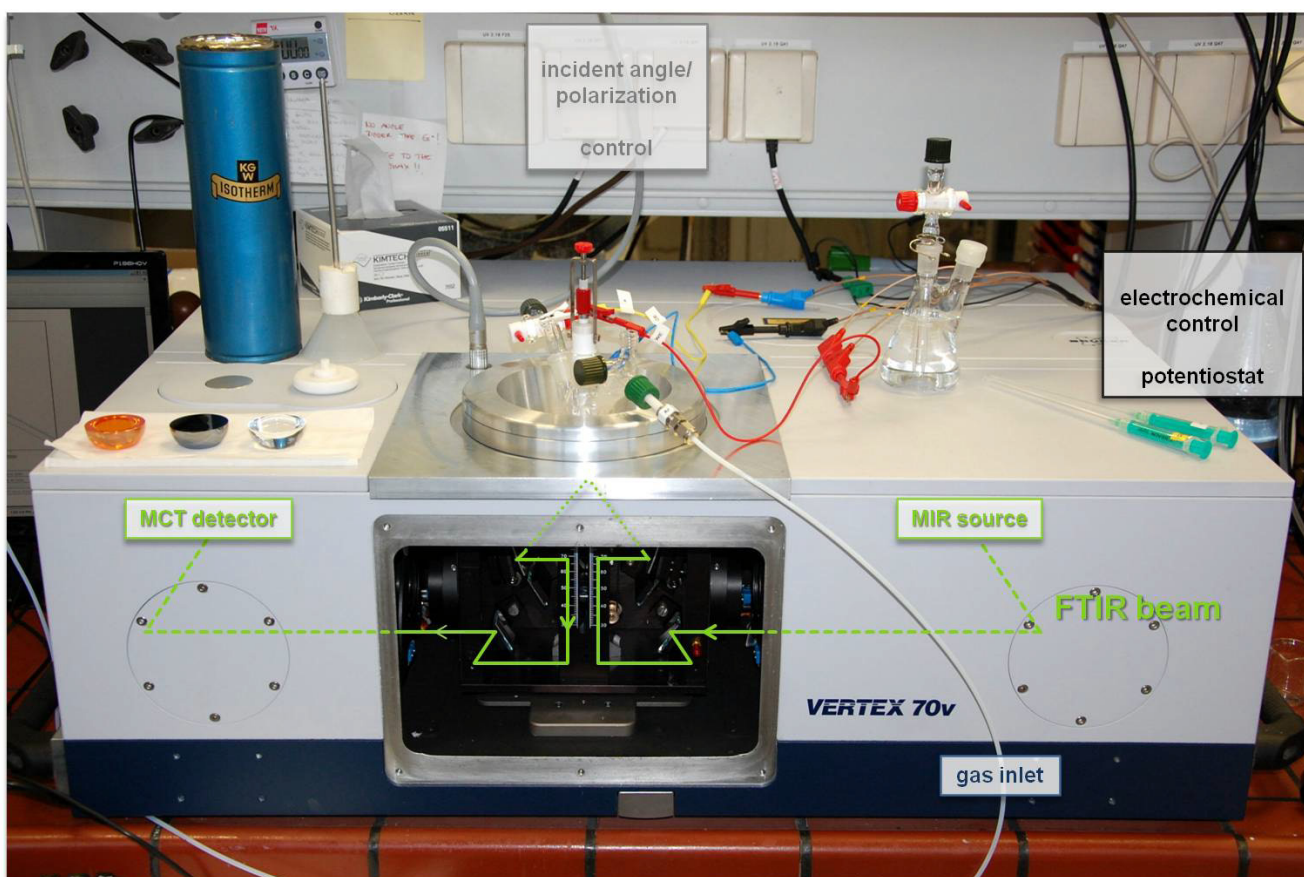


Figure 3.13: Picture of the *in situ* FTIR ATR/ER setup implemented in the Bruker70v sample compartment. The IR beam pathway throughout the mirror system of the angle incidence control ATR Veemax II is indicated green.

3.3. FTIR *in situ* EOR measurements in acidic and alkaline media

Ethanol oxidation in acidic electrolytes such as formic acid or sulfuric acid has been extensively studied with *in situ* FTIR methods over the last decades.^{5,61,84,92-95} In contrast to the *in situ* FTIR literature on the electro-oxidation of ethanol in acidic media, studies in alkaline media are sparse. In 1991 López-Atalya *et al.* employed SNIFTIRS approach to study ethanol oxidation at Pt single crystals in aqueous NaOH and Na₂CO₃.⁹⁶ More recent Lai *et al.* presented a comprehensive study of ethanol oxidation on polycrystalline Au and Pt electrodes using *in situ* external reflection FTIR as well as surface enhanced Raman spectroscopy (SERS) in sodium hydroxide solution.⁹⁷ Christensen *et al.* employed the same external reflection approach, studying the oxidation of methanol⁹⁸, formate⁹⁹ and ethanol²³ on polycrystalline Pt in 0.1 M KOH. Furthermore, recent studies presented ATR approach measurements on the investigation of ethanol oxidation on Pd film working electrodes by Yang *et al.*¹⁰⁰ and Pd, Au and PdAu carbon supported nanoparticle catalysts by Geraldes *et al.*¹⁰¹, both in potassium hydroxide solution.

Several criteria like spectral range, chemical and physical properties and sensitivity need to be considered when selecting an FTIR crystal material for a specific sample. The crystal should have a higher index of refraction than the sample. The majority of organic samples have refractive indices in the area of 1.5. Refractive indices of standard ATR crystals span from 2.4 to 4.0 - which in most cases provides sufficient sample to crystal differentiation. Inappropriate refractive index ratios may cause distortion of spectral features. These may be manifested by diminished peak symmetries, sharp baseline/peak shoulder transitions, and in extreme cases, presence of derivative-like features in the spectrum. All FTIR prisms have different spectral ranges. Selected suitable materials for FTIR prisms are listed in Table 3.1. The three different ATR prisms used with the *in situ* FTIR cell presented in this thesis are shown in Figure 3.14.



Figure 3.14: ZnSe, Si and CaF₂ prism for the custom made electrochemical *in situ* FTIR cell concept.

Specifically, in mid-IR the cutoff at low wavenumbers, i.e. the point at which the material is no longer permeable for infrared light, varies from approximately 1500 cm⁻¹ for silicon to 250 cm⁻¹ for thallium

bromiodide (KRs-5). To a certain extent, the cutoff values are also affected by the length (thickness) of the crystal. In light of these facts, it is important to determine whether the spectral features of the sample correspond with the spectral range of the selected FTIR prism. The prism must be chemically and physically compatible with the sample. Some crystal materials may react with samples. This will typically damage the crystal surface and may produce unpleasant side effects (e.g. acidic solutions, pH<5, may etch the ZnSe crystal, strong acids will generate toxic hydrogen selenide). Physical considerations are equally important as some crystals are more susceptible to pressure and temperature changes than others.

Table 3.1: Suitable materials for FTIR prisms and their physical properties.¹⁰²

	n₁	LWL	dp	Water Solubility	pH Range	Hardness
		cm⁻¹		g/100g		kg/mm²
AMTIR	2.5	625	1.70	Insoluble	1-9	170
Diamond/ZnSe	2.4	525	2.00	Insoluble	1-14	5,700
Germanium	4	780	0.66	Insoluble	1-14	550
KRs-5	2.37	250	2.13	0.05	5-8	40
Silicon	3.4	1500	0.85	Insoluble	1-12	1150
ZnS	2.2	850	3.86	Insoluble	5-9	240
ZnSe	2.4	525	2.00	Insoluble	5-9	120

n₁ = refractive index of ATR crystal

LWL = long wave length cut-off

d_p = depth of penetration in microns @ 1000 cm⁻¹ assuming sample refractive index of 1.5 and angle of incidence of 45°

3.4. Focus on the cell prism, penetration depth into the sample medium and resolution

Adjustment of focus

The ATR Veemax incident angle control allows focusing the incoming FTIR beam at a set point in x, y and z axis. The implemented cell on top of the angle control device has, therefore, to be adjusted exactly to that focus point in all three dimensions. Adjustment in z-axis cannot be changed in the implemented setup design and is ensured by the right cell geometry to be exactly on the surface of the ATR prism. The adjustment in x and y axis on top of the prism can be done manually, using a laser whose focus spot falls together with the focus spot of the infrared beam. As illustrated in Figure 3.15 a small droplet of water is applied with the working electrode in the exact center of the prism. A digital camera on top of the prism holder detects the beam pathway of the laser and the whole cell can be moved so that the drop of water and the focus point fall together.

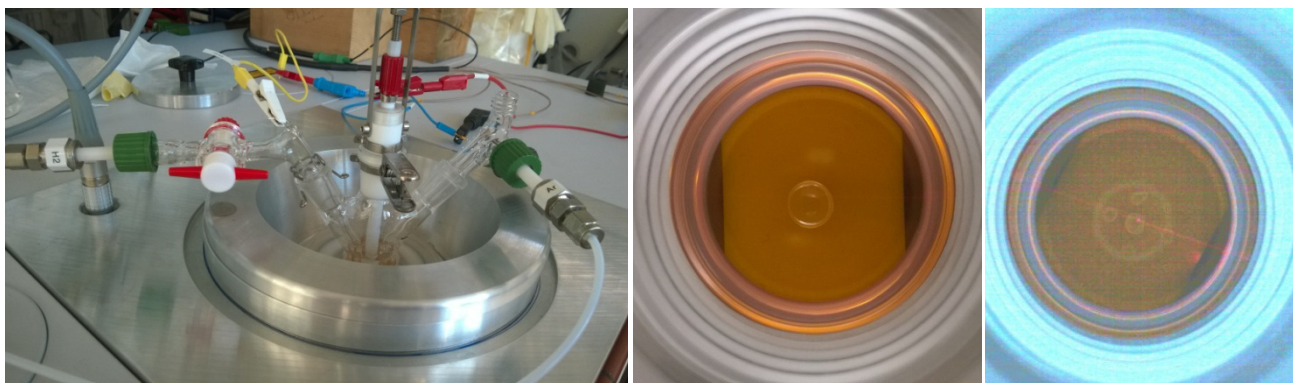


Figure 3.15: Setup of the FTIR cell. Focus of the Laser spot (Adjustment) on the prism. The Focus is adjusted by a concentric water drop.

Figure 3.16 shows the ATR spectra for a centered water drop adjusted to the ATR focus spot (blue) and for a ring of water droplets in a concentric circle around this adjusted ATR focus spot (gray). This demonstrates the range of ATR sensitivity closely to the focus point, water as a strong IR absorber can only be detected within this limitations.

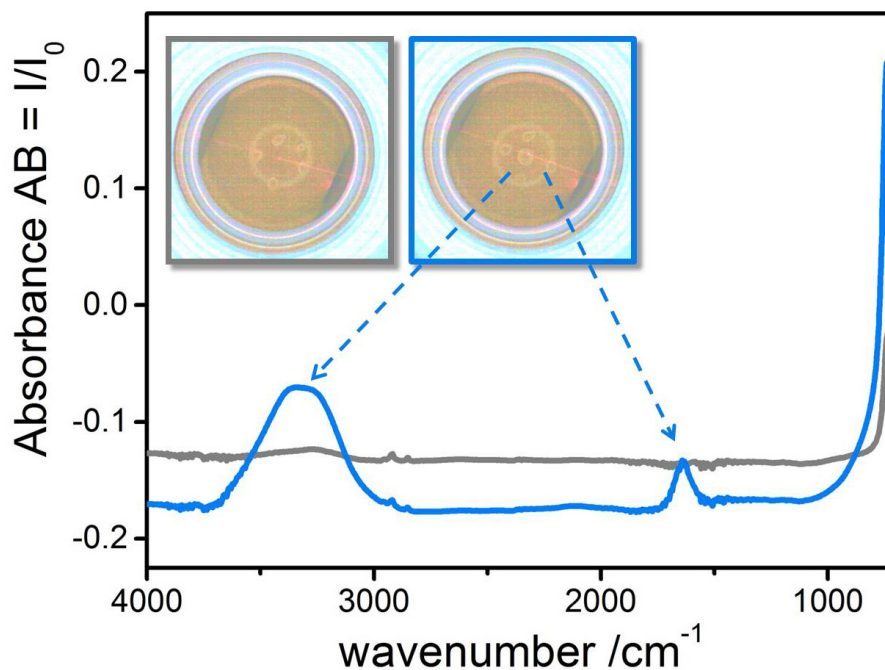


Figure 3.16: ATR Spectra for Adjustment of ZnSe window at 60°, background air. A water ring outside the Laser focus spot shows no water bands (gray), a water drop on the laser focus spot shows water bands around 3500 cm^{-1} and 1600 cm^{-1} .

The effective path length of the infrared beam in the sample must be sufficient to produce an adequate spectrum. This parameter is affected by both the number of reflections (more reflections yield higher absorbance) and the penetration depth. A higher angle of incidence results in less reflections and decreased penetration depth, lowering the overall absorbance of the spectrum. This is useful for the measurement of highly absorbing or high refractive index samples. Accordingly, a lower angle of incidence results in more reflections and an increased penetration depth.

Angle of incidence

The overall optical design, its optical path, mirrors quality and throughput, has great effects on analytical results. The angle of the refracted FTIR beam Θ_{refr} depends on both the angle of incidence Θ_i and the difference in refractive indices of the two mediums n_1 and n_2 (Figure 3.17).

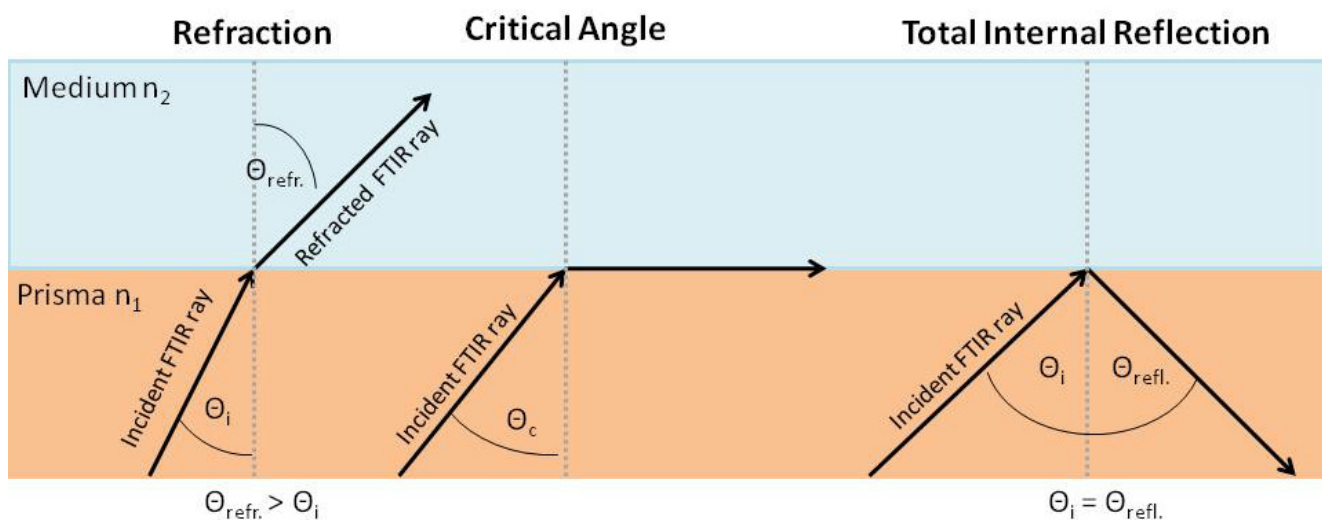


Figure 3.17: Critical Angle for Total Internal Reflection of FTIR light at the interface between the FTIR prism and the medium above it.

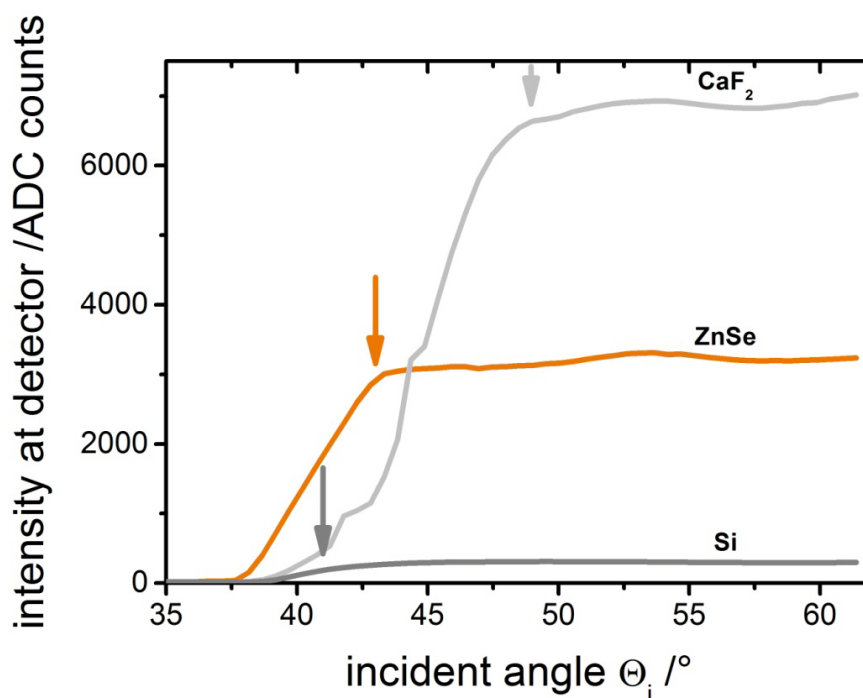


Figure 3.18: Intensity reaching the MCT detector in analog-to-digital counts (ADC) depending on different angles of incidence for different materials at the interface FTIR prism/air.

If Θ_i is smaller than the critical angle Θ_c , the incidence beam is refracted on the interface of the two mediums (here the prism and the electrolyte). If Θ_i reaches the critical angle Θ_c , the light is refracted perpendicular to the surface. Any higher angle of incidence leads to total internal reflection at the interface, where $\Theta_i = \Theta_{\text{refl}}$ because it is not passed through a second medium with differing refractive index anymore. Depending on the desired method of surpassing the catalyst sample, the angle of incidence has to be adjusted to provide refraction for external reflection or total internal reflection for ATR measurements. The intensity reaching the MCT detector of the cell depending on the angle of incidence for different FTIR prism materials is shown in Figure 3.18. The second medium is in this case is air over the prism.

Penetration depth

If the angle of incidence Θ_i is larger than the critical angle Θ_c , the incident beam is reflected on the surface while part of the wave penetrates to the thinner medium as an evanescent wave. The theoretical (d_p) and effective (d_e) penetration depth calculated for ZnSe/water interface in dependence of the wavelength of the incident beam are shown in Figure 3.19. The influence of the wavelength on the depth of penetration rises with lower wavelength, while the overall intensity stays fairly constant over a critical angle with higher angles of incidence. The best choice of angle of incidence for ATR experiments therefore is $\Theta_i = 45^\circ$, both for ZnSe as well as for Silicon.

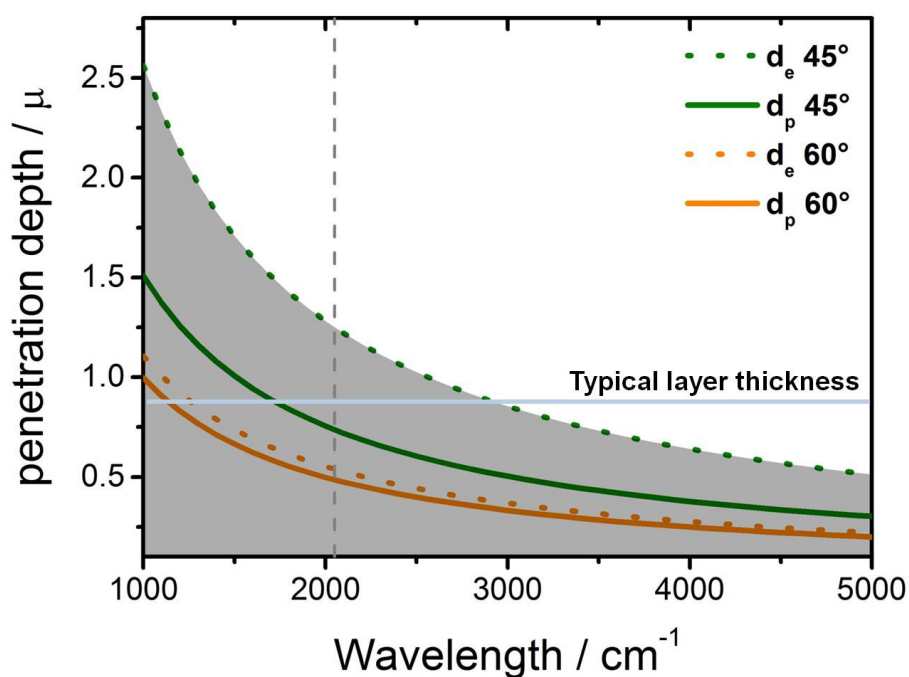


Figure 3.19: Theoretical (d_p) and effective (d_e) penetration depth calculated for ZnSe/water interface in dependence of the wavelength of the incident beam, the gray vertical dashed line indicates Pt-CO band at 2050 cm^{-1} , for $60^\circ \sim 0.55 \mu\text{m}$. Usual film thickness is between 0.04 and $0.78 \mu\text{m}$.¹⁰³

Resolution

An IR absorption spectra recorded at high resolution will the vibrational lines in the near IR are resolved into a number of individual lines which are due to vibrational-rotational transitions ($J_1 \rightarrow J_2$) that occur simultaneously with the vibrational transitions ($v_1 - v_2$). An ideal spectrum consists of lines that appear at the frequency corresponding to the transitions with intensity proportional to the number of molecules that made that tradition, which is mostly possible for spectra of ideal systems and single compounds. The selection rules for rotational-vibrational transitions are $\Delta J = 0, \pm 1$ and $\Delta v = \pm 1$. A rotational-vibrational spectrum consists of several lines separated equidistant (2 times the rotational constant B), grouped into two branches P and R, which are separated by a Q branch in the v_0 zone (Figure 3.20). The “poor” P branch is obtained by loss of rotational energy $\Delta J = -1$ while the “rich” R branch is obtained by gain of rotational energy $\Delta J = +1$. The Q branch for $\Delta J = 0$ is usually only obtained for polyatomic molecules with perpendicular vibrations.

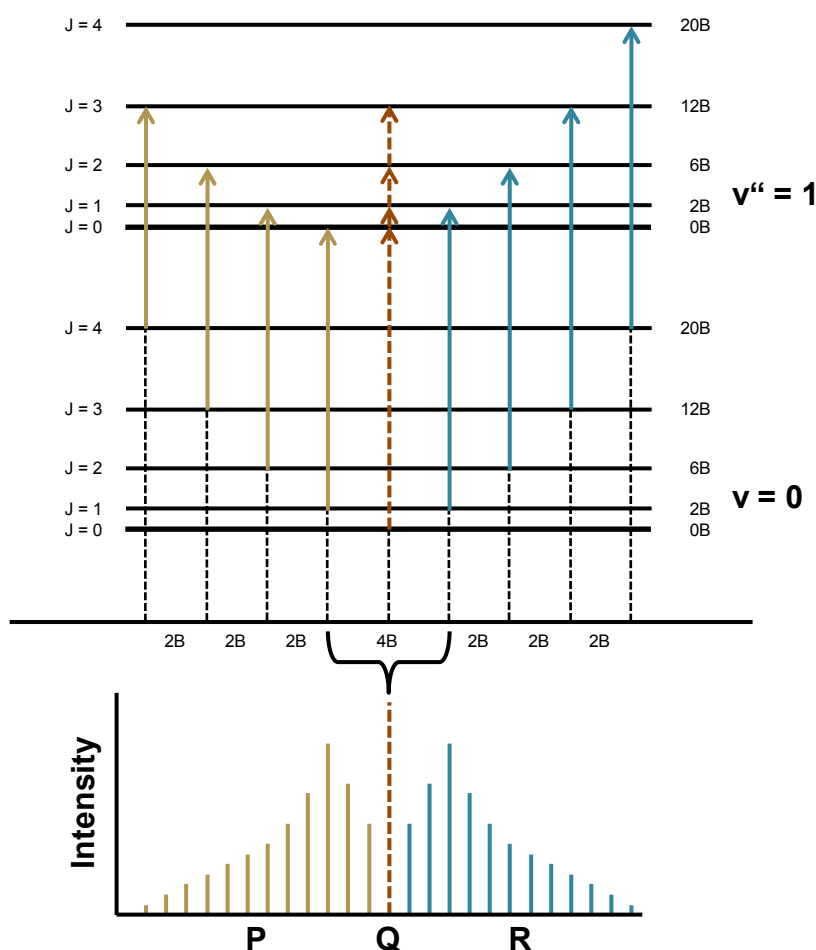


Figure 3.20: Scheme of the P, Q and R branch of a vibrational-rotational intensity profile and the corresponding rotational (ΔJ) and vibrational (Δv) transitions.

The *in situ* ATR spectra of CO₂ and CO_{ads} in 0.1 M HClO₄ at different resolutions in Figure 3.21 give a good example for the P, Q and R branches. As soon as the resolution is lower as the 2B distance between the rotational fine structure of CO₂, the rotational-vibrational spectra can only be seen as a broad band structure. For adsorbed CO, as can be expected, no rotational fine structure can be observed since the rotation is hindered because of the bond to the platinum surface.

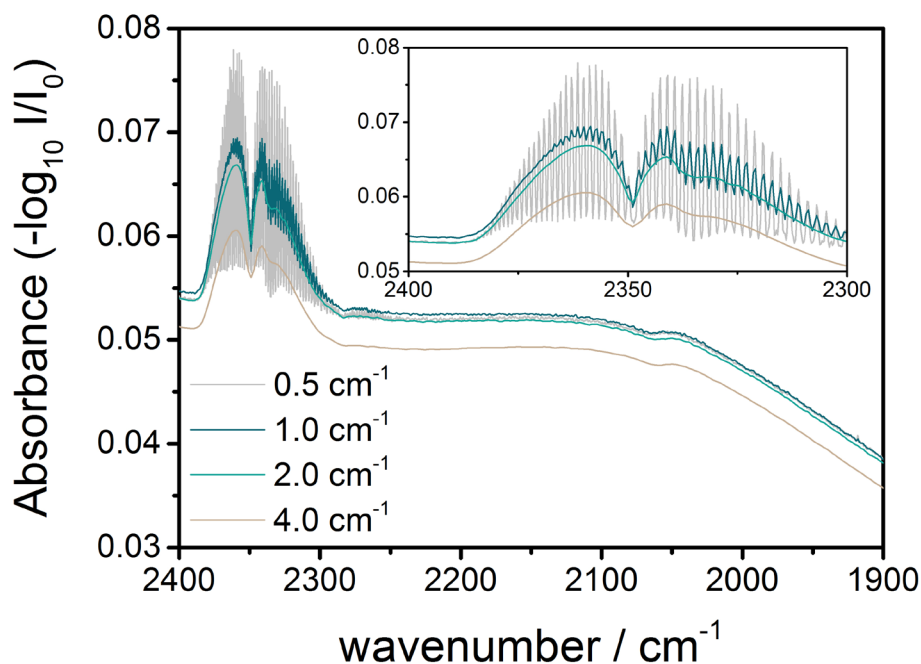


Figure 3.21: *In situ* ATR spectra of CO₂ and CO_{ads} on Pt/C in 0.1 M HClO₄ at different resolutions. 128 interferograms were added into one single spectrum. The insert shows an enhancement of the CO₂ region.

Since the acquisition time of the ATR spectra depends almost linear on the set resolution and the desired structural information is gained qualitatively from the ν_0 frequency of a certain species involved in the electrocatalytic reaction, resolutions higher as 4 cm⁻¹ are not necessary for the electrochemical *in situ* ATR spectroscopic experiments.

3.5. Electrochemistry in the *in situ* cell: Ethanol and carbon monoxide oxidation

The exact position of a band can vary due to strain effects on the catalysts surface, the position of adsorption on the surface and environmental changes due to the electrolyte. FTIR bands of typical molecular species involved in the EOR reaction and CO oxidation are listed in Table 3.2. ATR spectra of different reaction mixtures of possible educts and products were measured. Figure 3.22 shows the absorbance spectral features of ethanol, acetic acid and acetaldehyde individual, each dissolved in the electrolyte, as well as an equimolar reaction mixture. Unfortunately, the components cannot all be detected equally sufficient from the mixture. Whereas acetic acid and ethanol show distinctive features in spectral regions where no other contribution can be expected (acetaldehyde 1200 - 1400 cm^{-1} ; ethanol 1080 cm^{-1}), the identification of acetaldehyde in the reaction mixture is rather demanding.

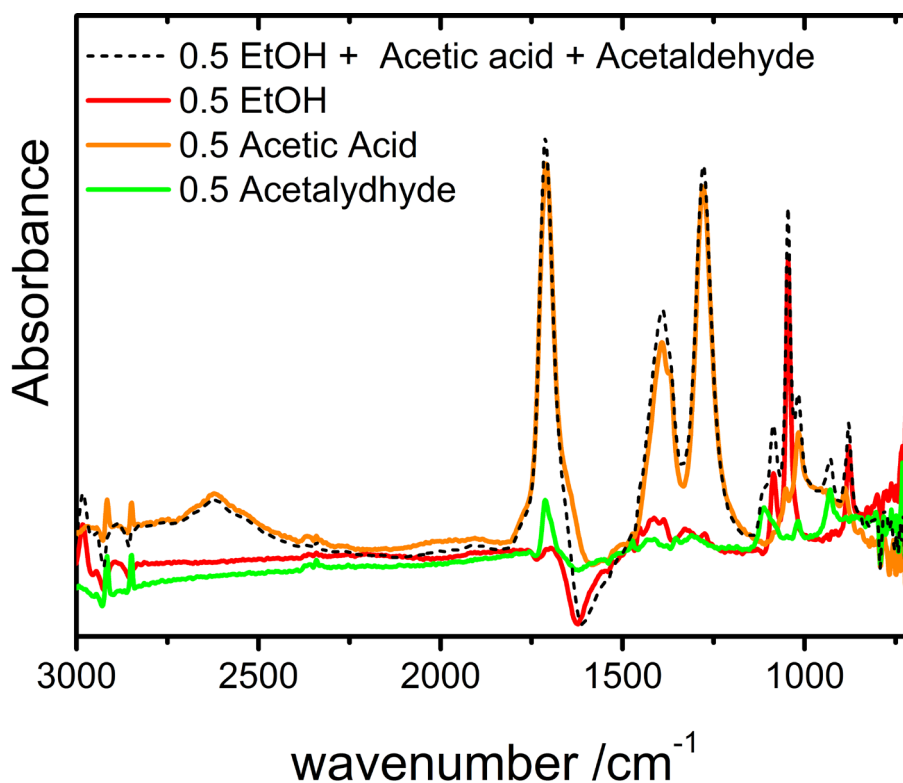


Figure 3.22: ATR spectra of ethanol oxidation reaction educts and products in 0.1 M HClO_4 . 128 scans, resolution = 4 cm^{-1} , background pure 0.1 M HClO_4 .

Table 3.2: FTIR bands and designated vibrational modes of different species involved in the EOR.^{104,105}

FTIR band [cm ⁻¹]	Species	Vibration mode
3500–3000	Water	ν (O–H) stretching
3000–2500	AAL	ν (C–H) asymmetric stretching of –CH ₃ ν (C–H) symmetric
3000	AA	ν (C–H) asymmetric stretching of –CH ₃ ν (C–H) symmetric
2343	CO ₂	ν (O=C=O) asymmetric stretching
2040	CO _L	ν (C=O) stretching (linear adsorbed)
2031	CO _L	ν (C=O) stretching (linear adsorbed)
1920	CO _B	ν (C=O) stretching (bridged adsorbed)
1850	CO _B	ν (C=O) stretching (bridged adsorbed)
1721	AAL	ν (C=O) stretching of –COH
1721	AA	ν (C=O) stretching of –COOH
1600	Water	δ (H–O–H) in-plane bending
1400	div	Bridging and bi-dentate acetate complexes from acetate species or from acetic acid at Pt surface
1397	AAL	δ (-CH ₃) symmetric bending
1370	AA	δ (-CH ₃) symmetric bending
1281	AA	Coupled δ (O–H) and ν (C=O) stretching of –COOH
1280	AA	Coupled δ (O–H) and ν (C=O) stretching of –COOH
1110	HClO ₄	ν (Cl–O) stretching
1110	AAL	δ_w (C–H) wagging
1067	Ethanol	δ (C–C–OH) bending

AAL=Acetaldehyde, AA=acetic acid

Electrooxidation of carbon monoxide

The electrochemical characteristics of CO adsorbed on noble metal surfaces, including the nature of the binding sites and the effects of the applied potential on the structural and electronic properties of the adsorbate/substrate system, make *in situ* electrochemical CO oxidation experiments a powerful probing tool for catalytic materials. The strong CO IR intensities can also be used to validate the accuracy of the corresponding electrochemical and spectroscopic properties of an *in situ* cell design. Figure 3.23 shows the first three scans of a cyclic voltammetric testing on Pt/C electrocatalyst (BASF) deposited as a film directly onto a ZnSe prism and contacted *via* a carbon cloth (Toray paper 030) with the working electrode (Glassy Carbon, Pine). CO was purged into 0.1 M HClO₄ and let to adsorb onto the platinum surface. Prior to the electrochemical testing it was removed from the electrolyte by purging with Ar. It can be seen that the electrochemical behavior inside the *in situ* electrochemical FTIR cell is very similar to the standard electrochemical rotating disc electrode (RDE) testing of CO on Pt.¹⁰⁶

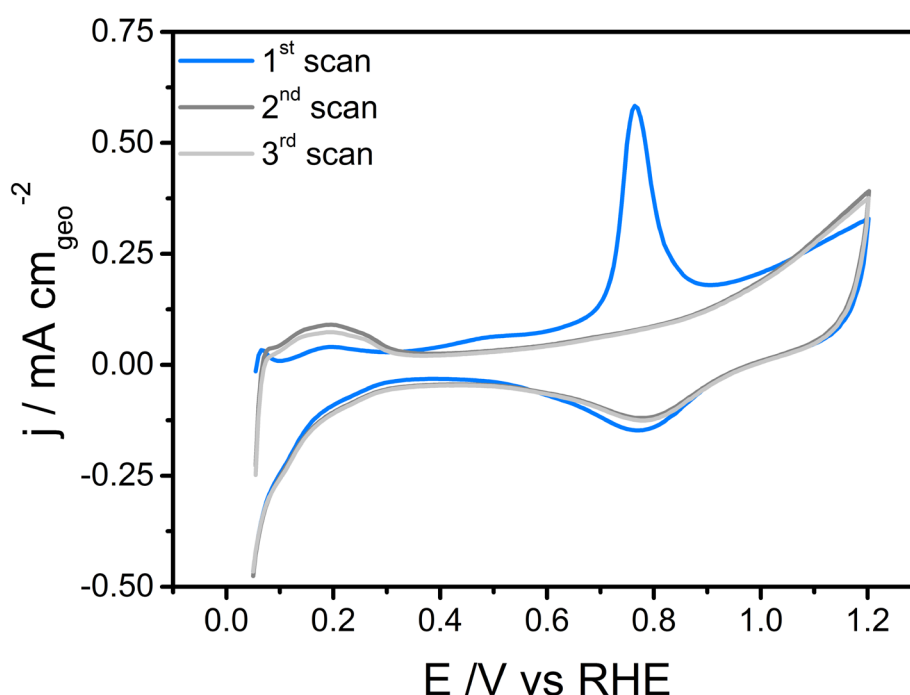


Figure 3.23: CV of the electrooxidation of CO on Pt/C (BASF) film deposited on ZnSe, contacted with Toray Paper 030 in 0.1 M HClO₄ with 20 mV s⁻¹. CO was adsorbed and then removed with Ar from the electrolyte prior to the measurement. Current density is normalized by the size of the GC working electrode (0.071 cm²).

A series of FTIR spectra is measured on the Pt/C film during the electrochemical testing: in pure electrolyte, with carbon cloth equipped as a working electrode at low potentials of

$E = 0.06$ V vs. RHE, after the saturation with CO, and after the catalytic stripping of the adsorbed CO. In Figure 3.24 depicts the corresponding *in situ* ATR spectra to Figure 3.23.

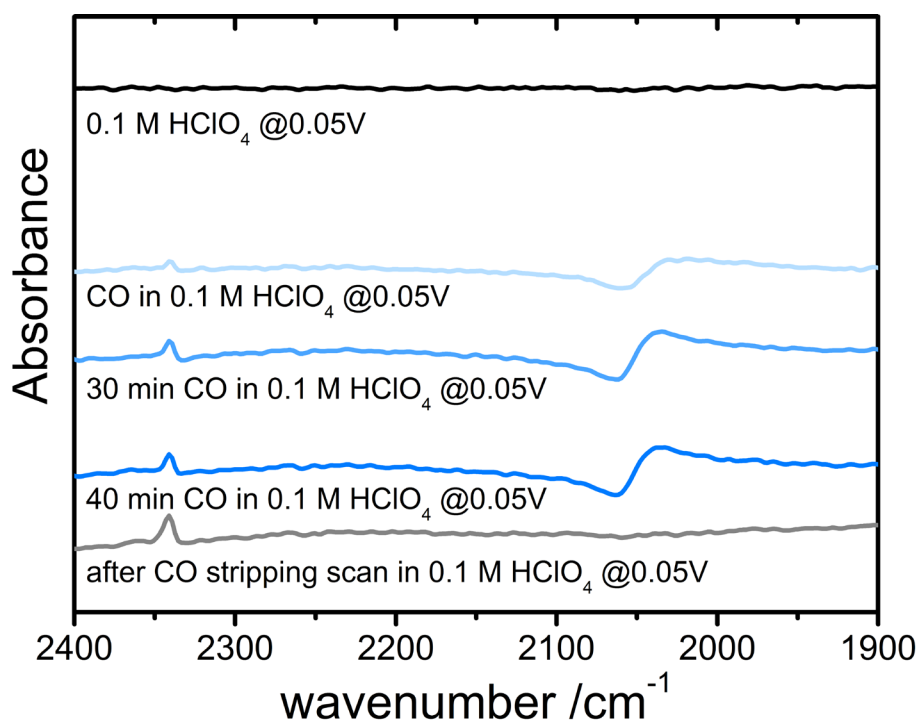


Figure 3.24: *In situ* ATR FTIR spectra during the electrooxidation of CO on Pt/C on ZnSe contacted with carbon cloth (Toray Paper 030) and a GC WE in 0.1 M HClO₄. Spectra background was recorded in pure electrolyte without applied potential. All spectra are recorded at 0.05 V vs. RHE before and after the respective cyclic voltammograms (Figure 3.23).

Electrooxidation of Ethanol

The *in situ* FTIR setup validation was finalized with measurements of the EOR on a Pt-Rh-Sn electrocatalytic system. Figure 3.25 shows the first scan of a cyclic voltammogram testing on a *PtRhSn/C* electrocatalyst (see Chapter 5) deposited as a film directly onto a ZnSe prism and contacted *via* a carbon cloth (Toray paper 030) with the working electrode (Glassy Carbon, Pine) in 0.5 M EtOH + 0.1 M HClO₄. As already seen for CO oxidation experiments, the electrochemical behavior inside the *in situ* electrochemical FTIR cell is very similar to standard electrochemical RDE testing of the EOR on *PtRhSn/C*.¹⁰⁷ Since the EOR reaction is conducted with a very low scan rate of 1 mVs⁻¹, a series of *in situ* FTIR spectra can be recorded during the scan. For each spectrum 128 single scans are averaged, the potential range of the respective averaged spectra are shown in the insert in Figure 3.25. The corresponding spectra are shown in Figure 3.26.

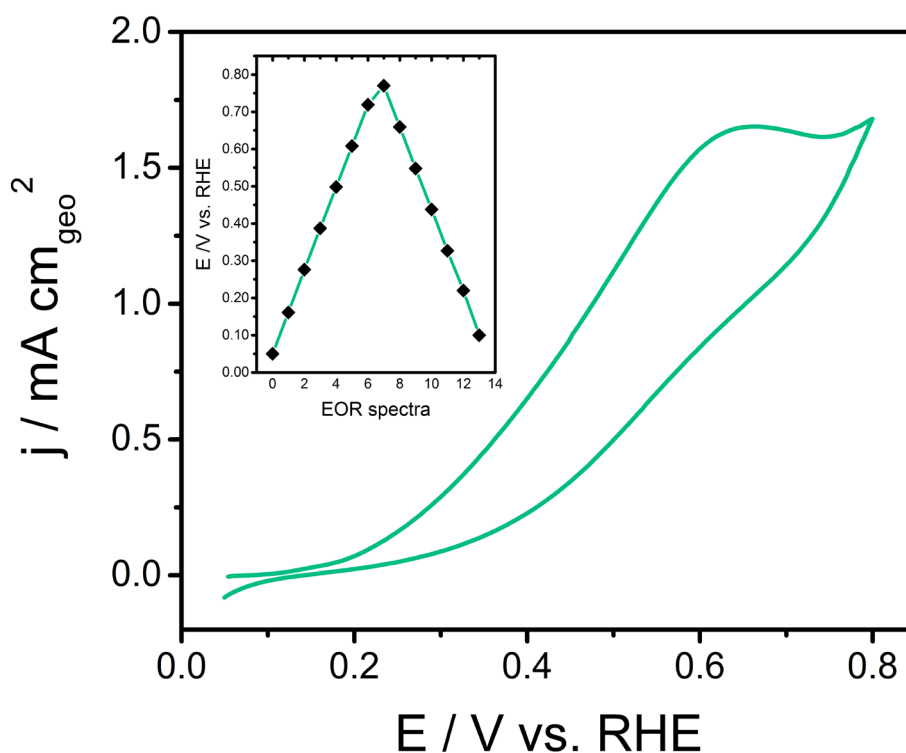


Figure 3.25: CV for the oxidation of EtOH on *PtRhSn/C* on ZnSe contacted with carbon cloth and GC WE in 0.5 M EtOH + 0.1 M HClO₄, scan rate = 1 mV s⁻¹. The insert shows the potential range of the respective averaged spectra shown in Figure 3.26.

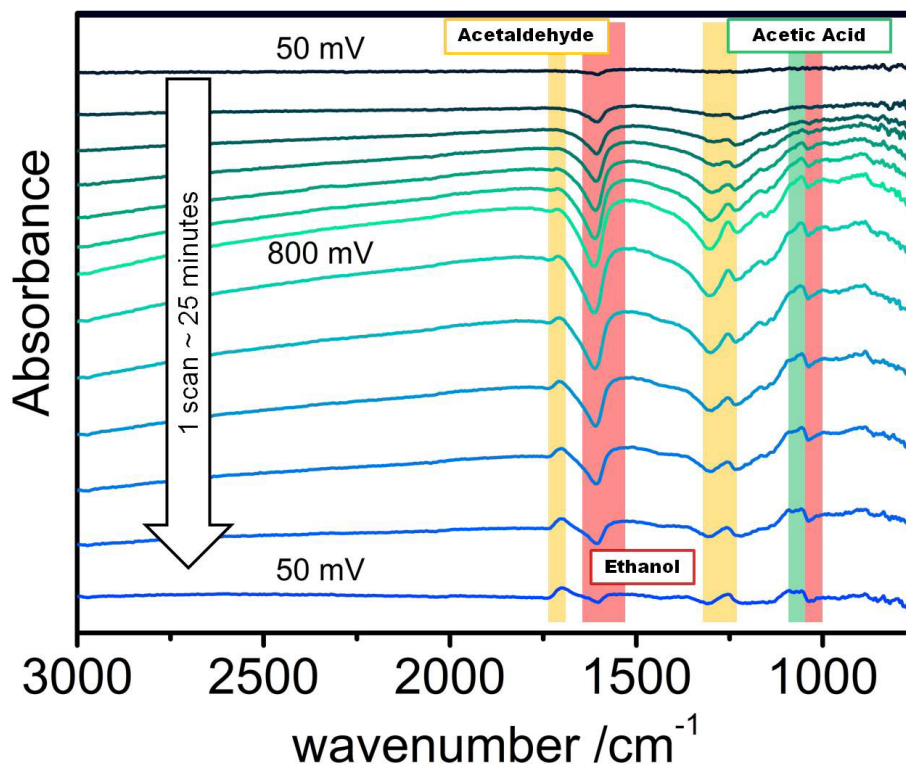


Figure 3.26: *In situ* ATR FTIR spectra during the first scan for the oxidation of EtOH on *PtRhSn/C* on ZnSe contacted with carbon cloth and GC WE in 0.5 M EtOH + 0.1 M HClO₄, scan rate = 1 mV s⁻¹. Spectra background was recorded at E_{ref} = 0.05 V vs. RHE. The potentials corresponding to each spectrum are indicated in the figure.

All absorption spectra were recorded during a linear sweep from 0.05 to 0.80 V vs. RHE. According to Table 3.2 the bands at 1700 and 1728 cm⁻¹ can be associated with acetaldehyde and/or acetic acid, which are byproducts due to the incomplete oxidation of ethanol. The bands at 1397 cm⁻¹ can be associated to acetic acid, the bands at 1110 cm⁻¹ to acetaldehyde and perchloric acid. Around 1080 cm⁻¹ are the bending bands of ethanol.⁵ No CO₂ bands can be observed at 2342 cm⁻¹, indicating that no complete oxidation of ethanol is achieved.

In order to investigate the long term stability of the cell setup as well as possible limitations due to a semi-thin film cell design with the carbon cloth reservoir for the ethanol containing electrolyte, a series of several cyclic voltammetric scans at higher scan rates was conducted. Figure 3.27 shows the first ten scan with 20 mVs⁻¹ of a cyclic voltammetric testing on the *PtRhSn/C* electrocatalyst (see Chapter 5) in 0.5 M EtOH + 0.1 M HClO₄ deposited as a film directly onto a ZnSe prism and contacted *via* a carbon cloth (Toray paper 030) with the working electrode (Glassy Carbon, Pine). While the overall current density drops with the number of scans, even the tenth scan still shows good EOR activity and all scans show similar onset potentials and the typical hysteresis behavior.

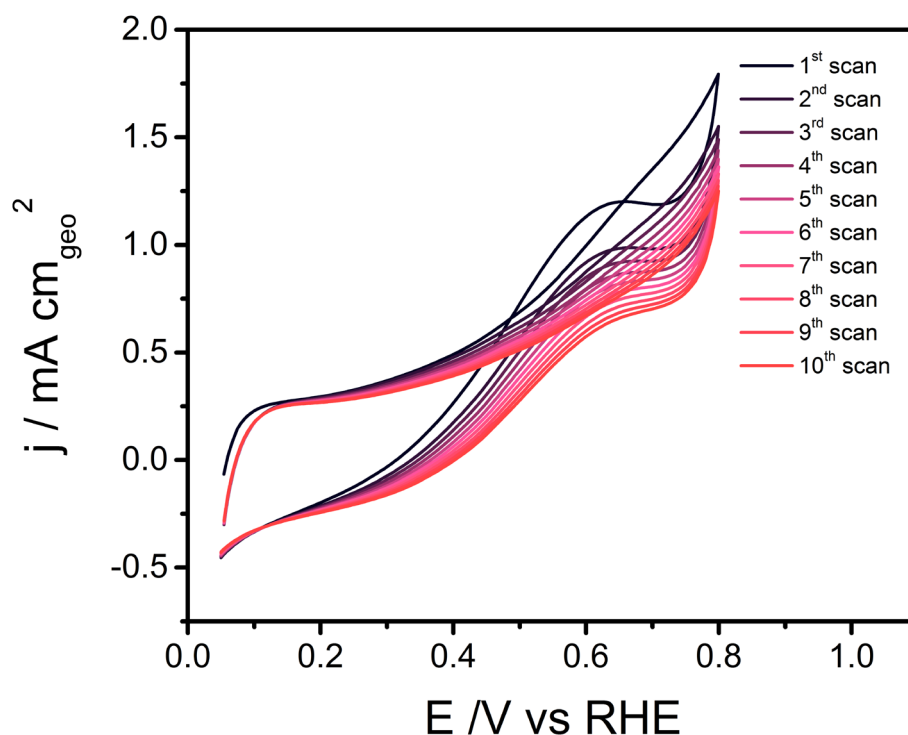


Figure 3.27: First 10 cyclic voltammograms for the oxidation of EtOH on *PtRhSn/C* on ZnSe contacted with carbon cloth and GC WE in 0.5 M EtOH + 0.1 M HClO₄ and cycled with 20 mVs⁻¹.

During each cyclic voltammetric scan, 128 single beam spectra are averaged and the respective absorption spectra are shown in Figure 3.28, using the ethanol containing electrolyte before EOR as a background spectra. The bands at 1700 and 1728 cm⁻¹ are growing stronger with each scan and can be associated with acetaldehyde and/or acetic acid, which are byproducts due to the incomplete oxidation of ethanol, similar to the single scan results (Figure 3.26). The bands at 1397 cm⁻¹ can be associated to acetic acid, the bands at 1110 cm⁻¹ to acetaldehyde and perchloric acid. It can be seen that the acetaldehyde bands are more dominant over time, indicating further oxidation of acetaldehyde and/or readsorption of acetaldehyde on the catalyst surface, is hindered in this catalytic system. Around 1080 cm⁻¹ are the bending bands of ethanol, their ongoing negative trend with the number of EOR scans shows the consumption of ethanol in the reaction medium at the catalyst film.⁵ As for the single scan experiment, also for more EOR reaction time no CO₂ bands at 2342 cm⁻¹ can be observed, indicating that no complete oxidation of ethanol is achieved.

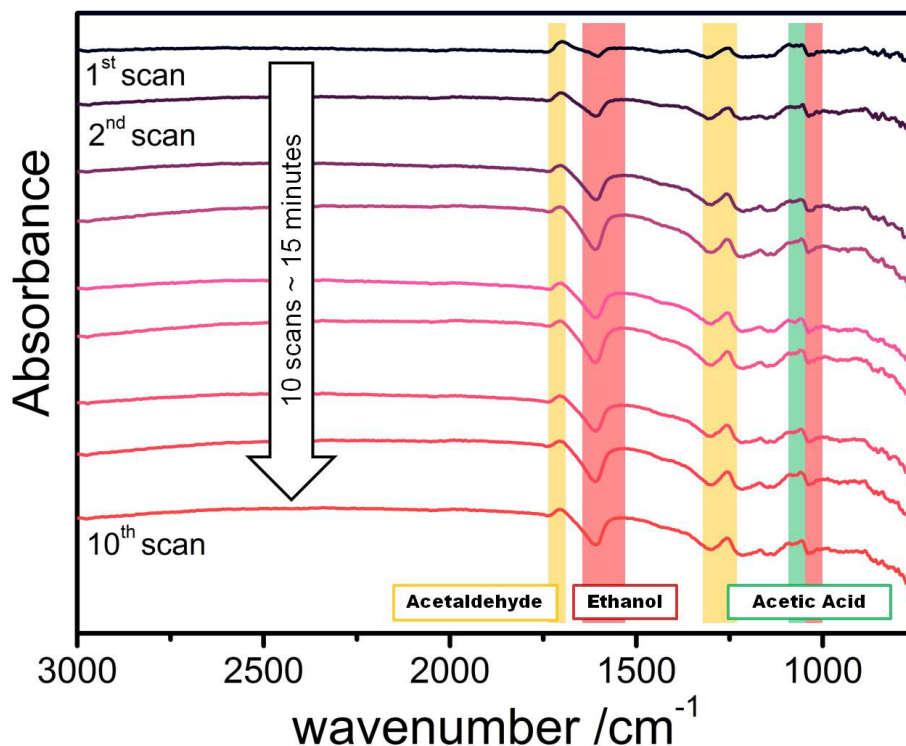


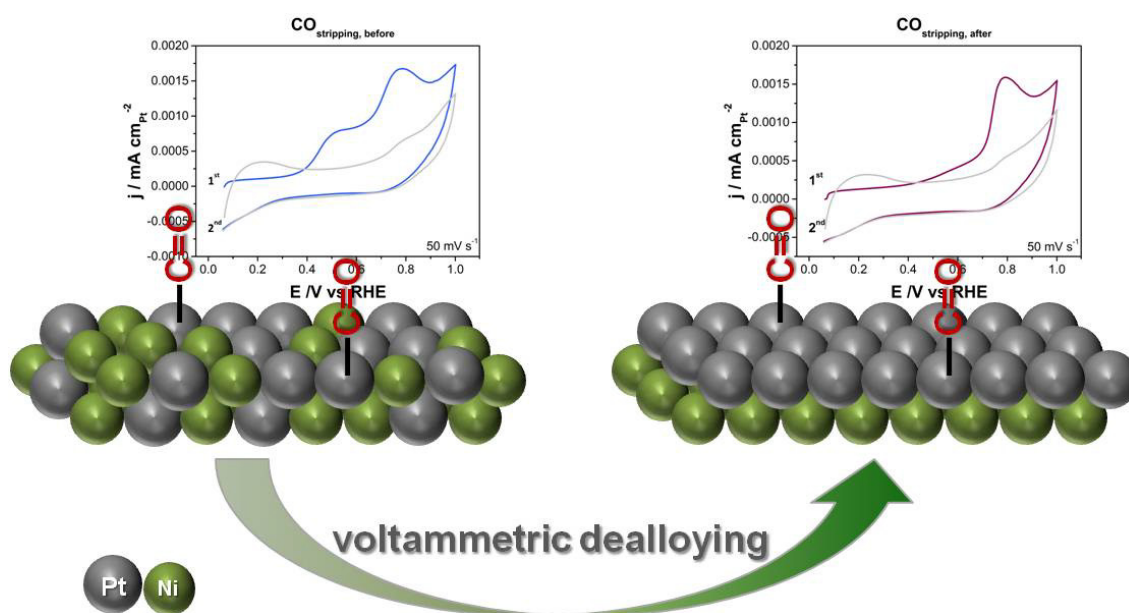
Figure 3.28: *In situ* ATR FTIR spectra corresponding to Figure 3.27 for the oxidation of EtOH on PtRhSn/C on ZnSe contacted with carbon cloth and GC WE in 0.5 M EtOH + 0.1 M HClO₄. The potential was cycled 10 times with 20 mVs⁻¹. Spectra background was recorded at E_{ref} = 0.05 V vs. RHE. The scans corresponding to each spectrum are indicated in the figure.

Conclusion

In conclusion, the innovative *in situ* FTIR cell setup design was successfully validated. The setup uses a novel design with carbon cloth, a conductive but inherent material, to connect the working electrode film while being permeable to water based electrolytes. Electrochemical current responses inside the cell are similar to RDE setup measurements and show little to no mass transport limitation within the measuring requirements. *In situ* FTIR spectra of adsorbed species on the catalyst film as well as features from the electrolyte over the catalyst film can be detected and correlated to species involved in the electrocatalytic oxidation of ethanol.

4. Strain effects on the catalytic properties of alloyed and dealloyed PtNi₃ surfaces studied by *in situ* ATR spectroscopy of the electrooxidation of adsorbed CO.

In this chapter, the important role of CO intermediates on the electrocatalytic surface is discussed. The strain effect on the surface due to the dealloying process occurring during electrocatalysis is investigated. The electrooxidation of carbon monoxide on PtNi₃ alloyed and dealloyed catalytic surfaces is studied with non-mass transport limited in situ electrochemical ATR spectroscopy.



4.1. CO adsorption on catalytic surfaces: the role of CO_L intermediates for the EOR activity

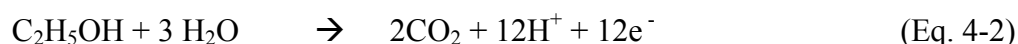
Modern DEFCs are mainly based on platinum electrocatalysts dispersed on carbon, although it is well known that pure Pt does not display best catalytic activity towards the electrooxidation of ethanol. This disadvantage is partly due to poisoning of the platinum active sites by intermediates generated from reactions occurring with the oxidation of ethanol, resulting in higher overpotentials.¹⁰⁸ Platinum itself is very well known to be rapidly poisoned on its surface by strongly adsorbed species coming from the dissociative adsorption of organic molecules, since a nearly complete layer of strongly adsorbed CO can be removed only at potentials higher than 0.5–0.6V.^{32,41,109} This long-known poisoning effect is observed with all organic molecules, and obviously also with ethanol. The only possibility to overcome this effect is to modify the electrode surface in such a way to increase, at low potentials, its coverage in oxygenated species (e.g. adsorbed OH) coming from the dissociation of water. These OH species are necessary to completely oxidize the dissociation species of alcohols to carbon dioxide.

On platinum, the first step on adsorption of ethanol involves δ-C-H dissociation, leading to the formation of adsorbed acetaldehyde:¹¹⁰



Adzic *et al.* reported several studies on ternary Pt-Rh-Sn electrocatalysts for the EOR.^{5,61,111} Their Pt-Rh-SnO₂ with varied Pt-Rh-Sn ratios showed less to no CO_L bands for linearly adsorbed CO intermediates. These CO_L bands only occur on pure Pt or Pt rich electrocatalysts and are not present on their active and selective catalysts for the complete EOR.¹¹¹ Therefore, they claim the high activity of their electrocatalysts is reflected in strong CO₂ band and negligible CO bands.

Surface-enhanced infrared measurements of the EOR on Pt by Shao *et al.* show that the partial oxidation of ethanol generates CH₃CHO and CH₃COOH species.²⁶ For their PtRhSnO₂ electrocatalyst, the generation of acetic acid is negligible while the yield of acetaldehyde is significantly decreased, and the negative-moving band for CO increases with rising potential. These data indicate that on this electrocatalyst, the C-C bond in ethanol is broken directly without going through the acetaldehyde step. The reaction predominantly involves ethanol oxidation to CO₂:



De Souza *et al.* conducted also several studies on ternary Pt-Rh-Sn electrocatalysts for the EOR with Sn incorporated into the Pt fcc lattice structure rather than SnO₂.^{30,112,113} CO stripping curves on their electrocatalysts suggest onset potentials for the oxidation of adsorbed CO around 0.6 V vs. RHE while *in situ* IRRAS measurements report onset potentials for the complete oxidation to CO₂ starting from

0.5 V vs. RHE. CO_L bands are present at low potentials on all electrocatalytical surfaces. For all of their catalysts the intensity of this band follows a volcano-type behavior, with a maximum at ~0.6 V vs. RHE. The subsequent decay in the intensity of the CO_L band is attributed to either increasing CO_L oxidation or decreasing CO_L formation. They claim that their observed potential dependence of CO₂ and CO bands suggests that CO_L is an intermediate leading to CO₂ formation.

De Souza *et al.* can, however, report only very late onset potentials for the formation of CO₂ in comparison with the results of Adzic *et al.*, suggesting their catalytic surfaces follow a more platinum-like behavior concerning the EOR, i.e. the CO species poison their active sites and allow efficient EOR activity only at high overpotentials, respectively. It seems the catalysts without CO intermediates at low potentials and earlier onset potentials hold an advantage due to the formation of highly active surface site ensembles that enable a different, more selective pathway at low overpotentials for the ethanol oxidation, without strongly bonded CO as an intermediate.

4.2. Dealloying of bimetallic nanoparticles and strain effect on the surface

The incorporation of metals into platinum has the potential to increase the performance of these electrocatalysts. For instance, metals such as Ru, Rh, W, Ni, and Sn are frequently employed as co-catalysts, in order to minimize the effect of Pt poisoning with CO and other by-products, thereby improving the catalytic activity.^{46,64,114-117} The addition of Ni as second or third element is claimed to be beneficial for the activity of Pt electrocatalysts as it reduces the oxidation potential of small organic molecules coupled with the rise in current density. For example, Almeida *et al.*¹¹⁸ showed that the onset of ethanol, as well as CO oxidation, is shifted towards lower potentials for Ni containing Pt/C and PtSn/C catalysts, and the overall catalytic activity is enhanced. The binary combination of platinum and nickel is a well known system as an outstanding electrocatalytic material for the electroreduction of molecular oxygen.^{39,54,55,65,66,106,119-121} The concept of voltammetric dealloying of non-noble metal rich nanoparticles proves as an effective method to prepare core-shell nanoparticle catalysts. The activity of PtNi electrocatalysts changes for dealloyed materials with core-shell like structures because platinum enriches at the surface, having modified electronic properties due to strain effects resulting from nickel layers below the platinum surface layers.^{54,65,66} The extent of the dealloying, due to porosity formation in bulk samples, is largely controlled by the ratio between the surface diffusion rate and the non-noble metal dissolution rate.^{119,122,123} Figure 4.1 demonstrates schematically the dealloying process of a bimetallic alloy (e.g. the Pt-Ni system).

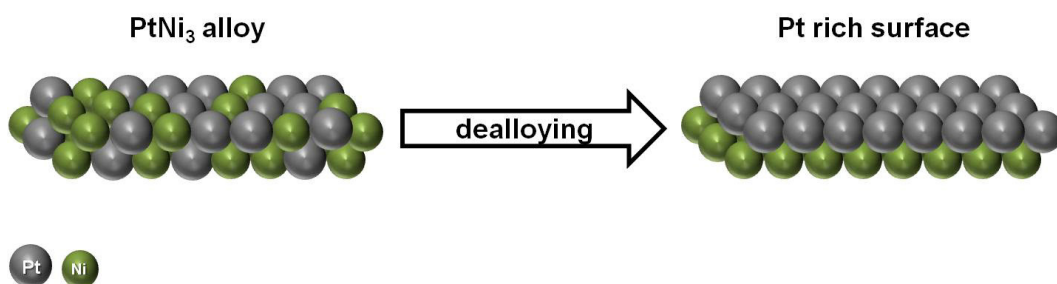


Figure 4.1: Schematic illustration of the dealloying process for PtNi₃/C. During the electrochemical dealloying Pt enriches at the surface.

According to molecular orbital (MO) theory, the binding energy of an adsorbate onto a metal surface is largely dependent on the electronic structure of the surface itself.¹²⁴ When hydrogen adsorbs on a Pt surface, the hydrogen 1s state interacts with the platinum 6s band, which results in the formation of a filled, low-lying bonding molecular orbital (MO) and an empty antibonding MO (Figure 4.2). The metal *d*-band hybridizes with the bonding (σ) orbital of the adsorbate to form bonding ($d-\sigma$) and antibonding ($d-\sigma$)* states, as illustrated in Figure 4.2. For noble metals, the ($d-\sigma$) state is filled, whereas the filling of the ($d-\sigma$)* state depends on the local electronic structure of the metal at the surface.¹²⁵

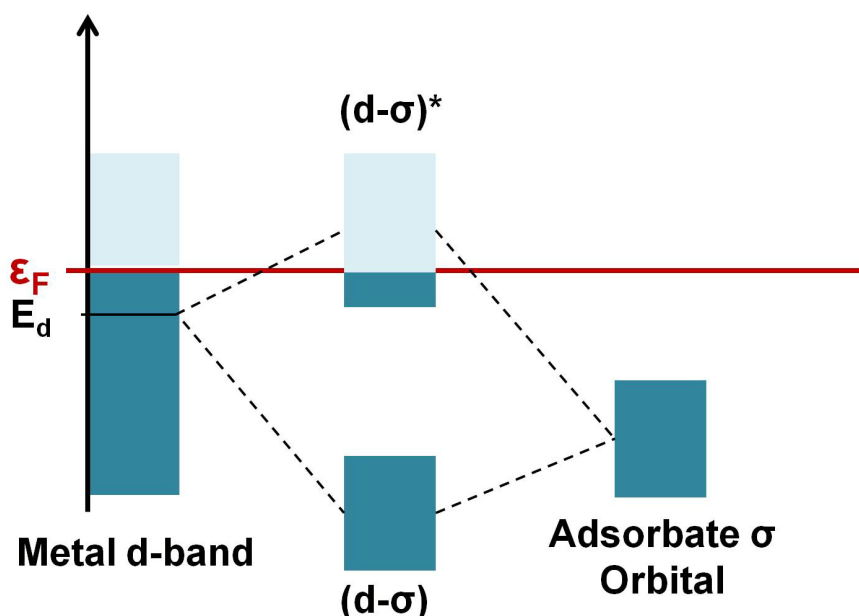


Figure 4.2: Molecular orbital energy level diagram for orbitals constructed from the overlap of metal *d*-band orbitals and an adsorbate σ orbital, resulting in the formation of a filled bonding ($d-\sigma$) molecular orbital and an empty antibonding ($d-\sigma$)* molecular orbital.

The qualitative trends found in the catalytic activity as a function of the strain or the coordination of the substrate atoms can be nicely explained invoking the *d*-band model^{126,127}: tensile strain, for

example, leads to a narrowing of the metal d band due to the reduced overlap of the wave functions. If the d -band is more than half filled, i.e., if the metal is a late transition metal, the band narrowing leads to an increased population of the d -band. Because of charge retention, the d band moves up in order to preserve d -band filling. According to the d -band model, an upshift of the d -band leads to a lower occupation of antibonding states in the molecule-surface interaction, thus, raising the interaction strength.

Using perturbation theory, a linear relationship between the d -band center shift $\delta\epsilon_d$ and the change in the chemisorption strength ΔE_d ,^{128,129}

$$\Delta E_d = -\frac{V^2}{|\epsilon_d - \epsilon_a|^2} \delta\epsilon_d \quad (\text{Eq. 4-3})$$

can be derived, where ϵ_a is an electronic adsorbate level and V is a coupling matrix element that is assumed to be constant for similar situations. The higher binding to lower-coordinated sites at nanostructured surfaces can be explained by a similar reasoning: a lower coordination, i.e., a smaller number of nearest neighbors, also leads to a band narrowing and a subsequent upshift of the d -band center. For early transition metals with a less than half-filled d -band, tensile strain or reduced coordination should have the opposite effect on the d -band center: the resulting band narrowing should lead to a downshift of the d -band center and, thus, to a reduced interaction with adsorbates. Hence, the dependence of adsorption energies on the strain and coordination should have the opposite behavior in early transition metals compared to late transition metals. Figure 4.3 shows a schematic illustration of the coupling between bandwidth and d -band center for a band with a fixed number of d -electrons.¹³⁰

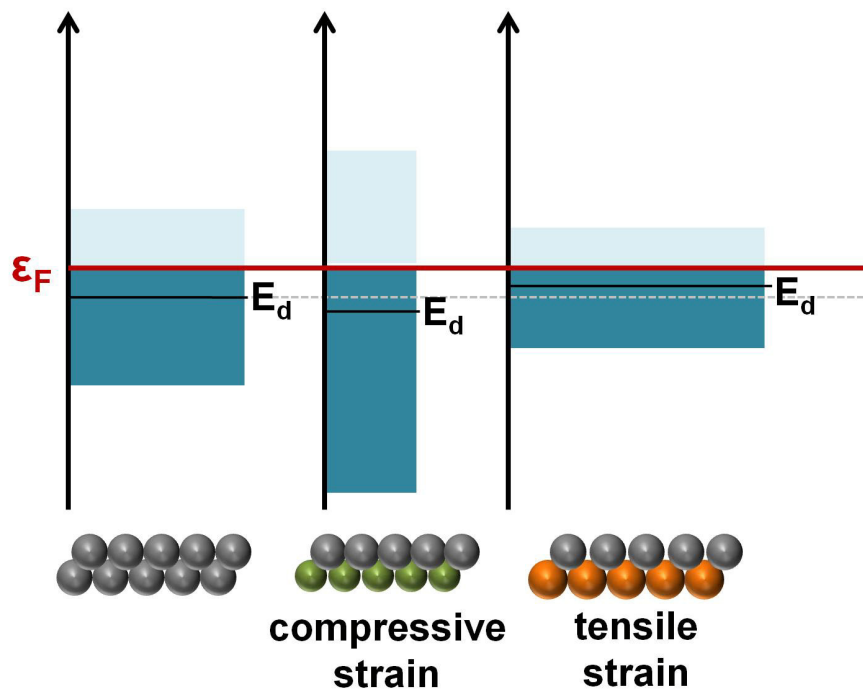


Figure 4.3: Illustration of the effect of compressive and tensile strain on the width and position of the d -band of an early transition metal. The local density of states due to compressive strain leads to a downshift of the d -band center E_d while the tensile strain leads to an upshift of E_d towards the Fermi level.

An increased filling of the antibonding $(d-\sigma)^*$ state corresponds to a destabilization of the metal-adsorbate interaction (weakened binding). From this model it is apparent that a higher d -band center E_d (with respect to the Fermi level) corresponds to an increase in energy (relative to the Fermi level) and subsequent decrease in filling of the $(d-\sigma)^*$ state, which means the metal-adsorbate system is less destabilized. In short, a higher d -band center (smaller $E_{dbc} - E_F$) results in stronger binding between the metal and the adsorbate. Similarly, a lower d -band center (larger $E_{dbc} - E_F$) means weaker binding. Even though this argument was made for the case of adsorption of hydrogen to metal surfaces, it seems to be a reasonable model for adsorption of oxygen, or any oxygen-containing species, as well.¹³¹ Platinum binds oxygen too strongly, which implies that its d -band center is too high. Alloying platinum with other non-precious metals lowers the d -band center (by both altering the electronics and inducing a degree of irregularity in the platinum lattice), which in turn causes the resulting alloy to bind oxygen more weakly than platinum.¹³² Thus, alloying provides a means of weakening of the surface electronic structure resulting in a minimized overpotential of the oxygen reduction reaction (ORR).

4.3. Experimental access to the strain effect due to dealloying: *in situ* FTIR spectroscopy

Strain and coordination effects in late transition metals have recently attracted a lot of attention as they can significantly change the electronic and catalytic properties of these metal surfaces.¹³³⁻¹³⁷ Strain effects occur, e.g., when a metal is grown pseudomorphically on another metal with a different lattice constant. Tensile strain of 1.5% can, for example, lower the dissociation barrier of CO by up to 0.2 eV which would enhance the dissociation rate constant by more than three orders of magnitude at room temperature.¹³⁵ Considerations based on effective strain are also important to understand the reactivity of metallic compounds such as surface alloys.¹³⁸ Adsorption of CO onto metal surfaces is generally described by the Blyholder model, schematically represented in (Figure 4.4a).¹³⁹

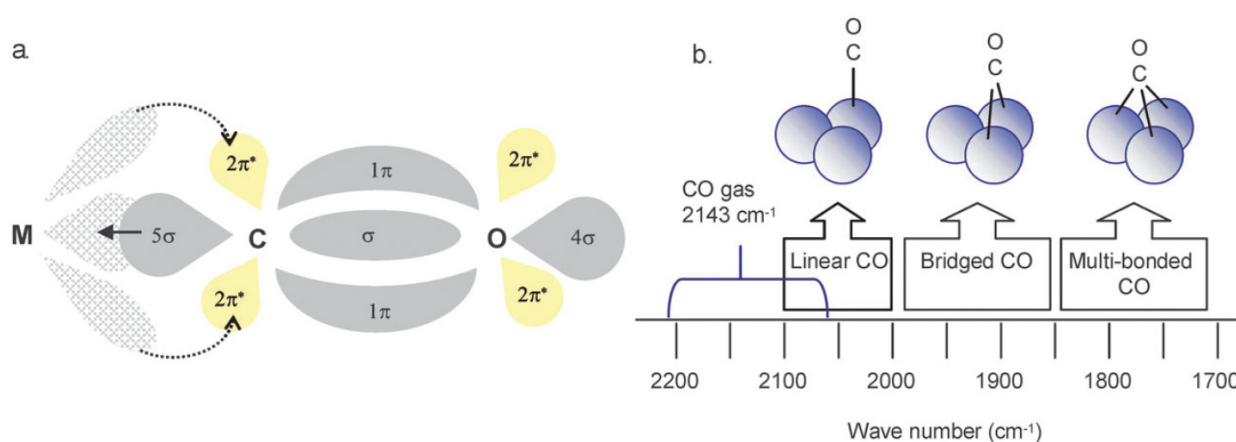


Figure 4.4: (a) Adsorption of CO onto metal surfaces according to Blyholder¹³⁹. (b) Ranges of IR peak position as a function of adsorption geometry on noble metal surfaces. Reproduced from Reference¹⁴⁰ with permission of The Royal Society of Chemistry.

According to this model electrons are donated from CO through the s-bond to the metal orbitals. At the same time, electron back-donation takes place from the metal to the empty 2p* orbitals of CO, resulting in a lower bond strength between C and O. Due to this decreased bond strength, the infrared absorption bands shift to lower wave numbers compared to gas phase CO at 2143 cm⁻¹. CO covers metal surfaces in different binding geometries, either directly on top (linear) of a metal atom, bridged between two metal atoms or multibonded between three metal atoms. This difference in binding geometry is visible by changes in IR peak position (C=O stretch frequency) due to a change in binding energy as illustrated in Figure 4.4b.^{141,142} The adsorption of CO onto Pt-containing surfaces is therefore an ideal tool to access the strain effect in binary catalytic surfaces with *in situ* FTIR spectroscopy.

While *in situ* FTIR spectroscopy is a commonly used tool for *in situ* analysis of electrocatalytic processes on metal surfaces like bulk Pt polycrystal and single-crystal electrodes, its application for real supported nanoparticle electrocatalysts is still highly demanding. Cheah *et al.*¹⁴³ studied CO

adsorption on carbon-supported Pt nanoparticles in the gas phase under operando conditions by quadrupole mass spectrometry and diffuse reflectance infrared fourier transform spectroscopy (DRIFTS). The C–O stretching vibration (ν_{CO}) bands were ascribed to CO adsorbed on Pt surface at (111)-terrace, (100)-terrace, edge, and kink sites in linear and bridged forms. An unexpected ν_{CO} band at 1703 cm^{-1} was observed upon CO adsorption and tentatively attributed to CO on surface Pt sites interacting through its oxygen end with the carbon support.

The investigation of CO adsorbed on Pt under fuel cell conditions, i.e. with an aqueous electrolyte phase above the catalytic surface instead of a gas phase, reveals slightly deferring spectral behavior. Next to the stretch mode of CO_2 (2360 cm^{-1}) linearly bound CO_L (2065 cm^{-1}) is expected in these spectra.¹⁴⁴⁻¹⁴⁶ Zhu *et. al* revealed that the oxidation of an CO ad-layer on sputtered Pt surfaces in perchloric acid results in addition to linear and bridged bonded CO in adsorbed carboxylic species.¹⁴⁷ They reported an interesting bipolar shape of the CO_L band. In general, a stretching frequency increases with increasing the electrode potential. A bipolar band of CO_L with an anomalous shape (i.e., a higher reflectance at higher wavenumbers) was first reported in 1994 in potential-difference IR spectra on a graphite basal plane covered with Pt particles.¹⁴⁸ This anomalous bipolar CO band was attributed to a potential-induced migration of chemisorbed CO molecules, from terraces at the reference potential (0.05 V vs. RHE) to edge or kink sites at the sample potential (0.3 or 0.4 V vs. RHE), assuming that the CO stretching frequency is higher for terraces (2070 cm^{-1}) than for edge or kink sites (2040 cm^{-1}).

In order to increase the understanding of the relation between catalyst surface composition and structure with the corresponding catalytic activity, the dealloying process at the surface and therefore change of Pt-CO and Ni-CO adsorption sites, respectively, can be investigated with *in situ* FTIR spectroscopy. Therefore, an alloyed PtNi_3 , synthesized *via* a polyol method, is dealloyed under potential control *via* extensive cyclic voltammetric cycling with fast scan rates^{55,66,106} and the change of the position of the Pt-CO band was monitored. The experimental protocol with all electrochemical and spectroscopic steps is depicted in Figure 4.5.

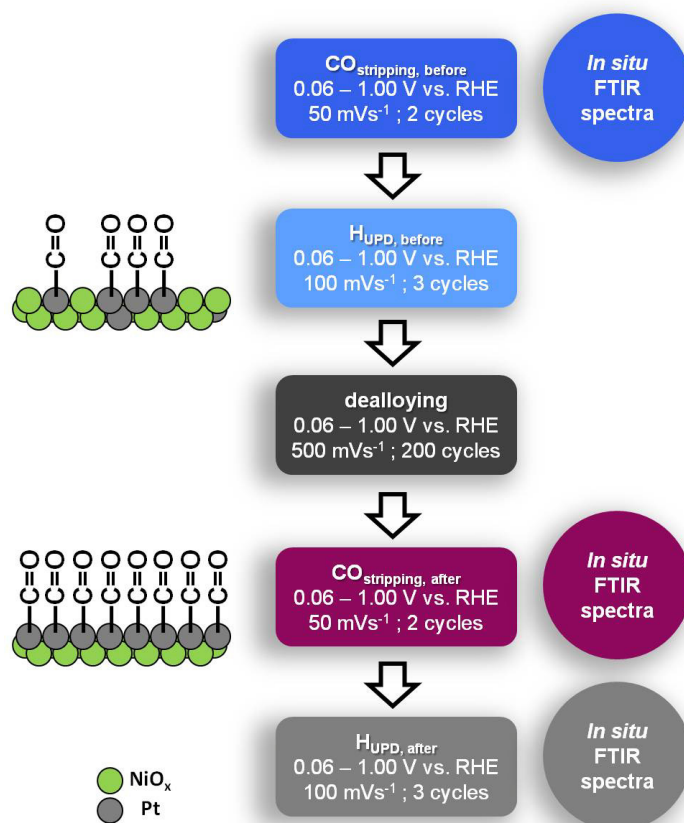


Figure 4.5: Experimental and spectroscopic dealloying protocol for PtNi₃/C electrocatalysts.

PtNi₃/C was implemented in the cell as an ink, contacted with carbon cloth and a non rotating GC electrode as working electrode and the potential was controlled while *in situ* ATR spectra were recorded. As shown in Figure 4.6, the dealloying process at a very high scan rate of $v = 500 \text{ mVs}^{-1}$ could be easily conducted in the *in situ* electrochemical FTIR setup, indicating that no mass transport phenomena hindered the dealloying process.

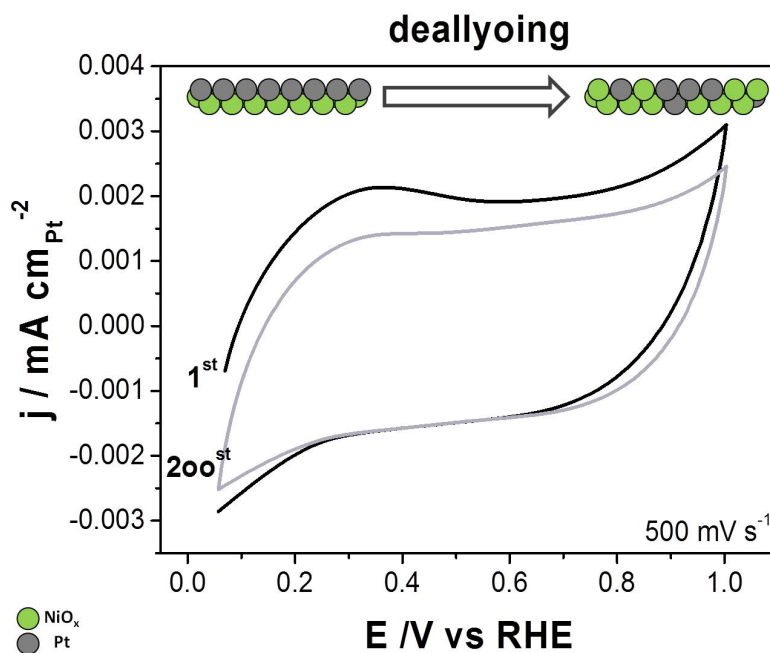


Figure 4.6: Dealloying process on PtNi₃/C in 0.1 M HClO₄, scan rate = 50 mV s⁻¹ at 25°C.

The electrochemical protocol starts in CO saturated electrolyte (0.1 M HClO₄). CO is stripped from the surface by oxidizing it in a forward scan to higher potentials before and after the dealloying process. Cyclic voltammetric scans in pure electrolyte were conducted following the CO stripping scans before and after the dealloying process, respectively (Figure 4.5). The active surface area SA of the catalyst was estimated by employing the reduction charge of hydrogen under potential deposition (H_{UPD}) based on the charge density for the formation of a fully covered Pt-H monolayer (210 μC/cm²)¹⁴⁹. CO-SA values¹⁰⁶ from the CO-oxidation charge were estimated accordingly, based on a fully covered Pt-CO layer (420 μC/cm²).

H_{UPD} CVs are shown in Figure 4.7. The corresponding surface areas before (SA_{HUPD,before} = 0.21 cm_{Pt}²) and after (SA_{HUPD,after} = 0.19 cm_{Pt}²) dealloying differ only slightly, indicating no big change upon dealloying for adsorption sites for hydrogen on the platinum surface.

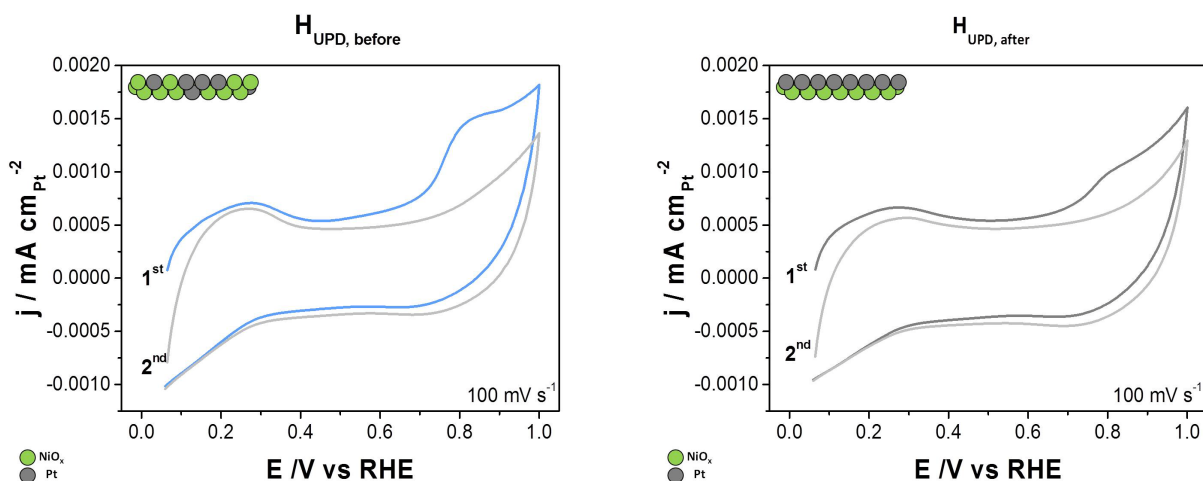


Figure 4.7: H_{UPD} *in situ* on PtNi_3/C before (left) and after (right) dealloying in 0.1 M HClO_4 , scan rate = 50 mV s^{-1} at 25°C . Current densities are normalized by SA from H_{UPD} desorption.

Figure 4.8 shows CO stripping voltammograms before and after dealloying. The voltammogram peak structure indicates successful dealloying: Pt-CO stripping peaks for Pt in close vicinity to Ni disappear while the Pt-CO peak for Pt in close vicinity to Pt and Ni remains. Ni rich surfaces are known to be more oxophilic and can, therefore, provide more Ni-OH species for CO oxidation.^{106,121} SA_{CO} values are both higher than the corresponding $SA_{H_{\text{UPD}}}$ values, as can be expected.¹⁰⁶ The SA_{CO} value decreases from before ($SA_{\text{CO, before}} = 0.99 \text{ cm}_{\text{Pt}}^2$) to after dealloying ($SA_{\text{CO, after}} = 0.62 \text{ cm}_{\text{Pt}}^2$), indicating less CO coverage or less available Pt active surface sites.

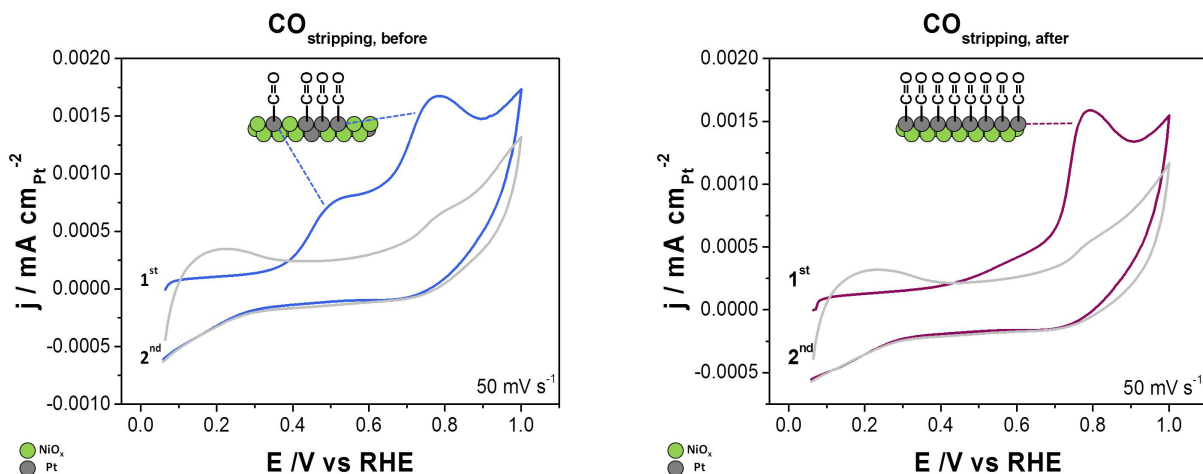


Figure 4.8: CO stripping *in situ* on PtNi_3/C before and after dealloying in 0.1 M HClO_4 , scan rate = 50 mV s^{-1} at 25°C . Current densities are normalized by SA from H_{UPD} desorption.

In situ ATR spectra, shown in Figure 4.9 were recorded before and after the dealloying process right before the CO stripping or H_{UPD} measurements, respectively. They show the presence and absence of the CO monolayer on the electrocatalytic surface during the different steps of the experimental

protocol (Figure 4.5). Over this experimental protocol, the CO₂ stretching band at 2342 cm⁻¹ increase with each CO oxidation step. The positive band at 2050 cm⁻¹ can be associated with the stretching of linear adsorbed CO on top of the platinum atoms of PtNi₃.

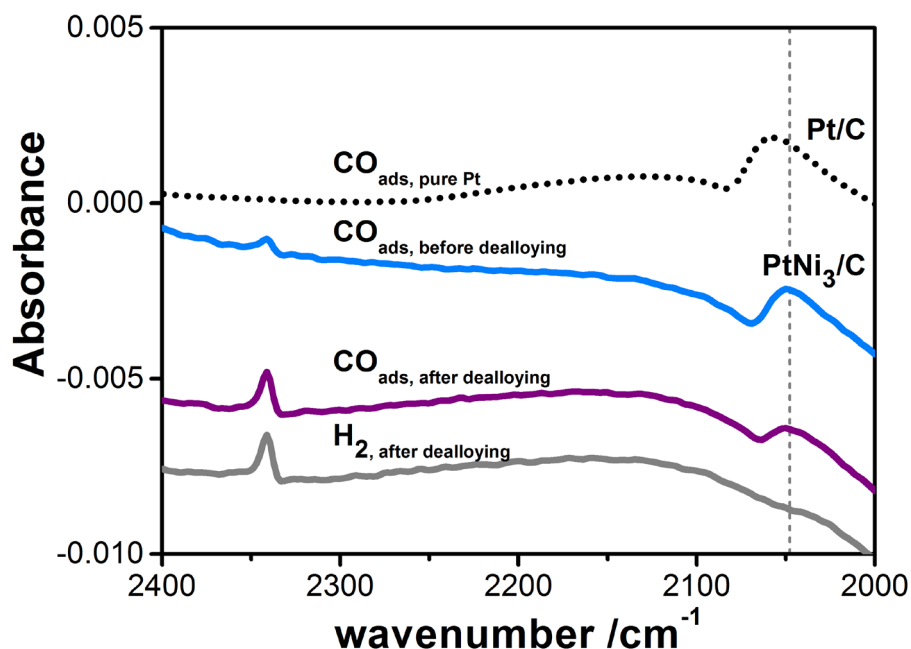


Figure 4.9: *In situ* ATR FTIR spectra of adsorbed CO on pure Pt/C and PtNi₃/C on ZnSe contacted with carbon cloth and GC WE in 0.5 M 0.1 M HClO₄. All spectra were recorded at E = 0.05 V vs. RHE, background spectrum I₀ was recorded without electrolyte.

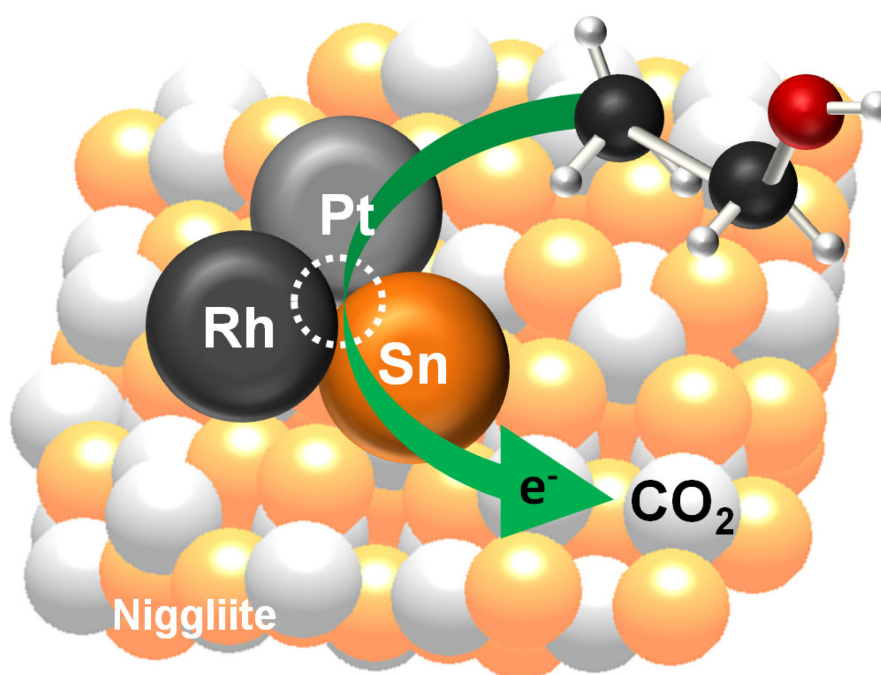
As seen in Figure 4.9, this $\nu_{\text{COads,before}}$ band for PtNi₃ before dealloying shows a red shift of $\sim 10 \text{ cm}^{-1}$ in comparison to pure Pt/C, indicating that CO bonds distinctly different on top of dealloyed core shell PtNi₃. For the dealloyed species, a small blue shift towards the pure Pt/C in comparison with $\nu_{\text{COads,after}}$ can be seen from the spectra. This indicates that the Pt richer surface of the dealloyed PtNi₃ changes its binding energy towards the adsorbed CO species, which is in accordance with the above described *d*-band theory.

Conclusion

The *in situ* electrochemical FTIR setup proves to offer insights not only of reactants of an electrocatalytic process on the investigated surfaces, but information of adsorbed species and possible intermediates. This allows valuable conclusions on the electronic state of the catalytically active surface, which can then be used to modify and design novel electrocatalysts for reactions like the EOR.

5. Ethanol electro-oxidation on ternary Platinum-Rhodium-Tin nanocatalysts: Insights in the atomic 3D structure of the active catalytic phase

Results of an investigation of the atomic structure of Platinum-Rhodium-Tin nanoalloys and their effect on ethanol oxidation reaction are reported in this chapter. Various electrocatalysts were synthesized using a polyol-type method either by simultaneous, consecutive or pseudo-consecutive reduction of precursors. Morphology, composition and atomic-scale structures were studied using advanced techniques. The relationship between the atomic-scale structural properties on one side and the electrocatalytic activity towards the oxidation of ethanol on the other was also studied. It was found that the activity of a simultaneously reduced PtRhSn/C catalyst with a solid solution structural state is considerably better than that of consecutively reduced nanoalloy electrocatalysts



The contents of this chapter have been published: Reprinted with permission from N. Erini, R. Loukrakpam, V. Petkov, E. A. Baranova, R. Yang, D. Teschner, Y. Huang, S. R. Brankovic and P. Strasser, *ACS Catal.*, **2014**, 4, 1859-1867.¹⁰⁷ Copyright 2014 American Chemical Society.

5.1. Introduction

Development of direct ethanol fuel cells (DEFCs) as alternate power sources has been a subject of intensive studies for fundamental and practical applications (e.g., the development of compact portable power as well as electric vehicle range extenders operating at high temperatures).⁷⁻¹⁰ Liquid fuels, like low carbon alcohols, such as methanol or ethanol, have higher volumetric and gravimetric energy densities, better energy efficiencies, and they offer easy handling, storage, and transportation, contrary to gaseous fuels.¹¹ Although methanol is of a particular interest for mobile applications such as electric vehicles, ethanol has some important advantages over methanol such as higher energy density (8 kWh kg⁻¹ vs. 6 kWh kg⁻¹, respectively), low toxicity, biocompatibility, and abundant availability. It is, however, not as easily oxidized to CO₂ and water as methanol. This is attributed to difficulties in the sluggish adsorption and cleavage of C-C bonds in ethanol and, by some authors, to the formation of CO intermediates leading to poisoning of the active sites on Pt catalysts.³⁻⁶ Complete ethanol electro-oxidation to CO₂ involves 12 electrons per molecule, whereas partial oxidation leads to byproducts like acetic acid or acetaldehyde, which reduce the Faradaic efficiency of the anodic reaction of DEFC. Efforts to develop highly active and selective electrocatalysts for the ethanol oxidation reaction (EOR) to CO₂ have therefore concentrated on the addition of co catalysts to platinum.³⁵ The most promising family of EOR nanocatalysts are currently based on mixtures of Pt, Rh and Sn.^{5,61,104,112,150-152} However, the optimal structural arrangement of the atoms of the three components in the surface and bulk of the final active catalyst to maximize activity and selectivity have not been clarified to date at an atomic scale.

Mechanistic details of the Rh and Sn-promoted oxidation of ethanol on Pt are also not well understood. It is believed that Rh increases the yield of CO₂ by promoting the C-C bond cleavage. However, there is reason that this hypothesis does not represent a comprehensive picture of the role of Rh in this family of catalysts. The role of Sn in the ternary Pt-Rh-Sn electrocatalysts is even more controversial.

A large number of previous studies have primarily focused on the effects of either alloying Sn into Pt^{6,153,154} or on the presence of SnO₂ species.^{52,116,155} SnO₂ is well-known for being potentially able to provide O species for the oxidation of intermediates produced during the dissociative adsorption of ethanol on Pt active sites (bifunctional mechanism).¹⁵⁶ Adzic *et al.*⁵ prepared an active PtRhSnO₂/C ethanol electrocatalysts using electrochemical underpotential deposition (UPD) of Pt and Rh atoms on carbon-supported SnO₂ nanoparticles in a fairly complex multistep process. The authors used X-ray absorption to learn about local Pt and Rh coordination and bond lengths; however, they did not address the 3D atomic arrangement of their active “quasi-random alloy”.

In a more recent report, Kowal *et al.* reported on a set of Pt–Rh–SnO₂ nanoparticle catalysts and proposed twinned Pt–Rh and SnO₂ crystallites with an optimal Pt/Rh/Sn = 3:1:4 ratio.^{61,152} As most authors, they gave no particular attention to the effect of the order of addition of the components. The catalytic effect of different metal ratios was also studied by Garcia-Rodriguez *et al.* by adding various amounts of Rh to a carbon-supported Pt₃Sn ethanol electrocatalysts.¹⁰⁴ Du *et al.* reported the synthesis of carbon-supported PtRhSnO₂ nanoclusters with simultaneous reduction of the precursor salts. This study reported two coexisting Sn phases in the Pt₅₂Rh₁₂Sn₃₆ material: metallic Sn in a PtRhSn homogeneous alloy and SnO₂ as a secondary phase.¹⁵⁷ Spinacé *et al.* reported PtSnRh/C electrocatalysts synthesized *via* an alcohol-reduction process using ethylene glycol and showed that this ternary catalyst and binary PtSn/C performed similarly for ethanol oxidation at RT, whereas the activity of binary PtRh/C electrocatalysts was very low. However, at 100 °C the ternary catalyst was found to exhibit superior performance compared to the two binary relatives.¹⁵¹ Lastly, Silva *et al.* reported a nonalloyed PtSn catalyst claiming preferred C–C bond cleavage. That catalyst showed conversion of ethanol to CO₂ but the conversion kinetics was prohibitively slow at practical DEFC anode potentials.¹¹²

A consensus is emerging that the catalytic activity of ternary Pt–Rh–Sn materials is generally superior to that of their binary relatives. However, important structural insights about the catalytically active bulk and surface phase are missing; in particular, the detailed three-dimensional atomic arrangement of the Pt, Rh, and Sn atoms of the active catalytic phase has remained unresolved, and so has the question whether crystalline homogeneous single phase materials, crystalline multiphase materials, or even phases with limited structural coherence (partially amorphous phases) are preferred. What adds to the confusion caused by the conflicting reports on the catalytic activity of ternary PtRhSnO₂ catalysts is the fact that no one has ever paid closer attention as to how the sequence of addition of the three metal components affects catalyst structure and activity. In other words, it is not clearly documented what detailed synthesis protocol was *actually conducive* for high catalytic activity and high CO₂ selectivity.

To address some of these questions and to gain better understanding of the desired 3D atomic arrangement of Pt, Rh and Sn in active EOR catalysts, we prepared a variety of different ternary Pt–Rh–Sn nanoparticle catalysts by varying the sequence in which each metal component entered the synthetic process of the final catalyst material. A comprehensive set of real and reciprocal space techniques was employed to explore composition, morphology, and atomic-scale structural coherence, most prominently synchrotron-based high-energy x-ray diffraction (HE-XRD), transmission electron microscopy (TEM) coupled with energy disperse x-ray spectroscopy (EDX), as well *in situ* Fourier transform infrared spectroscopy (*in situ* FTIR). What sets this study apart from earlier structural

investigations is the exploration of structural coherence using the atomic pair distribution function (PDF) analysis. This clearly underutilized yet powerful tool yields the PDF, which represents the degree and length of structural coherence and provides insight in the interatomic distances and atomic coordination shells incorporating contributions of both ordered and amorphous domains. The modeling of experimental PDFs provided us with structural motifs of the catalytically active phase. On the basis of our PDF analysis, we find that a novel single-phase ternary PtRhSn electrocatalysts displaying a Niggliite-type mineral structure with good structural coherence possesses high crystallinity and single phase ternary structure. XPS analysis confirms the presence of surface Sn oxide species, as can be expected for a non-noble metal as Sn in acidic solutions. This provides a high concentration of active sites on the catalyst surface, where Pt and Rh in their reduced state are in direct contact with oxidized Sn in order to exhibit the highest and most selective EOR activities toward the complete 12 electron oxidation of ethanol to CO₂, in sharp contrast with unalloyed phase separated nanocatalysts.

5.2. Experimental

Physico-chemical characterization of catalysts.

Inductively Coupled Plasma-Optical Emission Spectroscopy (ICP-OES). ICP-OES was used for compositional analysis. It was performed using a 715-ES-inductively coupled plasma analysis system (Varian). Six milligrams of each catalyst was suspended in 2 ml aqua regia and stirred for 1 h to let the acidic fumes out. The mixture was diluted with miliQ water to 10 ml, heated under pressure in a microwave (CEM Discover, 10 min ramp, 180 °C, 20 min hold), and consecutively diluted to two concentrations that were calibrated to a blank and three standards. Catalyst compositions were determined by the concentration, metal loading from the difference of metal content and initial mass, assuming the catalysts contained only Pt, Sn, and Rh. The standard concentrations were the following: 5, 10 and 25 ppm for Pt; 3, 10 and 20 ppm for Sn; and 1, 3 and 10 ppm for Rh. The chosen wavelengths for analysis were 265.9 nm for Pt, 343.5 nm for Rh and 189.9 nm for Sn.

Transmission electron microscopy (TEM) and energy

Dispersive x-ray Spectroscopy (EDX). Both TEM and EDX were used to study morphology and composition. A small amount of the electrocatalysts was dispersed *via* ultrasonication in 0.5 ml of hexane. A Cu grid coated with holey carbon film was impregnated with 2 μ L of the solution and air-dried. A FEI TECNAI G2 20 S-TWIN microscope, equipped with a GATAN MS794 P CCD-detector operated at 200 kV was used. The mean particle size was determined from the TEM images by counting of 50–200 particles. EDX data were collected for 120 s at an angle of 45° with respect to the sample holder. Cu K α x-ray Diffraction. Diffraction patterns were collected using a D8 Advance

diffractometer (Bruker) equipped with a Lynx Eye Detector and a KFL Cu 2K x-ray tube. The diffraction patterns were collected in a 20–80° 2θ range with a step size of 0.00142° dwelling for 30 s at every step. The XRD patterns were analyzed using the MDI Jade 8 software package. Bragg peak positions were compared with the reference XRD patterns (PDF data files, National Institute of Science and Technology).

High-Energy x-ray diffraction (HE-XRD) and pair distribution function (PDF) analysis.

Measurements were performed for electrocatalysts sealed inside glass capillaries on beam line 11IDC at the Advanced Photon Source, Argonne National Laboratory, USA, using synchrotron x-ray of 0.1080 Å wavelength. The diffraction data were reduced to the so-called structure factors, $S(q)$, and then Fourier transformed to the corresponding atomic PDFs $G(r)$, using the relationship:

$$G(r) = \frac{2}{\pi} \int_{q=0}^{q_{max}} q[S(q) - 1] \sin(qr) dq \quad (\text{Eq. 5-1})$$

where $q_{max} = 25 \text{ \AA}^{-1}$ in the present experiments. The wave vector q is defined as $q = 4\pi\sin(\theta)/\lambda$, where θ is half of the scattering angle and λ is the wavelength of the x-rays used. Note, as derived, atomic PDFs $G(r)$ are experimental quantities that oscillate around zero and show positive peaks at real space distances, r , where the local atomic density $\rho(r)$ exceeds the average one ρ_0 . This behavior can be expressed by the equation $G(r) = 4\pi r \rho_0 [\rho(r)/\rho_0 - 1]$, which is the formal definition of the PDF $G(r)$.⁷²

Electrochemical cell

All electrochemical measurements were carried out at RT using a Biologic SP 150 (Biologic) potentiostat. Experiments were carried out in a three-compartment electrochemical glass cell. The electrolytes were deaerated with high-purity N₂ gas (99.998% Linde, Germany) before every measurement. During the experiments, N₂ was purged over the electrolyte through the working electrode compartment.

A large surface area Pt counter electrode was contained in a separate compartment. A saturated mercury–mercury sulfate electrode (MMS) was inserted in a separate compartment of the cell *via* a Luggin capillary for setting desired overpotentials. All potentials reported here are given in respect to a reversible hydrogen electrode (RHE). Sulfuric acid (AnalaR NORMAPUR@ACS, 95%), ethanol (Commercial Alcohols, Inc., 100% ACS grade) and ultrapure water (18 MΩ cm. Millipore) were used to prepare the solutions.

Working electrode preparation

Catalyst inks were prepared by dispersing 6 mg of electrocatalyst powder in a mixture of 2.5 ml of ultrapure water, 0.5 ml of isopropanol, and 20 μL of 5 wt % Nafion solution (Aldrich). The mixture was ultrasonicated for 15 min. A glassy carbon disc electrode (GC-DE) (0.196 cm^2 geometrical surface area, Pine Research Instrumentation Company) was used as a support for the catalyst ink. Prior to use, the GC electrodes were prepared by polishing using a Nylon PSA sheet and 5 μm of α -alumina micropolish (0.10 mm) followed by a Microloth sheet and α -alumina micropolish (0.05 mm). The polished electrodes were rinsed thoroughly in ultrapure water and ethanol and then coated with 10 μL of a catalyst ink solution and dried in air, first at RT for 30 min and afterward at 50 $^\circ\text{C}$ for 15 min. Electrochemical Testing. Starting from open circuit potential, cyclic voltammograms (CVs) were carried out in 0.5 M H_2SO_4 to evaluate the hydrogen underpotential (H_{UPD}) charges between 0.05 and 0.40 V vs. RHE. EOR polarization curves (linear sweep voltammograms, LSVs) were collected in an electrolyte of 0.5 M $\text{C}_2\text{H}_5\text{OH}$ + 0.5 M H_2SO_4 . Potential limits were adjusted between 0.05 and 0.80 V for 20 cycles at 100 $\text{mV}\cdot\text{s}^{-1}$ and then recorded for five cycles at 20 $\text{mV}\cdot\text{s}^{-1}$. Here the second cycle is presented. In chronoamperometric (CA) measurements, first the potential was dropped in steps from open circuit potential to 0.45 V for 1 h. Nitrogen gas was bubbled prior to experiments for 15 min and purged over the solution during the experiment. Current densities were normalized by the electrochemically accessible surface area (SA) from H_{UPD} stripping.

5.3. Results and discussion

Five binary and ternary nanoparticle electrocatalysts were studied to clarify synergistic effects of an atomic vicinity of Pt, Rh, and Sn sites (Table 5.1). The electrocatalysts will henceforth be referred to using a nomenclature that includes the sequence of addition of the precursor materials. The “+” symbol indicates a stepwise addition. Thus, the ternary “PtRhSn/C” catalyst (catalyst 2 in Table 5.1) was prepared by simultaneous reduction, whereas for the ternary “Sn+Rh+Pt/C” catalysts, each precursor was added and reduced separately from left to right. Similarly, for the Sn+RhPt/C catalyst, Sn was reduced first, followed by simultaneous addition of Rh and Pt. The two binary catalysts Sn+Pt/C and PtRh/C were prepared accordingly as reference materials. The molar ratio of Pt/Rh/Sn was maintained at previously optimized ratios for high ethanol oxidation activity.⁶¹ Pt/Rh ratio in catalyst 1 was 3:1 and Pt/Sn in catalyst 5 was kept close to 1:1. We expected the possibility of homogeneous single phase formation upon co reduction of all three components (catalyst 1), whereas multiphases were likely outcomes for the stepwise materials. We note that Pt, Rh and Sn have very close atomic radii of 2.76, 2.69 and 2.80 \AA , respectively. By reducing the Sn precursor first, followed by Rh and/or Pt, we

systematically explored previously overlooked effects of the order of precursor addition on the detailed atomic distribution at bulk and interface and its critical effect on structure and catalytic activity.

Table 5.1: Size, molar composition and metal weight loading of the supported PtRhSn electrocatalysts. The + sign indicates a stepwise addition and reduction of precursors.

Catalysts	Atomic ratio (Pt:Rh:Sn)	Total metal loading wt%	Average particle size (nm)
1) PtRh/C	74:26:0	35.0	17.8 ± 7.3
2) PtRhSn/C	41:9:50	33.9	9.0 ± 2.9
3) Sn+Rh+Pt/C	46:7:47	28.5	18.9 ± 4.8
4) Sn+RhPt/C	45:8:47	21.9	15.9 ± 4.7
5) Sn+Pt/C	56:0:44	42.1	12.8 ± 2.6

Composition and morphology

ICP-OES analysis and EDX measurements confirmed chemical compositions of catalysts 2, 3 and 4 close to the targeted values regardless of the sequence of addition employed. The weight percent metal loading of catalysts on carbon support was also obtained from ICP-OES and independently cross-confirmed by EDX. The chemical composition (in terms of atomic ratios) and metal loading of the catalysts are shown in Table 5.1. TEM micrographs of the electrocatalysts (Figure 5.1) evidenced that the nanoparticles were well-distributed across the carbon support and largely spherical in shape with sizes ranging from 9 to 20 nm. The metal loadings ranged from 22 to 42% by weight. Mean particle diameters were estimated from TEM-derived size distribution histograms and are shown in Figure 5.2.

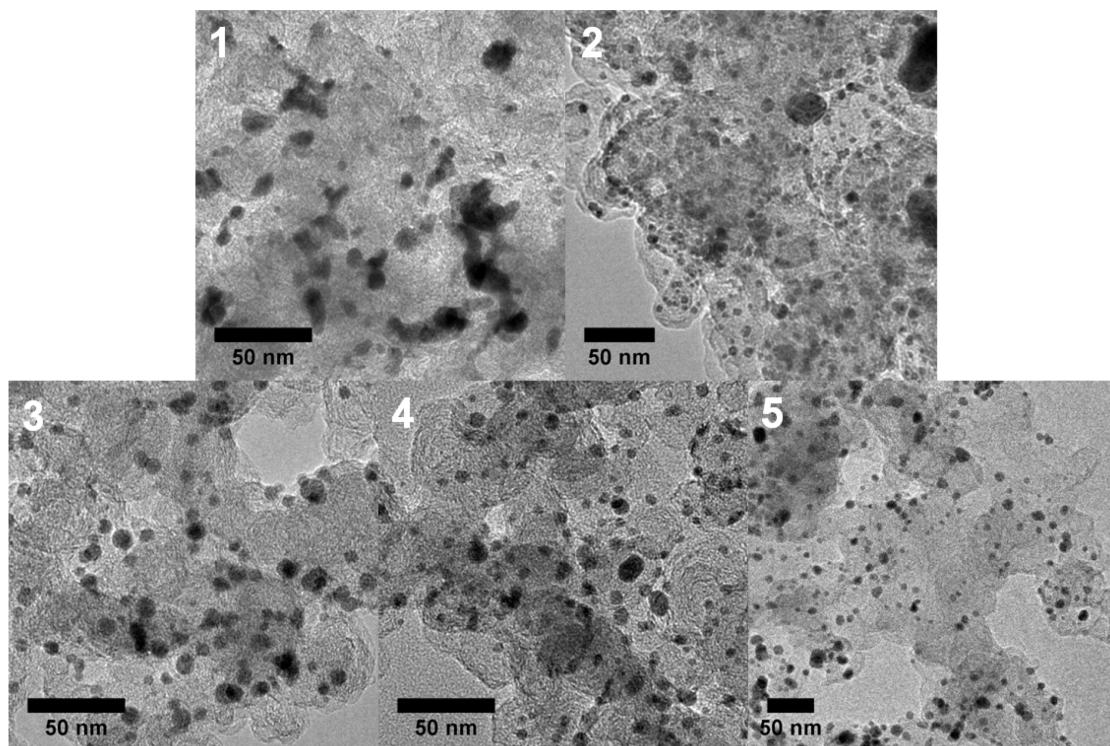


Figure 5.1: TEM micrographs of electrocatalyst: 1) PtRh/C, 17.8 ± 7.3 nm; 2) PtRhSn/C, 9.0 ± 2.9 nm; 3) Sn+Rh+Pt/C, 18.9 ± 4.8 nm; 4) Sn+RhPt/C, 15.9 ± 4.7 nm; and 5) Sn+Pt/C, 12.8 ± 2.6 nm.

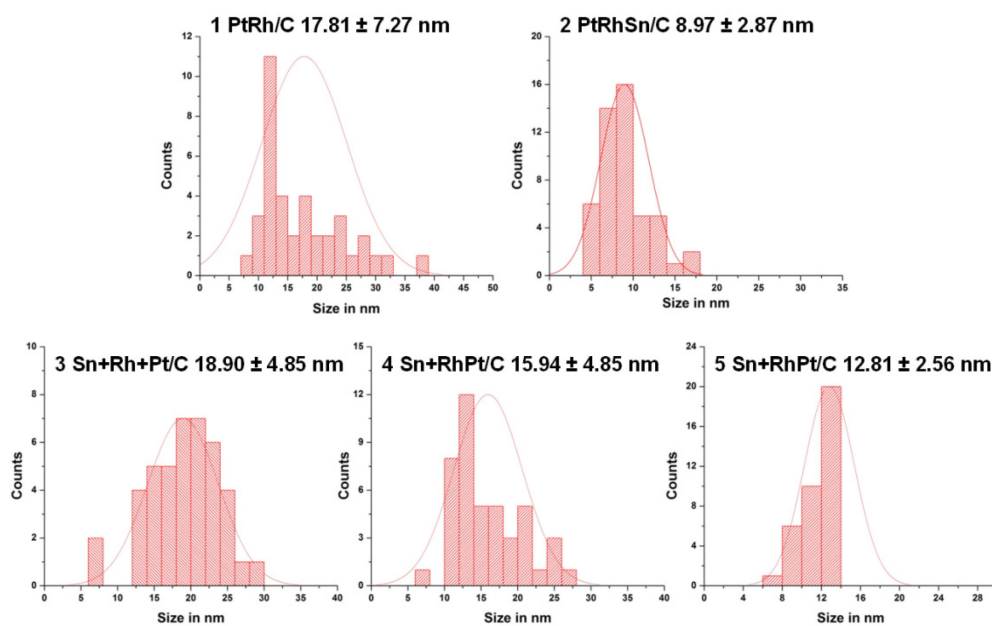


Figure 5.2: Mean particle diameter and size distribution histograms of electrocatalyst: 1) PtRh/C, 17.8 ± 7.3 nm; 2) PtRhSn/C, 9.0 ± 2.9 nm; 3) Sn+Rh+Pt/C, 18.9 ± 4.8 nm; 4) Sn+RhPt/C, 15.9 ± 4.7 nm; and 5) Sn+Pt/C, 12.8 ± 2.6 nm.

Atomic-Scale Structure

Conventional Cu $K\alpha$ XRD and synchrotron-based HE-XRD studies coupled to atomic pair distribution function (PDF) analysis was used to study the atomic-scale structural properties of all five electrocatalysts. XRD patterns are shown in Figure 5.3 and show relatively broad Bragg peaks, typical for nanosized particles with limited structural coherence. Still the peak patterns reveal important insight how the synthesis protocol affected the resulting bulk structure. The reflections of the PtRh/C catalysts suggest an essentially phase-pure Pt–Rh bimetallic phase. Both Pt and Rh show a face-centered cubic (fcc) space group $Fm\bar{3}m$ with very similar lattice constants of 3.9231 and 3.8031 Å, respectively. This favors the formation of homogeneous PtRh binary solid solutions over wide compositional ranges, as indicated by the Pt–Rh phase diagram.¹⁵⁰ This is why Pt and Rh diffraction peaks cannot be resolved separately in any of the XRD patterns. The (111) reflection was found between the Pt (111) and Rh (111) literature values of 39.764 and 41.069°, respectively, evidence alloy formation and bulk lattice compression compared to pure Pt.

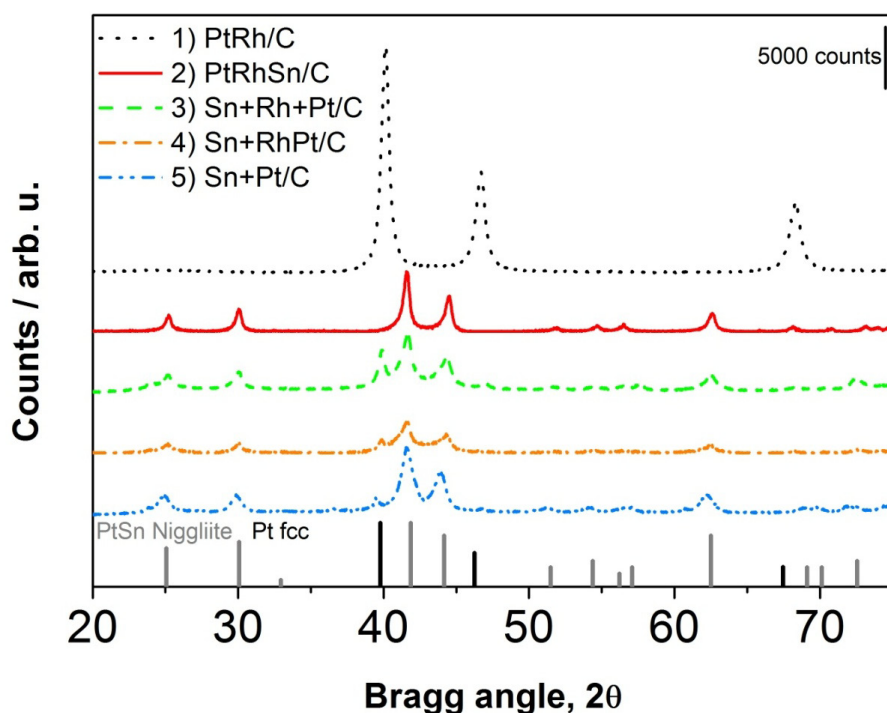


Figure 5.3: Cu $K\alpha$ XRD pattern of different catalyst: 1) PtRh/C, 2) PtRhSn/C, 3) Sn+Rh+Pt/C, 4) Sn+RhPt/C, and 5) Sn+Pt/C. Pure Pt fcc and pure PtSn-Niggliite diffraction patterns are indicated in black and gray lines, respectively.

Interestingly, the pattern of PtRhSn/C catalyst shows no peaks coinciding in position with those of the PtRh/C catalyst. This indicates the formation of an entirely new homogeneous phase with a characteristic peak pattern that can unambiguously be attributed to a hexagonal PtSn phase known as

the mineral Niggliite (Table 5.2). Given the chemical presence of Rh in the catalyst PtRhSn/C, the XRD pattern suggests that Rh atoms are substitutionally incorporated into the Niggliite lattice. The other Sn-containing catalysts also reveal the presence of the Niggliite phase, however, and show a secondary phase Pt or PtRh phase with additional reflections around $2\theta \sim 40^\circ$. Thus, stepwise precursor addition caused segregated metallic alloy phases. The presence of Rh (see Sn+Rh+Pt/C and Sn+RhPt/C) contracts the lattice of the secondary Pt phase and shifts its reflections to higher angles. Although absent in the XRD pattern of Figure 5.3, the presence of minor nanocrystalline or amorphous SnO_x phases, especially near the surface, cannot be ruled out.

Table 5.2: 2θ values of electrocatalysts in comparison with tabulated diffraction patterns.

PtRhSn/C samples					tabulated literature data		
1)PtRh/C	2)PtRhSn	3)Sn+Rh+Pt	4)Sn+RhPt	5) Sn+Pt	Pt fcc	Rh fcc	PtSn Niggliite (h k l)
	25.2	25.2	25.1	24.8			25.1 (1 0 0)
	30.0	30.0	30.0	29.9			30.1 (1 0 1)
40.2		39.9	39.8	39.5	39.8	41.1	(1 1 1)
	41.6	41.7	41.6	41.6			41.8 (1 0 2)
	44.5	44.3	44.3	43.9			44.1 (1 1 0)
46.7		47.1		46.8	46.2	47.8	(2 0 0)

To explore the 3D atomic arrangement of Pt, Rh, and Sn atoms regardless of their structural coherence (i.e., for both nanocrystalline and amorphous phases), we conducted synchrotron-based HE-XRD experiments coupled to atomic pair distribution functions (PDF) analysis. HE-XRD and atomic PDFs are rapidly emerging as a very efficient technique in studying the atomic-scale structure of nanosized materials.^{158,159}

A set of synchrotron HE-XRD patterns collected at $\lambda = 0.1080 \text{ \AA}$ is shown in Figure 5.4 A. The atomic PDFs extracted from the synchrotron XRD patterns are shown by the gray scatter points in Figure 5.4 B. By definition, experimental PDFs show positive peaks at distances separating pairs of atoms (i.e., where the local atomic density exceeds the average one). From these data, we can derive the immediate coordination of each atom in the entire 3D lattice, which provides the full atomic 3D structure of the nanocatalysts. The one-dimensional attenuations in the PDF ultimately die down to

around zero at the structural coherence length (crystallite size) of the catalysts. Inspection of the peak envelopes evidence that all catalysts show nanocrystalline structures with coherence lengths between 15 and 20 Å.

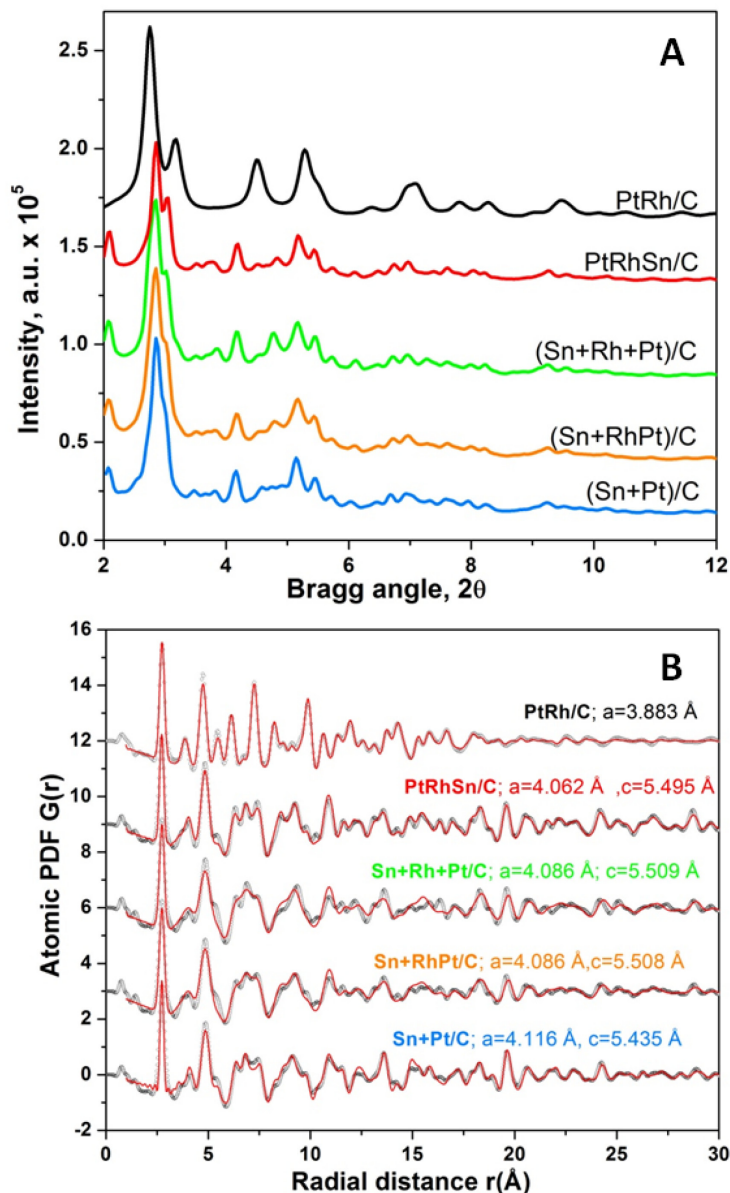


Figure 5.4: (A) Synchrotron-based HEXRD patterns collected at $\lambda=0.1080$ Å for 1) PtRh/C, 2) PtRhSn/C, 3) Sn+Rh+Pt/C, 4) Sn+RhPt/C, and 5) Sn+Pt/C. (B) Atomic pair distribution functions (PDFs) derived from the XRD patterns (gray symbols) and computed from structure models (red solid lines). The refined lattice parameters are given by each data set.

To derive real-space 3D structural motifs of the catalyst phases, computational PDFs based on suitable structural models of PtRh- and Sn-containing phases were fitted to the experimental PDFs. The PDF of the PtRh/C catalyst (Figure 5.4 B) can be approximated with a structure model featuring a face-centered-cubic (fcc) lattice occupied by Rh and Pt atoms in a random manner (Figure 5.5). The PDFs

for the Sn-containing catalysts, on the other hand, are well-approximated by a model featuring a hexagonal lattice of the type found in the mineral Niggliite with an overall Pt₁Sn₁ stoichiometry and where Rh atoms randomly replace Pt atoms. Fitted unit cell parameters are shown in Figure 5.4 B, indicating that the fcc unit cell parameter of the PtRh/C catalyst (3.883 Å) is smaller than that of pure Pt 3.910 Å, commensurate with a lattice-contracted disordered alloy. The differences in the PDF peak oscillation pattern between PtRh/C and the four Sn-containing materials (see, for instance, in the 5–10 Å range) underscore their distinctly different structural atomic arrangement. The Sn-containing catalysts show similar oscillations, radial distances and short-order crystallinity. Structural differences manifest themselves largely in variations of the unit cell dimensions “a” and “c” (Figure 5.5). Close inspection of the PDF patterns reveals sharper and more intense PDF peaks for the PtRhSn/C catalyst compared to the other Sn-containing materials (e.g., at pair distances 4.5 and 11 Å). Seemingly a subtle difference, this important detail, however, hints to enhanced structural order in surface and bulk. In light of the structural analysis, XRD and HE-XRD/PDF evidence the prevalent formation of a ternary substitutional solid solution consisting of Sn, Pt and Rh with Niggliite structure. Increasing phase homogeneity upon simultaneous addition of precursors resulted in increasing lattice contraction and structural order. The surface of the Niggliite particles is illustrated in Figure 5.5 C and D. It exposes Sn, Pt and the doped Rh atoms in close vicinity with a high concentration of active ternary sites for the ethanol oxidation.

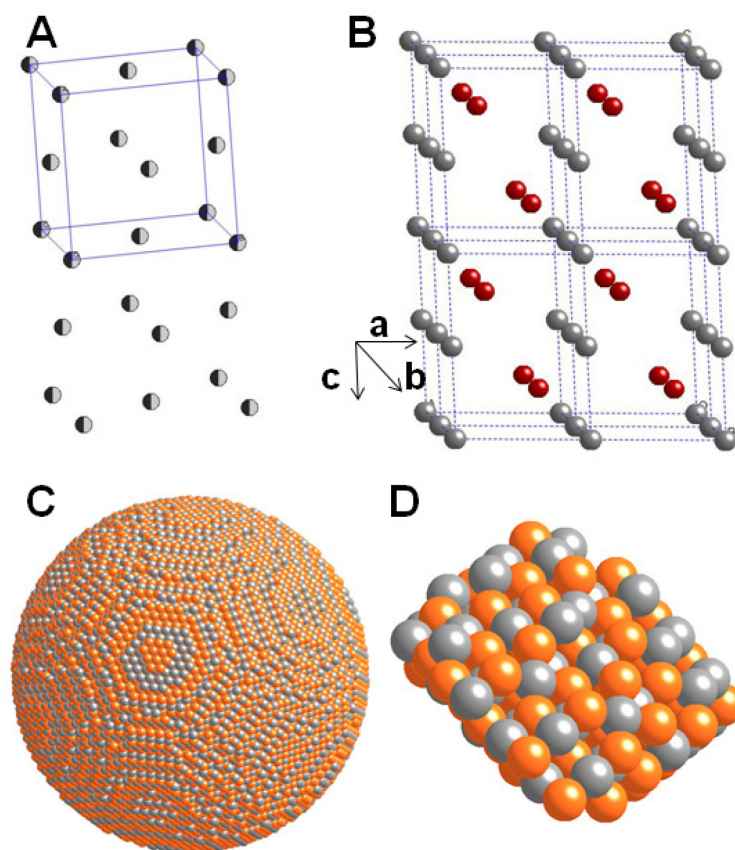


Figure 5.5: (A) PDF-derived 3D structural model of an fcc lattice, randomly occupied by Rh and Pt atoms (gray balls). Unit cell is given by lines. (B) A hexagonal, Niggliite structure featuring alternating layers of Pt (gray balls) and Sn (red balls) atoms. Spherical model of Niggliite structured particle (C) and excerpt of the particle surface (D) with Sn (orange balls) and Pt sited doped randomly with Rh (gray balls).

Electrocatalytic ethanol oxidation activity

To correlate catalyst structure and composition with the electrocatalytic EOR polarization behavior, cyclic voltammograms in 0.5 M H_2SO_4 (Figure 5.6) and linear sweep voltammograms (LSVs) in 0.5 M H_2SO_4 and 0.5 M $\text{C}_2\text{H}_5\text{OH}$ (Figure 5.7) were collected. In addition, potentiostatic chronoamperometric (CA) experiments were performed to examine the catalytic performance and catalyst stability at an electrode potential of technical interest for extended period of times (Figure 5.8). Current densities were normalized by the electrochemically accessible surface area (SA) from HUPD stripping.

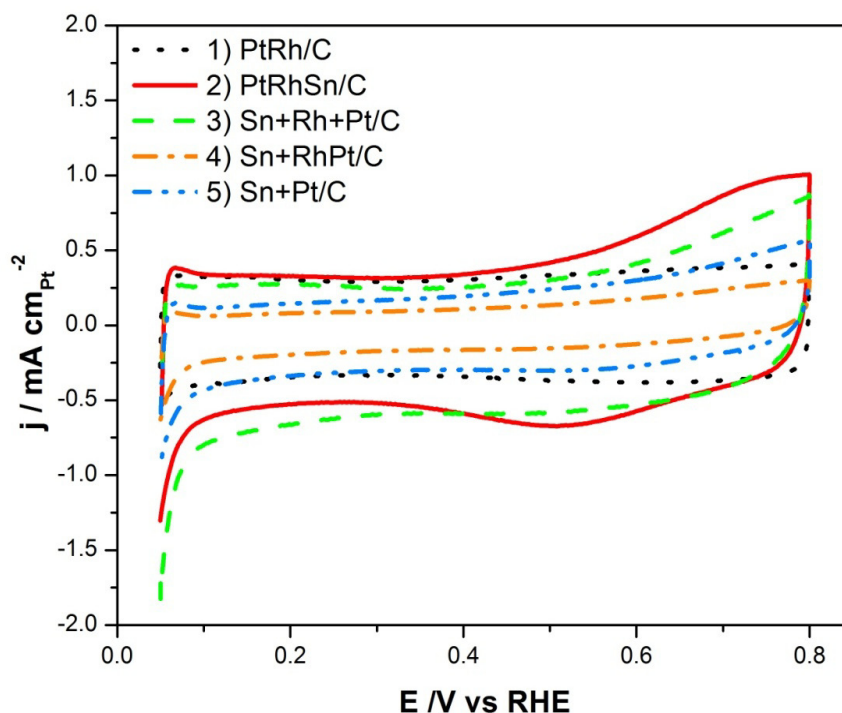


Figure 5.6: Cyclic voltammograms (CVs) of 1) PtRh/C, 2) PtRhSn/C, 3) Sn+Rh+Pt/C, 4) Sn+RhPt/C, and 5) Sn+Pt/C EOR catalysts in 0.5 M H_2SO_4 . Current densities are normalized by the electrochemically accessible surface area (SA) from H_{UPD} stripping with a scan rate of 20 mV/s.

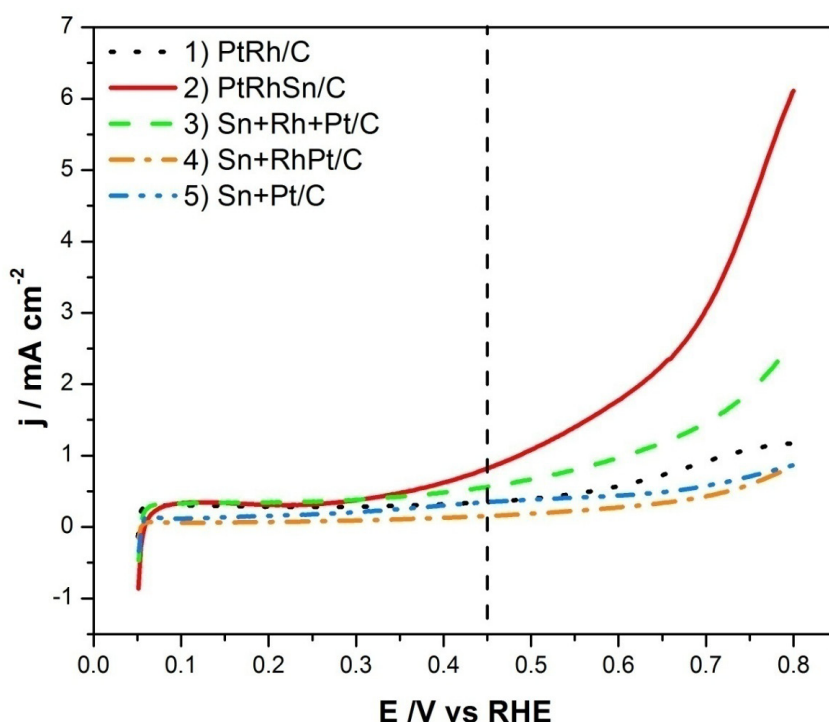


Figure 5.7: Polarization curves of the electrocatalytic ethanol oxidation reaction (EOR): 1) PtRh/C, 2) PtRhSn/C, 3) Sn+Rh+Pt/C, 4) Sn+RhPt/C, and 5) Sn+Pt/C recorded in 0.5 M H_2SO_4 and 0.5 M $\text{C}_2\text{H}_5\text{OH}$. Current densities are normalized by the electrochemically accessible surface area (SA) from H_{UPD} stripping with a scan rate of 20 mV/s. The vertical dashed line marks the potential of the chronoamperometric experiment in Figure 5.8.

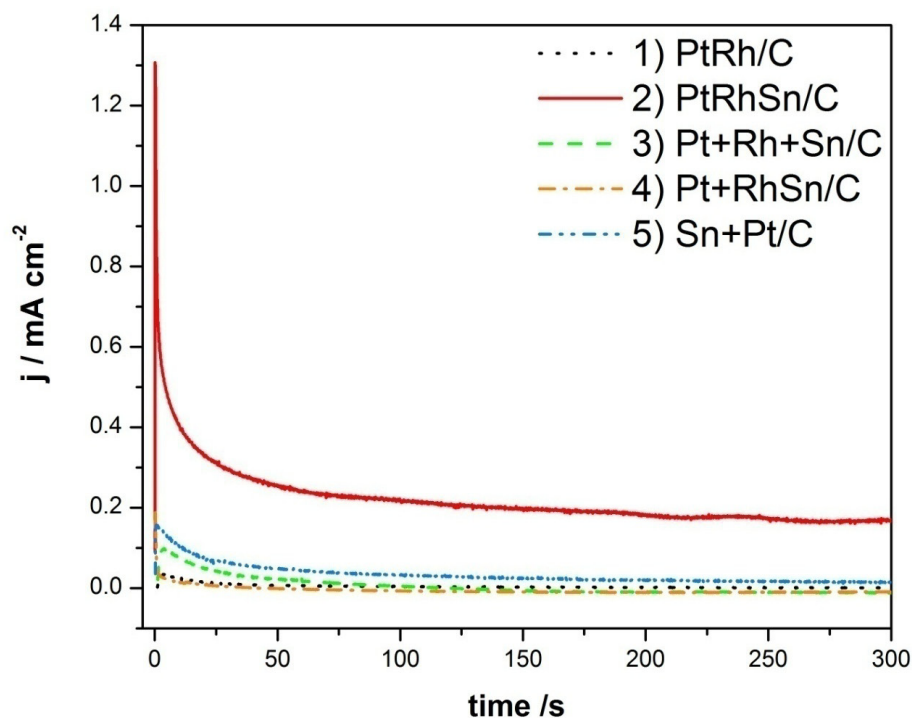


Figure 5.8: Potentiostatic chronoamperometry of the Pt-Rh-Sn/C electrocatalysts at $E = +0.45$ V vs. RHE recorded in 0.5 M H_2SO_4 and 0.5 M EtOH. Current densities are normalized by the electrochemically accessible surface area (SA) from H_{UPD} stripping.

Table 5.3 reports relevant experimental activity data. Clearly, the single-phase PtRhSn/C catalyst dramatically outperformed the other catalysts, both under potentiodynamic scan and under potentiostatic test conditions. This suggests that the homogeneous Rh-doped Pt–Sn Niggliite structure (Figure 5.4) must have formed the catalytically most active surface sites under reactive conditions. Our bulk structural conclusions yield only limited clues about the atomic structure of possible active crystal surfaces. Although in principle controlled by the bulk structure, the active surface depends on a large number of additional factors such as crystal facet orientation, compositional segregation of elements, or partial loss of crystal ordering during reactive conditions. The surface chemistry is discussed in detail at the end of this chapter. The presence of a secondary PtRh metallic alloy phase, as seen for catalysts 3, 4, and 5 in Figure 5.3, proved without exception detrimental to the experimental catalytic activity. This appears plausible considering that phase-separated Pt/Rh metal atoms are lost for the formation of active ternary active sites on the surface of Niggliite phases. PtRh alloy sites without atomic neighborhood of oxophilic Sn species may activate ethanol, yet lack sufficient active oxygenates to efficiently remove carbonous adsorbates resulting in lower catalytic activity. A similar conclusion can be drawn from the comparison of the two binary catalysts, PtRh/C and Sn+Pt/C. Well-alloyed PtRh/C fails to maintain sustained EOR activities, likely due to rapid buildup of tightly bound carbonous surface species. The lower activity of Sn+RhPt/C as the Sn+Pt/C catalyst indicates that the

beneficial effect of Rh itself may contribute to the overall activity, but it is influencing predominantly the selectivity toward CO₂. This confirms earlier reports on the beneficial role of Sn species in the oxidation of organic molecules.

Table 5.3: Electrochemical EOR activity of Pt-Rh-Sn/C catalysts: electrochemical surface area (ECSA), current densities at 0.45 V vs. RHE and 0.6 V vs. RHE during voltammetric scans, and current density at constant 0.45 V vs. RHE after 300 s.

Catalyst	i @ 0.45V	i @ 0.60V	i @ 0.45V@300s	ECSA
by SA	/mA cm⁻²			cm²·mg_{Pt}⁻¹
1) PtRh/C	0.35	0.58	7.02 · 10 ⁻⁴	10.7
2) PtRhSn/C	0.82	1.78	1.66 · 10 ⁻¹	26.5
3) Sn+Rh+Pt/C	0.57	0.97	~0	12.1
4) Sn+RhPt/C	0.15	0.27	~0	33.5
5) Sn+Pt/C	0.35	0.44	1.50 · 10 ⁻²	15.5
by ECSA	/mA·cm⁻²·mg⁻¹_{Pt}			
1) PtRh/C	1.80 · 10 ⁻³	2.78E-03	3.61 · 10 ⁻⁶	
2) PtRhSn/C	3.78 · 10 ⁻³	8.14 · 10 ⁻³	7.59 · 10 ⁻⁴	
3) Sn+Rh+Pt/C	1.64 · 10 ⁻³	2.82 · 10 ⁻³	~ 0	
4) Sn+RhPt/C	9.26 · 10 ⁻⁴	1.71 · 10 ⁻³	~ 0	
5) Sn+Pt/C	2.35 · 10 ⁻³	2.98 · 10 ⁻³	1.01 · 10 ⁻⁴	
mass based	/mA mg⁻¹_{Pt}			
1) PtRh/C	3.75	5.77	0.01	
2) PtRhSn/C	21.69	46.79	4.36	
3) Sn+Rh+Pt/C	6.89	11.82	~ 0	
4) Sn+RhPt/C	4.92	9.09	~ 0	
5) Sn+Pt/C	5.42	6.85	0.23	

Although the general beneficial effect of Rh for C-C bond splitting has been well-documented,^{111,160} the relative activities of Sn+RhPt/C and Sn+Pt/C strongly evidence that the detailed chemical and structural state of Rh atoms is critical to fully unfold activity enhancements. The structure–activity relations of the single-phase Rh-doped Niggliite structure (PtRhSn/C) are consistent with an earlier hypothesis⁵ about the beneficial effect of a “quasi random PtRhSn alloy”. However, the present Rh-doped Niggliite electrocatalysts displayed 4 and 5 times higher current densities at +0.45 V and +0.60 V, respectively, than a similar $\text{PtRhSnO}_2/\text{C}$ catalyst.¹⁵² Improved EOR activity was also observed in comparison to an earlier PtRhSn catalyst with the same 3:1:4 ratio,⁶¹ and compared to a Rh-content optimized Rh-PtSn/C catalyst.¹⁰⁴

Surface Chemistry of the Most Active PtRhSn/C Catalyst

PtRhSn/C catalysts were studied by XPS before acid exposure (BAE) and after acid exposure (AAE) under EOR reaction conditions. The Pt 4f, Rh 3d, and Sn 3d spectra (Figure 5.9) were very similar before and after acidic exposure, with Pt being essentially metallic and Sn existing largely in a SnO_2 state near the surface. The low binding energy shoulder at ~ 485 eV indicated some metallic contribution. As Sn was unlikely to be in the elemental Sn state, the most likely scenario is the formation of a Rh-doped Pt–Sn alloy in the near-surface region, consistent with the XRD and HE-XRD results in the bulk. Rh 3d (5/2) spectra at ~ 310 eV suggested the presence of metallic Rh. A slight presence of oxide (Rh_2O_3) is observed after acid treatment.

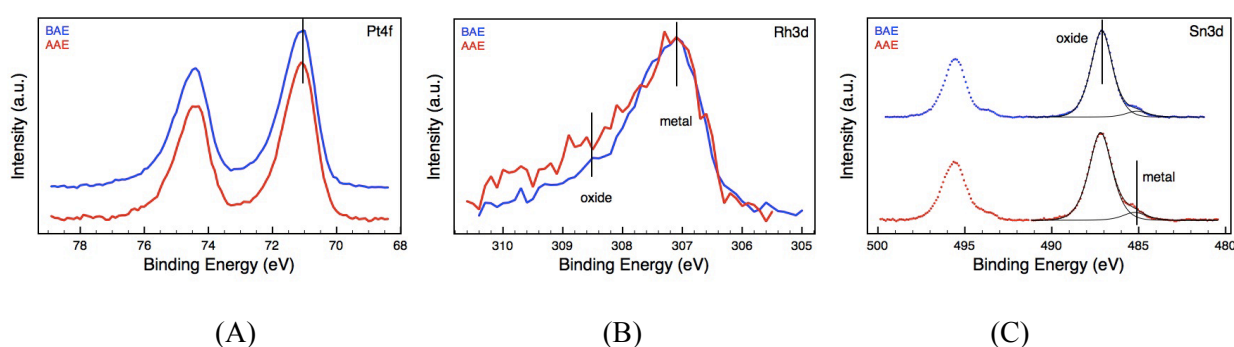


Figure 5.9: Pt 4f (A), Rh 3d (B) and Sn 3d (C) XP spectra for PtRhSn/C before (BAE: blue) and after (AAE: red) acid treatment. Photoelectron kinetic energy: 550 eV.

The quantitative elemental composition is provided in Table 5.4. These data show a constant $(\text{Pt} + \text{Rh})/\text{Sn}$ ratio near the surface and some small loss of precious metals and Sn upon acid treatment. Converted into relative molar ratios, the near surface composition of the Niggliite phase before acid treatment was about $\text{Pt/Rh/Sn} = 66:25:9$ and changed only very slightly after acid treatment to $68:23:9$. This suggests that the original Niggliite bulk phase with molar ratio of $\text{Pt/Rh/Sn} = 41:9:50$ transformed

into SnO₂ and a noble metal-enriched phase at the surface due to the exposure to air and aqueous electrolyte. There is a notable increase of the oxygen content of the AAE sample, probably due to functionalization of the carbon support.

Table 5.4: Quantitative analysis of the XPS peaks of PtRhSn/C at KE: 550 eV. BAE denotes before acid exposure and AAE denotes after acid exposure.

Samples	Rh/Pt	(Rh+Pt+Sn)/C	(Pt+Rh)/Sn	O/C
BAE	0.38	0.023	0.39	0.04
AAE	0.34	0.018	0.39	0.18

From the XPS data, we conclude that the active surface of the bulk single-phase Niggliite PtRhSn/C catalyst evolved into active catalytic sites characterized by uniformly distributed metallic Pt, Sn, and Rh surface sites in atomic neighborhood to oxophilic surface SnO₂. These are supported on the homogeneous bulk PtRh –Sn Niggliite phase. The close interaction of the Pt/Rh/Sn and SnO₂ moieties appears instrumental in the high electrocatalytic activity performance.

Reaction Intermediates and CO₂ Selectivity

Mechanistic aspects, including reactive surface intermediates and products of the EOR on the active Rh-doped Niggliite phase electrocatalyst (PtRhSn/C) was studied using *in situ* FTIR. Special emphasis was placed on an analysis of whether ethanol can be oxidized in a 12 electron pathway to CO₂. Figure 5.10 reports *in situ* SNIFTIRS spectra of the intermediates and products during ethanol oxidation between +0.15 V to +1.15 V versus RHE. Following earlier analyses under similar conditions, we assign the following bands: around 2300 cm⁻¹ to the asymmetric CO₂ stretching mode; around 1700 cm⁻¹ to C=O stretching in acetic acid and acetaldehyde; around 1390-1410 cm⁻¹ to O-C-O stretching of adsorbed acetate; around 1350 cm⁻¹ to CH₃ in-plane bending mode; around 1280 cm⁻¹ to C-O stretching of acetic acid; around 900 cm⁻¹ to the C-C-O asymmetric stretching of acetaldehyde; and the broad band at 1100 cm⁻¹ to ClO⁻⁴.¹⁶¹

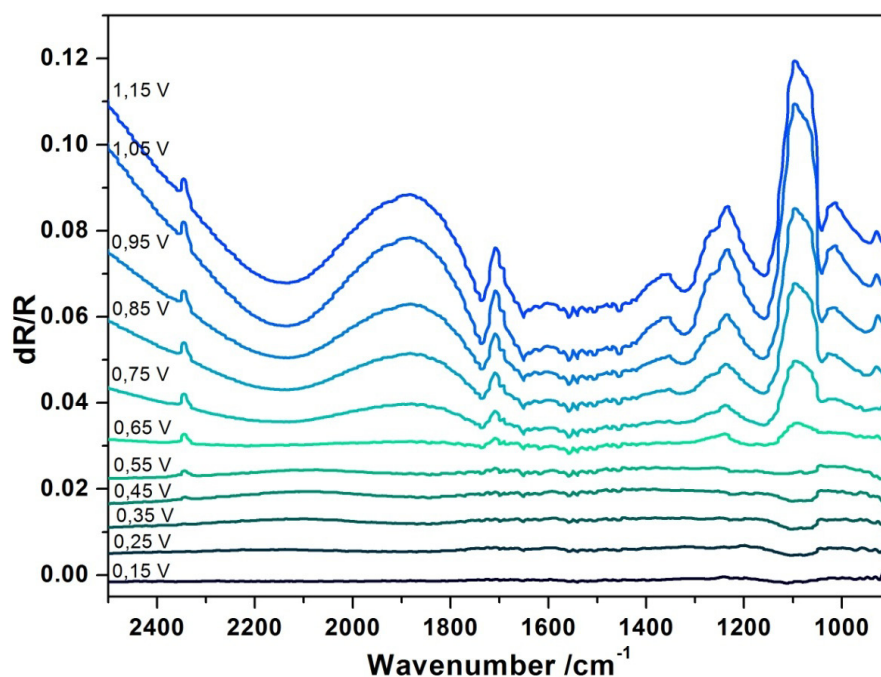


Figure 5.10: SNIFTIRS spectra during ethanol oxidation on PtRhSn/C between +0.15 V and +1.15 V vs. RHE. Conditions: 0.1M HClO₄ + 0.5M C₂H₅OH. The spectrum at +0.10 V is used as background.

The *in situ* FTIR data in Figure 5.10 provide evidence for the formation of CO₂ during EOR as a result of C–C bond splitting in ethanol by a 12 electron oxidation process. CO₂ evolution commences as early as 0.45 V and gradually increases with electrode potential. This is, to our knowledge, one of the earliest onsets of the 12 electron oxidation pathway reported in the literature.^{5,61,104} Characteristic peaks stemming from acetic acid and acetaldehyde suggested partial incomplete oxidation. Hence, like most other earlier materials the Niggliite phase of the PtRhSn/C catalyst induces both C–C bond splitting (complete oxidation) and partial oxidation of ethanol.

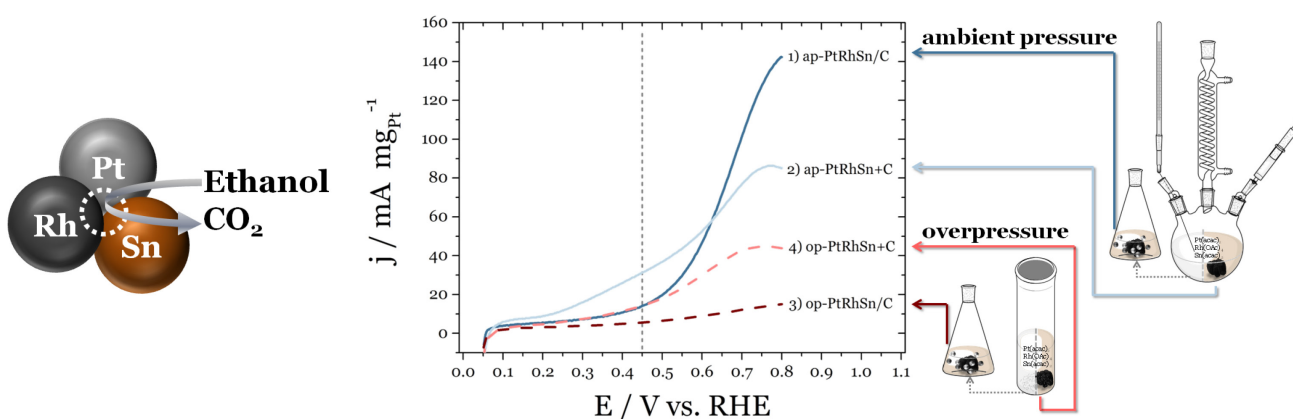
Conclusions

We have presented the synthesis, the structural bulk and surface characterization, and the electrocatalytic activity and selectivity of nanostructured ternary Pt–Rh–Sn materials in defined stoichiometric ratios. Unlike earlier studies, we have placed special emphasis on the exploration of the detailed 3D atomic arrangement and chemical surface states of the catalytically active phases and components; we also addressed the previously overlooked question as to the order in which the ternary catalysts were assembled in the synthetic process. Scattering data and atomic PDF analysis revealed, for the first time, a single-phase Rh-doped Pt–Sn Niggliite structure as the preferred and catalytically most active nanocrystalline phase. On its surface, metallic Pt and Rh are atomically mixed with a SnO₂ phase, giving rise to active-surface-site ensembles. Only owing to simultaneous reduction of all three

precursors was the phase-pure ternary Niggliite phase experimentally accessible. Secondary PtRh metal alloy phases proved detrimental to catalytic activity. The EOR activity of the homogeneous Niggliite material outperformed a previous EOR catalyst of the PtRhSn family. *In situ* spectroscopy confirmed the favorable activity by an early CO₂ onset potential of the complete 12 electron oxidation pathway. Our structural conclusions as to the active catalytic phase represent a significant step forward in our understanding of structural and mechanistic aspects of this class of catalytic materials. The present methodologies and structural insights will aid in the materials-by-design approach for further improved direct ethanol fuel cell (DEFC) catalysts as well as for catalysts for the oxidation of liquid small organics in general.

6. Comparative assessment of synthetic strategies toward active Platinum-Rhodium-Tin electrocatalysts for efficient ethanol electro-oxidation

In this chapter the electrocatalytic activity of nanostructured ternary Pt-Rh-Sn materials by microwave assisted overpressure and ambient pressure synthesis towards the EOR is described and the synthesis, structural bulk and surface characterization of several catalysts with a defined stoichiometric ratio from a variety of synthesis routes are presented. The activity-synthetic protocol correlations provide insights in the formation of a high concentration of active surface site ensembles directly on to the carbon under ambient pressure conditions.



The contents of this chapter have been published: Reprinted from N. Erini, P. Krause, M. Gliech, R. Yang, Y. Huang and P. Strasser, *J. Power Sources*, **2015**, 294, 299-304.¹⁶² Copyright 2015 with permission from Elsevier.

6.1. Abstract

The present work explores the effect of autoclave-based autogenous-pressure versus ambient pressure conditions on the synthesis and properties of carbon-supported Pt-Rh-Sn nanoparticle electrocatalysts. The Pt-Rh-Sn nanoparticles were characterized by x-ray spectroscopy, electron microscopy and mass spectroscopy and deployed as catalysts for the electrocatalytic ethanol oxidation reaction. Pt-Rh-Sn catalysts precipitated with carbon already present showed narrow particle size distribution around 7 nm, while catalysts supported on carbon after particle formation showed broader size distribution ranging from 8-16 nm, similar metal loadings between 40 and 48 wt% and similar atomic ratios of Pt:Rh:Sn of 30:10:60. The highest ethanol oxidation activity associated with exceptionally low ethanol oxidation onset potential was observed for ambient-pressure catalysts with the active ternary alloy phase formed in presence of the carbon supports. In contrast, catalysts prepared under ambient pressure in a two-step approach, involving alloy particle formation followed by particle separation and subsequent deposition on the carbon support, yielded the highest mass activities. Based on the observed synthesis-activity correlations, a comparative assessment is provided of the synthetic techniques at high versus low pressures, and in presence and absence of carbon support. Plausible hypotheses in terms of particle dispersion and interparticle distance accounting for these observed differences are discussed.

6.2. Introduction

Platinum is a commonly used anodic material in acidic low temperature fuel cells. Since alcohol oxidation on pure platinum doesn't reach the desired activities, research in the field of Direct Ethanol Fuel Cells (DEFC) has focused widely on the development of binary and ternary Pt-based alloys.^{5,7,163} The introduction of ternary electrocatalytical systems for the ethanol oxidation reaction (EOR) in recent research efforts has brought the development of DEFC as alternate power sources a big step forward.^{10,61} Ethanol is of a particular interest for mobile applications such as electric vehicles, due to high energy density 8 kWh kg^{-1} , low toxicity, biocompatibility and abundant availability. It is, however, not easily oxidized completely to CO_2 and water. This is due to difficulties in the C-C bond cleavage in ethanol and the reaction may involve several different mechanism pathways with the formation of a high number of reaction intermediates such as CH_x species or acetaldehyde and, to some extent, to the formation of CO-intermediates leading to poisoning of the active sites on Pt catalysts.^{3-6,48,93,164} Efforts to develop highly active and selective EOR electrocatalysts have therefore concentrated on the addition of co-catalysts to platinum.³⁵⁻³⁹

Our previous research focused on the promising family of EOR nanocatalysts based on mixtures of Pt, Rh and Sn.^{5,61,104,107,112,150-152,165} In a recent comprehensive study on a set of Pt-Rh-SnO₂ nanoparticle catalysts an optimal Pt-Rh-Sn atomic ratio of 3:1:4 has been proposed.⁶¹ In our previous work we addressed the optimal structural arrangement of the atoms of the three components in the surface and bulk of the final active catalyst. On its surface, metallic Pt and Rh are atomically mixed with Sn, giving rise to active-surface-site ensembles. Our aim was to maximize activity and selectivity and find a single-phase Rh-doped Pt-Sn Niggliite structure as the preferred and catalytically most active nanocrystalline phase.¹⁰⁷ Synthesis routes to nanoparticle EOR catalysts containing Platinum, Rhodium and Sn range from impregnation-reductions methods¹⁰⁴ to deposition of metal atoms on oxide surfaces followed by galvanic displacement⁵. We implemented in our work a modified polyol method in dioctylether solvent⁶⁷, controlling the temperature during the reaction with a heating mantel. This approach yields ternary single phased catalyst with SnO_x next to metallic Pt and Rh on the surface in close proximity. Recent reports also claim improved electrocatalytic stability and elevated activities for ternary electrocatalysts by microwave-assisted selective deposition of nanoparticles onto carbon⁶⁹ and ternary PtSn@Rh/C systems by a two-step microwave-assisted polyol method as a promising catalyst preparation method for optimizing the Pt-Sn-Rh ternary system for EOR application.⁶⁸

In order to compare the two synthesis approaches and clearly establish a preferable synthetic approach towards PtRhSn catalysts, we first compared a one-pot reduction of metal precursors at ambient pressures both in the presence and absence of carbon support (referred to as “*ap-PtRhSn+C*” and “*ap-PtRhSn/C*”; *ap materials*). Synthesis conditions followed our previously used polyol method under a temperature control using a standard laboratory heating mantel device. Thereafter, we compared two variations of the two synthesis routes involving microwave-assisted temperature control in an autoclave associated with autogeneous overpressure conditions (referred to as “*op-PtRhSn+C*” and “*op-PtRhSn/C*; *op materials*”).

6.3. Experimental section

6.3.1. Catalyst preparation

All electrocatalysts (40 wt.% of metal loadings, Pt:Rh:Sn atomic ratios of 3:1:4) were prepared using Pt(acac)₂, Rh₂(OAc)₄, Sn(acac)₂ as metal sources, 1,2-tetradecandiol, oleic acid and oleylamine in dioctylether as reducing and capping agents and Ketjen Black as support. All precursors were mixed together, for the direct supported electrocatalysts including carbon, heated up to 260 °C and hold for 30 minutes. Whereas the heating mantel temperature controlled process (resulting in the “*ap-PtRhSn+C*” and the “*ap-PtRhSn/C*” materials) the reaction mixture was under ambient pressure conditions, in the microwave-assisted temperature-controlled process autogenous pressures up to

30 bar and could built up inside the reaction mixture (resulting in the “*op-PtRhSn+C*” and the “*op-PtRhSn/C*” materials). Ketjen black carbon was sonicated for one hour on ice. Unsupported alloy particles (in case of the “*ap-PtRhSn/C*” and the “*op-PtRhSn/C*”) were precipitated with isopropanol, redispersed in n-hexane and added to the Ketjen black carbon dispersion, sonicated for another hour on ice and stirred overnight at RT.. All particles were finally separated by centrifugation, freeze-dried and the residue dried in a furnace under N₂, oxidized under O₂/N₂ and calcinated by heating under H₂/Ar atmosphere (see detailed information in previous publication¹⁰⁷).

6.3.2. Catalyst characterization

Inductively coupled plasma- optical emission spectroscopy (ICP-OES) was used for compositional analysis; performed using a 715-ES-inductively coupled plasma analysis system (Varian). Transmission Electron Microscopy (TEM) and Energy dispersive x-ray spectroscopy (EDX) were carried out using a FEI TECNAI G² 20 S-TWIN microscope operated at 200 kV, equipped with a GATAN MS794 P CCD-detector to study morphology and composition. The mean particle size was determined from TEM images by counting of at least 50 particles. Cu K α x-ray diffraction patterns were collected using a D8 Advance diffractometer (Bruker) equipped with a Lynx Eye Detector and KFL Cu 2K x-ray tube. The diffraction patterns were collected in a 20–80° 2 θ range with a step size of 0.00142° dwelling for 30 s at every step. The XRD patterns were analyzed using the MDI Jade 8 software package. Bragg peak positions were compared with the reference XRD patterns (PDF data files, National Institute of Science and Technology).

6.3.3. Electrochemical measurements

All electrochemical measurements were carried out in a three-compartment electrochemical glass cell at room temperature using a Biologic SP 150 potentiostat. All potentials reported here are given in respect to a reversible hydrogen electrode (RHE). The 0.5 M C₂H₅OH + 0.1 M HClO₄ electrolyte was deaerated with high-purity N₂ before every measurement. During the experiments N₂ was purged over the electrolyte. A large surface area Pt counter electrode was contained in a separate compartment. A saturated mercury-mercury sulfate electrode (MMS) was inserted in a separate compartment of the cell *via* a Luggin capillary for setting desired overpotentials. As the working electrode a polished glassy carbon disc electrode (0.196 cm² geometrical surface area) was coated with 10 μ l of a catalyst ink solution. Catalysts inks were prepared by ultrasonication of 6 mg of electrocatalyst powder in a mixture of 2.0 ml of ultrapure water, 0.5 ml isopropanol and 20 μ l of 5 wt. % Nafion solution for 15 min.

6.4. Results and discussion

6.4.1. Structural characterization of the Pt-Rh-Sn catalysts

The Pt:Rh:Sn atomic ratios obtained by ICP and EDX were similar to the intended ratio (Table 6.1). The local atomic ratios from EDX measurement differ slightly from the overall ratios in the ICP results, which can be expected since they represent a more local estimation of the atomic concentration. TEM micrographs and their corresponding size distribution histograms of the electrocatalysts (Figure 6.1) evidenced that the nanoparticles were well distributed across the carbon support and largely spherical in shape. The mean diameters for the nanoparticles reduced in the present of carbon (*PtRhSn+C*) were around 7 nm and showed little agglomeration. The nanoparticles that were supported after reduction (*PtRhSn/C*) showed stronger agglomeration, while the mean diameter of the nanoparticles is around 11 nm.

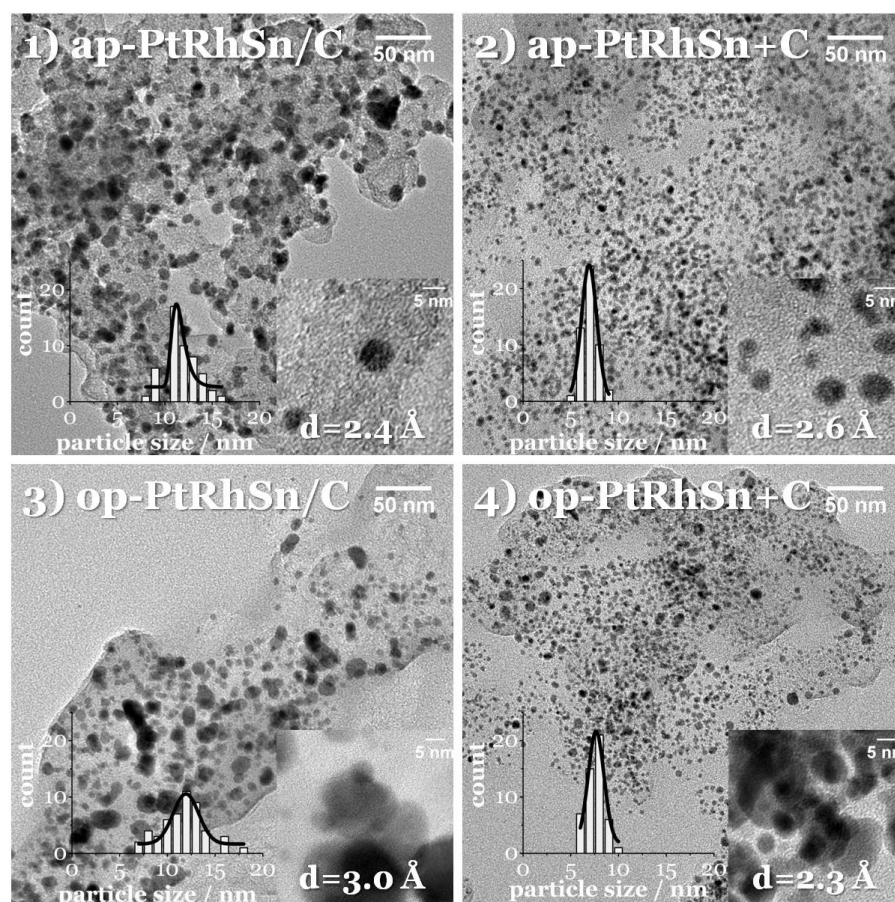


Figure 6.1: TEM micrographs and particle size distribution diagrams of the as-prepared electrocatalyst: 1) ap-PtRhSn/C, 2) ap-PtRhSn+C, 3) op-PtRhSn/C and 4) op-PtRhSn+C. Exemplary insets with higher magnification for each sample show different lattice spacing found in all samples.

Furthermore the size distribution of metal particles is broader, when the particles were supported on carbon after reduction and precipitation as pictured in the diagrams in Figure 6.1. The higher

magnification images also depicted in Figure 6.1 reveal different lattice spacing found in all samples and shown here exemplary with the four different catalysts: 2.3 Å can be attributed to Pt fcc (111) or Niggliite (101) (Fig.1 op-PtRhSn+C); 2.4 Å can be attributed to SnO₂ Rutile (202) (Fig.1 ap-PtRhSn/C) and 2.6 Å to the SnO₂ Rutile (101) (Fig.1 ap-PtRhSn+C) plane, respectively. The lattice spacing of 3.0 Å can be attributed to the Niggliite (101) plane (Fig.1 op-PtRhSn/C). The metal loadings ranged in the narrow region from 40 to 48% by weight.

The XRD patterns of the Pt-Rh-Sn electrocatalysts are shown in Figure 6.2. All diffractograms show relatively broad Bragg peaks, typical for nanosized particles with limited structural coherence lengths. All samples showed the typical cubic phased (fcc) reflections between the respective Pt and Rh literature values [(111): 39.764 and 41.069°], evidencing alloy formation and bulk lattice compression compared to pure Pt; as well as more prominent hexagonal phased PtSn (Niggliite) diffraction patterns [(102): 41.846°] where Rh statistically substituted Pt in the lattice.¹⁰⁷

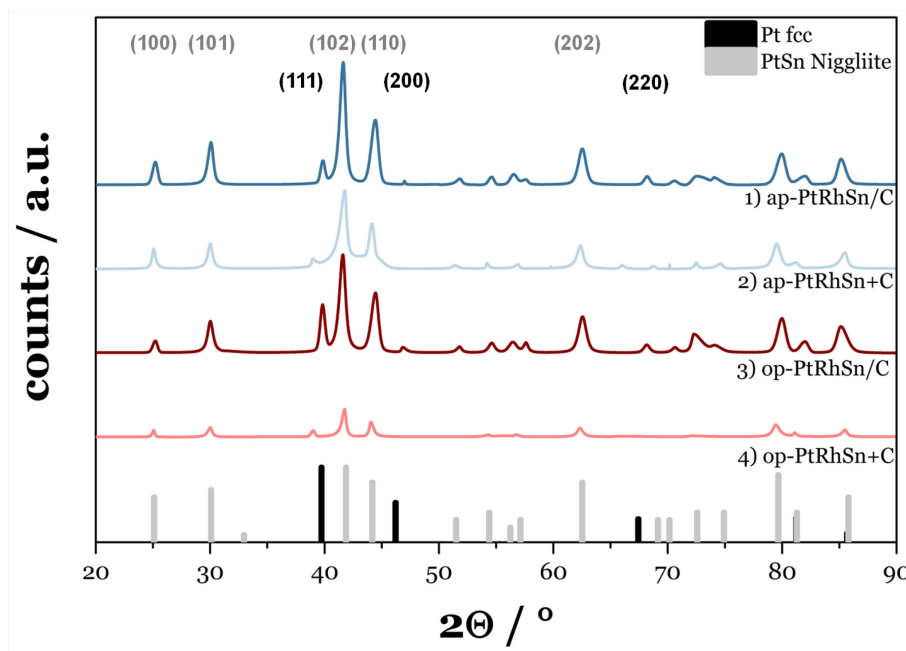


Figure 6.2: Cu K α XRD patterns of electrocatalyst: 1) ap-PtRhSn/C, 2) ap-PtRhSn+C, 3) op-PtRhSn/C and 4) op-PtRhSn+C. Pure Pt fcc and pure PtSn Niggliite diffraction patterns are indicated in black and grey, respectively.

Both Pt and Rh show a face-centered cubic (fcc) space group Fm3m with very similar lattice constants of 3.9231 Å and 3.8031 Å, respectively. This favors the formation of homogeneous PtRh binary solid solutions over wide compositional ranges, as indicated by the Pt–Rh phase diagram.¹⁵⁰ This is why Pt and Rh diffraction peaks cannot be separately resolved in the XRD patterns. In general, the *ap materials* showed higher intensities and higher ratios of hexagonal to cubic diffraction peak intensities than the *op materials*. The as-reduced supported electrocatalysts materials show in

comparison broader diffraction peaks and smaller intensities as the corresponding first reduced, precipitated and then supported materials, indicating that the crystallite sizes are larger when the precursors are reduced without carbon present. Although absent in the XRD pattern of Figure 6.2, the presence of minor nanocrystalline or amorphous SnO_x phases, especially near the surface, cannot be ruled out. This is also indicated by the lattice spacing on the surface of some nanoparticles found by TEM throughout all samples.

Table 6.1: Molar composition, metal weight loading and crystallite sizes of the supported PtRhSn electrocatalysts.

Catalysts	Pt:Rh:Sn atomic ratio (ICP)	Total metal loading /wt%	Pt:Rh:Sn atomic ratio (EDX)	Particle size (TEM) /nm
1) ap-PtRhSn/C	32:12:56	42	42:7:51	11.3±1.7
2) ap-PtRhSn+C	30:12:58	40	44:16:50	6.5±0.8
3) op-PtRhSn/C	33:11:57	48	38:12:50	11.2±2.3
4) op-PtRhSn+C	30:11:59	42	32:6:62	7.1±0.8

6.4.2. Electrochemical characterization of the Pt-Rh-Sn catalysts

To correlate catalyst structure and composition with the electrocatalytic EOR polarization behavior, cyclic voltammograms (CV) in 0.1 M HClO₄ as well as in 0.5 M Ethanol (EtOH) and 0.1 M HClO₄ (Figure 6.3) were collected. The first two full scans are shown in (Figure 6.4 and Figure 6.5). In addition, potentiostatic chronoamperometric (CA) experiments were performed to examine the catalytic performance and catalyst stability at an electrode potential of technical interest (0.45 V vs. RHE) for extended period of times (Figure 6.6). While current densities were normalized only by the amount of Platinum present on the electrode surface, the reduction charge of Hydrogen under potential deposition (H_{UPD}) was additionally employed to estimate electrochemically active surface area (ECSA) values for the two catalysts based on the charge density for the formation of a fully covered Pt-H monolayer ($210 \mu\text{C}/\text{cm}^2$)¹⁴⁹. CO-ECSA values¹⁰⁶ from the CO-oxidation charge could not be used to compare the two surface systems due to the poor CO oxidation activity of the *Pt-Rh-Sn* surface. Mass based current density forward scans of the first CV in Ethanol containing electrolytes are shown in Figure 6.4. The ECSA values are given in Table 6.2 alongside mass activity values for different potentials and after 300 s.

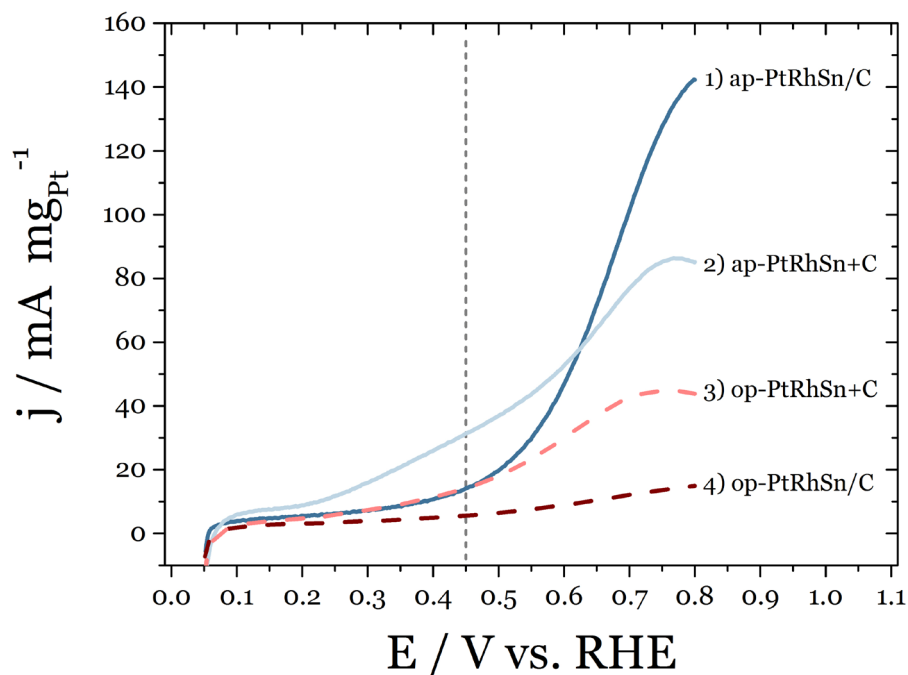


Figure 6.3: Electrocatalytic activity for the ethanol oxidation reaction (EOR) on 1) ap-PtRhSn/C, 2) ap-PtRhSn+C, 3) op-PtRhSn/C and 4) op-PtRhSn+C recorded in 0.5 M C₂H₅OH + 0.1 M HClO₄. First forward scan with a scan rate of 20 mV/s. Current densities are normalized by the amount of Pt present on the working electrode surface (~ 3 μg Pt+Rh).

Table 6.2: Electrochemical EOR activity of PtRhSn catalysts: electrochemical surface area (ECSA), current densities at 0.45 V vs. RHE and 0.80 V vs. RHE during voltammetric scans, and current density at constant 0.45 V vs. RHE after 300 s.

Catalysts	ECSA	Pt loading	j @ 0.45V	j @ 0.80V	j @ 0.45V@300s
	m _{Pt} ² g _{Pt} ⁻¹	μg cm _{geo} ⁻²	mA mg _{Pt} ⁻¹	mA mg _{Pt} ⁻¹	mA mg _{Pt} ⁻¹
1) ap-PtRhSn/C	8.4	13	14.3	142.3	3.3
2) ap-PtRhSn+C	5.4	20	31.3	85.2	9.1
3) op-PtRhSn/C	3.3	27	5.6	15.0	0.1
4) op-PtRhSn+C	3.6	22	14.4	43.8	2.2

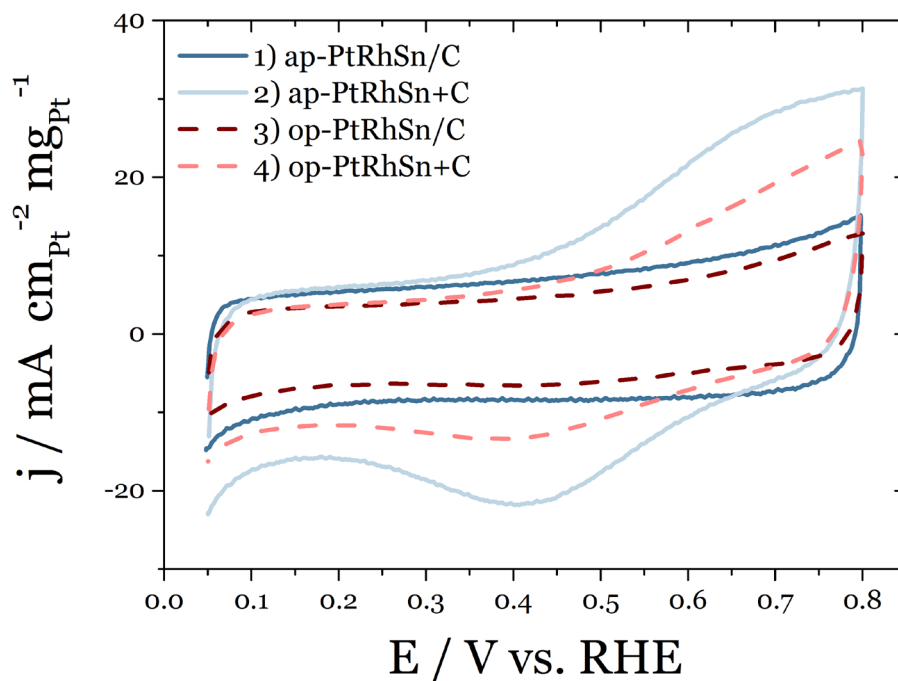


Figure 6.4: First scan for 1) ap-PtRhSn/C, 2) ap-PtRhSn+C, 3) op-PtRhSn/C and 4) op-PtRhSn+C recorded in 0.1 M HClO₄ with a scan rate of 20 mV/s. Current densities are normalized by the amount of Pt present on the working electrode surface (~ 3 μg Pt+Rh).

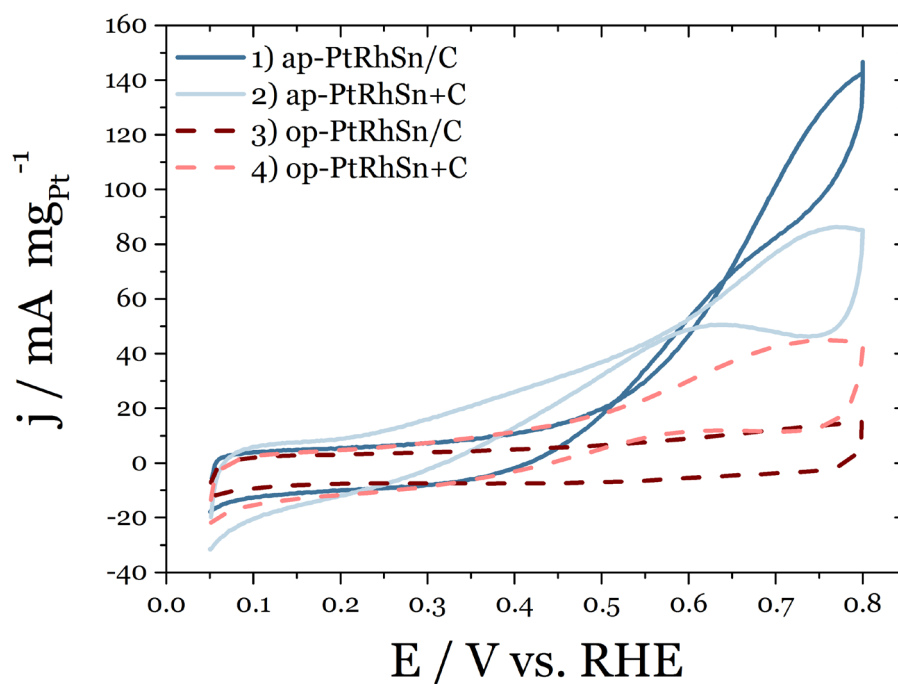


Figure 6.5: First two scans of the electrocatalytic ethanol oxidation reaction (EOR): 1) ap-PtRhSn/C, 2) ap-PtRhSn+C, 3) op-PtRhSn/C and 4) op-PtRhSn+C recorded in 0.5 M H₂SO₄ and 0.5 M EtOH with a scan rate of 20 mV/s. Current densities are normalized by the amount of Pt present on the working electrode surface (~ 3 μg Pt+Rh).

The electrocatalysts synthesized using the ambient pressure methods with conventional heating (*ap materials*) showed clearly higher activity for the EOR compared to the catalysts that were prepared under elevated pressures (*op materials*). In particular, *ap-PtRhSn+C* showed an exceptionally early onset potential of less than 0.20 V vs. RHE and the highest mass activity for the low potential region until 0.60 V vs. RHE. At this potential *ap-PtRhSn/C* started to outperform *ap-PtRhSn+C*, showing the highest Pt mass activity at around 0.80 V vs. RHE. While the mass activity of *op-PtRhSn+C* showed a similar onset potential and lower peak current densities compared to the *ap materials*, *op-PtRhSn/C* showed low EOR activity over the entire potential range. The ECSA for *ap-PtRhSn/C* is the highest with $8.4 \text{ mPt}^2 \text{ gPt}^{-1}$ followed by $5.4 \text{ mPt}^2 \text{ gPt}^{-1}$ for *ap-PtRhSn+C*. The *op materials* showed in general only about half of this activity around $3 \text{ mPt}^2 \text{ gPt}^{-1}$. This indicates a Pt richer surface of the *ap materials*.

The observed synthesis-activity correlations can be explained by the formation of well-dispersed catalyst nanoparticles with limited agglomeration, in case that the carbon support is present during precursor reduction. This would lead to low EOR onset potentials compared to the more agglomerated step wise prepared catalysts. The activity cross-over observed for the *ap materials* would be plausibly explained by a prevalent selectivity for the 2 and 4 electron products (acetaldehyde or acetic acid) for the more dispersed particles, whereas the more agglomerated particles with their smaller interparticle distance, thanks to enhanced readsorption, would show a higher selectivity for the higher electron products associated with a higher mass activity at higher overpotentials.^{18,166,167} The lowest overall activity of *op-PtRhSn/C* correlates with the lowest ratio of hexagonal to cubic phased alloy formation as seen from XRD, supporting the notion that a high concentration of active surface site ensembles formed by a Niggliite structure of the particle is of importance for the achievement of high EOR activities.¹⁰⁷ The relative chronoamperometric performances at 0.45 V vs. RHE of the four distinct electrocatalysts (Figure 6.7) are in good accordance with the corresponding mass activities in Figure 6.3 at the same potentials. All materials showed stable catalytic behavior over extended periods of time.

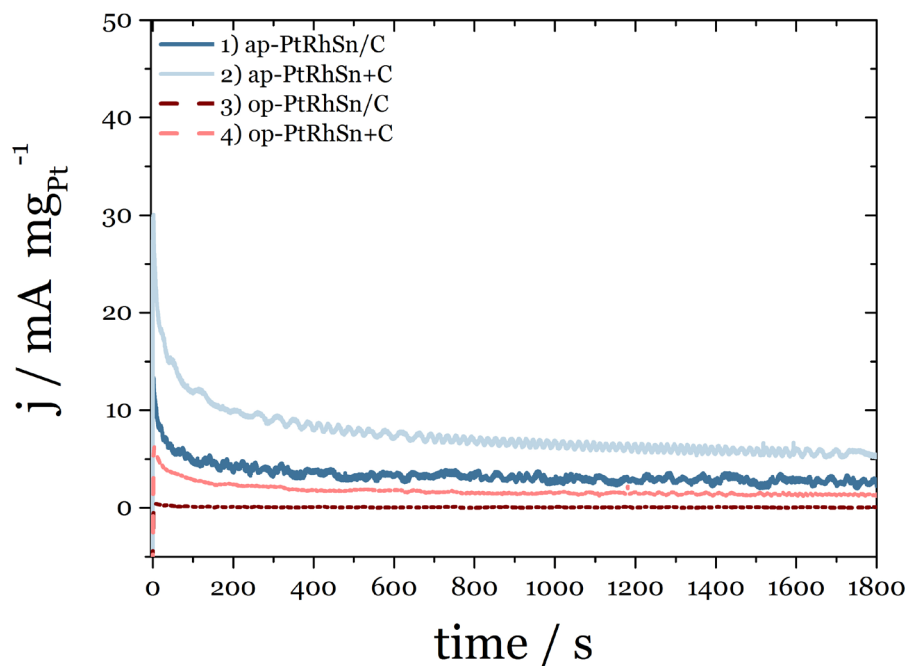


Figure 6.6: Electrocatalytic activity for the ethanol oxidation reaction (EOR) on 1) *ap*-PtRhSn/C, 2) *ap*-PtRhSn+C, 3) *op*-PtRhSn/C and 4) *op*-PtRhSn+C recorded in 0.5 M C₂H₅OH + 0.1 M HClO₄. Potentiostatic chronoamperometry at E = +0.45 V vs. RHE. Current densities are normalized by the amount of Pt present on the working electrode surface (~ 3 μg Pt+Rh).

In order to estimate the catalytic performance related to the state-of-the-art in ternary EOR electrocatalysis, we compared the performance to the most promising catalysts in literature. The *ap*-PtRhSn+C catalyst displayed four times higher current densities at +0.45 V in acidic media than a similar PtRhSnO₂/C catalyst¹⁵² and as an earlier PtRhSn catalyst with the same 3:1:4 ratio.⁶¹ Brouzgou *et. al* compared a variety of DEFC anode catalysts with increasing Pt loading on the working electrode surface and established a certain region between 0.1-1.0 mA cm_{Pt}²@0.70 V vs. RHE in where most of the reported catalyst to date belong.⁹² Figure 6.7 shows that both *ap materials* lay within this region.

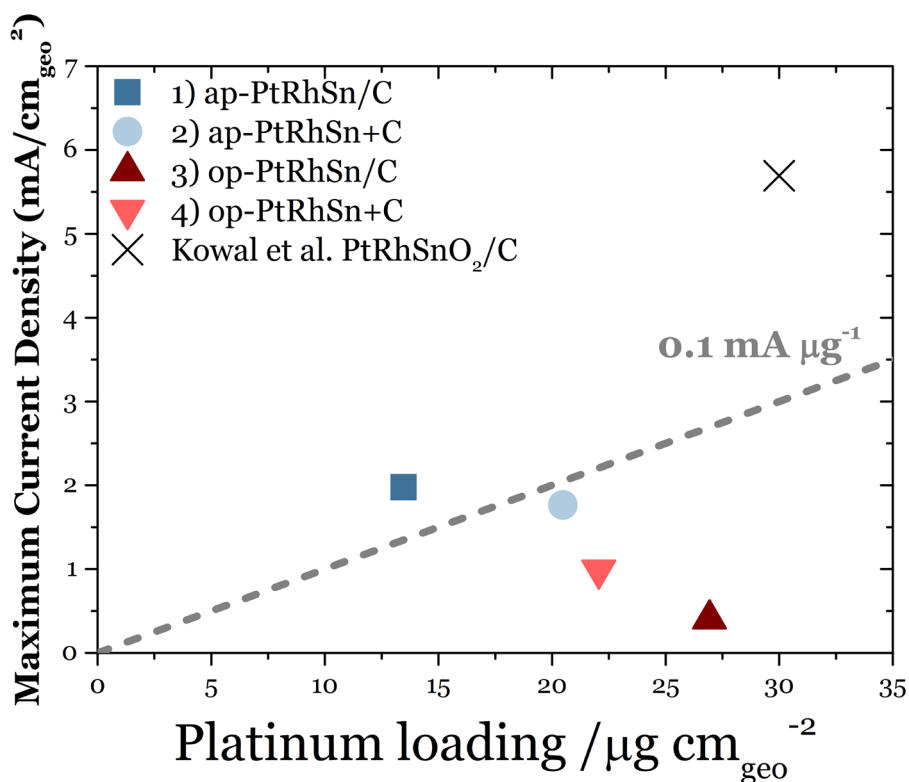


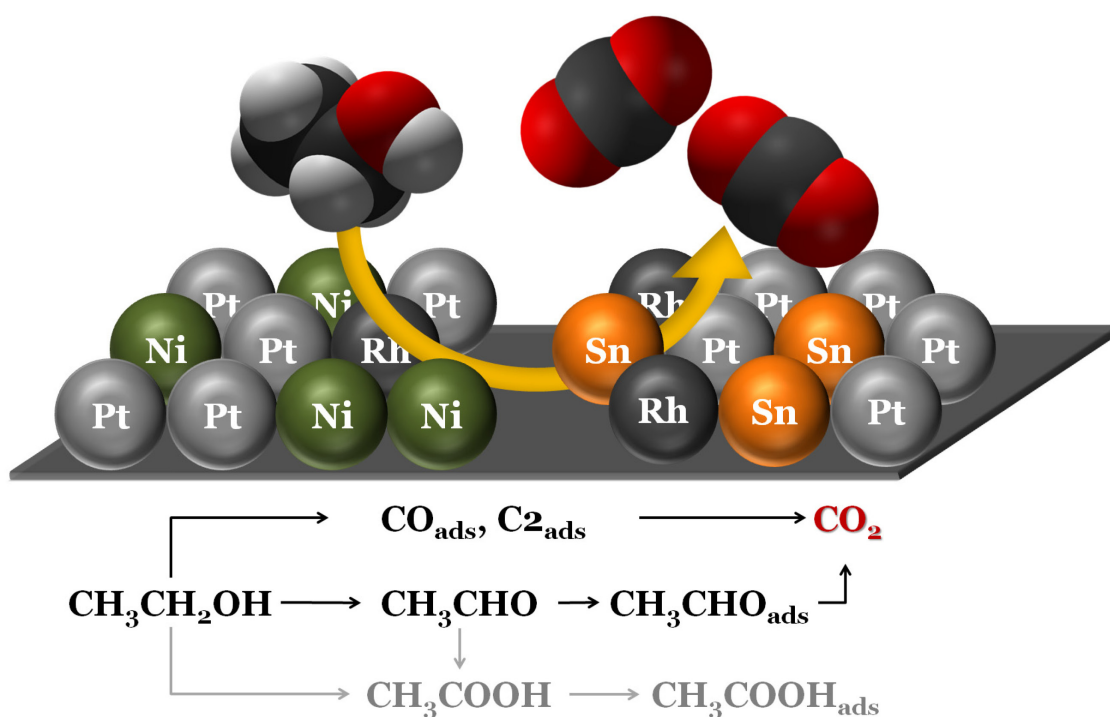
Figure 6.7: Current density (mA cm $_{\text{geo}}^{-2}$ at 0.70 V vs. RHE) dependency on the platinum loading ($\mu\text{g cm}^{-2}$) for ethanol electro-oxidation on 1) ap-PtRhSn/C, 2) ap-PtRhSn+C, 3) op-PtRhSn/C and 4) op-PtRhSn+C recorded in 0.5 M C $_2$ H $_5$ OH + 0.1 M HClO $_4$ with a scan rate of 20 mV/s according to Brouzgou *et al.*⁹². Current densities are normalized by the geometrical area of the working electrode surface (0.196 cm 2). For comparison PtRhSnO $_2$ /C by Kowal *et al.*⁵ is included.

6.5. Conclusions

Both ambient and overpressure synthesis approaches resulted in carbon supported Pt-Rh-Sn electrocatalysts that exhibited high performance for ethanol oxidation in acidic medium. The x-ray diffractograms show fcc PtRh and hexagonal PtRhSn phases. The highest overall activity is shown by materials synthesized at ambient pressures, with very early onset potentials for an on-carbon-reduced-precursor synthesis approached catalyst *ap-PtRhSn+C* and the highest mass activity for *ap-PtRhSn/C*. This could indicate the formation of a high concentration of surface site ensembles on the carbon during the reduction of the precursors that lead to higher activities at lower potentials, possibly towards the complete ethanol oxidation. Further work is now necessary to investigate the product and intermediate distribution on the different surfaces with qualitative *in-situ* techniques in order to help elucidate the mechanisms of ethanol-electrooxidation.

7. Exceptional Activity of a Pt-Rh-Ni Ternary Nanostructured Catalyst for the Electrochemical Oxidation of Ethanol: Study of optimal oxygen-donating species for the ternary electrocatalytical system.

In this chapter a highly active ternary single-phased fcc PtRhNi/C nanoparticle electrocatalyst for the EOR is introduced. A new highly active ternary single-phased cubic PtRhNi/C nanoparticle electrocatalyst is reported and its morphology, composition and electrochemical activity discussed in comparison with our state-of-art PtRhSn/C electrocatalyst. The EOR activity of the PtRhNi/C material outperformed the benchmark PtRhSn/C material in acidic and alkaline media, showing high stability especially in alkaline media. The higher intrinsic ethanol oxidation activity of the Ni containing electrocatalyst is lending support to the notion that surface NiOx is an excellent oxygenate-supplying catalyst component for the oxidation of ethanol.



The contents of this chapter have been published: Reprinted from N. Erini, S. Rudi, V. Beermann, P. Krause, R. Yang, Y. Huang and P. Strasser, *ChemElectroChem.*, **2015**, 2, 903-908.¹⁶⁵ Copyright 2015 with permission from John Wiley & Sons, Inc..

7.1. Introduction

Direct Ethanol Fuel Cells (DEFC) have been a subject of intensive studies for fundamental and practical applications as alternate power sources (e.g. the development of compact portable power as well as electric vehicle range extenders operating at high temperatures).⁷⁻¹⁰ As a fuel, ethanol has high volumetric and gravimetric energy densities (8 kWh kg^{-1}), good energy efficiencies, and offers easy handling, storage and transportation, contrary to gaseous fuels.¹¹ Its low toxicity, biocompatibility and abundant availability in combination with the availability from renewable resources make ethanol an almost ideal fuel. Its oxidation, however, proceeds often incomplete resulting in a number of byproducts rather than CO_2 . This is due to difficulties in the C-C bond cleavage in ethanol and, to some extent, to the formation of CO-intermediates leading to poisoning of the active sites on Pt catalysts.²⁻⁶ Complete ethanol electro-oxidation to CO_2 involves 12 electrons per molecule, while partial oxidation leads to by-products like acetic acid or acetaldehyde which reduce the Faradaic efficiency of the anodic reaction of DEFC. Efforts to develop highly active and selective electrocatalysts for ethanol oxidation reaction (EOR) to CO_2 have therefore concentrated on the addition of co-catalysts to platinum.³⁵⁻³⁹ Alloying Pt with highly oxophilic transition metals such as Rh, Ni or Sn has been a promising strategy to modify the electrocatalytic surface properties of Pt in order to supply active oxygen-containing species, such as OH, that readily oxidize adsorbed molecular fragments while reducing the cost of the catalyst considerably.^{2,40} To achieve this goal, the oxophilic component is assumed to be present as an oxide species at the surface of the operating catalyst.

Our past research focused on the promising family of EOR nanocatalysts based on mixtures of Pt, Rh and Sn.^{5,61,104,107,112,150-152} In particular, we uncovered and characterized the optimal 3D structural arrangement of the atoms of the three components at the surface and bulk of the final active catalyst to maximize activity and selectivity and found a single-phase Rh-doped PtSn bulk Niggliite structure as the preferred and catalytically most active nanocrystalline phase. On its surface, metallic Pt and Rh were atomically mixed with a SnO_2 phase representing the active surface-site ensembles. While the ternary ensemble of the three metals led to high oxidation activities, it is also known that nanocrystalline Pt and its Ni based binary alloy belong to the most active catalysts for the catalytic oxidation of organic molecules.⁵³⁻⁵⁵ We therefore developed the hypothesis that the partial random substitution of Pt with Rh in Pt-Ni bulk alloys could lead to active EOR electrocatalysts due to the formation of unique Pt-Rh-NiOx surface ensembles.

Mechanistic details of the Rh and Ni-promoted oxidation of ethanol on Pt are still not well understood. It is believed that Rh increases the yield of CO_2 by promoting the C-C bond cleavage. However, there is reason to believe that this hypothesis does not represent a comprehensive picture of the role of Rh in

this family of catalysts. According to the bifunctional mechanism, the synergistic effect results from the fact that hydrous surface alpha-Ni(OH)_x activates water molecules and provides preferential sites for OH species ($\text{H}_2\text{O} \rightarrow \text{OH}_{\text{ads}} + \text{H}^+ + \text{e}^-$) at lower potentials than Pt. Abundant -OH_{ads} species are necessary to completely oxidize the CH_x or CO surface fragments to CO₂ ($\text{CO}_{\text{ads}} + \text{OH}_{\text{ads}} \rightarrow \text{CO}_2 + \text{H}^+ + \text{e}^-$) avoiding electrode poisoning.¹⁶⁸ Beyhan *et al.* studied the catalytic effect of Ni and Rh added to PtSn catalyst and the influence to the cleavage of ethanol with in-situ FTIR, finding it more beneficial for the complete oxidation than the addition of Pd or Co.² Soundararajan *et al.* synthesized a set of Pt and Pt-Ni alloy nanoparticle catalysts by electrochemical deposition, showing that the Pt-Ni alloy formation leads to higher activities in alkaline media for EOR.⁶³ Bonesi *et al.* investigated high surface area carbon-supported binary PtSn and ternary PtSnNi and PtSnRh catalysts for EOR at elevated temperatures, concluding that the ternary catalysts show elevated activities.⁶⁴

Assuming that Rh indeed facilitates the bond breaking with Sn or Ni being the responsible oxygen species provider, a combination Pt, Rh and Ni should result in an even higher active EOR catalyst, but to the best of our knowledge to this date there have been no reports on ternary Pt-Rh-Ni catalyst systems for the EOR. This is why, in this report, we prepared ternary single-phase *PtRhNi/C* nanoparticle catalysts and benchmarked their electrocatalytic activity and stability for the EOR to the corresponding state-of-art Sn-containing electrocatalyst. We compared and contrasted their structure, morphology and catalytic performance and conclude that Ni offers great catalytic performance benefits over Sn. We are confident that this study will spark more research in the use of Ni in the oxidation of small organic molecules.

7.2. Experimental

Synthesis of PtRhSn/C: The synthesis of *PtRhSn/C* has been described previously.¹⁰⁷ In summary, 351.97 mg Pt(acac)₂, 75.25 mg Rh₂(OAc)₄ and 0.48 ml Sn(acac)₂, as well as 622.47 mg 1,2-tetradecandiol, 0.48 ml oleic acid and 0.50 ml oleylamine were dissolved in dioctylether (60 ml), heated to 260 °C and hold for 30 minutes, precipitated with isopropanol and the precipitated particles redispersed in n-hexane and added to a dispersion of Ketjen black carbon and stirred overnight at RT. The particles were separated by centrifugation, freeze-dried and the residue dried in a furnace under N₂, oxidized under O₂/N₂ and calcinated by heating under H₂/Ar atmosphere (see detailed information in previous publication¹⁰⁶).

Synthesis of PtRhNi/C: To prepare Pt₂₆Rh₅Ni₆₉ alloy core shell nanoparticles 0.9 mmol Ni(OAc)₂·4 H₂O, 1.2 mmol 1,2-tetradecandiol, 0.3 ml oleylamine and 0.3 ml oleic acid were

dispersed in dibenzyl (50 ml) under a nitrogen atmosphere, stirred for 5 min at 80°C, and heated to 210°C. After subsequent 30 min time periods, Pt(acac)₂ (0.3 mmol), then Rh₂(OAc)₄ (0.03 mmol), and finally Pt(acac)₂ (0.1351 mmol) were added; each was dissolved in 1,2-dichlorobenzene (3 ml). After a further 30 min, the reaction mixture was cooled rapidly and the nanoparticles were precipitated with mixture of dichloromethane (5 ml) and ethanol (20 ml). Vulcan XC 72R (278.1 mg) was dispersed in toluene (60 ml) and subjected to ultrasonication for 5 min; then, pure ethanol (10 ml) was added, followed by the reaction mixture, and everything was stirred for 24 h (at RT). The particles were separated by centrifugation, washed 3--4 times with ethanol, freeze-dried, and the residue was heated in a furnace under an air atmosphere to 180°C, at which it was held for 1 h to remove surfactants before being placed in a N₂ atmosphere for 30 min to remove any oxygen. Then, a H₂/Ar (4 vol % H₂) gas mixture was fed for 30 min at 180°C to remove N₂ before the temperature was raised to 240°C to reduce any possible oxidized Ni on the surface and to enhance the atomic mixing of Ni and Pt.

Physico-chemical characterization of catalysts: The characterization and electrochemical testing protocol for *PtRhSn/C* has been described in detail¹⁰⁷ and is similar to the one for *PtRhNi/C*. *Inductively coupled plasma- optical emission spectroscopy (ICP-OES)* was used for compositional analysis; performed using a 715-ES-inductively coupled plasma analysis system (Varian). The standard concentrations were 2, 4.5 and 7.5 ppm for Pt and Ni; 3, 10 and 20 ppm for Sn and 0.7, 2.8 and 5.6 ppm for Rhodium. The chosen wavelengths for concentration determination were 203.646 nm, 214.424 nm, 265.495 nm and 306.471 nm for Pt; 216.555 nm, 221.648 nm, 222.295 nm, 222.486 nm, 227.021 nm, 230.299 nm and 231.604 nm for Ni; 233.477 nm, 246.103 nm, 249.078 nm, 343.488 nm and 369.236 nm for Rhodium and 189.9 nm for Sn. *Transmission electron microscopy (TEM) and Energy dispersive x-ray spectroscopy (EDX)* was used to study morphology and composition. A Cu-grid (200 mesh) coated with holey carbon film was impregnated with the sample solution and air-dried at 60 °C. A FEI TECNAI G² 20 S-TWIN microscope, equipped with a GATAN MS794 P CCD-detector operated at 200 kV was used. The mean particle size was determined from the TEM images by counting of at least 200 particles. EDX data were collected for 120 s at an angle of 45° with respect to the sample holder. *Cu K α x-ray diffraction (XRD)* patterns were collected using a D8 Advance diffractometer (Bruker) equipped with a Lynx Eye Detector and KFL Cu 2K x-ray tube. The diffraction patterns were collected in a 20–80° 2 θ range with a step size of 0.00142° dwelling for 30 s for *PtRhSn/C* and a step size of 0.05° dwelling for 10 s for *PtRhNi/C* at every step. The XRD patterns were analyzed using the MDI Jade 8 software package. Bragg reflex positions were compared with the reference XRD patterns (PDF data files, International Center for Diffraction Data). *Electrochemical measurements:* Polished glassy carbon working electrodes were coated with 10 μ l catalyst ink (*PtRhSn/C*: 6 mg electrocatalyst powder; 2.0 ml of ultrapure water; 0.5 ml isopropanol; 20 μ l of

5 wt. % Nafion solution; *PtRhNi/C*: 8 mg electrocatalyst powder; 3.98 ml of ultrapure water; 1.0 ml isopropanol; 20 μ l of 5 wt. % Nafion solution) and measured with a Biologic SP 150 potentiostat in an electrochemical glass cell with Pt wire as counter and saturated MMS (in HClO₄) or saturated SCE (in KOH) as reference electrode. KOH and HClO₄ electrolytes were freshly made and purged with Nitrogen prior and during experiments.

7.3. Results and discussion

Two ternary electrocatalysts *PtRhSn/C* and *PtRhNi/C* were successfully synthesized and studied to investigate the influence of Ni and Sn as oxygen donating species for the EOR. The atomic ratios of the as synthesized samples were characterized by coupled ICP-OES and presented in Table 7.1. Both catalysts were deliberately designed having <10 % atomic molar ratios in Rh, a molar Pt ratio of around 30 % , while the oxygen-donating species Sn/Ni were designed to have about double molar ratio than Pt. The weight loading of both catalysts was designed to be very similar. Additional experiments showed that the catalyst performance was insensitive to changes in the Rh content in the 5-12 % range.

Table 7.1: Size, molar composition and metal weight loading of the supported PtRhSn and PtRhNi electrocatalysts.

Catalysts	Atomic ratio (Pt:Rh:Sn/Ni)	Total metal loading wt%	Average particle size (nm)
1) PtRhSn/C	32:12:56	24	4.7 \pm 0.1
2) PtRhNi/C	26:5:69	28	11.7 \pm 0.1

TEM micrographs of the electrocatalysts (Figure 7.1) evidenced that the nanoparticles were well distributed across the carbon support with sizes ranging from 6 nm to 12 nm. Mean particle diameters were estimated from TEM derived size distribution histograms and are inserted in the TEM graphs in Figure 1. *PtRhNi/C* nanoparticles showed an irregular, close to spherical shape most likely due to the agglomeration of 2-3 particles during the synthesis. *PtRhSn/C* nanoparticles are spherical with broad size rang 2 – 18 nm.

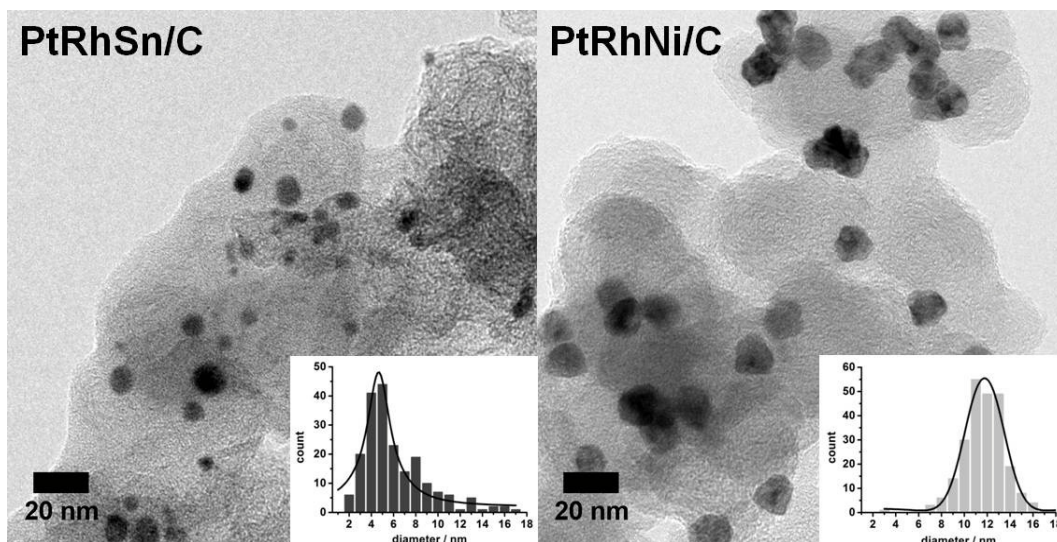


Figure 7.1: TEM micrographs and size distribution histograms of electrocatalysts: PtRhSn/C, 4.7 ± 0.1 nm and PtRhNi/C, 11.7 ± 0.1 nm.

Figure 7.2 shows the fitted x-ray powder diffraction (XRD) patterns of the prepared samples. The carbon features were taken out by background subtraction. Both XRD patterns show relatively broad Bragg peaks, typical for nanosized particles with limited structural coherence. The *PtRhSn/C* catalyst shows a typical hexagonal $P6_3/mmc$ pattern due to a major Niggliite phase for PtSn (#00-025-0614) at 25.1 (100), 30.0 (101), 41.8 (102), 44.1 (110) and 62.5 (202) as well as diffraction peaks (#00-004-0802) at 39.8 (111) and 46.2 (200) due to a separate minor Pt-rich face-centered cubic phase. Pt and Rh diffraction peaks cannot be resolved in XRD patterns because they form a homogenous PtRh binary solid solution over wide compositional ranges, as indicated by the Pt-Rh phase diagram (not shown here). Earlier studies suggested that Rh incorporates randomly into the Niggliite lattice substituting Pt atoms.^{107,150} *PtRhNi/C* shows a single-phase face centered cubic diffraction pattern; the diffraction peaks lay, in accordance with the atomic mixture of the three metals, between the reflexes of Pt, Rh and Ni. No reflexes for pure metallic Pt, Rh or Ni can be observed, indicating alloy formation of all three metals. However, due to the slightly non-symmetric diffraction peaks of the *PtRhNi/C* catalyst the existence of a second fcc phase cannot be completely excluded.

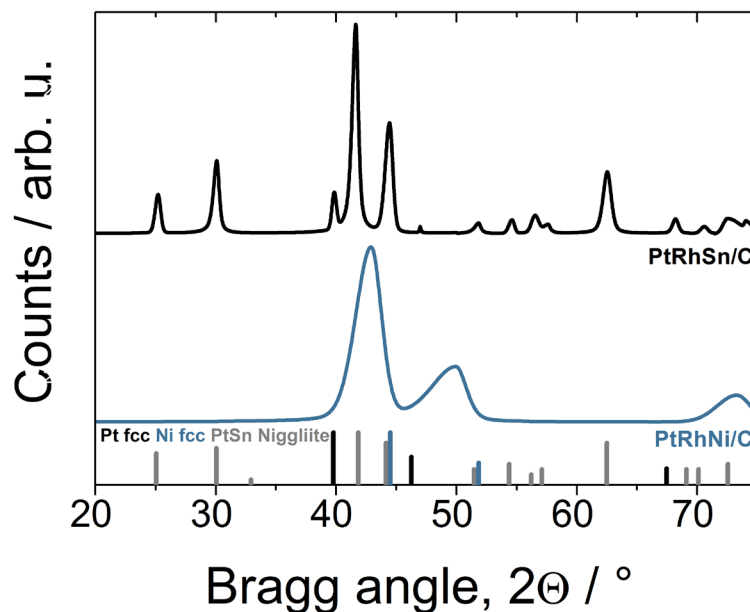


Figure 7.2: Fitted CuK α XRD patterns of PtRhSn/C and PtRhNi/C. The carbon features were taken out by background subtraction. Pure Pt fcc, pure Ni fcc, and pure PtSn Niggliite diffraction patterns are indicated in black, blue, and gray lines, respectively.

The catalytic activity of the prepared *PtRhNi/C* towards ethanol electrooxidation was evaluated in both acidic and alkaline 0.1 M electrolyte and compared with *PtRhSn/C*. Since the platinum surface content of the two catalysts varied due to their distinctly different crystal symmetry, a mass activity metric was used to evaluate the cyclic voltammetric and chronoamperometric measurements. To correlate catalyst structure and composition with the electrocatalytic EOR polarization behavior, cyclic voltammograms (CV) in 0.1 M KOH and in 0.1 M HClO₄ as well as in 0.5 M Ethanol (EtOH) in 0.1 M KOH and 0.1 M HClO₄ (Figure 7.3) were collected. The first two full scans in pure electrolyte are shown in Figure 7.4 and for the ethanol oxidation in Figure 7.5. In addition, potentiostatic chronoamperometric (CA) experiments were performed to examine the catalytic performance and catalyst stability at an electrode potential of technical interest (0.45 V vs. RHE) for extended period of times (Figure 7.9) in acidic and alkaline media. Although the current densities were only normalized by the amount of platinum-group metals (PGMs) present on the electrode surface, the reduction charge of hydrogen under potential deposition (H_{UPD}) was additionally employed to estimate electrochemically active surface area (ECSA) values for the two catalysts based on the charge density for the formation of a fully covered Pt-H monolayer ($210 \mu\text{C}/\text{cm}^2$)¹⁴⁹. Mass-based current density H_{UPD} and the forward scans of the first CV in ethanol-containing electrolytes are shown in Figure 7.3. The specific activity and geometric current density equivalents are shown in Figure 7.6 and Figure 7.7. The ECSA values are given in Table 7.2 alongside mass activity values for different potentials and after 300 s. CO-ECSA

values¹⁰⁶ from the CO-oxidation charge could not be used to compare the two surface systems, owing to the poor CO oxidation activity of the *PtRhSn/C* surface (Figure 7.8).

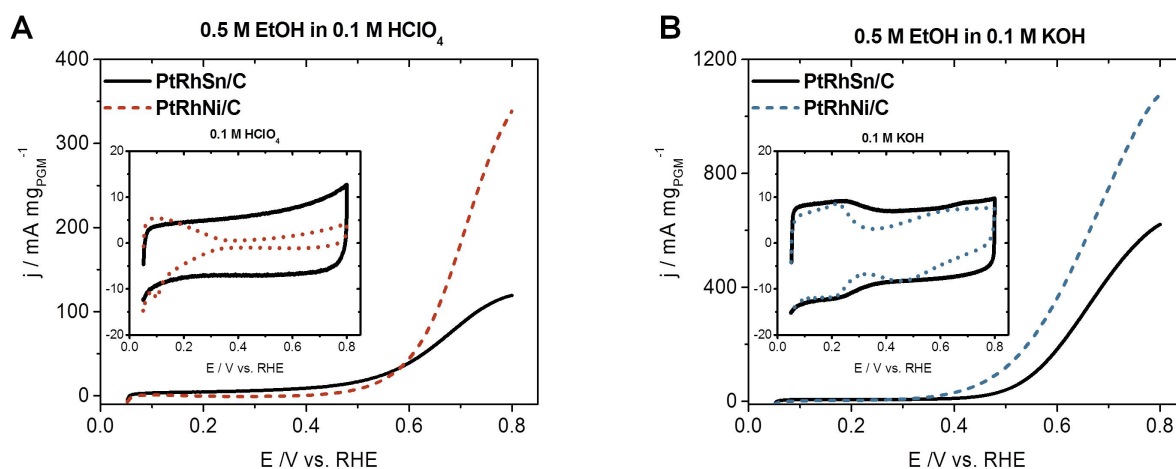


Figure 7.3: Polarization curves of PtRhSn/C and PtRhNi/C in pure 0.1 M HClO₄ (A) and 0.1 M KOH (B) and the ethanol oxidation reaction (EOR) in acidic media (C, 0.1 M HClO₄) and alkaline media (D, 0.1 M KOH) containing 0.5 M Ethanol. Current densities are normalized by the mass of Pt present on the working electrode.

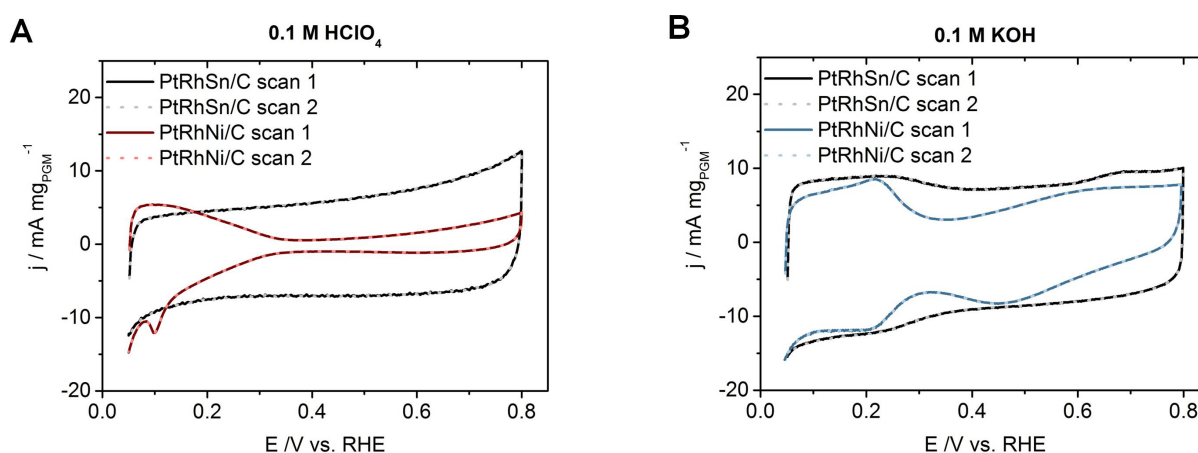


Figure 7.4: First two polarization curves of PtRhSn/C and PtRhNi/C in pure 0.1 M HClO₄ (A) and 0.1 M KOH (B). Current densities are normalized by the mass of Pt group metals present on the working electrode. Scan rate is 20 mV s⁻¹.

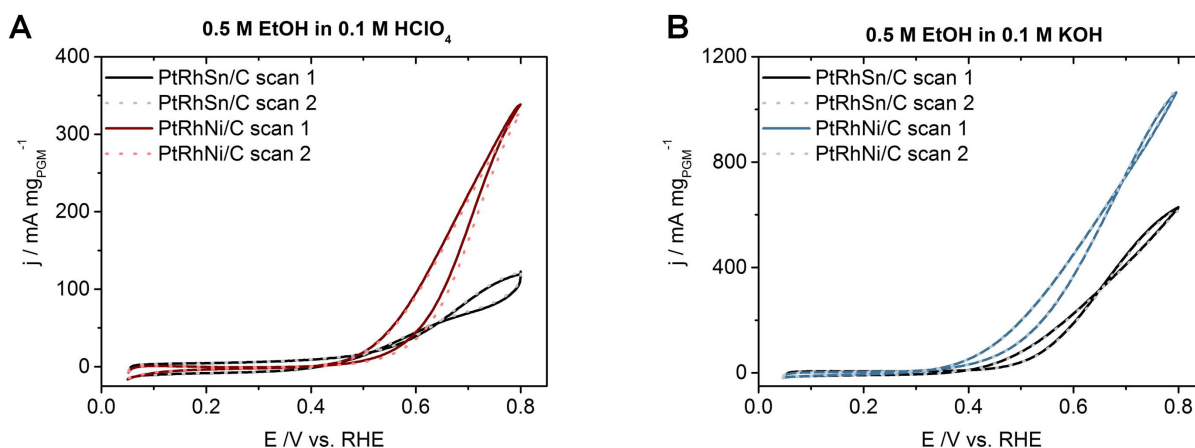


Figure 7.5: First two polarization curves of the ethanol oxidation reaction (EOR) on PtRhSn/C and PtRhNi/C in acidic media (A, 0.1 M HClO₄) and alkaline media (B, 0.1 M KOH) containing 0.5 M Ethanol. Current densities are normalized by the mass of Pt group metals present on the working electrode. Scan rate is 20 mV s⁻¹.

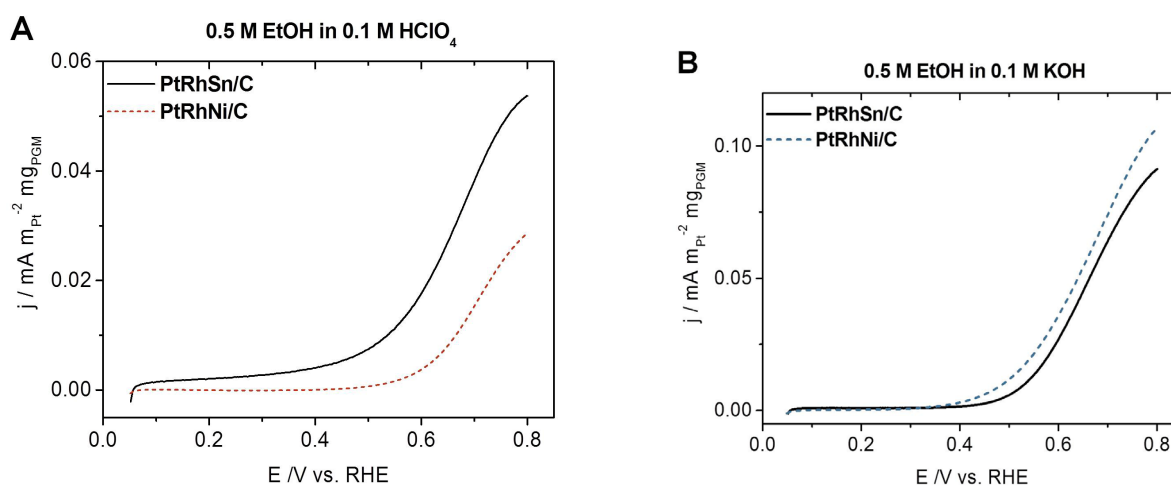


Figure 7.6: Specific activity polarization curves of the ethanol oxidation reaction (EOR) on PtRhSn/C and PtRhNi/C in acidic media (A, 0.1 M HClO₄) and alkaline media (B, 0.1 M KOH) containing 0.5 M Ethanol. Current densities are normalized by the Electrochemical Active Surface Area from H_{UPD} measurements. Scan rate is 20 mV s⁻¹.

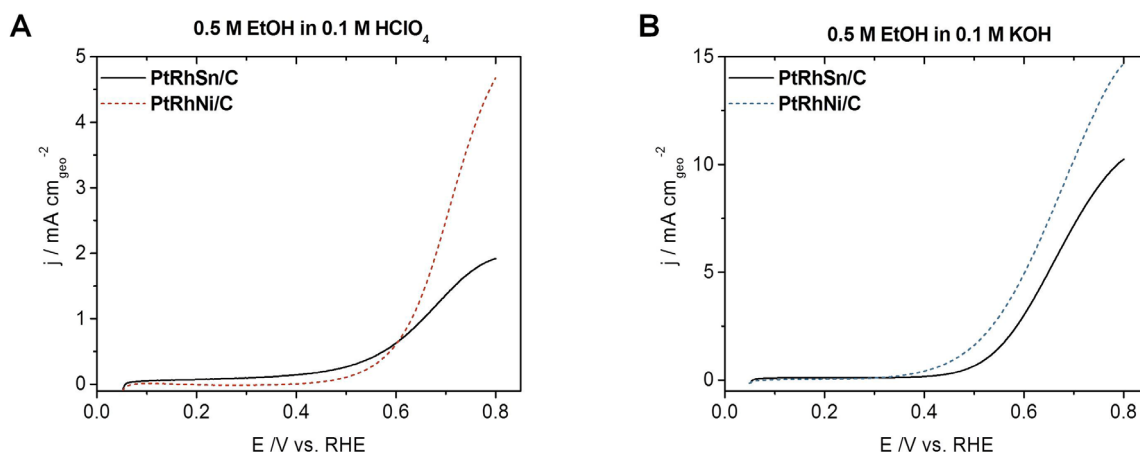


Figure 7.7: Geometric current density polarization curves of the ethanol oxidation reaction (EOR) on PtRhSn/C and PtRhNi/C in acidic media (A, 0.1 M HClO₄) and alkaline media (B, 0.1 M KOH) containing 0.5 M Ethanol. Current densities are normalized by the Geometrical Surface Area of the working electrode (0.196 cm²). Scan rate is 20 mV s⁻¹.

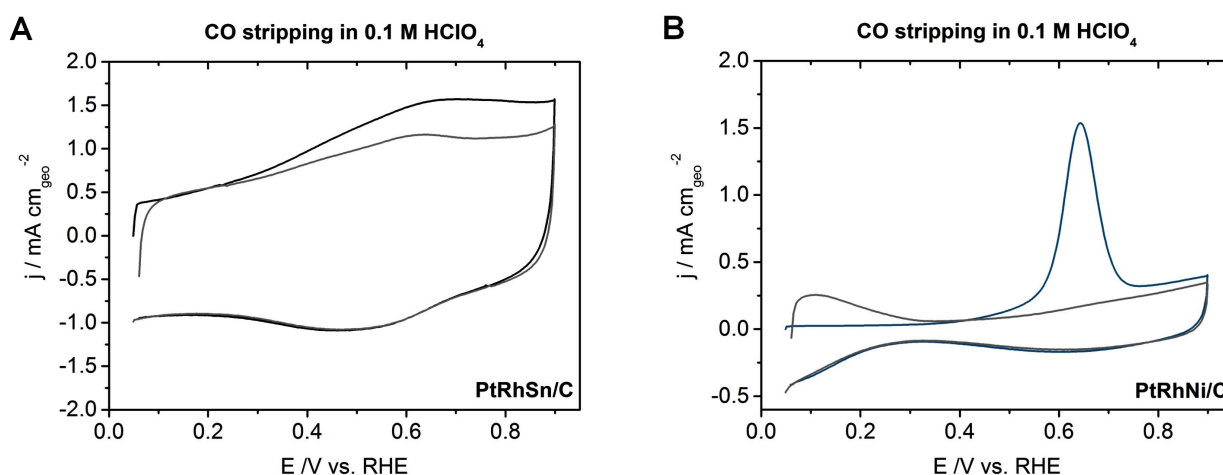


Figure 7.8: Cyclovoltograms of CO stripping on PtRhSn/C (A) and PtRhNi/C (B) in 0.1 M HClO₄. Prior to measurements a monolayer of CO was adsorbed on the surface by bubbling CO in the electrolyte and excess CO removed consecutively by bubbling Ar, both under potential control. Current densities are normalized by the Geometrical Surface Area of the working electrode (0.196 cm²).

Table 7.2: Electrochemical EOR activity of PtRhSn/C and PtRhNi/C catalysts: electrochemical surface area (ECSA), current densities at 0.45 V vs. RHE and 0.60 V vs. RHE during voltammetric scans, and current density at constant 0.45 V vs. RHE after 300 s.

Catalyst	ECSA	j @ 0.45V	j @ 0.80V	j @ 0.45V@300s	electrolyte media
	m ² mg _{Pt} ⁻¹	mA mg _{Pt} ⁻¹	mA mg _{Pt} ⁻¹	mA mg _{Pt} ⁻¹	
1) PtRhSn/C	6.4	12.0	119.2	2.7	0.1 M HClO ₄
	22.2	18.3	605.4	3.7	0.1 M KOH
2) PtRhNi/C	32.0	2.8	378.8	0.7	0.1 M HClO ₄
	19.8	62.6	1071.0	16.3	0.1 M KOH

The ECSA for PtRhNi/C is highest in acidic media with 32.0 m² g_{Pt}⁻¹, similar for both catalysts in alkaline media with 19.8 m² g_{Pt}⁻¹ for PtRhNi/C and 22.2 m² g_{Pt}⁻¹ for PtRhSn/C catalysts, while the value for the Sn-containing catalysts in acidic media is much lower at 6.4 m² g_{Pt}⁻¹, indicating Pt/Rh rich surface for PtRhNi/C catalyst and Sn rich surface for PtRhSn catalyst. Figure 7.3 shows the mass activity of the electrocatalysts in acidic and alkaline media. PtRhNi/C has a forward anodic peak of 1071.1 mA mg_{Pt}⁻¹ in alkaline media, nearly double as high as PtRhSn/C in alkaline media with 605.4 mA mg_{Pt}⁻¹ and three times as high as the peak in acidic media. The lowest activity shows PtRhSn/C in acidic media with 119.2 mA mg_{Pt}⁻¹. The decrease in the onset anodic potential indicates the enhancement in the kinetics of the ethanol oxidation reaction and can also hint for an earlier C-C bond break. These results validate that the novel PtRhNi/C nanoparticle catalyst shows high catalytic activity towards ethanol electrooxidation in both alkaline and acid media.

To date, the results have plausibly been explained by the ability of Ni(OH)_x phases, which form on the surface facets of Ni-containing bulk phases, to act as efficient oxygen-donating entities.^{53,121,169,170} Subbaraman *et al.* already demonstrated that the addition of Ni(OH)₂ to a platinum electrode surface manifests a significant increase in hydrogen evolution reaction (HER) activity, owing to a bifunctional effect, where edges of Ni(OH)₂ clusters promote the dissociation of water and the formation of intermediates, which can then adsorb on the nearby Pt surfaces.¹⁷¹ Consistent with this explanation is the reduced EOR activity at 0.45 V vs. RHE in acid media, where Ni(OH)_x phases gradually leach from the top surface; in contrast, the EOR performance in alkaline media is greatly enhanced because of the stability of Ni(OH)_x phases under these conditions. The superior EOR activity of the PtRhNi

catalyst at high overpotentials (+0.80 V vs. RHE) can be explained by the enhanced presence of surface active oxygenates, such as OH, which help segregate Ni(OH)_x to the surface solutions.^{106,121,172]} Although the general beneficial effect of Rh for C-C bond splitting has been well documented,^{111,121,160} the comparison of PtRhSn/C and PtRhNi/C shows that the oxygen-donating effect of Ni versus Sn appears to be enhanced and, thus, leads to higher activities for the Ni-containing systems. The PtRhSn/C catalyst displayed three times higher current densities at +0.80 V in acidic media than a similar PtRhSnO₂/C catalyst¹⁵² and an earlier reported PtRhSn catalyst with the same 3:1:4 ratio.⁶¹ Brouzgou *et al.* compared a variety of DEFC anode catalysts with increasing Pt loadings on the working electrode surfaces and established a certain region between 0.1 - 1.0 mA cm_{Pt}²@0.70 V vs. RHE in which most of the reported catalyst to date belonged.⁹² PtRhSn/C already lies within the region (0.10 mA cm_{Pt}²) and PtRhNi/C outperforms it (0.21 mA cm_{Pt}²), as does a previously reported PtRhSnO₂/C catalyst from Kowal *et al.* (0.19 mA cm_{Pt}²).⁵ The PtRhNi/C catalyst also outperformed a binary PtNi EOR electrocatalyst in alkaline media reported by Soundararajan *et al.*⁶³

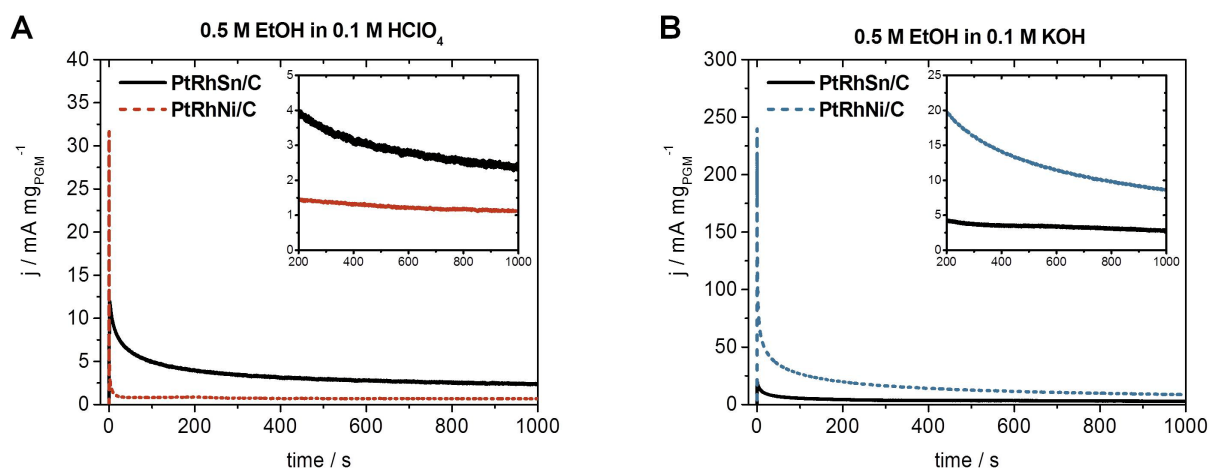


Figure 7.9: Potentiostatic chronoamperometry for the electrocatalytic ethanol oxidation reaction (EOR) on PtRhSn/C and PtRhNi/C at $E = 0.45$ V vs. RHE in A: acidic media (0.1 M HClO₄) and B: alkaline media (0.1 M KOH) with 0.5 M Ethanol. Current densities are normalized by the mass of Pt present on the working electrode.

The stability of both electrocatalysts was investigated through CA measurements at $E = 0.45$ V vs. RHE (Figure 7.9). PtRhSn/C shows similar current density values after 300 s in both electrolytes, whereas PtRhNi/C shows only very small mass activity in acidic media, but with 19 mA mg_{PGM}⁻¹, which is ten times as high compared to all other measurements in alkaline media. It is clearly shown that the Ni-containing ternary alloy electrocatalyst has excellent durability towards ethanol electrooxidation in alkaline media, but its stability in acidic media is lower, owing to Ni(OH)_x

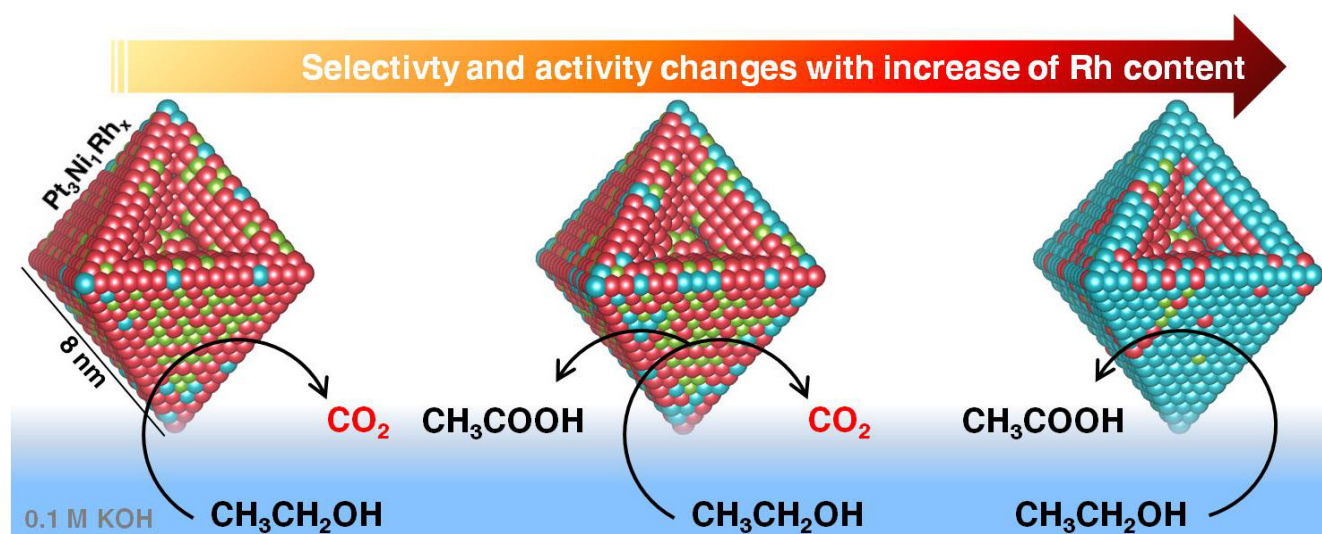
dissolution in acidic media. All results confirm that PtRhNi/C possesses excellent catalytic performance towards ethanol electrooxidation, especially at higher potentials in alkaline media, and presents great promise for future applications in DEFCs.

7.4. Conclusions

We have presented the successful synthesis of an fcc single-phase PtRhNi/C nanoparticle catalyst, discussed its structural characterization, and contrasted its electrocatalytic activity towards ethanol electrooxidation with a state of art Pt-Rh-Sn benchmark catalyst. The EOR activity of the PtRhNi/C material was significantly higher than that of a Niggliite-type PtRhSn/C catalyst or similar electrocatalysts reported in literature. We are confident that the family of Ni-containing PtRh EOR electrocatalysts will spark interest in theoretical materials-by-design approaches and will be a promising catalyst lead structure for further-improved DEFC catalysts, as well as for catalysts to be used in the oxidation of liquid small organics in general. Future research will focus on the product distribution and mechanistic activity--structure relations of these novel PtRhNi EOR electrocatalysts.

8. Exceptional early onset potential for C-C bond breaking on highly active shaped $\text{Pt}_3\text{Ni}_1\text{-Rh}_x/\text{C}$ alloy nanoparticles as novel electrocatalysts for the Ethanol Oxidation Reaction in alkaline media

This chapter presents controlled Pt-Ni-Rh octahedral electrocatalysts with excellent stability by controlling the reduction process of metal precursors in the presences of carbonyl species. This electrocatalysts show previously unachieved onset potentials as early as 0.1 V vs. RHE while being highly selective towards the complete oxidation towards CO_2 . This phenomenal ability to break the carbon bond at such low overpotential near the reversible potential of the anodic complete oxidation of ethanol has not been achieved with existing state of the art catalysts. In situ electrochemical ATR studies indicate that changes in low Rh content of the highly crystalline octahedral $\text{Pt}_3\text{Ni}_1\text{Rh}_x$ are crucial for this electrocatalysts activity.



8.1. Abstract

Ethanol in direct liquid fuel cells is an almost ideal source of sustainable energy. Efficient electrocatalytic material research for its oxidation has to deal with a complicated reaction mechanism, i.e. the need for C-C bond breaking. High activity and selectivity are both desired in unison while avoiding poisoning effects due to possible organic byproducts. We have developed for the first time shape-controlled *Pt-Ni-Rh* octahedral electrocatalysts with excellent current yields that show previously unachieved onset potentials as early as 0.1 V vs. reversible hydrogen electrode, while being highly selective to complete oxidation towards CO₂. This phenomenal ability to break the carbon bond at such low overpotential near the reversible potential has not been achieved with existing state of the art catalysts. Our comprehensive characterization and *in situ* electrochemical ATR studies indicate that the formation of a ternary surface site ensemble around the octahedral $Pt_3Ni_1Rh_x$ nanoparticles is crucial for this electrocatalyst activity.

8.2. Introduction

The conversion of ethanol in direct ethanol fuel cells (DEFCs) directly into electrical energy has been a subject of intensive studies for fundamental and practical applications as power sources (e.g., the development of compact portable power, as well as electric vehicle range extenders operating at high temperatures).⁷⁻¹⁰ As a fuel, ethanol has high volumetric and gravimetric energy density (8 kWh kg⁻¹), good energy efficiency, and offers easy handling, storage and transportation, in contrast to gaseous fuels.¹¹ Its low toxicity and biocompatibility, in combination with its availability from renewable resources makes ethanol an almost ideal fuel. The ethanol oxidation reaction (EOR), however, is often incomplete, resulting in a number of byproducts other than CO₂. This is due to difficulties in C-C bond cleavage and, to some extent, to the formation of CO-intermediates leading to poisoning of the active sites on the catalyst.²⁻⁶ The complete EOR involves 12 electrons per molecule, while partial oxidation leads to byproducts such as acetic acid or acetaldehyde, which reduces the Faradaic efficiency of the anodic side of DEFCs. Alloying Pt with highly oxophilic transition metals such as Rh, Ni or Sn has been a promising strategy to modify the electrocatalytic surface properties of Pt in order to supply active oxygen-containing species, such as OH, which readily oxidize adsorbed molecular fragments while reducing the cost of the catalyst considerably.^{2,37,38,40,107,162,173,174} The oxophilic component is assumed to be present as an oxide species on the surface of the operating catalyst in order to achieve this goal.

8.3. Results and discussion

Higher electrocatalytic activities are to be expected for polyhedral shapes in comparison to their unshaped counterparts, since polyhedral surface facets provide better preconditions for the formation of ordered active surface site ensembles.¹⁷⁵ In order to elucidate the beneficial shape-controlling effects for electrocatalysts, octahedral Pt-Ni-Rh with fixed Pt:Ni ratios and different Rh contents ($Pt_3Ni_1Rh_x\text{-oct/C}$) in the form of supported nanoparticles were prepared using a wet-chemical approach with metal carbonyls present during the reduction process using a mixture of oleylamine and oleic acid as solvents, where the atomic ratio of Pt:Ni:Rh was 3:1:x and x was varied between the equivalent of 1 and 6 atomic %. The bulk composition of the resulting $PtNiRh\text{-1/C}$, $PtNiRh\text{-3/C}$ and $PtNiRh\text{-6/C}$ was controlled by adjusting the initial Pt, Ni and Rh precursor ratios. The high Pt content was chosen to ensure sufficient active surface site formation and to determine the influence of changes in the minimal amounts of Rh in terms of selectivity to different ethanol oxidation pathways. The bulk composition and metal loading, which were determined by inductively coupled plasma (ICP) optic spectroscopy, proved to be close to the desired nominal values (Table 8.1).

Table 8.1: Size, molar composition and metal weight loading of the supported $PtNiRh\text{-oct/C}$ electrocatalysts.

Catalysts	Atomic ratio (Pt:Ni:Rh)	Total metal loading wt%	Average particle size (nm)	
			as prepared	after 1 st EOR scan
1) $PtNiRh\text{-1/C}$	71:28:1	25	8.0 ± 1.0	7.9 ± 1.2
2) $PtNiRh\text{-3/C}$	77:20:3	31	7.9 ± 1.2	7.7 ± 1.2
3) $PtNiRh\text{-6/C}$	67:27:6	21	7.3 ± 1.2	7.2 ± 1.1

Transmission electron microscopy (TEM) images of the electrocatalysts (Figure 8.1) showed that in all three samples the nanoparticles were well distributed across the carbon support and largely regular octahedral in shape, enclosed by eight {111} facets. Mean edge lengths, which were estimated from TEM, derived edge length histograms inserted in the TEM micrographs in Figure 8.1 and listed in Table 8.1, vary in a narrow range from 7.2 ± 1.1 nm to 8.0 ± 1.0 nm. The higher magnification images reveal a lattice spacing of 0.23 nm, which can be attributed to Pt fcc (111) in all samples. An additional lattice spacing of 0.19 nm in samples $PtNiRh\text{-1/C}$ and $PtNiRh\text{-6/C}$ can be attributed to Pt fcc (200).

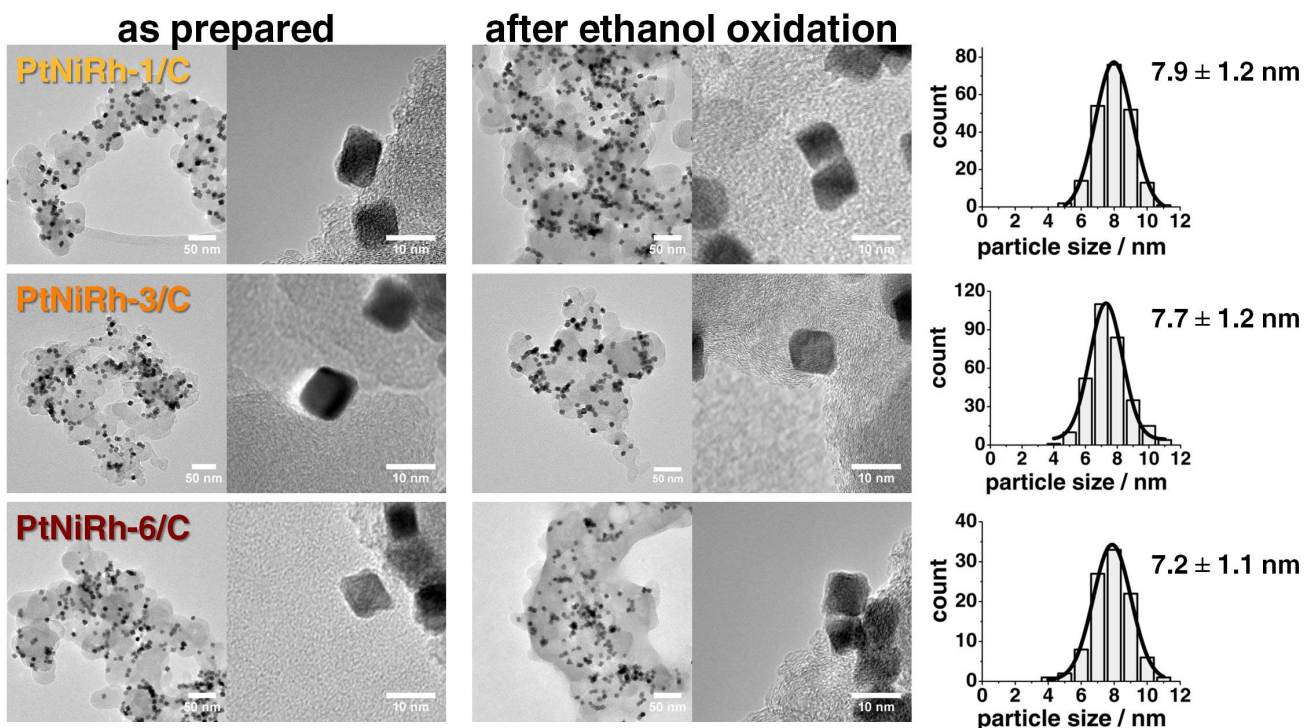


Figure 8.1: TEM micrographs and edge length distribution histograms of *PtNiRh-oct/C* electrocatalysts as prepared (top) and after one scan in 0.5 M EtOH in 0.1 M KOH (bottom).

Figure 8.2 a-c shows atomic-scale high angle annular dark field scanning TEM (HAADF)/ (STEM) images of the different $Pt_3Ni_1Rh_x-oct/C$ catalyst nanoparticles after the first EOR cycle, approximately oriented along $\langle 110 \rangle$, with octahedral morphologies. Figure 8.2 d-i shows corresponding energy dispersive x-ray spectroscopy (EDX) composition maps. For all nanoparticles and all compositions, the EDX maps clearly confirm an enrichment of Ni at the facets and the presence of a Pt-rich frame, which can be identified by a Pt-rich strip in the center of each particle (Figure 8.2 d-f). The Pt and Ni elemental distribution in each particle clearly corresponds to that reported in earlier work.^{53,176} Shape-selective nanocatalysts offer activity benefits based on structural sensitivity and high surface area. We recently showed that octahedral PtNi nanoparticle catalysts show exceptional oxygen reduction activity gain over state-of-the-art unshaped Pt electrocatalysts.⁶⁵ We followed the morphological and compositional evolution of shaped Pt alloy octahedral nanoparticles in electrochemical environments and correlated it with their exceptional catalytic activity, finding that octahedra preferentially leach in their facet centers and evolve into ‘concave octahedra’.⁵³

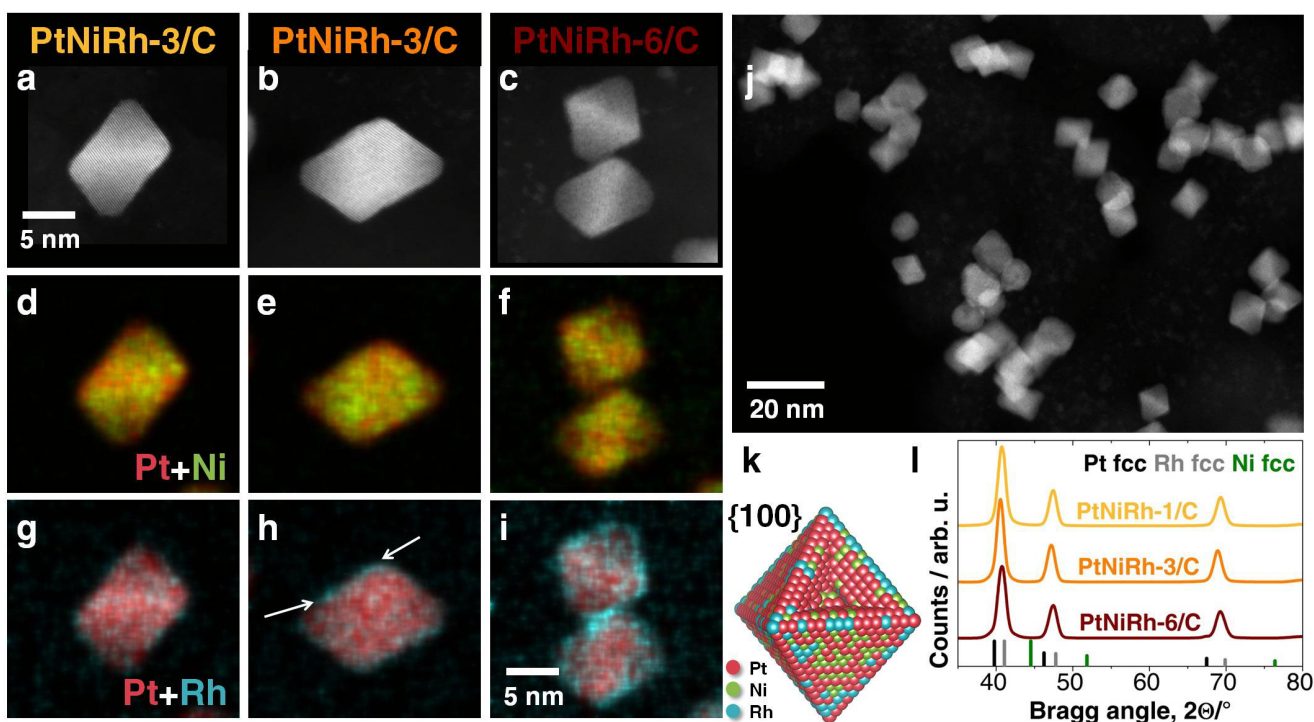


Figure 8.2: Atomic-scale Z-contrast STEM images and composition profile analysis of $Pt_3Ni_1Rh_x$ -oct/C octahedral nanoparticles. HAADF STEM images (a-c,j) and EDX composition map analysis (d-i) after the first EOR scan of $PtNiRh-1/C$ (a,d,g), $PtNiRh-3/C$ (b,e,h) and $PtNiRh-6/C$ (c,f,i) octahedral nanoparticles oriented close to $\langle 110 \rangle$. (j) Overview HAADF STEM image of $PtNiRh-6/C$. (d-f) EDX composition map showing the distribution of Pt (red) and Ni (green) and (g-i) Pt (red) and Rh (blue), respectively. (k) Ball schematic sketch shows the Rh-rich shell and mixed Ni, Rh and Pt core (l) Cu K_α XRD pattern of the three $Pt_3Ni_1Rh_x$ -oct/C electrocatalysts shown alongside the expected peak positions for pure fcc Pt, pure fcc Rh and pure fcc Ni, indicated using black, grey and green lines, respectively.

EDX composition maps for $PtNiRh-1/C$ nanoparticles with the lowest Rh content show a speckled distribution of Rh over the nanoparticle, which gives rise to isolated Rh-rich patches (Figure 8.2g). With a higher Rh content for $PtNiRh-3/C$, an accumulation of Rh at the surfaces of the octahedral particles is observed (Figure 8.2h, highlighted by arrows). For $PtNiRh-6/C$, i.e. the particles with the highest Rh content, the EDX maps indicate the formation of a compact Rh-rich shell around each octahedral particle (Figure 8.2i). The formation of a compact Rh-rich shell is more obvious for slightly smaller nanoparticles (Figure 8.3). HAADF/STEM images acquired before the first EOR scan are shown in Figure 8.4 and an overview over all samples is given in Figure 8.5. The compositions of the individual particles in Figure 8.2, measured using EDX are $Pt_{71}Ni_{25}Rh_4$, $Pt_{72}Ni_{23}Rh_5$ and $Pt_{66}Ni_{23}Rh_{11}$, respectively, in close agreement with the ICP results for the bulk samples. The EDX composition maps indicate that the Pt and Ni distribution is the same as after the first EOR scan, i.e. they indicate the formation of Ni-rich facets and a Pt-rich frame in each particle. Remarkably, this means that the

nanocatalysts, which are uniform in size and shape, show high tolerance towards the reaction conditions, proving them to be very suitable for applications in DEFCs.

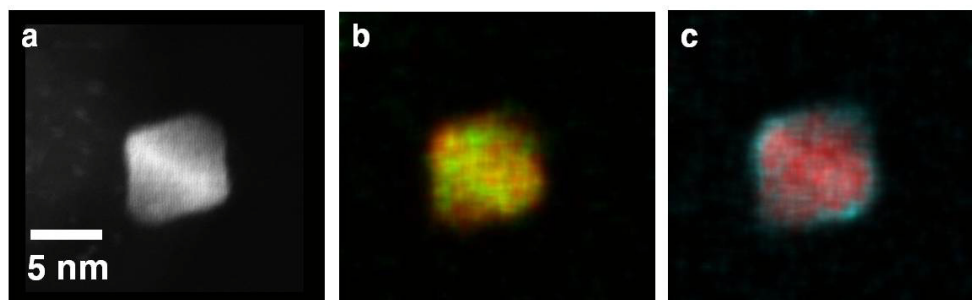


Figure 8.3: Atomic-scale composition profile analysis of PtNiRh-6/C octahedral nanoparticles. HAADF STEM image (a) and EDX composition map analysis (b-c) after the first EOR scan of a *PtNiRh-6/C* octahedral nanoparticle (6.5 nm). (b) EDX composition map showing the distribution of Pt (red) and Ni (green) and (c) Pt (red) and Rh (blue), respectively.

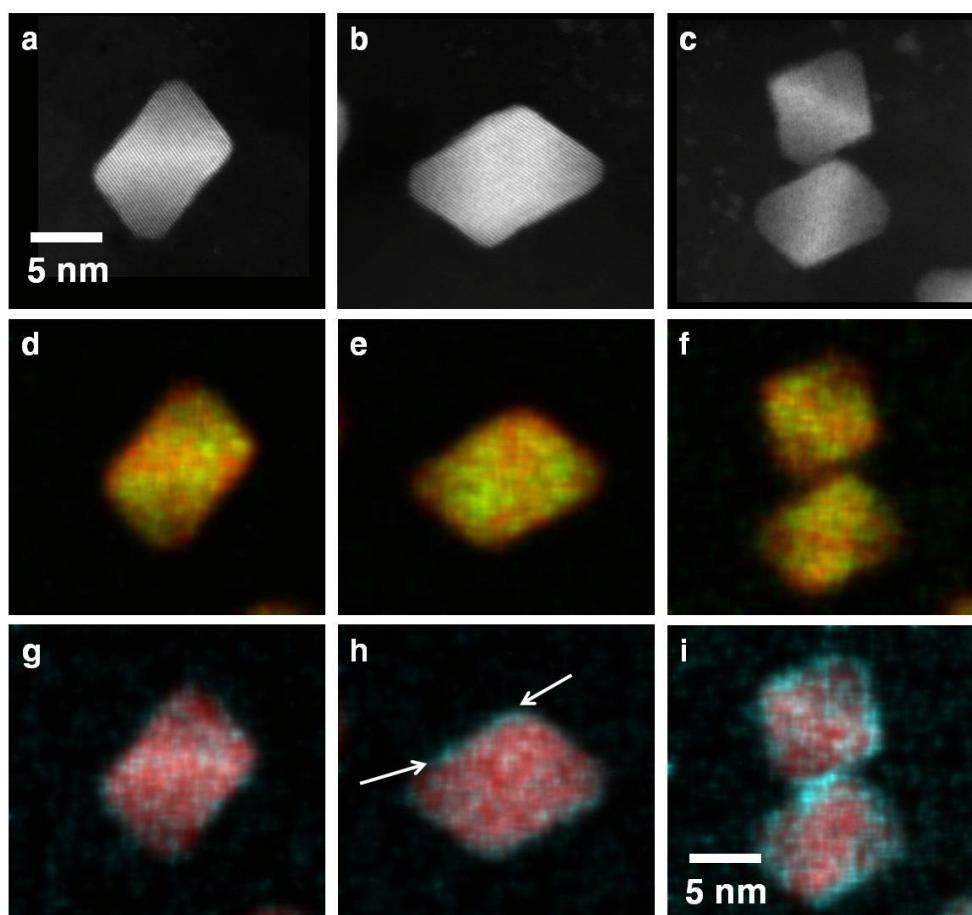


Figure 8.4: Atomic-scale Z-contrast STEM images and composition profile analysis of as-prepared $Pt_3Ni_1Rh_x$ -oct/C octahedral nanoparticles. HAADF STEM images (a-c) and EDX composition map analysis (d-i) of *PtNiRh-1/C* (a,d,g), *PtNiRh-3/C* (b,e,h) and *PtNiRh-6/C* (c,f,i) octahedral nanoparticles oriented close to $\langle 110 \rangle$. (d-f) EDX composition map showing the distribution of Pt (red) and Ni (green) and (g-h) Pt (red) and Rh (blue), respectively.

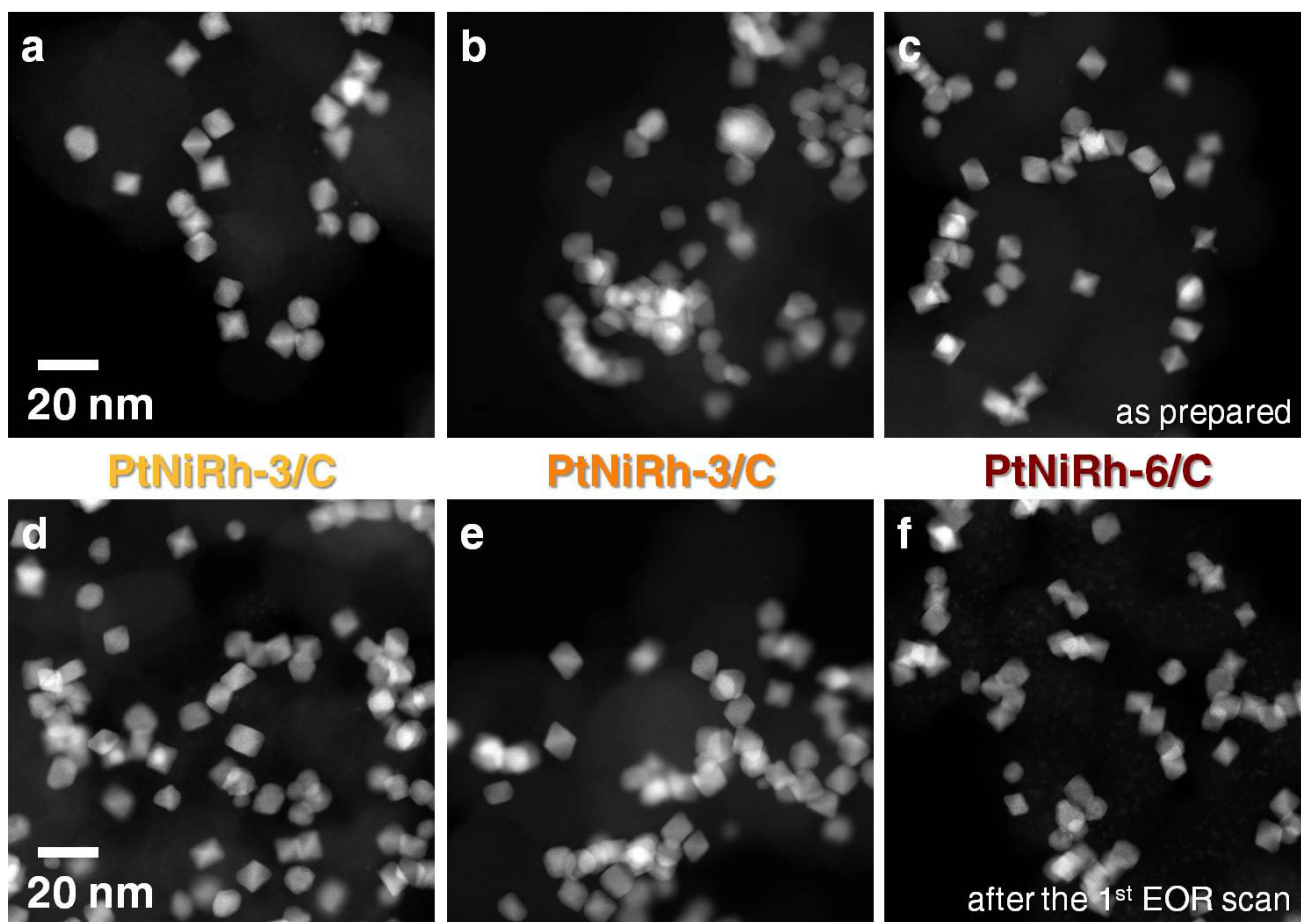


Figure 8.5: Comparison of HAADF STEM images, as prepared and after the first EOR scan on $Pt_3Ni_1Rh_x$ -oct/C octahedral nanoparticles. HAADF STEM images before (a-c) and after (d-f) the first EOR scan for $PtNiRh-1/C$ (a,d), $PtNiRh-3/C$ (b,e) and $PtNiRh-6/C$ (c,f,) mainly octahedral nanoparticles.

All fitted x-ray diffraction (XRD) powder patterns of all $Pt_3Ni_1Rh_x$ -oct/C specimens show relatively broad Bragg peaks, typical for nano-sized particles with limited structural coherence (Figure 8.21). There are no superlattice peaks discernible below $2\theta=35^\circ$, indicating a substitutional solid solution alloy. All of the electrocatalysts show a single-phase face centered cubic diffraction pattern; as also revealed by the lattice spacing visible in micrographs. The diffraction peaks are consistent with an atomic mixture of the three metals, as they lie between the reflections expected for Pt, Rh and Ni. No reflections for pure metallic Pt, Rh or Ni are observed, indicating alloy formation for all three compositions. However, as a result of the slightly asymmetric diffraction peaks of the $Pt_3Ni_1Rh_x$ -oct/C catalysts, the presence of a second fcc phase cannot be completely excluded. The theoretical $2\theta_{theo}$ values listed in Table 8.2, which are derived from the atomic ratio of Pt:Ni from ICP results (Table 8.1), are in good agreement with the experimental $2\theta_{exp}$ values for all of the samples and (hkl) reflections.

Table 8.2: Comparison of the experimental 2θ values with theoretical 2θ values for all *PtNiRh-oct/C* electrocatalysts deriving from Vegard's law for fcc phases.^{177,178}

Catalyst	(hkl)	d_{theo} [Å]	$2\theta_{\text{theo}}$	$2\theta_{\text{exp}}$
1) PtNiRh-1/C	(111)	2.200	41.0	40.7
	(200)	1.905	47.7	47.4
	(220)	1.347	69.8	69.3
2) PtNiRh-3/C	(111)	2.217	40.7	40.5
	(200)	1.920	47.3	47.2
	(220)	1.358	69.1	69.9
3) PtNiRh-6/C	(111)	2.199	41.0	40.7
	(200)	1.904	47.7	47.5
	(220)	1.346	69.8	69.3

The catalytic activity of the *Pt₃Ni₁Rh_x-oct/C* electrocatalysts towards ethanol electrooxidation in alkaline media was evaluated to correlate the catalyst structure and composition with electrocatalytic EOR polarization behavior. Linear sweep voltammograms (LSVs) recorded in ethanol containing electrolyte (Figure 8.6a, b) revealed high activity towards the EOR for all of the *Pt₃Ni₁Rh_x-oct/C* electrocatalysts. Measurements of the reduction charge of hydrogen under potential deposition (H_{UPD}) from cyclic voltammograms (CVs) in pure electrolyte were used to estimate the electrochemically active surface area (ECSA) values for the three catalysts based on the charge density for the formation of a fully covered Pt-H monolayer ($210 \mu\text{C}/\text{cm}^2$).¹⁴⁹ ECSA values are highest for *PtNiRh-6/C* with $31.3 \text{ m}^2 \text{ g}_{\text{Pt}}^{-1}$, followed by *PtNiRh-3/C* with $24.0 \text{ m}^2 \text{ g}_{\text{Pt}}^{-1}$ and lowest for *PtNiRh-1/C* with $19.6 \text{ m}^2 \text{ g}_{\text{Pt}}^{-1}$. Figure 2a shows the specific activity of the electrocatalysts in alkaline media: *PtRhNi-3/C* has the highest forward anodic peak of $13.0 \text{ mA cm}_{\text{ECSA}}^{-2} \mu\text{g}_{\text{Pt}}$, nearly as high as that for *PtNiRh-1/C* with $12.2 \text{ mA cm}_{\text{ECSA}}^{-2} \mu\text{g}_{\text{Pt}}$ and one order of magnitude lower than that for *PtNiRh-6/C* with $7.0 \text{ mA cm}_{\text{ECSA}}^{-2} \mu\text{g}_{\text{Pt}}$.

All of the ECSA values are listed in detail in Table 8.3, alongside specific activity values for different potentials and after 1800 s. The decrease in the onset anodic potential indicates an enhancement in the kinetics of the ethanol oxidation reaction and also suggests an earlier C-C bond break. These results indicate that the novel octahedral *Pt₃Ni₁Rh_x-oct/C* nanoparticle catalyst shows high catalytic activity towards ethanol electrooxidation in alkaline media. This behavior is plausibly explained by the ability

of Ni(OH)_x phases, which form on the surface facets of the Ni-containing bulk phases, to act as efficient oxygen-donating entities.^{53,121,169,170} The addition of Ni(OH)₂ to a Pt electrode surface results in a significant increase in hydrogen evolution reaction (HER) activity due to a bifunctional effect, whereby the edges of Ni(OH)₂ clusters promote the dissociation of water and the formation of intermediates, which can then adsorb on nearby Pt surfaces.¹⁷¹

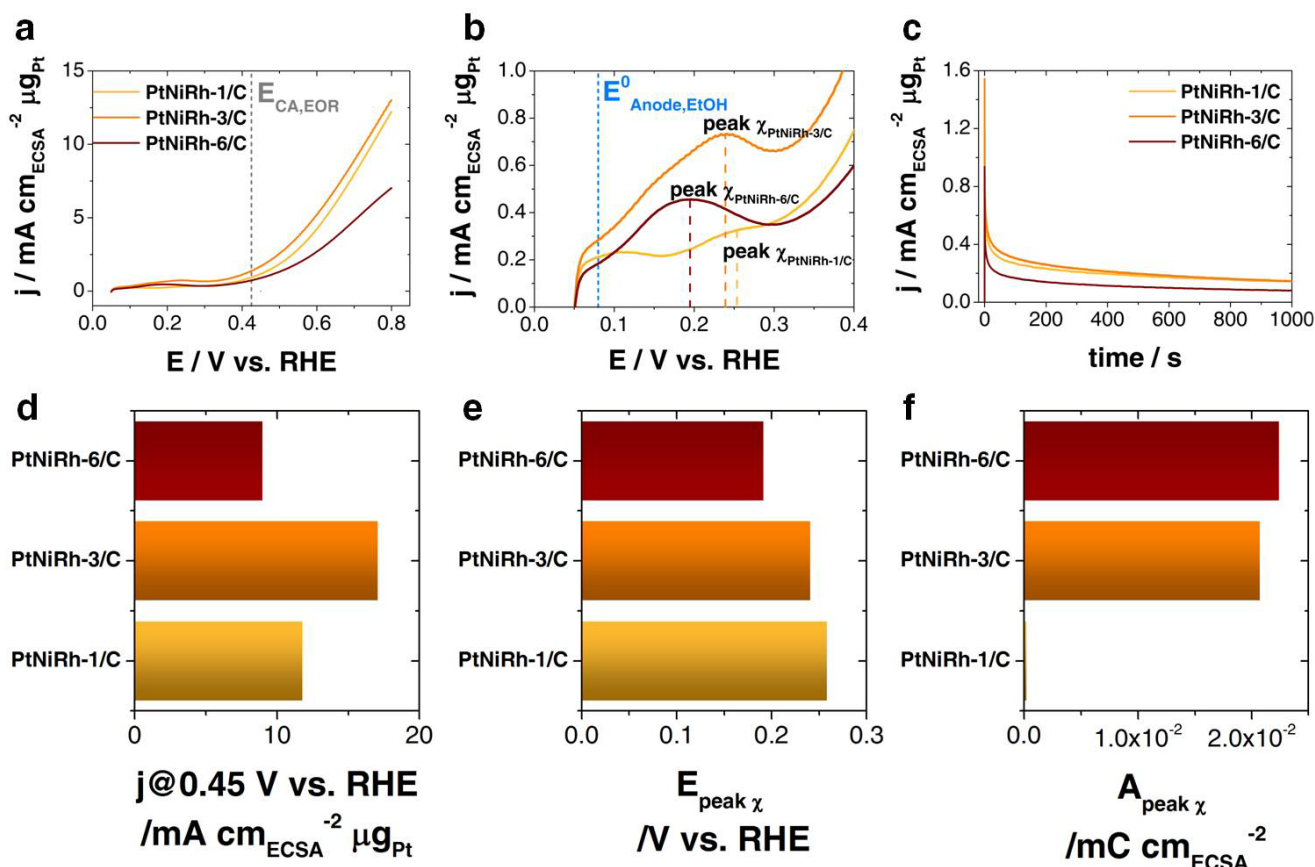


Figure 8.6: Electrochemical studies on carbon supported $Pt_3Ni_1Rh_x$ -oct/C octahedral catalysts. First forward scan (a,b) with a scan rate of 20 mV s^{-1} and potentiostatic chronoamperometry (c) at 0.45 V vs. RHE of the ethanol oxidation reaction (EOR) on the three $Pt_3Ni_1Rh_x$ -oct/C electrocatalysts in 0.1 KOH containing 0.5 M ethanol. Current densities are normalized by the ECSA from H_{UPD} in pure electrolyte and the amount of Pt present on the working electrode. The vertical grey dashed line marks the potential of technical interest used for the chronoamperometric experiment in c. Comparison of the EOR specific activity at 0.45 vs. RHE during the first forward scan (d), the corresponding potential to the early onset peak χ maximum (e) and the respective charge of peak χ (f) of the three $Pt_3Ni_1Rh_x$ -oct/C octahedra.

The stability of the electrocatalysts was investigated using chronoamperometric measurements at $E = 0.45$ V vs. RHE (Figure 8.6c). All of the $Pt_3Ni_1Rh_x$ -oct/C electrocatalysts showed excellent durability towards the EOR in alkaline media. The observed stationary activity after the initial current drop is in good agreement with the activity ranking of the electrocatalysts in the potentiodynamic measurements at the equivalent potential (Figure 8.6d). The $Pt_3Ni_1Rh_x$ -oct/C octahedral

electrocatalysts all outperformed corresponding spherical *PtRhNi/C* electrocatalysts¹⁶⁵, indicating that the shape of the catalysts has a decisive influence on the catalytic properties of the surface site ensembles. Based on specific activity, *PtNiRh-6/C* shows a factor of four times higher activity at the potential of technical interest (0.45 V vs. RHE) and still double the activity at the end potential of the first forward scan. At this point, the activity is three times the activity reported for a binary PtNi EOR electrocatalyst.⁶³ In summary, all electrochemical results confirm that octahedral *Pt₃Ni₁Rh_x-oct/C* exhibits excellent catalytic performance towards the EOR and, therefore, offers great promise for applications in DEFCs in the future.

Table 8.3: Electrochemical EOR activity of *PtNiRh-oct/C* catalysts: electrochemical surface area (ECSA), current densities at 0.45 V vs. RHE and 0.80 V vs. RHE during voltammetric scans, and current density at constant 0.45 V vs. RHE after 1800 s.

Catalyst	ECSA	j @ 0.45V	j @ 0.80V	j @ 0.45V@1800s
	m ² g _{Pt} ⁻¹	mA cm _{ECSA} ⁻² μg _{Pt}	mA cm _{ECSA} ⁻² μg _{Pt}	mA cm _{ECSA} ⁻² μg _{Pt}
1) PtNiRh-1/C	19.6	1.2	12.2	0.2
2) PtNiRh-3/C	24.0	1.7	13.0	0.2
3) PtNiRh-6/C	31.3	0.9	7.0	0.1

Even more interestingly, electrochemical investigation of the ethanol oxidation reaction on the octahedral *Pt₃Ni₁Rh_x-oct/C* surfaces revealed exceptionally early onset potential features near the reversible oxidation potential for ethanol oxidation (Figure 8.6b, $E^0_{\text{Anode}} \sim 0.08$ V vs. RHE, pH 14)¹⁷⁹ in the first forward scans (hereinafter: *peak* χ), which was not observed in similar investigations on spherical nanoparticle *PtRhNi/C* catalysts.¹⁶⁵ To the best of our knowledge, such early onset potentials for ethanol oxidation with such low overpotentials have not been reported to date. Although it already occurs in the H_{UPD} region, it can be ruled out that *peak* χ originates from the underpotential deposition of hydrogen on the catalyst surface. This is because, in general, hydrogen features are inhibited on all catalysts that are active for the ethanol oxidation reaction due to the strong adsorption of ethanol molecules on the active sites.¹⁸⁰ Figure 8.6d-f summarizes the EOR activity at 0.45 V vs. RHE, the potential of the maximum of the onset feature in the first EOR scan, as well as the area under that feature. The first scan onset feature appears at earlier potentials and shows a higher corresponding area under the current density curve with higher amounts of Rh in the catalyst (*PtNiRh-6/C* > *PtNiRh-3/C* >

PtNiRh-1/C). This behavior does not correlate directly with the overall EOR activity; the *PtNiRh-3/C* electrocatalyst shows the highest activity for the EOR, indicating a maximum for a certain atomic mixture of Pt, Ni and Rh on the surface.

The potential-dependent selectivity for this variety of organic products on such exceptionally active ethanol oxidation electrocatalysts can best be studied using *in situ* vibrational spectroscopy techniques, such as *in situ* Fourier Transformation Infrared (FTIR) spectroscopy. Our modified attenuated total reflection (ATR) FTIR cell setup allows the investigation of supported nanoparticle ink films almost identical with standard rotating disc electrode films. The ink solution of supported electrocatalysts is deposited directly onto the ATR prism, avoiding intensity loss due to the lack of a sputtered layer of a conducting material such as Au. The electrochemical connection is made via a carbon cloth material that provides a reservoir of electrolyte over the catalyst, minimizing mass transport limitations and polarization effects, which are common problems of external reflection thin film configurations. We correlated activity with selectivity towards certain pathways of the ethanol oxidation reaction, by following the selectivity of the three $Pt_3Ni_1Rh_x$ -*oct/C* electrocatalysts.

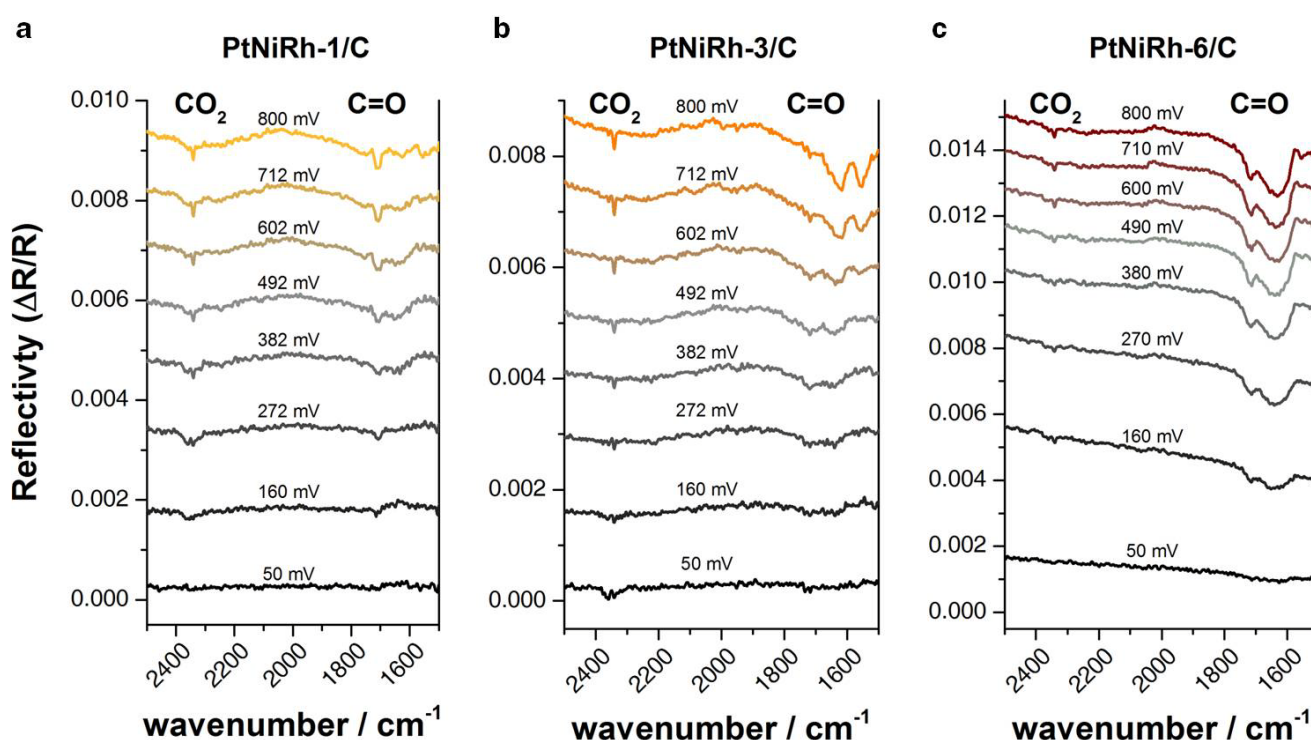


Figure 8.7: *In situ* FTIR ATR spectra for identifying the intermediates and products of ethanol oxidation on supported $Pt_3Ni_1Rh_x$ -*oct/C* octahedral electrocatalysts. *In situ* FTIR ATR spectra recorded during the electrooxidation of ethanol on (a) *PtNiRh-1/C*, (b) *PtNiRh-3/C* and (c) *PtNiRh-6/C*. 128 interferograms (resolution 4 cm^{-1}) were collected and combined for each spectrum. The working electrode potential ranges during the first linear sweep voltammetry with a scan rate of 1 mVs^{-1} in 0.5 M EtOH in 0.1 M KOH are indicated in the figures.

Figure 8.7 shows recorded spectra from all three catalysts during the first forward scan of ethanol oxidation in alkaline media. Carbon dioxide (CO_2), acetic acid (CH_3COOH) and acetaldehyde (CH_3CHO) are the potential products deriving from ethanol oxidation. According to previous studies, the 1410 and 1554 cm^{-1} bands can be attributed to $\nu_s(\text{OCO})$ of bridge-bonded acetate and $\nu_{as}(\text{OCO})$ of solution acetate, respectively; the 1354 cm^{-1} band is assigned to the in-plane bending vibrations of the $-\text{CH}_3$ group of the adsorbed acetate [$\delta(\text{CH}_3)$], while the $1671\text{--}1844\text{ cm}^{-1}$ band is due to CO_{ad} species [$\nu(\text{CO}_{\text{ad}})$] and the $\nu(\text{C}=\text{O})$ carbonyl vibration is responsible for the observed $\sim 1700\text{ cm}^{-1}$ band.^{21,23,181-184} The negative going reflectivity bands for $\nu(\text{CO}_2) = 2342\text{ cm}^{-1}$ indicate complete oxidation of ethanol while the bands around 1700 cm^{-1} can be attributed to the partial oxidation of ethanol towards acetic acid and acetaldehyde. It is generally accepted that the oxidation of ethanol proceeds via a dual pathway mechanism, as shown in Figure 8.8.^{5,16-28}

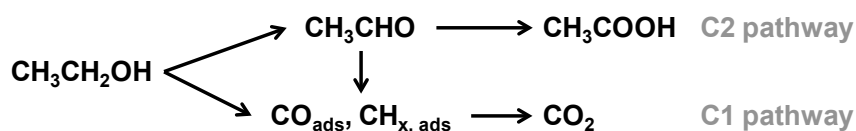


Figure 8.8: Intermediates and products occurring on the anodic side of the direct ethanol fuel cell. Schematic representation of the dual pathway mechanism for the electrooxidation of ethanol.

Ethanol can be oxidized to C2 structured acetaldehyde and subsequently to acetic acid, transferring only 4 electrons in the process. Acetic acid marks a ‘dead end’ in the mechanism, since its further oxidation is very difficult under ambient conditions.¹⁸ Alternatively, the C-C bond can be broken in ethanol and also in acetaldehyde, yielding adsorbed single C species such as CO_{ads} and $\text{CH}_{x,\text{ads}}$.^{17,29} These species can subsequently be oxidized to CO_2 , yielding 12 electrons in total. The single C adsorbates normally require a high overpotential to be oxidized,^{18,33} thereby reducing the overall efficiency of the reaction. The integrated band intensities can therefore best be attributed to the two different pathways and are correlated in Figure 8.9 with the corresponding first *in situ* forward scan with 1 mVs^{-1} in the electrochemical cell.

The *in situ* scans show the same early onset *peak* χ , as can be observed from the electrochemical testing. *PtNiRh-1/C* shows a very early onset of CO_2 production and nearly no band growth in the C2 pathway region. *PtNiRh-6/C* has a late onset for CO_2 but nearly instant production of C2 pathway products, even at low potentials. The most active *PtNiRh-3/C* catalyst shows an early onset of CO_2 , but not as high a rise in the band area as does the *PtNiRh-1/C*, while also showing an early onset for the production of C2 pathway products. The lowest overall activity for the three electrocatalysts also corresponds with the absence of CO_2 band growth, as can be intuitively explained by the dominance of

the 4 or 2 electron yield per molecule for this pathway, while complete oxidation yields 12 electrons per molecule.

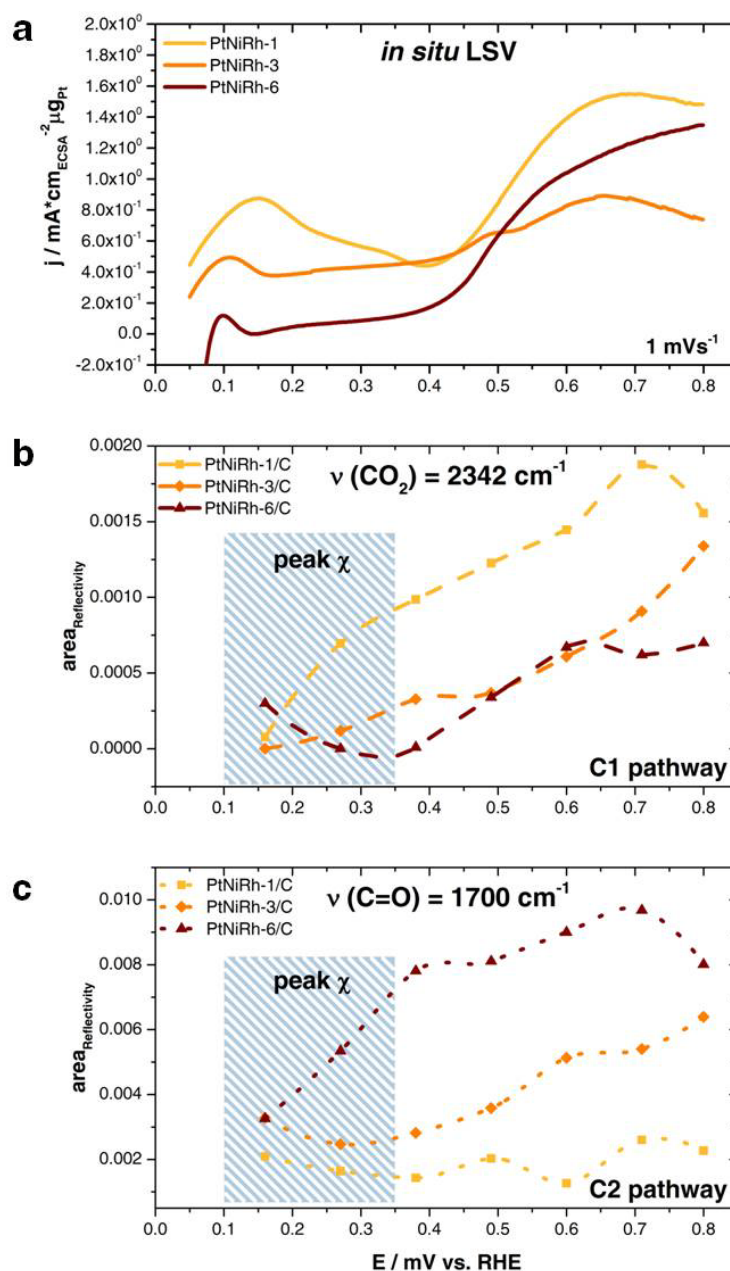


Figure 8.9: Selectivity-activity relationship for ethanol oxidation on supported Pt₃Ni₁Rh_x octahedral electrocatalysts. First *in situ* linear sweep voltammetry scans (a) and corresponding integrated *in situ* FTIR ATR band intensities of (b) CO₂ (2342 cm⁻¹) and (c) partial oxidation pathway for CH₃CHO and CH₃COOH (1700 cm⁻¹) of PtNiRh-*oct*/C electrocatalysts during the electrooxidation of ethanol on PtNiRh-1/C, PtNiRh-3/C and PtNiRh-6/C. 128 interferograms (resolution 4 cm⁻¹) were collected and combined for each spectrum. The working electrode potential ranges during the first linear sweep voltammetry with a scan rate of 1 mVs⁻¹ in 0.5 M EtOH in 0.1 M KOH are indicated in the figures.

Interestingly, the dominance of the complete oxidation of *PtNiRh-1/C* alone cannot account for the highest overall activity; the highest current density yields correlate with surface active sites that can promote both reaction pathways, as in *PtNiRh-3/C*. The second scan electrochemical features show the expected lack of a *peak* χ in the current response, in comparison with the first scan. Both *PtNiRh-1/C* and *PtNiRh-3/C* show C1 pathway onset features between 0.3 and 0.4 V vs. RHE, while *PtNiRh-6/C* still shows only little oxidation towards CO₂. This behavior coincides with the microstructural observation of an already formed Rh-rich shell, which appears to inhibit complete oxidation by blocking important ternary surface site ensembles on the {111} facets that are capable of splitting ethanol effectively at such low overpotentials. Nevertheless, the Rh-rich shell provides a remarkable early onset for the oxidation of ethanol *via* the C2 pathway.

8.4. Conclusions

In summary we found that the successful synthesis of octahedral *Pt₃Ni₁Rh_x-oct/C* electrocatalysts with a designed variation in Rh percentage leads to highly shape-controlled supported nanoparticles. All catalysts show a narrow edge length distribution and high crystallinity as well as good electrochemical activity and stability towards the oxidation of ethanol. *In situ* FTIR studies reveal prevalence for the complete oxidation of ethanol via a C1 pathway for the lowest Rh content, with well distributed ternary surface site ensembles on the octahedral facets, while the C2 pathway dominates for the catalyst with the highest Rh content and an already formed Rh shell. The overall specific activity peaks for *PtNiRh-3/C*, possibly due to the simultaneous occurrence of both reaction pathways. Our study strongly suggests that for a low Rh content, i.e. before the formation of PtNi-alloy-core-Rh-shell octahedra, a higher concentration of active surface site ensembles comprising all three metal components prevails, resulting in the ability to break the C-C bond at exceptionally low overpotentials near the reversible potential of the anodic complete oxidation of ethanol, which could not be achieved with existing state of the art catalysts.

8.5. Experimental

Synthesis of *PtNiRh-oct/C*: Platinum(II)acetylacetonate (Pt(acac)₂, Pt 48% min.), nickel(II)acetylacetonate (Ni(acac)₂, 95.0 %), tungsten hexacarbonyl (W(CO)₆, 97.0 %) and oleic acid (OAc, 90 %) were obtained from Alfa Aesar; rhodium(III)acetylacetonate (Rh(acac)₃, 97.0 %), oleylamine (OAm, 70.0 %) and acetic acid (HA₂, 99.9 %) were obtained from Sigma Aldrich; dibenzylether (Bn₂O, 98.0 %) was obtained from Fluka. All chemicals were used as received. In order

to prepare *Pt-Ni-Rh* octahedral nanoparticles $\text{Pt}(\text{acac})_2$ (0.102 mmol), $\text{Ni}(\text{acac})_2$ (0.234 mmol), $\text{Rh}(\text{acac})_3$ (0.003 mmol, 0.005 mmol, 0.012 mmol), OAm (12 mL) and OAc (8 mL) were added into a 100 ml three-neck-flask under reflux. The reaction mixture was stirred for 5 minutes under nitrogen atmosphere at 60 °C, followed by raising the temperature to 130 °C. At this temperature, nitrogen purging was stopped, $\text{W}(\text{CO})_6$ (0.389 mmol) was added rapidly and the reaction mixture was heated to 230 °C and then stirred for 40 minutes. Then, the reaction mixture was cooled down to room temperature and toluene (10 mL) and ethanol (30 ml) were added to it. The supernatant was removed by centrifugation (7800 rpm for 5 min) and dispersed in toluene (20 mL). The dispersion was added to a dispersion of Vulcan XC 72R (0.04 g) in toluene (20 mL) and sonicated for 1 h. Ethanol (10 mL) was then added and the Pt-Rh-Ni/C catalyst was centrifuged (7800 rpm for 10 min). The resulting particles were added to acetic acid (40 mL) and refluxed for 30 min at 60 °C. After the mixture was cooled, the particles were washed with ethanol (30 mL) three times and dried for 12 h in air.

Electrochemical measurements: Polished glassy carbon working electrodes were coated with 10 μL catalyst ink (4 mg electrocatalyst powder; 2.5 mL of ultrapure water; 0.5 mL isopropanol; 15 μL of 5 wt. % Nafion solution) and measured with a Biologic SP 150 potentiostat in an electrochemical glass cell with Pt wire as counter and a saturated SCE (in KOH) as a reference electrode. The electrolyte was freshly made and purged with nitrogen prior to and during experiments. Current densities were normalized by ECSA and the amount of Platinum present on the electrode surface. The characterization and electrochemical testing protocol for *PtRhNi-oct/C* has been described in detail elsewhere.¹⁶⁵

Scanning transmission electron microscopy (STEM) was performed using a FEI Titan 80-200 (“ChemSTEM”) electron microscope, equipped with a C_s -probe corrector (CEOS GmbH) and a high-angle annular dark field (HAADF) detector. The microscope was operated at 200 kV. In order to achieve “Z-Contrast” conditions, a probe semi-angle of 25 mrad and an inner collection semi-angle of the detector of 88 mrad were used. Compositional maps were obtained with energy-dispersive x-ray spectroscopy (EDX) using four large-solid-angle symmetrical Si drift detectors. For EDX analysis, Pt L, Ni K and Rh L peaks were used. The error of the EDX composition measurement is +/- 2 at.%.

Cu K_α x-ray diffraction (XRD) patterns were collected using a D8 Advance diffractometer (Bruker) equipped with a Lynx Eye Detector and KFL Cu 2K x-ray tube. The diffraction patterns were collected over a 20–80° 2θ range with a step size of 0.05°, dwelling for 10 s at every step. The XRD patterns were analyzed using the MDI Jade 8 software package. Bragg reflection positions were compared with reference XRD patterns (PDF data files, International Center for Diffraction Data). Carbon features were taken out by background subtraction

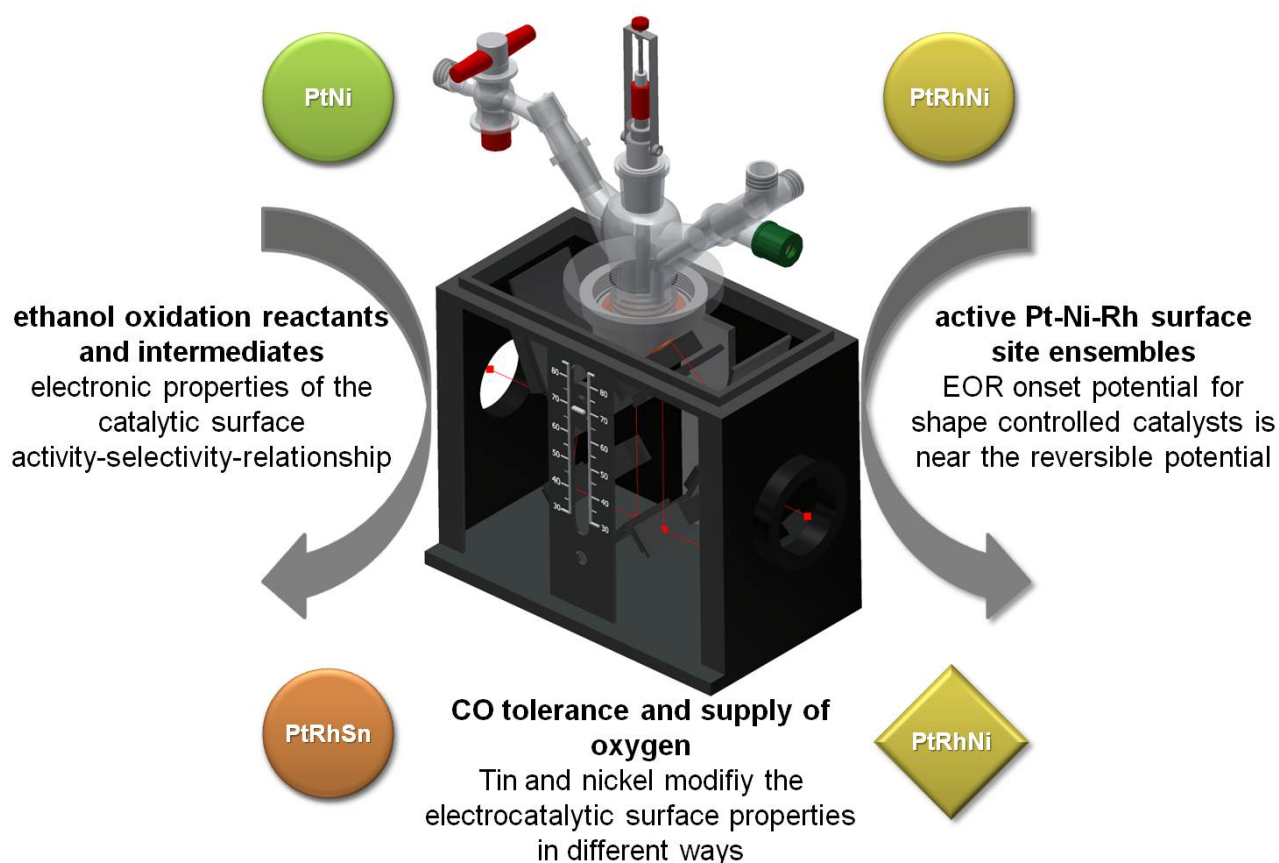
***In situ* ATR FTIR spectroscopy** was used to investigate the IR bands of adsorbed species on the catalyst surface under potential control. The spectra were collected in a custom-made glass cell with a Bruker Vertex 70v FTIR spectrometer equipped with an MCT detector cooled with liquid nitrogen. A built-in gold mesh was used as counter electrode and a real RHE for reference. All *in situ* electrochemical measurements were controlled using a Metrohm Autolab PGSTAT204 potentiostat. An unpolarized beam was focused with a Pine Veemax II onto the sample spot of the cell. The spectral resolution was set to 4 cm^{-1} and 128 interferograms were added together for each spectrum. Spectra are given in Reflectivity units defined as $\Delta R/R = R_{E2}-R_{E1}/R_{E1}$ with two single beam spectra R at applied potentials E_1 and E_2 . Here the reference spectrum R_{E1} was collected in the same solution with 0.5 M EtOH and 0.1 M KOH immediately before the investigated potential scan at the respective start potential. A Si hemisphere was used as the IR window and an ink of the electrocatalyst sample (1 mg in 0.8 ml isopropanol and 0.2 ml milli-Q water) was deposited on the prism on the IR beam ATR focus spot and contacted with Toray Paper 060 carbon cloth and a Pine glassy carbon rod fixating the carbon cloth. The complete beam pathway was under vacuum more than 24 hours prior to each measurement.

Inductively coupled plasma- optical emission spectroscopy (ICP-OES) was used for compositional analysis, performed using a 715-ES-inductively coupled plasma analysis system (Varian). Standard concentrations were 2, 4.5 and 7.5 ppm for Pt and Ni and 0.7, 2.8 and 5.6 ppm for Rh. The chosen wavelengths for concentration determination were 203.646 nm, 214.424 nm, 265.495 nm and 306.471 nm for Pt; 216.555 nm, 221.648 nm, 222.295 nm, 222.486 nm, 227.021 nm, 230.299 nm and 231.604 nm for Ni and 233.477 nm, 246.103 nm, 249.078 nm, 343.488 nm and 369.236 nm for Rh.

Transmission electron microscopy (TEM) was used to study nanoparticle morphology. A Cu grid (200 mesh) coated with a holey carbon film was impregnated with the sample solution and air-dried at $60\text{ }^\circ\text{C}$. An FEI TECNAI G² 20 S-TWIN microscope, equipped with a GATAN MS794 P CCD-detector operated at 200 kV was used. The mean particle size was determined from the TEM images by counting of at least 200 particles.

9. Summary and conclusions

This chapter summarizes and concludes the preceding chapters and provides an overview over the most important results of this thesis. Finally, a compilation of future perspectives resulting from these collected insights is given.



9.1. Summary

This thesis has addressed studies on new highly active electrocatalytical concepts for the ethanol oxidation reaction in acidic and alkaline media, and emphasized, besides synthesis-activity relations, on selectivity investigations with an optimized custom build *in situ* FTIR cell setup.

It is generally accepted that the oxidation of ethanol proceeds *via* a dual pathway, resulting not only in CO₂ but also in byproducts like acetic acid and acetaldehyde.^{5,16-28} The role of the intermediates for the different pathways is still controversial, CO intermediates or CH_x fragments are both discussed to be key species for highly active oxidation pathways. Lately the absence of CO intermediates is believed to correlate with promoted early onset complete oxidation, because they are considered to be responsible for poisoning the active sites on Pt catalysts.³⁻⁶ In order to investigate mechanistic effects like these together with selectivity-activity-relations, an innovative *in situ* FTIR cell setup was designed and successfully validated within this work. The setup uses a new ATR approach with carbon cloth, a conductive but inherent material to connect the working electrode film with the potentiostat while being permeable to water based electrolytes. Electrochemical current responses inside the cell were similar to standard RDE setup measurements and showed little to no mass transport limitation within the measuring requirements. *In situ* FTIR spectra of adsorbed species on the catalyst film as well as features from the electrolyte over the catalyst film could be detected and correlated to species involved in the electrocatalytic oxidation of ethanol.

In order to address the problems of incomplete oxidation of ethanol to CO₂ and water, either attributed to difficulties in the adsorption and cleavage of C-C bonds in ethanol or to intermediates like CO, efforts to develop highly active and selective electrocatalysts for ethanol oxidation reaction (EOR) to CO₂ have been focused on the addition of co-catalysts to platinum.³⁵⁻³⁹ Alloying Pt with highly oxophilic transition metals such as Rh, Ni or Sn has been described as a promising strategy to modify the electrocatalytic surface properties of Pt in order to supply active oxygen-containing species for the ethanol electrooxidation. In this work, mechanistic studies on the established binary PtNi electrocatalytical system (chapter 4) were followed by synthetic studies. Platinum and rhodium have been combined with tin (chapter 5 to 7) or nickel (chapter 7 and 8) aiming for novel ternary single phased nanocatalysts with increased EOR activity.

Electrochemical in situ FTIR investigations of the catalytic surface (chapter 4): The *in situ* electrochemical FTIR setup designed and validated in this thesis (chapter 3.5) offers not only insights of reactants of an electrocatalytic process on the investigated surfaces, but also information of adsorbed species and possible intermediates. This could be shown for *in situ* CO oxidation at different steps of a dealloying process on PtNi₃ electrocatalysts allowing for valuable conclusions on the

electronic state of the catalytically active surface. The obtained information can be used to modify and design novel electrocatalysts for reactions like the EOR.

Pt-Rh-Sn: the influence of synthetic reduction steps (chapter 5): The activity and selectivity of nanostructured ternary Pt-Rh-Sn materials in defined stoichiometric ratios was studied with a special emphasis on the exploration of the detailed 3D atomic arrangement and chemical surface states of the catalytically active phases and components. It was proven that the order in which the ternary catalysts were assembled in the synthetic process had an important impact for the resulting bulk phase crystallinity of the nanoparticle electrocatalysts. Scattering data and atomic PDF analysis revealed a single-phase Rh-doped Pt-Sn Niggliite structure as the preferred and catalytically most active nanocrystalline phase. On its surface, metallic Pt and Rh are atomically mixed with a SnO₂ phase, giving rise to active-surface-site ensembles. Only by simultaneous reduction of all three precursors was the phase-pure ternary Niggliite phase experimentally accessible. The EOR activity of the homogeneous Niggliite material outperformed previously reported comparable EOR catalysts of the PtRhSn family. *In situ* spectroscopy confirmed the favorable activity by an early CO₂ onset potential of the complete 12 electron oxidation pathway. On the other hand binary PtRh metal alloy phases proved detrimental to catalytic activity.

Pt-Rh-Sn: the influence of supporting conditions and synthetic environmental conditions (chapter 6): This chapter explored the effect of autoclave-based autogenous pressure versus ambient pressure conditions on the synthesis and properties of carbon-supported Pt-Rh-Sn nanoparticle electrocatalysts. The Pt-Rh-Sn nanoparticles were characterized by x-ray spectroscopy, electron microscopy and mass spectroscopy and deployed as catalysts for the electrocatalytic ethanol oxidation reaction. All catalysts showed fcc PtRh and hexagonal PtRhSn phases with similar metal loadings between 40 and 48 wt% and similar atomic ratios of Pt:Rh:Sn (30:10:60). Pt-Rh-Sn catalysts supported on carbon after particle formation showed broader size distribution ranging from 8-16 nm compared to catalysts precipitated in presence of carbon (particle size distribution around 7 nm). The highest overall activity was shown by materials synthesized at ambient pressures, with very early onset potentials for an on-carbon-reduced-precursor catalyst *ap-PtRhSn+C* and the highest mass activity for *ap-PtRhSn/C*. This could indicate the formation of a high concentration of surface site ensembles on the carbon during the reduction of the precursors that lead to higher activities at lower potentials, possibly towards the complete ethanol oxidation.

Pt-Rh-Ni vs. Pt-Rh-Sn: the influence of the oxygen donating species on the formation of active surface site ensembles (chapter 7): A fcc single-phase PtRhNi/C nanoparticle catalyst was successfully synthesized and its electrocatalytic activity contrasted towards ethanol electrooxidation

with our Pt-Rh-Sn benchmark catalyst concept. Interestingly, the EOR activity of the PtRhNi/C material was significantly higher than that of the Niggliite-type PtRhSn/C catalyst or any similar electrocatalysts reported in literature. Ni(OH)_x phases, that form on the surface facets of Ni-containing bulk phases, are well known to act as efficient oxygen-donating entities.^{53,121,169,170} Consistent with this explanation is the reduced stability of the PtRhNi/C materials in acid media, where Ni(OH)_x phases gradually leach from the top surface; in contrast, the EOR performance in alkaline media is greatly enhanced because of the stability of Ni(OH)_x phases under these conditions. The superior EOR activity of the PtRhNi catalyst at high overpotentials can be explained by the enhanced presence of surface active oxygenates, such as OH, which help segregate Ni(OH)_x to the catalyst surface.^{106,121,172]} Although the general beneficial effect of Rh for C-C bond splitting has been well documented,^{111,121,160} we could gain insights in the oxygen-donating effect of Ni vs. Sn. The comparison of PtRhSn/C and PtRhNi/C shows higher activities for the Ni-containing systems, proving it as the superior third component for a ternary Pt-Rh based catalytic concept in alkaline media.

Pt-Rh-Ni: influence of shape-controlled electrocatalysts on the onset potential and selectivity (chapter 8): Finally, the extension of the well investigated electrocatalytical concept of a ternary system containing Pt, Rh and Ni, preferred over Sn as the oxygen-donating species, led to investigations on the effect of shape-controlled nanoparticles on the EOR activity. A transfer of well-known synthetic protocols to our catalytic system, which is conducted to create octahedral *PtNiRh-oct/C* electrocatalysts with designed variation in Rh percentage (1-6 at. %), yielded highly shape-controlled supported nanoparticles. All catalysts showed narrow edge length distribution and high crystallinity as well as good electrochemical activities and stability towards the oxidation of ethanol. *In situ* FTIR studies revealed prevalence for the complete oxidation of ethanol *via* a C1 pathway for the lowest Rh content (1 at. %) while the C2 pathways dominate for the catalyst with the highest Rh content (6 at. %) where also a Rh shell was formed on the octahedra. The overall specific activity is highest for the *PtNiRh-oct/C* (3 at. %) that shows CO₂ production in parallel with C1 products, possibly due to the simultaneous occurrence of both reaction pathways. However, low Rh-contents octahedra particles also hold the ability to break the C-C bond at exceptionally low overpotentials near the reversible potential of the anodic complete oxidation of ethanol, which has not been achieved before with existing state of the art catalysts. This strongly suggests that active surface site ensembles utilizing all three metal components prevail in higher concentration on these surfaces and possible hint to a new kind of catalytic phase.

9.2. Conclusions

The above summarized structural conclusions in regard to the active catalytic phase of the present electrocatalytic concepts represent a significant step forward in our understanding of structural and mechanistic aspects of this class of catalytic materials. From the overview presented in Figure 9.1 it can clearly be seen that all electrocatalysts investigated in this thesis outperformed the previous reported comparable catalytic systems in both acidic and alkaline media, with only PtRhNi/C showing slightly lower but still comparable results in acidic electrolyte due to leaching effects. We saw that the formation of active surface site ensembles in large quantities mainly dominates the activity and selectivity of the investigated electrocatalytic systems.

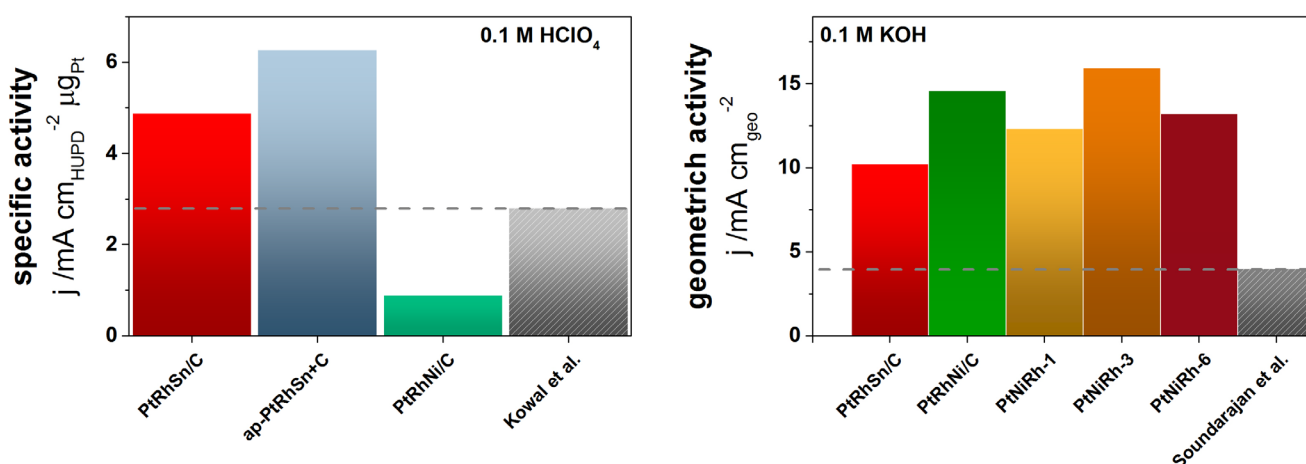


Figure 9.1: Comparison of all electrocatalysts investigated in this thesis with comparable benchmark literature catalysts in acidic (0.1 M HClO₄, Lit: PtRhSnO₂ from Li *et al.*⁶¹) and alkaline (0.1 M KOH, Lit: PtNi/C from Soundararajan *et al.*⁶³) media.

Our *in situ* FTIR setup approach proved to be sufficient for the investigation of adsorbed species like CO on Pt-rich PtNi₃ surfaces. Since all *in situ* measurements in the presence of ethanol showed no CO related bands in the recorded spectra we can exclude the presence of CO intermediates on our electrocatalytic surfaces during the electrooxidation of ethanol. At the same time we were able to identify early onset potentials of complete oxidation towards CO₂ on Pt-Rh-Sn; which were outperformed by the onset nearly as low as the reversible potential of the EOR in alkaline media by the octahedral Pt-Rh-Ni electrocatalytic system. This exceptionally low overpotential needed for the oxidation of ethanol, here observed for the first time, leads to two main conclusions:

- The higher order of the shape-controlled bulk structure results in defined active surface site ensembles consisting of all three metals, possible with modified electronic properties on the surface due to strain effects, which hold the possibility to oxidize ethanol and break the C-C bond easily.

- These specific surface site ensembles prove to be highly selective towards the adsorption of ethanol in contrast to any poisoning species like CO.

The lack of adsorbed CO in any EOR *in situ* spectra in this thesis can be supported by two possible explanations:

- CO does not easily adsorb onto the ternary catalytic surfaces. This is supported by the lack of CO oxidation activity in RDE CO stripping experiments on the Pt-Rh-Sn surfaces, which were conducted to estimate the ECSA of the catalysts.
- On highly active surface site ensembles for EOR, like the ones for the introduced Pt-Rh-Sn and Pt-Rh-Ni catalyst concepts in this thesis, no intermediate step involving CO fragments is involved in the reaction pathway. This theory is supported by the CO oxidation investigation on spherical PtNiRh/C electrocatalysts, which showed low CO oxidation activity only in the absence of ethanol and no CO adsorption bands once ethanol was present.

9.3. Perspectives

We are confident that the family of ternary Sn- or Ni-containing PtRh EOR electrocatalysts will spark interest in theoretical materials-by-design approaches and will be a promising catalyst structure for further-improved DEFC catalysts, as well as for catalysts to be used in the oxidation of liquid small hydrocarbons in general. Future research will have to focus on the product distribution and mechanistic activity-structure relations of these novel electrocatalysts. Based on the present results, the future perspective and challenges regarding the investigation of the active phase of the introduced catalytic concepts are the following:

- The further investigation of CO tolerance under EOR reaction conditions. For example, the adsorption of CO on electrocatalytic surfaces could be studied in presence and absence of ethanol in order to gain insights whether ethanol blocks the CO adsorption. In a second step, a sensitive technique like liquid chromatography (HPLC) could elucidate whether CO intermediates are formed during the ethanol synthesis, but not adsorbed onto the ternary surface sites.
- The electronic properties of the alloyed/ dealloyed bimetallic Pt-Ni system could be further investigated by generating binding strength correlations from CO-adsorption bands in relation to different dealloying protocols. Changes during *in situ* FTIR scans and varying onset potentials for the CO oxidation could provide valuable insights in the surface properties and its potential for the electrooxidation of hydrocarbon species.

- An important task in general is thoroughly identifying the ternary active surface site ensemble and elucidating the electronic structure of the catalytic phase, which is only indirectly accessed by vibrational spectroscopy (CO binding strength onto the catalytic surface), the direct *in situ* investigation of the electronic properties could be done with EELS; the spin states depending on the applied potential to the surface could be investigated e.g. with Mößbauer spectroscopy.
- The improvement of the shape control of the synthetic protocol to extend to different shapes and, therefore, a variety of defined catalytic surfaces in order to learn more about the influence of shape and therefore strain on the electronic and catalytic properties.
- The extension of the present catalytic concept to other, related anodic fuel cell reactions like the electrooxidation of methanol, formic acid or the hydrogen evolution reaction.
- Gaining a more complete point of view over the entire fuel cell with selectivity investigations in regard to the cathodic ORR reaction. The beneficial minimization of cross-over effects could be possible on the present CO tolerant anodic catalysts, which are desired to show only little Pt-oxidation-reduction activity at high overpotentials, as could be observed for the ternary Pt-Rh-Sn catalytic concept.

References

- (1) Berzelius, J. J. *Edin. New Phil. Jrnl.* **1836**, *21*, 223.
- (2) Beyhan, S.; Léger, J.-M.; Kadırgan, F. *Appl. Catal., B* **2014**, *144*, 66.
- (3) Hitmi, H.; Belgsir, E. M.; Leger, J. M.; Lamy, C.; Lezna, R. O. *Electrochim. Acta* **1994**, *39*, 407.
- (4) Iwasita, T.; Pastor, E. *Electrochim. Acta* **1994**, *39*, 531.
- (5) Kowal, A.; Li, M.; Shao, M.; Sasaki, K.; Vukmirovic, M. B.; Zhang, J.; Marinkovic, N. S.; Liu, P.; Frenkel, A. I.; Adzic, R. R. *Nat. Mater.* **2009**, *8*, 325
- (6) Colmati, F.; Antolini, E.; Gonzalez, E. R. *Appl. Catal., B* **2007**, *73*, 106.
- (7) Antolini, E. *J. Power Sources* **2007**, *170*, 1.
- (8) Wang, H.; Jusys, Z.; Behm, R. J. *J. Phys. Chem. B* **2004**, *108*, 19413.
- (9) de Souza, J. P. I.; Queiroz, S. L.; Bergamaski, K.; Gonzalez, E. R.; Nart, F. C. *J. Phys. Chem. B* **2002**, *106*, 9825.
- (10) Linares, J. J.; Rocha, T. A.; Zignani, S.; Paganin, V. A.; Gonzalez, E. R. *Int. J. Hydrogen Energy* **2013**, *38*, 620.
- (11) Zhou, W.; Zhou, Z.; Song, S.; Li, W.; Sun, G.; Tsiakaras, P.; Xin, Q. *Appl. Catal., B* **2003**, *46*, 273.
- (12) James, D. D.; Bennett, D. V.; Li, G.; Ghumman, A.; Helleur, R. J.; Pickup, P. G. *Electrochem. Commun.* **2009**, *11*, 1877.
- (13) Cases, F.; Vázquez, J. L.; Pérez, J. M.; Aldaz, A. *J. Electroanal. Chem. Interfacial Electrochem.* **1991**, *310*, 403.
- (14) Wan, C.-H.; Chen, C.-L. *Int. J. Hydrogen Energy* **2009**, *34*, 9515.
- (15) Parsons, R.; VanderNoot, T. *J. Electroanal. Chem. Interfacial Electrochem.* **1988**, *257*, 9.
- (16) Schmiemann, U.; Müller, U.; Baltruschat, H. *Electrochim. Acta* **1995**, *40*, 99.
- (17) Shin, J.; Tornquist, W. J.; Korzeniewski, C.; Hoaglund, C. S. *Surf. Sci.* **1996**, *364*, 122.
- (18) Lai, S. C. S.; Koper, M. T. M. *Faraday Discuss.* **2008**, *140*, 399.
- (19) Colmati, F.; Tremiliosi-Filho, G.; Gonzalez, E. R.; Berna, A.; Herrero, E.; Feliu, J. M. *Faraday Discuss.* **2008**, *140*, 379.
- (20) Lai, S. C. S.; Koper, M. T. M. *PCCP* **2009**, *11*, 10446.
- (21) Figueiredo, M. C.; Santasalo-Aarnio, A.; Vidal-Iglesias, F. J.; Solla-Gullon, J.; Feliu, J. M.; Kontturi, K.; Kallio, T. *Appl. Catal., B* **2013**, *140*, 378.
- (22) Li, M.; Liu, P.; Adzic, R. R. *J. Phys. Chem. Lett.* **2012**, *3*, 3480.
- (23) Christensen, P. A.; Jones, S. W. M.; Hamnett, A. *J. Phys. Chem. C* **2012**, *116*, 24681.
- (24) Kim, I.; Han, O. H.; Chae, S. A.; Paik, Y.; Kwon, S. H.; Lee, K. S.; Sung, Y. E.; Kim, H. *Angew. Chem. Int. Ed.* **2011**, *50*, 227032274.
- (25) Iwasita, T.; Pastor, E. *Electrochim. Acta* **1994**, *39*, 531.
- (26) Shao, M. H.; Adzic, R. R. *Electrochim. Acta* **2005**, *50*, 2415.
- (27) Rao, V.; Hariyanto, n.; Cremers, C.; Stimming, U. *Fuel Cells* **2007**, *7*, 417.

- (28) Heinen, M.; Jusys, Z.; Behm, R. J. *ECS Trans.* **2009**, *25*, 259.
- (29) Lai, S. C. S.; Kleyne, S. E. F.; Rosca, V.; Koper, M. T. M. *J. Phys. Chem. C* **2008**, *112*, 19080.
- (30) de Souza, E. A.; Giz, M. J.; Camara, G. A.; Antolini, E.; Passos, R. R. *Electrochim. Acta* **2014**, *147*, 483.
- (31) Martins, C. A.; Fernández, P. S.; Troiani, H. E.; Martins, M. E.; Camara, G. A. *J. Electroanal. Chem.* **2014**, *717–718*, 231.
- (32) Vigier, F.; Rousseau, S.; Coutanceau, C.; Leger, J.-M.; Lamy, C. *Top. Catal.* **2006**, *40*, 111.
- (33) Chang, S. C.; Leung, L. W. H.; Weaver, M. J. *J. Phys. Chem.* **1990**, *94*, 6013.
- (34) Hamann, C. H.; Hamnett, A.; Vielstich, W. *Electrochemistry*; 2 ed.; Wiley-VCH: Weinheim, 2007.
- (35) Song, S.; Tsiakaras, P. *Appl. Catal., B* **2006**, *63*, 187.
- (36) Oezaslan, M.; Hasche, F.; Strasser, P. *J. Electrochem. Soc.* **2012**, *159*, B444.
- (37) Hasche, F.; Oezaslan, M.; Strasser, P. *ChemCatChem* **2011**, *3*, 1805.
- (38) Oezaslan, M.; Hasche, F.; Strasser, P. *J. Electrochem. Soc.* **2012**, *159*, B394.
- (39) Gan, L.; Heggen, M.; O'Malley, R.; Theobald, B.; Strasser, P. *Nano Lett.* **2013**, *13*, 1131.
- (40) Hsieh, C.-T.; Lin, J.-Y.; Wei, J.-L. *Int. J. Hydrogen Energy* **2009**, *34*, 685.
- (41) Vigier, F.; Coutanceau, C.; Perrard, A.; Belgsir, E. M.; Lamy, C. *J. Appl. Electrochem.* **2004**, *34*, 439.
- (42) Souza-Garcia, J.; Herrero, E.; Feliu, J. M. *ChemPhysChem* **2010**, *11*, 1391.
- (43) Camara, G. A.; de Lima, R. B.; Iwasita, T. *Electrochem. Commun.* **2004**, *6*, 812.
- (44) Rousseau, S.; Coutanceau, C.; Lamy, C.; Léger, J. M. *J. Power Sources* **2006**, *158*, 18.
- (45) Giz, M. J.; Camara, G. A.; Maia, G. *Electrochem. Commun.* **2009**, *11*, 1586.
- (46) Lima, F. H. B.; Gonzalez, E. R. *Electrochim. Acta* **2008**, *53*, 2963.
- (47) Fujiwara, N.; Friedrich, K. A.; Stimming, U. *J. Electroanal. Chem.* **1999**, *472*, 120.
- (48) Léger, J. M.; Rousseau, S.; Coutanceau, C.; Hahn, F.; Lamy, C. *Electrochim. Acta* **2005**, *50*, 5118.
- (49) Vigier, F.; Coutanceau, C.; Hahn, F.; Belgsir, E. M.; Lamy, C. *J. Electroanal. Chem.* **2004**, *563*, 81.
- (50) Del Colle, V.; Souza-Garcia, J.; Tremiliosi-Filho, G.; Herrero, E.; Feliu, J. M. *PCCP* **2011**, *13*, 12163.
- (51) Zhou, W.-P.; Axnanda, S.; White, M. G.; Adzic, R. R.; Hrbek, J. *J. Phys. Chem. C* **2011**, *115*, 16467.
- (52) Purgato, F. L. S.; Olivi, P.; Léger, J. M.; de Andrade, A. R.; Tremiliosi-Filho, G.; Gonzalez, E. R.; Lamy, C.; Kokoh, K. B. *J. Electroanal. Chem.* **2009**, *628*, 81.
- (53) Cui, C. H.; Gan, L.; Heggen, M.; Rudi, S.; Strasser, P. *Nat. Mater.* **2013**, *12*, 765.
- (54) Hasche, F.; Oezaslan, M.; Strasser, P. *J. Electrochem. Soc.* **2012**, *159*, B25.
- (55) Rudi, S.; Tuaeov, X.; Strasser, P. *Electrocatalysis* **2012**, *3*, 265.

- (56) Lamy, C.; Rousseau, S.; Belgsir, E. M.; Coutanceau, C.; Leger, J. M. *Electrochim. Acta* **2004**, *49*, 3901.
- (57) Zhou, W. J.; Song, S. Q.; Li, W. Z.; Zhou, Z. H.; Sun, G. Q.; Xin, Q.; Douvartzides, S.; Tsiakaras, P. *J. Power Sources* **2005**, *140*, 50.
- (58) Colmati, F.; Antolini, E.; Gonzalez, E. R. *J. Power Sources* **2006**, *157*, 98.
- (59) Wang, H.; Jusys, Z.; Behm, R. J. *J. Power Sources* **2006**, *154*, 351.
- (60) Chu, Y. H.; Shul, Y. G. *Int. J. Hydrogen Energy* **2010**, *35*, 11261.
- (61) Li, M.; Kowal, A.; Sasaki, K.; Marinkovic, N.; Su, D.; Korach, E.; Liu, P.; Adzic, R. R. *Electrochim. Acta* **2010**, *55*, 4331.
- (62) Zhao, L.; Mitsushima, S.; Ishihara, A.; Matsuzawa, K.; Ota, K.-i. *Chinese Journal of Catalysis* **2011**, *32*, 1856.
- (63) Soundararajan, D.; Park, J. H.; Kim, K. H.; Ko, J. M. *Current Applied Physics* **2012**, *12*, 854.
- (64) Bonesi, A.; Garaventa, G.; Triaca, W. E.; Castro Luna, A. M. *Int. J. Hydrogen Energy* **2008**, *33*, 3499.
- (65) Cui, C.; Gan, L.; Li, H.-H.; Yu, S.-H.; Heggen, M.; Strasser, P. *Nano Lett.* **2012**, *12*, 5885.
- (66) Rudi, S.; Gan, L.; Cui, C.; Gliech, M.; Strasser, P. *J. Electrochem. Soc.* **2015**, *162*, F403.
- (67) Loukrakpam, R.; Wanjala, B. N.; Yin, J.; Fang, B.; Luo, J.; Shao, M.; Protsailo, L.; Kawamura, T.; Chen, Y.; Petkov, V.; Zhong, C.-J. *ACS Catal.* **2012**, *2*, 1461.
- (68) Song, S.; He, C.; Liu, J.; Wang, Y.; Brouzgou, A.; Tsiakaras, P. *Appl. Catal., B* **2012**, *119–120*, 227.
- (69) Russo, P. A.; Ahn, M.; Sung, Y.-E.; Pinna, N. *RSC Advances* **2013**, *3*, 7001.
- (70) Cuesta, A. In *Vibrational Spectroscopy at Electrified Interfaces*; John Wiley & Sons, Inc.: 2013, p 266.
- (71) Bard, A. *Electrochemical Methods*; 2 ed.; Wiley, 2001.
- (72) Petkov, V. *Synchrotron Radiat News* **2009**, *22*, 29.
- (73) Jauncey, G. E. M. *Proc. Natl. Acad. Sci. U. S. A.* **1924**, *10*, 57.
- (74) Bluhm, H.; Hävecker, M.; Knop-Gericke, A.; Kleimenov, E.; Schlögl, R.; Teschner, D.; Bukhtiyarov, V. I.; Ogletree, D. F.; Salmeron, M. *J. Phys. Chem. B* **2004**, *108*, 14340.
- (75) Salmeron, M.; Schlögl, R. *Surf. Sci. Rep.* **2008**, *63*, 169.
- (76) Yeh, J. J.; Lindau, I. *At. Data Nucl. Data Tables* **1985**, *32*, 1.
- (77) Bürgi, T.; Baiker, A. In *Adv. Catal.*; Bruce, C. G., Helmut, K., Eds.; Academic Press: 2006; Vol. Volume 50, p 227.
- (78) Harrick, N. J.; Interscience Publishers: New York, 1967.
- (79) Meier, D. M.; Urakawa, A.; Mader, R.; Baiker, A. *Rev. Sci. Instrum.* **2009**, *80*, 094101.
- (80) Colthup, N. B.; Orloff, M. K. *Spectrochim Acta a-M* **1971**, *A 27*, 1299.
- (81) Colthup, N. B.; Daly, L. H.; Wiberley, S. E. In *Introduction to Infrared and Raman Spectroscopy (Third Edition)*; Colthup, N. B., Daly, L. H., Wiberley, S. E., Eds.; Academic Press: San Diego, 1990, p 1.
- (82) Pettinger, B.; Lipkowski, J.; Hoon-Khosla, M. *J. Electroanal. Chem.* **2001**, *500*, 471.

- (83) Russell, A. E.; Blackwood, D.; Anderson, M. R.; Pons, S. *J. Electroanal. Chem. Interfacial Electrochem.* **1991**, *304*, 219.
- (84) Iwasita, T.; Nart, F. C. *Prog. Surf. Sci.* **1997**, *55*, 271.
- (85) Munk, J.; Christensen, P. A.; Hamnett, A.; Skou, E. *J. Electroanal. Chem.* **1996**, *401*, 215.
- (86) Stamenković, V.; Arenz, M.; Ross, P. N.; Marković, N. M. *J. Phys. Chem. B* **2004**, *108*, 17915.
- (87) Zhang, J.; Lu, J.; Cha, C.; Feng, Z. *J. Electroanal. Chem. Interfacial Electrochem.* **1989**, *265*, 329.
- (88) Nichols, R. J.; Bewick, A. *Electrochim. Acta* **1988**, *33*, 1691.
- (89) Roth, J. D.; Weaver, M. J. *Anal. Chem.* **1991**, *63*, 1603.
- (90) De Souza, R. F. B.; Silva, J. C. M.; Simoes, F. C.; Calegari, M. L.; Neto, A. O.; Santos, M. C. *Int. J. Electrochem. Sci.* **2012**, *7*, 5356.
- (91) Loukrakpam, R.; Yuan, Q.; Petkov, V.; Gan, L.; Rudi, S.; Yang, R.; Huang, Y.; Brankovic, S. R.; Strasser, P. *PCCP* **2014**, *16*, 18866.
- (92) Brouzgou, A.; Song, S. Q.; Tsiakaras, P. *Appl. Catal., B* **2012**, *127*, 371.
- (93) Rabis, A.; Rodriguez, P.; Schmidt, T. J. *ACS Catal.* **2012**, *2*, 864.
- (94) Iwasita, T.; Vielstich, W. *J. Electroanal. Chem. Interfacial Electrochem.* **1988**, *257*, 319.
- (95) Iwasita, T. *J. Electroanal. Chem.* **1990**, *295*, 215
- (96) López-Atalaya, M.; Morallón, E.; Cases, F.; Vázquez, J. L.; Pérez, J. M. *J. Power Sources* **1994**, *52*, 109.
- (97) Lai, S. C. S.; Kleijn, S. E. F.; Öztürk, F. T. Z.; van Rees Vellinga, V. C.; Koning, J.; Rodriguez, P.; Koper, M. T. M. *Catal. Today* **2010**, *154*, 92.
- (98) Christensen, P. A.; Linares-Moya, D. *J. Phys. Chem. C* **2009**, *114*, 1094.
- (99) Christensen, P. A.; Hamnett, A.; Linares-Moya, D. *PCCP* **2011**, *13*, 11739.
- (100) Yang, Y.-Y.; Ren, J.; Li, Q.-X.; Zhou, Z.-Y.; Sun, S.-G.; Cai, W.-B. *ACS Catal.* **2014**, *4*, 798.
- (101) Geraldés, A. N.; da Silva, D. F.; Pino, E. S.; da Silva, J. C. M.; de Souza, R. F. B.; Hammer, P.; Spinacé, E. V.; Neto, A. O.; Linardi, M.; dos Santos, M. C. *Electrochim. Acta* **2013**, *111*, 455.
- (102) PIKE Technologies: 2015.
- (103) Garsany, Y.; Singer, I. L.; Swider-Lyons, K. E. *J. Electroanal. Chem.* **2011**, *662*, 396.
- (104) García-Rodríguez, S.; Rojas, S.; Peña, M. A.; Fierro, J. L. G.; Baranton, S.; Léger, J. M. *Appl. Catal., B* **2011**, *106*, 520.
- (105) Cantane, D. A.; Gonzalez, E. R. *J. Electrochem. Soc.* **2012**, *159*, B355.
- (106) Rudi, S.; Cui, C.; Gan, L.; Strasser, P. *Electrocatalysis* **2014**, *5*, 408.
- (107) Erini, N.; Loukrakpam, R.; Petkov, V.; Baranova, E. A.; Yang, R.; Teschner, D.; Huang, Y.; Brankovic, S. R.; Strasser, P. *ACS Catal.* **2014**, *4*, 1859.
- (108) Neto, A. O.; Dias, R. R.; Tusi, M. M.; Linardi, M.; Spinacé, E. V. *J. Power Sources* **2007**, *166*, 87.
- (109) Lamy, C.; Lima, A.; LeRhun, V.; Delime, F.; Coutanceau, C.; Léger, J.-M. *J. Power Sources* **2002**, *105*, 283.
- (110) Willsau, J.; Heitbaum, J. *J. Electroanal. Chem. Interfacial Electrochem.* **1985**, *194*, 27.

- (111) Li, M.; Zhou, W. P.; Marinkovic, N. S.; Sasaki, K.; Adzic, R. R. *Electrochim. Acta* **2013**, *104*, 454.
- (112) Silva, J. C. M.; Parreira, L. S.; De Souza, R. F. B.; Calegari, M. L.; Spinacé, E. V.; Neto, A. O.; Santos, M. C. *Appl. Catal., B* **2011**, *110*, 141.
- (113) Neto, A. O.; Nandenha, J.; Assumpção, M. H. M. T.; Linardi, M.; Spinacé, E. V.; de Souza, R. F. B. *Int. J. Hydrogen Energy* **2013**, *38*, 10585.
- (114) Maillard, F.; Peyrelade, E.; Soldo-Olivier, Y.; Chatenet, M.; Chañet, E.; Faure, R. *Electrochim. Acta* **2007**, *52*, 1958.
- (115) Liu, Z.; Ling, X. Y.; Su, X.; Lee, J. Y.; Gan, L. M. *J. Power Sources* **2005**, *149*, 1.
- (116) Lim, D.-H.; Choi, D.-H.; Lee, W.-D.; Lee, H.-I. *Appl. Catal., B* **2009**, *89*, 484.
- (117) Deivaraj, T. C.; Chen, W.; Lee, J. Y. *J. Mater. Chem.* **2003**, *13*, 2555.
- (118) Almeida, T. S.; Kokoh, K. B.; De Andrade, A. R. *Int. J. Hydrogen Energy* **2011**, *36*, 3803.
- (119) Strasser, P. *Rev. Chem. Eng.* **2009**, *25*, 255.
- (120) Tuae, X.; Rudi, S.; Petkov, V.; Hoell, A.; Strasser, P. *ACS Nano* **2013**, *7*, 5666.
- (121) Cui, C.; Ahmadi, M.; Behafarid, F.; Gan, L.; Neumann, M.; Heggen, M.; Cuenya, B. R.; Strasser, P. *Faraday Discuss.* **2013**, *162*, 91.
- (122) Strasser, P. In *Chemical Energy Storage* 2012.
- (123) Strasser, P.; Koh, S.; Anniyev, T.; Greeley, J.; More, K.; Yu, C.; Liu, Z.; Kaya, S.; Nordlund, D.; Ogasawara, H.; Toney, M. F.; Nilsson, A. *Nat Chem* **2010**, *2*, 454.
- (124) Rossmeisl, J.; Karlberg, G. S.; Jaramillo, T.; Nørskov, J. K. *Faraday Discuss.* **2009**, *140*, 337.
- (125) Hammer, B.; Nørskov, J. K. *Nature* **1995**, *376*, 238.
- (126) Ruban, A.; Hammer, B.; Stoltze, P.; Skriver, H. L.; Nørskov, J. K. *J. Mol. Catal. A: Chem.* **1997**, *115*, 421.
- (127) Hammer, B.; Nørskov, J. K. *Surf. Sci.* **1995**, *343*, 211.
- (128) Hammer, B.; Nielsen, O. H.; Nørskov, J. K. *Catal. Lett.* **1997**, *46*, 31.
- (129) Pallassana, V.; Neurock, M.; Hansen, L. B.; Hammer, B.; Nørskov, J. K. *Physical Review B* **1999**, *60*, 6146.
- (130) Bligaard, T.; Nørskov, J. K. *Electrochim. Acta* **2007**, *52*, 5512.
- (131) Stamenkovic, V.; Mun, B. S.; Mayrhofer, K. J. J.; Ross, P. N.; Markovic, N. M.; Rossmeisl, J.; Greeley, J.; Nørskov, J. K. *Angew. Chem. Int. Ed.* **2006**, *45*, 2897.
- (132) Quaino, P.; Santos, E.; Soldano, G.; Schmickler, W. *Advances in Physical Chemistry* **2011**, *2011*, 14.
- (133) Schnur, S.; Groß, A. *Physical Review B* **2010**, *81*, 033402.
- (134) Gsell, M.; Jakob, P.; Menzel, D. *Science* **1998**, *280*, 717.
- (135) Mavrikakis, M.; Hammer, B.; Nørskov, J. K. *Phys. Rev. Lett.* **1998**, *81*, 2819.
- (136) Greeley, J.; Kjekshus, W. P.; Mavrikakis, M. *Angew. Chem. Int. Ed.* **2004**, *43*, 4296.
- (137) Kibler, L. A.; El-Aziz, A. M.; Hoyer, R.; Kolb, D. M. *Angew. Chem. Int. Ed.* **2005**, *44*, 2080.
- (138) Sakong, S.; Mosch, C.; Gro PCCP **2007**, *9*, 2216.

- (139) Blyholder, G. *J. Phys. Chem.* **1964**, *68*, 2772.
- (140) Mojet, B. L.; Ebbesen, S. D.; Lefferts, L. *Chem. Soc. Rev.* **2010**, *39*, 4643.
- (141) van Santen, R. A. *Journal of the Chemical Society, Faraday Transactions 1: Physical Chemistry in Condensed Phases* **1987**, *83*, 1915.
- (142) Kuhn, W. K.; Szanyi, J.; Goodman, D. W. *Surf. Sci.* **1992**, *274*, L611.
- (143) Cheah, S. K.; Bernardet, V. P.; Franco, A. A.; Lemaire, O.; Gelin, P. *J. Phys. Chem. C* **2013**, *117*, 22756.
- (144) Beden, B.; Lamy, C.; de Tacconi, N. R.; Arvia, A. J. *Electrochim. Acta* **1990**, *35*, 691.
- (145) Ianniello, R.; Schmidt, V. M.; Stimming, U.; Stumper, J.; Wallau, A. *Electrochim. Acta* **1994**, *39*, 1863.
- (146) Leung, L. W. H.; Chang, S. C.; Weaver, M. J. *The Journal of Chemical Physics* **1989**, *90*, 7426.
- (147) Zhu, Y.; Uchida, H.; Watanabe, M. *Langmuir* **1999**, *15*, 8757.
- (148) Christensen, P. A.; Hamnett, A.; Munk, J.; Troughton, G. L. *J. Electroanal. Chem.* **1994**, *370*, 251.
- (149) Shao, M.; Odell, J. H.; Choi, S.-I.; Xia, Y. *Electrochem. Commun.* **2013**, *31*, 46.
- (150) Colmati, F.; Antolini, E.; Gonzalez, E. R. *J. Alloys Compd.* **2008**, *456*, 264.
- (151) Spinace, E. V.; Dias, R. R.; Brandalise, M.; Linardi, M.; Neto, A. O. *Ionics* **2010**, *16*, 91.
- (152) Kowal, A.; Gojković, S. L.; Lee, K. S.; Olszewski, P.; Sung, Y. E. *Electrochem. Commun.* **2009**, *11*, 724.
- (153) Zhu, M.; Sun, G.; Xin, Q. *Electrochim. Acta* **2009**, *54*, 1511.
- (154) Kim, J. H.; Choi, S. M.; Nam, S. H.; Seo, M. H.; Choi, S. H.; Kim, W. B. *Appl. Catal., B* **2008**, *82*, 89.
- (155) Liu, Z.; Hong, L.; Tay, S. W. *Mater. Chem. Phys.* **2007**, *105*, 222.
- (156) De Souza, R. F. B.; Parreira, L. S.; Rascio, D. C.; Silva, J. C. M.; Teixeira-Neto, E.; Calegari, M. L.; Spinace, E. V.; Neto, A. O.; Santos, M. C. *J. Power Sources* **2010**, *195*, 1589.
- (157) Du, W.; Wang, Q.; LaScala, C. A.; Zhang, L.; Su, D.; Frenkel, A. I.; Mathur, V. K.; Teng, X. *J. Mater. Chem.* **2011**, *21*, 8887.
- (158) Loukrakpam, R.; Shan, S.; Petkov, V.; Yang, L.; Luo, J.; Zhong, C.-J. *J. Phys. Chem. C* **2013**, *117*, 20715.
- (159) Loukrakpam, R.; Wanjala, B. N.; Yin, J.; Fang, B.; Luo, J.; Shao, M.; Protsailo, L.; Kawamura, T.; Chen, Y.; Petkov, V.; Zhong, C.-J. *ACS Catal.* **2011**, *1*, 562.
- (160) Teran, F. E.; Santos, D. M.; Ribeiro, J.; Kokoh, K. B. *Thin Solid Films* **2012**, *520*, 5846.
- (161) Konopka, D. A.; Li, M.; Artyushkova, K.; Marinkovic, N.; Sasaki, K.; Adzic, R.; Ward, T. L.; Atanassov, P. *J. Phys. Chem. C* **2011**, *115*, 3043.
- (162) Erini, N.; Krause, P.; Glied, M.; Yang, R.; Huang, Y.; Strasser, P. *J. Power Sources* **2015**, *294*, 299.
- (163) Beyhan, S.; Coutanceau, C.; Léger, J.-M.; Napporn, T. W.; Kadirgan, F. *Int. J. Hydrogen Energy* **2013**, *38*, 6830.
- (164) Silva, J. C. M.; De Souza, R. F. B.; Parreira, L. S.; Neto, E. T.; Calegari, M. L.; Santos, M. C. *Appl. Catal., B* **2010**, *99*, 265.

- (165) Erini, N.; Rudi, S.; Beermann, V.; Krause, P.; Yang, R.; Huang, Y.; Strasser, P. *ChemElectroChem* **2015**, *2*, 903.
- (166) Ono, L.; Roldán-Cuenya, B. *Catal. Lett.* **2007**, *113*, 86.
- (167) Schneider, A.; Colmenares, L.; Seidel, Y. E.; Jusys, Z.; Wickman, B.; Kasemo, B.; Behm, R. J. *PCCP* **2008**, *10*, 1931.
- (168) Hsieh, C.-T.; Lin, J.-Y. *J. Power Sources* **2009**, *188*, 347.
- (169) Balbuena, P. B.; Altomare, D.; Vadlamani, N.; Bingi, S.; Agapito, L. A.; Seminario, J. M. *J. Phys. Chem. A* **2004**, *108*, 6378.
- (170) Novacek, P.; Varga, P. *Surf. Sci.* **1991**, *248*, 183.
- (171) Subbaraman, R.; Tripkovic, D.; Strmcnik, D.; Chang, K.-C.; Uchimura, M.; Paulikas, A. P.; Stamenkovic, V.; Markovic, N. M. *Science* **2011**, *334*, 1256.
- (172) Ahmadi, M.; Behafarid, F.; Cui, C.; Strasser, P.; Cuenya, B. R. *ACS Nano* **2013**, *7*, 9195.
- (173) Strasser, P. *J. Comb. Chem.* **2008**, *10*, 216.
- (174) Liu, Z.; Koh, S.; Yu, C.; Strasser, P. *J. Electrochem. Soc.* **2007**, *154*, B1192.
- (175) Oezaslan, M.; Hasche, F.; Strasser, P. *J Phys Chem Lett* **2013**, *4*, 3273.
- (176) Gan, L.; Cui, C.; Heggen, M.; Dionigi, F.; Rudi, S.; Strasser, P. *Science* **2014**, *346*, 1502.
- (177) Leppert, L.; Albuquerque, R. Q.; Kümmel, S. *Physical Review B* **2012**, *86*, 241403.
- (178) Vegard, L. *Z. Physik* **1921**, *5*, 17.
- (179) Atkins, P.; de Paula, J. *Atkins' Physical Chemistry*; 10th ed.; Oxford University Press, 2014.
- (180) Iwasita, T.; Xia, X. H.; Liess, H. D.; Vielstich, W. *J. Phys. Chem. B* **1997**, *101*, 7542.
- (181) Heinen, M.; Jusys, Z.; Behm, R. J. *J. Phys. Chem. C* **2010**, *114*, 9850.
- (182) Fang, X.; Wang, L. Q.; Shen, P. K.; Cui, G. F.; Bianchini, C. *J. Power Sources* **2010**, *195*, 1375.
- (183) Zhou, Z.-Y.; Wang, Q.; Lin, J.-L.; Tian, N.; Sun, S.-G. *Electrochim. Acta* **2010**, *55*, 7995.
- (184) Li, M.; Guo, W. Y.; Jiang, R. B.; Zhao, L. M.; Shan, H. H. *Langmuir* **2010**, *26*, 1879.

Appendix

List of abbreviations

AA	acetic acid	HUPD	hydrogen underpotential deposition
AAE	after acid exposure	ICP-OES	Inductively coupled plasma optical emission spectroscopy
AAL	acetaldehyde	IR	infrared
AB	absorbance	IRRAS	infrared reflection absorption spectroscopy
ADC	analog-to-digital counts	LSV	linear sweep voltogram
ap	ambient pressure	LWL	long wave length cut-off
ATR	attenuated total reflection	MCT	mercury cadmium telluride
BAE	before acid exposure	MO	molecular orbital
CA	chronoamperometry	op	over pressure
CE	counter electrode	ORR	oxygen reduction reaction
CV	cyclovoltogram	PDF	pair distribution function
DE	disc electrode	PEM	proton exchange membrane
d_e	effective penetration depth	PGM	platinum group metals
DEFC	direct ethanol fuel cell	R	reflectivity
DL	double layer	RDE	rotating disc electrode
d_p	penetration depth	RE	reference electrode
ECSA	electrochemically active surface area	RHE	reversible hydrogen electrode
E_d	d band center	RT	room temperature
EDX	energy dispersive x-ray spectroscopy	SA	active surface area
EELS	electron energy loss spectroscopy	SERS	surface enhanced Raman spectroscopy
E_F	Fermi level	SFG	sum frequency generation spectroscopy
EOR	ethanol oxidation reaction	SNIFTIRS	subtractively normalized interfacial FTIR spectroscopy
ER	external reflectance	STEM	scanning transmission electron microscopy
ERAS	external reflection absorption spectroscopy	T	transmittance
fcc	face centered cubic	TEM	transmission electron microscopy
FT	Fourier Transform	UHV	ultra high vacuum
FTIR	Fourier Transform Infrared	UPD	electrochemical underpotential deposition
GC	glassy carbon	WE	working electrode
HAADF	high angle annular dark field	XPS	x-ray photoelectron spectroscopy
HEXRD	high energy x-ray diffraction	XRD	x-ray diffraction
HRTEM	high resolution transmission electron microscopy		

Table of figures

Figure 1.1: Schematic representation of the dual pathway mechanism for the electrooxidation of ethanol.....	4
Figure 1.2: Working principle of a direct ethanol fuel cell.....	5
Figure 2.1: Schematic visualization of the different catalytic systems investigated for their ethanol oxidation reactivity (PtRhSn and PtRhNi systems) and for their CO oxidation behavior (PtNi).....	9
Figure 2.2: Synthesis scheme for the platinum-rhodium-tin containing electrocatalysts and the implemented variations that were used in this thesis. All precursors could be reduced consecutive or simultaneous, under different pressure conditions, and carbon support could be added during or after the reduction.	11
Figure 2.3: Synthesis scheme for the platinum-rhodium-nickel containing electrocatalysts and the implemented variations that were used in this thesis. All precursors could be reduced consecutive or simultaneous, under different pressure conditions, and carbon support could be added during or after the reduction.	11
Figure 2.4: Picture of the three-electrode electrochemical cell setup. 1) working electrode WE, 2) counter electrode CE, 3) reference electrode RE, 4) rotator, 5) Luggin-Haber capillary, 6) frit, 7) gas connection and 8) faucet.	13
Figure 2.5: Proposed model of the double-layer region under conditions where anions are specifically adsorbed. Adapted from Bard <i>et al.</i> ⁷¹	14
Figure 2.6: Schematic visualization of the Bragg equation. Maximum scattered intensity is only observed when the phase shift adds to a multiple of the incident wavelength.	17
Figure 3.1: Experimental geometry for attenuated total reflection (ATR) IR spectroscopy and penetration depth of the evanescent wave from the ATR crystal into the bulk electrolyte.	23
Figure 3.2: Theoretical calculation of the effective penetration depth d_e in dependence of the wavelength λ and the angle of incidence θ_i . Refraction indices are set $n_1/n_2 = 1.8$	24
Figure 3.3: Schematic drawing of the IR beam path in an IRRAS cell for solid-liquid interface investigation. Reprinted with permission from Reference ⁷⁹ . Copyright 2009, AIP Publishing LLC.	26
Figure 3.4: Dipole moment changes in certain molecular vibrations ⁸¹ and active and inactive IR components of the dipole moment.	26
Figure 3.5: Scheme of the SNIFTIRS experiment and multilayer configuration used in SNIFTIRS simulation. Reprinted from Reference ⁸² with permission from Elsevier.....	28
Figure 3.6: Scheme of the <i>in situ</i> IRRAS cell for pure Pt single crystal working electrodes cell by Iwasita <i>et al.</i> ⁸⁴ Reprinted from Reference ⁸⁴ with permission from Elsevier.....	30
Figure 3.7: Scheme of a) the preparation chamber for thin catalyst layers for b) the upgraded spectroelectrochemical cell for <i>in situ</i> IRRAS measurements at elevated temperatures by Stamenkovic <i>et al.</i> ⁸⁶ based on the initial design by Iwasita <i>et al.</i> ⁸⁴ . GI is the gas inlet (bubbler), TC the thermocouple, WE the working electrode, CH the cartridge heater, CE the counter electrode, and RE the reference electrode. Reprinted with permissions from Reference ⁸⁶ . Copyright 2004 American Chemical Society.....	30
Figure 3.8: Scheme of the different electrochemical <i>in situ</i> FTIR cell working principles.....	31
Figure 3.9: Picture (left) and sketch (right) of the custom-made <i>in situ</i> electrochemical setup cell (ER and ATR) for the investigation of the ethanol oxidation reaction. The cell consist of a spectroscopic bottom part with the ATR prism fixated by a prism holder and a connecting plate to the electrochemical glass cell that contains the gas inlet, the working electrode with an adjustment screw, the reference electrode, and the counter electrode (not included in the sketch).	32

Figure 3.10: Sketch of the <i>in situ</i> FTIR ATR/ER setup implemented in the Bruker70v sample compartment. The IR beam pathway throughout the mirror system of the angle incidence control ATR Veemax II is indicated green.....	33
Figure 3.11: Sketch of the <i>in situ</i> FTIR ATR/ER cell from above (left) and from below (right). The cell has to be adjusted in a way that the ATR beam spot is exactly focused where the working electrode is implemented from above.....	33
Figure 3.12: Sketch of the vacuum sealed <i>in situ</i> FTIR ATR/ER setup implemented in the Bruker70v sample compartment.	34
Figure 3.13: Picture of the <i>in situ</i> FTIR ATR/ER setup implemented in the Bruker70v sample compartment. The IR beam pathway throughout the mirror system of the angle incidence control ATR Veemax II is indicated green.....	34
Figure 3.14: ZnSe, Si and CaF ₂ prism for the custom made electrochemical <i>in situ</i> FTIR cell concept.	35
Figure 3.15: Setup of the FTIR cell. Focus of the Laser spot (Adjustment) on the prism. The Focus is adjusted by a concentric water drop.	37
Figure 3.16: ATR Spectra for Adjustment of ZnSe window at 60°, background air. A water ring outside the Laser focus spot shows no water bands (gray), a water drop on the laser focus spot shows water bands around 3500 cm ⁻¹ and 1600 cm ⁻¹	38
Figure 3.17: Critical Angle for Total Internal Reflection of FTIR light at the interface between the FTIR prism and the medium above it.	39
Figure 3.18: Intensity reaching the MCT detector in analog-to-digital counts (ADC) depending on different angles of incidence for different materials at the interface FTIR prism/air.	39
Figure 3.19: Theoretical (d _p) and effective (d _e) penetration depth calculated for ZnSe/water interface in dependence of the wavelength of the incident beam, the gray vertical dashed line indicates Pt-CO band at 2050 cm ⁻¹ , for 60° ~0.55 μm. Usual film thickness is between 0.04 and 0.78 μm. ¹⁰³	40
Figure 3.20: Scheme of the P, Q and R branch of a vibrational-rotational intensity profile and the corresponding rotational (ΔJ) and vibrational (Δv) transitions.....	41
Figure 3.21: <i>In situ</i> ATR spectra of CO ₂ and CO _{ads} on Pt/C in 0.1 M HClO ₄ at different resolutions. 128 interferograms were added into one single spectrum. The insert shows an enhancement of the CO ₂ region.	42
Figure 3.22: ATR spectra of ethanol oxidation reaction educts and products in 0.1 M HClO ₄ . 128 scans, resolution = 4 cm ⁻¹ , background pure 0.1 M HClO ₄	43
Figure 3.23: CV of the electrooxidation of CO on Pt/C (BASF) film deposited on ZnSe, contacted with Toray Paper 030 in 0.1 M HClO ₄ with 20 mV s ⁻¹ . CO was adsorbed and then removed with Ar from the electrolyte prior to the measurement. Current density is normalized by the size of the GC working electrode (0.071 cm ²).	45
Figure 3.24: <i>In situ</i> ATR FTIR spectra during the electrooxidation of CO on Pt/C on ZnSe contacted with carbon cloth (Toray Paper 030) and a GC WE in 0.1 M HClO ₄ . Spectra background was recorded in pure electrolyte without applied potential. All spectra are recorded at 0.05 V vs. RHE before and after the respective cyclovoltgrams (Figure 3.23).	46
Figure 3.25: CV for the oxidation of EtOH on PtRhSn/C on ZnSe contacted with carbon cloth and GC WE in 0.5 M EtOH + 0.1 M HClO ₄ , scan rate = 1 mV s ⁻¹ . The insert shows the potential range of the respective averaged spectra shown in Figure 3.26.....	47
Figure 3.26: <i>In situ</i> ATR FTIR spectra during the first scan for the oxidation of EtOH on PtRhSn/C on ZnSe contacted with carbon cloth and GC WE in 0.5 M EtOH + 0.1 M HClO ₄ , scan rate = 1 mV s ⁻¹ . Spectra background was recorded at E _{ref} = 0.05 V vs. RHE. The potentials corresponding to each spectrum are indicated in the figure.	48

Figure 3.27: First 10 cyclovoltograms for the oxidation of EtOH on <i>PtRhSn/C</i> on ZnSe contacted with carbon cloth and GC WE in 0.5 M EtOH + 0.1 M HClO ₄ and cycled with 20 mV s ⁻¹	49
Figure 3.28: <i>In situ</i> ATR FTIR spectra corresponding to Figure 3.27 for the oxidation of EtOH on <i>PtRhSn/C</i> on ZnSe contacted with carbon cloth and GC WE in 0.5 M EtOH + 0.1 M HClO ₄ . The potential was cycled 10 times with 20 mV s ⁻¹ . Spectra background was recorded at E _{ref} = 0.05 V vs. RHE. The scans corresponding to each spectrum are indicated in the figure.....	50
Figure 4.1: Schematic illustration of the dealloying process for <i>PtNi₃/C</i> . During the electrochemical dealloying Pt enriches at the surface.....	54
Figure 4.2: Molecular orbital energy level diagram for orbitals constructed from the overlap of metal <i>d</i> -band orbitals and an adsorbate σ orbital, resulting in the formation of a filled bonding (d-σ) molecular orbital and an empty antibonding (d-σ)* molecular orbital.....	54
Figure 4.3: Illustration of the effect of compressive and tensile strain on the width and position of the <i>d</i> -band of an early transition metal. The local density of states due to compressive strain leads to a downshift of the <i>d</i> -band center E _d while the tensile strain leads to an upshift of E _d towards the Fermi level.....	56
Figure 4.4: (a) Adsorption of CO onto metal surfaces according to Blyholder ¹³⁹ . (b) Ranges of IR peak position as a function of adsorption geometry on noble metal surfaces. Reproduced from Reference ¹⁴⁰ with permission of The Royal Society of Chemistry.....	57
Figure 4.5: Experimental and spectroscopic dealloying protocol for <i>PtNi₃/C</i> electrocatalysts.....	59
Figure 4.6: Dealloying process on <i>PtNi₃/C</i> in 0.1 M HClO ₄ , scan rate = 50 mV s ⁻¹ at 25°C.....	60
Figure 4.7: H _{UPD} <i>in situ</i> on <i>PtNi₃/C</i> before (left) and after (right) dealloying in 0.1 M HClO ₄ , scan rate = 50 mV s ⁻¹ at 25°C. Current densities are normalized by SA from H _{UPD} desorption.....	61
Figure 4.8: CO stripping <i>in situ</i> on <i>PtNi₃/C</i> before and after dealloying in 0.1 M HClO ₄ , scan rate = 50 mV s ⁻¹ at 25°C. Current densities are normalized by SA from H _{UPD} desorption.....	61
Figure 4.9: <i>In situ</i> ATR FTIR spectra of adsorbed CO on pure Pt/C and <i>PtNi₃/C</i> on ZnSe contacted with carbon cloth and GC WE in 0.5 M 0.1 M HClO ₄ . All spectra were recorded at E = 0.05 V vs. RHE, background spectrum I ₀ was recorded without electrolyte.....	62
Figure 5.1: TEM micrographs of electrocatalyst: 1) <i>PtRh/C</i> , 17.8 ± 7.3 nm; 2) <i>PtRhSn/C</i> , 9.0 ± 2.9 nm; 3) <i>Sn+Rh+Pt/C</i> , 18.9 ± 4.8 nm; 4) <i>Sn+RhPt/C</i> , 15.9 ± 4.7 nm; and 5) <i>Sn+Pt/C</i> , 12.8 ± 2.6 nm.....	70
Figure 5.2: Mean particle diameter and size distribution histograms of electrocatalyst: 1) <i>PtRh/C</i> , 17.8 ± 7.3 nm; 2) <i>PtRhSn/C</i> , 9.0 ± 2.9 nm; 3) <i>Sn+Rh+Pt/C</i> , 18.9 ± 4.8 nm; 4) <i>Sn+RhPt/C</i> , 15.9 ± 4.7 nm; and 5) <i>Sn+Pt/C</i> , 12.8 ± 2.6 nm.....	70
Figure 5.3: Cu Kα XRD pattern of different catalyst: 1) <i>PtRh/C</i> , 2) <i>PtRhSn/C</i> , 3) <i>Sn+Rh+Pt/C</i> , 4) <i>Sn+RhPt/C</i> , and 5) <i>Sn+Pt/C</i> . Pure Pt fcc and pure PtSn-Niggliite diffraction patterns are indicated in black and gray lines, respectively.....	71
Figure 5.4: (A) Synchrotron-based HEXRD patterns collected at λ=0.1080 Å of 1) <i>PtRh/C</i> , 2) <i>PtRhSn/C</i> , 3) <i>Sn+Rh+Pt/C</i> , 4) <i>Sn+RhPt/C</i> , and 5) <i>Sn+Pt/C</i> . (B) Atomic pair distribution functions (PDFs) derived from the XRD patterns (gray symbols) and computed from structure models (red solid lines). The refined lattice parameters are given by each data set.....	73
Figure 5.5: (A) PDF-derived 3D structural model of an fcc lattice, randomly occupied by Rh and Pt atoms (gray balls). Unit cell is given by lines. (B) A hexagonal, Niggliite structure featuring alternating layers of Pt (gray balls) and Sn (red balls) atoms. Spherical model of Niggliite structured particle (C) and excerpt of the particle surface (D) with Sn (orange balls) and Pt sited doped randomly with Rh (gray balls).....	75

Figure 5.6: Cyclic voltammograms (CVs) of 1) PtRh/C, 2) PtRhSn/C, 3) Sn+Rh+Pt/C, 4) Sn+RhPt/C, and 5) Sn+Pt/C EOR catalysts in 0.5 M H ₂ SO ₄ . Current densities are normalized by the electrochemically accessible surface area (SA) from H _{UPD} stripping with a scan rate of 20 mV/s.	76
Figure 5.7: Polarization curves of the electrocatalytic ethanol oxidation reaction (EOR): 1) PtRh/C, 2) PtRhSn/C, 3) Sn+Rh+Pt/C, 4) Sn+RhPt/C, and 5) Sn+Pt/C recorded in 0.5 M H ₂ SO ₄ and 0.5 M C ₂ H ₅ OH. Current densities are normalized by the electrochemically accessible surface area (SA) from H _{UPD} stripping with a scan rate of 20 mV/s. The vertical dashed line marks the potential of the chronoamperometric experiment in Figure 5.8.	76
Figure 5.8: Potentiostatic chronoamperometry of the Pt-Rh-Sn/C electrocatalysts at E = +0.45 V vs. RHE recorded in 0.5 M H ₂ SO ₄ and 0.5 M EtOH. Current densities are normalized by the electrochemically accessible surface area (SA) from H _{UPD} stripping.	77
Figure 5.9: Pt 4f (A), Rh 3d (B) and Sn 3d (C) XP spectra for PtRhSn/C before (BAE: blue) and after (AAE: red) acid treatment. Photoelectron kinetic energy: 550 eV.	79
Figure 5.10: SNIFTIRS spectra during ethanol oxidation on PtRhSn/C between +0.15 V and +1.15 V vs. RHE. Conditions: 0.1M HClO ₄ + 0.5M C ₂ H ₅ OH. The spectrum at +0.10 V is used as background.	81
Figure 6.1: TEM micrographs and particle size distribution diagrams of the as-prepared electrocatalyst: 1) ap-PtRhSn/C, 2) ap-PtRhSn+C, 3) op-PtRhSn/C and 4) op-PtRhSn+C. Exemplary insets with higher magnification for each sample show different lattice spacing found in all samples.	87
Figure 6.2: Cu K α XRD patterns of electrocatalyst: 1) ap-PtRhSn/C, 2) ap-PtRhSn+C, 3) op-PtRhSn/C and 4) op-PtRhSn+C. Pure Pt fcc and pure PtSn Niggliite diffraction patterns are indicated in black and grey, respectively.	88
Figure 6.3: Electrocatalytic activity for the ethanol oxidation reaction (EOR) on 1) ap-PtRhSn/C, 2) ap-PtRhSn+C, 3) op-PtRhSn/C and 4) op-PtRhSn+C recorded in 0.5 M C ₂ H ₅ OH + 0.1 M HClO ₄ . First forward scan with a scan rate of 20 mV/s. Current densities are normalized by the amount of Pt present on the working electrode surface (~ 3 μ g Pt+Rh).	90
Figure 6.4: First scan for 1) ap-PtRhSn/C, 2) ap-PtRhSn+C, 3) op-PtRhSn/C and 4) op-PtRhSn+C recorded in 0.1 M HClO ₄ with a scan rate of 20 mV/s. Current densities are normalized by the amount of Pt present on the working electrode surface (~ 3 μ g Pt+Rh).	91
Figure 6.5: First two scans of the electrocatalytic ethanol oxidation reaction (EOR): 1) ap-PtRhSn/C, 2) ap-PtRhSn+C, 3) op-PtRhSn/C and 4) op-PtRhSn+C recorded in 0.5 M H ₂ SO ₄ and 0.5 M EtOH with a scan rate of 20 mV/s. Current densities are normalized by the amount of Pt present on the working electrode surface (~ 3 μ g Pt+Rh).	91
Figure 6.6: Electrocatalytic activity for the ethanol oxidation reaction (EOR) on 1) ap-PtRhSn/C, 2) ap-PtRhSn+C, 3) op-PtRhSn/C and 4) op-PtRhSn+C recorded in 0.5 M C ₂ H ₅ OH + 0.1 M HClO ₄ . Potentiostatic chronoamperometry at E = +0.45 V vs. RHE. Current densities are normalized by the amount of Pt present on the working electrode surface (~ 3 μ g Pt+Rh).	93
Figure 6.7: Current density (mA cm _{geo} ⁻² at 0.70 V vs. RHE) dependency on the platinum loading (μ g cm ⁻²) for ethanol electro-oxidation on 1) ap-PtRhSn/C, 2) ap-PtRhSn+C, 3) op-PtRhSn/C and 4) op-PtRhSn+C recorded in 0.5 M C ₂ H ₅ OH + 0.1 M HClO ₄ with a scan rate of 20 mV/s according to Brouzgou <i>et al</i> ⁹² . Current densities are normalized by the geometrical area of the working electrode surface (0.196 cm ²). For comparison PtRhSnO ₂ /C by Kowal <i>et al.</i> ⁵ is included.	94
Figure 7.1: TEM micrographs and size distribution histograms of electrocatalysts: PtRhSn/C, 4.7 \pm 0.1 nm and PtRhNi/C, 11.7 \pm 0.1 nm.	100

Figure 7.2: Fitted CuK α XRD patterns of PtRhSn/C and PtRhNi/C. The carbon features were taken out by background subtraction. Pure Pt fcc, pure Ni fcc, and pure PtSn Niggliite diffraction patterns are indicated in black, blue, and gray lines, respectively.	101
Figure 7.3: Polarization curves of PtRhSn/C and PtRhNi/C in pure 0.1 M HClO ₄ (A) and 0.1 M KOH (B) and the ethanol oxidation reaction (EOR) in acidic media (C, 0.1 M HClO ₄) and alkaline media (D, 0.1 KOH) containing 0.5 M Ethanol. Current densities are normalized by the mass of Pt present on the working electrode.	102
Figure 7.4: First two polarization curves of PtRhSn/C and PtRhNi/C in pure 0.1 M HClO ₄ (A) and 0.1 M KOH (B). Current densities are normalized by the mass of Pt group metals present on the working electrode. Scan rate is 20 mV s ⁻¹	102
Figure 7.5: First two polarization curves of the ethanol oxidation reaction (EOR) on PtRhSn/C and PtRhNi/C in acidic media (A, 0.1 M HClO ₄) and alkaline media (B, 0.1 M KOH) containing 0.5 M Ethanol. Current densities are normalized by the mass of Pt group metals present on the working electrode. Scan rate is 20 mV s ⁻¹	103
Figure 7.6: Specific activity polarization curves of the ethanol oxidation reaction (EOR) on PtRhSn/C and PtRhNi/C in acidic media (A, 0.1 M HClO ₄) and alkaline media (B, 0.1 M KOH) containing 0.5 M Ethanol. Current densities are normalized by the Electrochemical Active Surface Area from H _{UPD} measurements. Scan rate is 20 mV s ⁻¹	103
Figure 7.7: Geometric current density polarization curves of the ethanol oxidation reaction (EOR) on PtRhSn/C and PtRhNi/C in acidic media (A, 0.1 M HClO ₄) and alkaline media (B, 0.1 M KOH) containing 0.5 M Ethanol. Current densities are normalized by the Geometrical Surface Area of the working electrode (0.196 cm ²). Scan rate is 20 mV s ⁻¹	104
Figure 7.8: Cyclic voltammograms of CO stripping on PtRhSn/C (A) and PtRhNi/C (B) in 0.1 M HClO ₄ . Prior to measurements a monolayer of CO was adsorbed on the surface by bubbling CO in the electrolyte and excess CO removed consecutively by bubbling Ar, both under potential control. Current densities are normalized by the Geometrical Surface Area of the working electrode (0.196 cm ²).	104
Figure 7.9: Potentiostatic chronoamperometry for the electrocatalytic ethanol oxidation reaction (EOR) on PtRhSn/C and PtRhNi/C at E = 0.45 V vs. RHE in A: acidic media (0.1 M HClO ₄) and B: alkaline media (0.1 KOH) with 0.5 M Ethanol. Current densities are normalized by the mass of Pt present on the working electrode.	106
Figure 8.1: TEM micrographs and edge length distribution histograms of <i>PtNiRh-oct/C</i> electrocatalysts as prepared (top) and after one scan in 0.5 M EtOH in 0.1 M KOH (bottom).	111
Figure 8.2: Atomic-scale Z-contrast STEM images and composition profile analysis of Pt₃Ni₁Rh_x-oct/C octahedral nanoparticles. HAADF STEM images (a-c,j) and EDX composition map analysis (d-i) after the first EOR scan of <i>PtNiRh-1/C</i> (a,d,g), <i>PtNiRh-3/C</i> (b,e,h) and <i>PtNiRh-6/C</i> (c,f,i) octahedral nanoparticles oriented close to $\langle 110 \rangle$. (j) Overview HAADF STEM image of <i>PtNiRh-6/C</i> . (d-f) EDX composition map showing the distribution of Pt (red) and Ni (green) and (g-i) Pt (red) and Rh (blue), respectively. (k) Ball schematic sketch shows the Rh-rich shell and mixed Ni, Rh and Pt core (l) Cu K α XRD pattern of the three <i>Pt₃Ni₁Rh_x-oct/C</i> electrocatalysts shown alongside the expected peak positions for pure fcc Pt, pure fcc Rh and pure fcc Ni, indicated using black, grey and green lines, respectively.	112
Figure 8.3: Atomic-scale composition profile analysis of PtNiRh-6/C octahedral nanoparticles. HAADF STEM image (a) and EDX composition map analysis (b-c) after the first EOR scan of a <i>PtNiRh-6/C</i> octahedral nanoparticle (6.5 nm). (b) EDX composition map showing the distribution of Pt (red) and Ni (green) and (c) Pt (red) and Rh (blue), respectively.	113
Figure 8.4: Atomic-scale Z-contrast STEM images and composition profile analysis of as-prepared Pt₃Ni₁Rh_x-oct/C octahedral nanoparticles. HAADF STEM images (a-c)	

and EDX composition map analysis (d-i) of *PtNiRh-1/C* (a,d,g), *PtNiRh-3/C* (b,e,h) and *PtNiRh-6/C* (c,f,i) octahedral nanoparticles oriented close to $\langle 110 \rangle$. (d-f) EDX composition map showing the distribution of Pt (red) and Ni (green) and (g-h) Pt (red) and Rh (blue), respectively. 113

Figure 8.5: Comparison of HAADF STEM images, as prepared and after the first EOR scan on $Pt_3Ni_1Rh_x$ -oct/C octahedral nanoparticles. HAADF STEM images before (a-c) and after (d-f) the first EOR scan for *PtNiRh-1/C* (a,d), *PtNiRh-3/C* (b,e) and *PtNiRh-6/C* (c,f,) mainly octahedral nanoparticles. 114

Figure 8.6: Electrochemical studies on carbon supported $Pt_3Ni_1Rh_x$ -oct/C octahedral catalysts. First forward scan (a,b) with a scan rate of 20 mV s^{-1} and potentiostatic chronoamperometry (c) at 0.45 V vs. RHE of the ethanol oxidation reaction (EOR) on the three *Pt₃Ni₁Rh_x-oct/C* electrocatalysts in 0.1 KOH containing 0.5 M ethanol . Current densities are normalized by the ECSA from H_{UPD} in pure electrolyte and the amount of Pt present on the working electrode. The vertical grey dashed line marks the potential of technical interest used for the chronoamperometric experiment in c. Comparison of the EOR specific activity at 0.45 vs. RHE during the first forward scan (d), the corresponding potential to the early onset peak χ maximum (e) and the respective charge of peak χ (f) of the three *Pt₃Ni₁Rh_x-oct/C* octahedra. 116

Figure 8.7: In situ FTIR ATR spectra for identifying the intermediates and products of ethanol oxidation on supported $Pt_3Ni_1Rh_x$ -oct/C octahedral electrocatalysts. *In situ* FTIR ATR spectra recorded during the electrooxidation of ethanol on (a) *PtNiRh-1/C*, (b) *PtNiRh-3/C* and (c) *PtNiRh-6/C*. 128 interferograms (resolution 4 cm^{-1}) were collected and combined for each spectrum. The working electrode potential ranges during the first linear sweep voltammetry with a scan rate of 1 mVs^{-1} in 0.5 M EtOH in 0.1 M KOH are indicated in the figures. 118

Figure 8.8: Intermediates and products occurring on the anodic side of the direct ethanol fuel cell. Schematic representation of the dual pathway mechanism for the electrooxidation of ethanol. 119

Figure 8.9: Selectivity-activity relationship for ethanol oxidation on supported $Pt_3Ni_1Rh_x$ octahedral electrocatalysts. First *in situ* linear sweep voltammetry scans (a) and corresponding integrated *in situ* FTIR ATR band intensities of (b) CO_2 (2342 cm^{-1}) and (c) partial oxidation pathway for CH_3CHO and CH_3COOH (1700 cm^{-1}) of *PtNiRh-oct/C* electrocatalysts during the electrooxidation of ethanol on *PtNiRh-1/C*, *PtNiRh-3/C* and *PtNiRh-6/C*. 128 interferograms (resolution 4 cm^{-1}) were collected and combined for each spectrum. The working electrode potential ranges during the first linear sweep voltammetry with a scan rate of 1 mVs^{-1} in 0.5 M EtOH in 0.1 M KOH are indicated in the figures. 120

Figure 9.1: Comparison of all electrocatalysts investigated in this thesis with comparable benchmark literature catalysts in acidic (0.1 M HClO_4 , Lit: PtRhSnO_2 from Li *et al.*⁶¹) and alkaline (0.1 M KOH , Lit: PtNi/C from Soundararajan *et al.*⁶³) media. 128

List of tables

Table 3.1: Suitable materials for FTIR prisms and their physical properties. ¹⁰²	36
Table 3.2: FTIR bands and designated vibrational modes of different species involved in the EOR. ^{104,105}	44
Table 5.1: Size, molar composition and metal weight loading of the supported PtRhSn electrocatalysts. The + sign indicates a stepwise addition and reduction of precursors.	69
Table 5.2: 2 θ values of electrocatalysts in comparison with tabulated diffraction patterns.	72
Table 5.3: Electrochemical EOR activity of Pt-Rh-Sn/C catalysts: electrochemical surface area (ECSA), current densities at 0.45 V vs. RHE and 0.6 V vs. RHE during voltammetric scans, and current density at constant 0.45 V vs. RHE after 300 s.	78
Table 5.4: Quantitative analysis of the XPS peaks of PtRhSn/C at KE: 550 eV. BAE denotes before acid exposure and AAE denotes after acid exposure.	80
Table 6.1: Molar composition, metal weight loading and crystallite sizes of the supported PtRhSn electrocatalysts.	89
Table 6.2: Electrochemical EOR activity of PtRhSn catalysts: electrochemical surface area (ECSA), current densities at 0.45 V vs. RHE and 0.80 V vs. RHE during voltammetric scans, and current density at constant 0.45 V vs. RHE after 300 s.	90
Table 7.1: Size, molar composition and metal weight loading of the supported PtRhSn and PtRhNi electrocatalysts.	99
Table 7.2: Electrochemical EOR activity of PtRhSn/C and PtRhNi/C catalysts: electrochemical surface area (ECSA), current densities at 0.45 V vs. RHE and 0.60 V vs. RHE during voltammetric scans, and current density at constant 0.45 V vs. RHE after 300 s.	105
Table 8.1: Size, molar composition and metal weight loading of the supported <i>PtNiRh-oct/C</i> electrocatalysts.	110
Table 8.2: Comparison of the experimental 2 θ values with theoretical 2 θ values for all <i>PtNiRh-oct/C</i> electrocatalysts deriving from Vegard's law for fcc phases. ^{177,178}	115
Table 8.3: Electrochemical EOR activity of <i>PtNiRh-oct/C</i> catalysts: electrochemical surface area (ECSA), current densities at 0.45 V vs. RHE and 0.80 V vs. RHE during voltammetric scans, and current density at constant 0.45 V vs. RHE after 1800 s.	117

Danksagung

Mein großer Dank geht an Prof. Dr. Peter Strasser für die Bereitstellung dieses spannenden und anspruchsvollen Promotionsthemas, neben der fachlichen und finanziellen Unterstützung vor allem für die persönliche Art und Weise der Betreuung und das in mich gesetzte Vertrauen selbständig und nach meinen eigenen hohen Ansprüchen forschen zu dürfen. Ich möchte Prof. Dr. Rüdiger-Albert Eichel für die Übernahme des Zweitgutachtens danken, insbesondere nachdem meine Begeisterung für das Thema mit einem durch ihn betreuten Praktikumsversuch vor vielen Jahren und Semestern begann. Ich danke Prof. Friedrich für die Übernahme des Prüfungsvorsitzes. Ich bedanke mich beim BMBF für die Aufnahme in das spannende und lehrreiche deutsch-chinesische Netzwerk zur Elektromobilität und allen involvierten internationalen Projektpartnern für viele interessante und anregende Diskussionen und Eindrücke auf unseren Meetings.

Meine große Dankbarkeit gilt Prof. Parmaconi Rodriguez, ohne dessen Unterstützung und bewundernswerte Einstellung zu Wissenschaft und Forschung diese Arbeit wohl nicht möglich gewesen wäre. Ich bedanke mich außerdem bei Prof. Dr. Marc Koper und Prof. Dr. Kylie Vincent für die kooperative Unterstützung meiner Forschungstätigkeit. Ich möchte mich bei Paul Krause, Dr. Stefan Rudi, Vera Beermann, Manuel Gliech, Annette Wittebrock und Rameshwori Loukrakpam für die praktische Unterstützung im Labor und ihren Beitrag zu weiten Teilen der hier vorgestellten Ergebnisse bedanken. Frau Mikaela Görli danke ich für die unglaublichen 3D Modellbilder des FTIR Setups, die diese Arbeit wunderschön abgerundet haben. Bei allen Autoren, mit denen ich gemeinsam veröffentlichen durfte, möchte ich mich für ihren Beitrag durch Daten, Kommentare und Unterstützung zur Perfektionierung unserer gemeinsamen Publikationen besonders danken. Dem gesamten Werkstattteam danke ich für die hervorragende und schnelle Anfertigung aller meiner ausgefallenen und ungewöhnlichen Wünsche. Frau Sabrina Wenzel danke ich für ihre Unterstützung über Promotionsangelegenheiten und Organisatorisches hinaus. Frau Dr. Stefanie Kühl danke ich für das unglaublich wertvolle Korrekturlesen im Paket mit der moralischen Unterstützung.

Ein ganz besonderes und herzliches Dankeschön gilt natürlich meinem gesamten Arbeitskreis, allen Weggefährten die vor mir den nächsten Schritt in ihr Leben nach der Promotion gegangen sind und alle die mich bis zum Ende begleitet und unterstützt haben, sei es durch viel fachliche Hilfsbereitschaft oder die herzliche Aufnahme in ein Team und eine Gruppe. Meine Zeit mit euch in Berlin war geprägt von vielen anregenden Gesprächen, regem Austausch und viel Freude. Ich hoffe euch auch in Zukunft noch oft innerhalb und außerhalb der elektrochemischen Clique treffen zu dürfen.

Meine Liebe und mein Dank für meine Familie, meinen Mann und meine Freunde sind für mich zu groß, um sie in Worte zu fassen. Das Glück, euch in meinem Leben zu haben, hat mich auf jedem Schritt hierher begleitet.

Σ' αγαπάω, βλάκος μου. Ας πάμε τώρα, απ' την γη στον ουρανό!

